3D Printing of Flexible Ionic Liquid Gel Sensors

Julian Smith-Jones

A dissertation

submitted in partial fulfillment of the

requirements for the degree of

Doctor of Philosophy

University of Washington

2023

Reading Committee:

Alshakim Nelson, Chair

Matthew R. Golder

Douglas A. Reed

Program Authorized to Offer Degree:

Chemistry

University of Washington

Abstract

3D Printing of Flexible Ionic Liquid Gel Sensors

Julian Smith-Jones

Chair of the Supervisory Committee:
Alshakim Nelson
Chemistry

3D printing has gained popularity due to the ability to fabricate complex structures from materials ranging from hard materials such as metal and concrete to softer materials including hydrogels and ion gels. Stretchable conductive materials have also attracted great attention due to their potential applications as strain sensors, wearable electronics, soft robotics, and medical devices. The fabrication of these materials with customized object geometries is desirable, but the methods to achieve them are still highly limited. 3D printing via vat photopolymerization can easily generate sophisticated object geometries, but there is still a significant need to print with materials that afford improved conductivity, mechanical properties, elastic recovery, and durability. Additionally, while 3D printing enables control over sensor design in multiple dimensions, customizability of a sensor toward different individual use cases is still limited because each sensor

requires a new design and manufacturing step. This thesis focuses on the development of ionic liquid gels as materials for conductive, elastomeric sensors. Chapter 1 serves as an introduction to 3D printing in general and discusses why ionic liquids are ideal materials for flexible devices. Chapter 2 discusses the application of ion gels as sensors and examines the effects of altering resin components on mechanical properties. Chapter 3 builds on these sensors by incorporating multiple ionic liquids into one structure. The difference in mechanical and elastic recovery properties produces shape transformation when strain is applied to the multi-material constructs. Lastly, chapter 4 seeks to improve the customizability of these ion gel sensors by incorporating dynamic bonds into the polymer networks to form covalent adaptable networks (CANs). The reversable covalent bonds introduced to the networks allow post-printing modification of the gels and facilitate fabrication of modular strain sensors.

TABLE OF CONTENTS

LIST OF FIGURES

LIST OF TABLES

LIST OF SCHEMES

ACKNOWLEDGEMENTS

I would like to begin by thanking Al Nelson for allowing me the opportunity to conduct research in his lab. I joined the Nelson lab at the end of my fourth year of graduate school, after I decided to leave my prior group. This was a difficult time for me since the decision to leave was one I had hoped to avoid, and I was weighing whether I wanted to continue with finishing my PhD. I thank Professor Xiaosong Li for meeting with me during this time as well and suggesting that I consider my other research interests before deciding to leave the department. After looking at several groups, I found the polymer chemistry being conducted in the Nelson lab. The science was compelling and seemed applicable industrially, which was the direction I felt I wanted to proceed in after graduate school. I reached out to friends I had in the group at that time, and they all spoke highly of the work they were doing and of Al as a PI. I decided to join the group, and everything I heard was exactly what I experienced. Al is a great PI. He is always friendly and willing to offer advice, whether it be about analyzing data or revising my CV. His expectations were always clear, and he took it upon himself to meet with us throughout the year to make sure we were on track and making progress with our projects and other goals. Al is also a great motivator and always encouraged me to present my research at conferences whenever possible. During my time in the group our lab joined the NSF center for the chemistry of molecularly optimized networks (MONET), and Al chose me to be the point person for our group. This gave me the opportunity to present at their annual meetings, collaborate with labs at schools across the country, and to expand my network by interfacing with other scientists with similar interests. I am grateful for being accepted into the group and for the support I received along the way.

I also want to thank my family for supporting me through this journey. Since elementary school my mom has always been a voice of reason and encouragement during my studies. No matter where I was studying at the time, she made a point to visit me and her visits were refreshing. She also was an instrumental part in convincing me to continue with graduate school. I appreciate the articles my dad would send me periodically. Some were more relevant than others, but they were always interesting and reminded me to think forward and explore interests beyond what I may be working on in the lab. My brother and I didn't talk all the time since we were both busy, but I have great memories of the time he visited and always looked forward to talking to him and his family over the holidays about our accomplishments over the past year. I am also appreciative of my girlfriend Arlesa and her son Zamani. Our time together has been great, and it pushes me to become more efficient and prioritize what is most important to accomplish that day.

I would like to thank my lab mates and the undergraduate students we've had come through the lab. These are the people I spent the most time with and had a large impact on my research. Our postdoc Fang was my mentor when I joined the group, and she was incredibly helpful in getting me adjusted to the chemistry done in the lab. We worked on a number of projects together that turned into publications and I'm grateful for her guidance. Jenn Wong was a member of my cohort who I first reached out to about potentially joining the Nelson lab, and her efficiency inspired me to do better work. Eva Sanchez was a postdoc when I first joined, and she was always willing to help me conduct experiments and provide insight. Just after Fang, Jenn, and Eva left, we got a new postdoc, Naroa Sadaba. Much like the others, she was a great resource when deciding what experiment to do next and was always willing to help me find the best setup. On multiple occasions we were on campus late in the mechanical engineering department trying to collect data on the Instron. Cem Millik, who I sat next to every day since joining the lab, was a great friend to

talk to and was always willing to let me bounce ideas off him, whether they be lab related or otherwise. We also spent many nights playing video games, which was a nice change of pace. Gokce Altin-Yavuzarslan was a graduate student in our lab when I joined, and she helped convince me that the Nelson lab was a great place to do research. Nathan Ballinger was an undergraduate student who joined the lab just before I did, and we began working on a project together after his first mentor Jenn graduated. Nathan was a pleasure to work with every day. He worked hard, had a positive attitude, and we frequently had discussions about the NBA while we were waiting for a reaction to finish. The younger members of our lab, Rowina, Chelsea, Siwei, Toni, Shannon, and Kinsey, have been a joy to work with as well. They brought new energy to the lab and helped me begin to see myself as more of a mentor rather than just a graduate student. I also appreciate the interactions I've had with the undergraduate and visiting students that have come through the lab. They all contributed to the positive and collaborative atmosphere we had in the group.

Lastly, I would like to thank the friends I've made during my time at UW. I have good memories of my cohort in our first year, struggling through homework sets in Rab's room. I also have fond memories of Friendsgiving dinners at Emily Cliffs house along with Tyler Robison, William Miller, Alex Dohoda, TK Kluherz, and some of their close friends. Alex has been a great friend throughout graduate school, and I value the conversations we've had about chemistry and other random topics at restaurants and bars over the years. Whenever I had a question regarding organic synthesis, I would always look for him and more often than not I came back with useful advice. I also thank Jon Kephart for being a good friend, watching my lizard when I'm out of town, and allowing me to cat-sit for him when he goes on a trip. All of the people mentioned here and some I may have unintentionally left off made my time at UW memorable, and I am glad we got to spend time together.

DEDICATION

This work is dedicated to my mom Karen Mendez, my dad Franklin Jones, my brother Avon Jackson and his family, and to the members of the Nelson lab who helped me achieve my goal.

Chapter 1. INTRODUCTION

1.1 Introduction to 3D Printing and Stimuli Responsive Materials

Additive manufacturing, also known as 3D printing, is a manufacturing technique developed in the late 1970s and early 1980s where an object is fabricated layer by layer.[1-6] This approach contrasts traditional manufacturing methods such as subtractive manufacturing (e.g. milling), whereby an object is created from a large block of material such as metal or plastic, and material is removed until the desired object is obtained.[7,8] Molding is another traditional manufacturing method in which a liquid substance is introduced to a hollow mold, causing the substance to adopt the shape of the mold's interior as it solidifies following application of compression or heat. 3D printing offers several benefits over these more traditional methods, including reduction of waste and lower costs. Subtractive manufacturing generates significant amounts of waste that may not be reusable in the next round of production.[7,9] Molding limits waste, however it remains difficult to create molds of objects with complex geometries. In addition, rapid design iteration is restricted in molding because it is costly and time consuming to fabricate a new mold for each new design.[6,9] 3D printing offers a solution to these issues because only the required parts of a desired object are printed, limiting material use and waste. Objects intended for 3D printing are created digitally using computer aided design (CAD) software, which provides the ability to rapidly iterate new designs at low cost and without the need to create new molds.

There are a variety of types of 3D printing, such as fused deposition modeling (FDM), direct ink writing (DIW), stereolithography apparatus (SLA), selective laser sintering (SLS), and binder jetting, among others.[4,8,10-14] The type of printer employed depends on the properties of the materials used, such as whether the material is a powder, photo-responsive liquid resin, or plastic

which can be melted. A wide range of materials are available for 3D printing, including hard materials such as ceramics, metals, and concrete, as well as softer materials such as sugars, hydrogels, and ion gels.[8,10,12,15-26] Applications for 3D printed objects are also wide ranging. Industrial 3D printers are used to create larger objects such as houses and parts for ships, automobiles, and aircraft. Smaller objects which can be 3D printed include healthcare monitors, soft robots, food, toys, and proof of concept prototypes.[27-41] 3D printing technology has improved sufficiently such that two-photon lithography has been utilized to 3D print sculptures on the tip of a pencil, with features possessing nm resolution.[42]

The increase in popularity of 3D printing has given rise to the field of 4D printing, where 3D objects change properties in response to external stimuli, with time serving as the fourth dimension.[11,15,17,18,25,43-63] These stimuli responsive materials have been designed to change shape or mechanical properties in response to light, heat, pH, magnetic field, and strain. Examples of stimuli responsive materials include mechanical grippers for soft robotics,[43,61,62] magneto-responsive polymer networks which change shape in response to external magnetic fields,[25,59,63] and flexible sensors which change shape upon the application of strain.[17,18]

1.2 Introduction of Ionic Liquids as Materials for Flexible Sensors

Ionic liquids (ILs) are organic salts which are liquid at temperatures below 100 °C. These materials consist of organic cations paired with organic or inorganic anions. The cations tend to be large, bulky, and asymmetric, which causes frustration of crystallization.[64-66] ILs are useful materials for 3D printing because they have highly tunable chemical structures, allowing for precise adjustment of material properties toward a desired application. For example, the anion can be altered to make the IL more or less hydrophobic, and substituents can be added to the organic cation to affect the viscosity or photo-responsive properties of the liquid salts. Due to their ionic nature ILs are also

conductive, and coulombic interactions lead to low vapor pressures. As a result, IL-swollen polymer networks are resistant to evaporation, which allows these ion gels to maintain their properties over extended periods of time. This is in contrast to water swollen networks (hydrogels), which are significantly affected by factors such as drying out as well as ambient conditions such as pH, humidity, and temperature. Changes to these conditions will affect the water content of the gel, which will considerably alter the performance of the material due to swelling or loss of water.[34,35,37,41]

ILs can be used to create elastomeric sensors for use in flexible devices. Applications for flexible sensors include healthcare monitors,[16,21,39-41,65,67] actuators and sensors in soft robotics,[12,14,28-33,48,61,62,68] and artificial skins.[34-38,69] Notable examples containing ILs include an ionic skin (i-skin) developed by Hao et al.[36] The material was ultra-stretchable (strain at break >10,000%), with an operating temperature range of −40 to 150 °C. The i-skin was comprised of poly (zwitterionic ionic liquid)-co-poly (acrylic acid) networks swollen with 1-ethyl-3-methyl-imidazolium ethyl sulfate and could be SLA 3D printed into wearable sensors used for monitoring human motion. Chossat et al.[69] utilized an IL-swollen network to develop a tactile sensor. A silicon-based elastomer was fabricated into a microchannel matrix filled with 1-ethyl-3-methylimidazolium ethyl sulfate which allowed predictable and reproducible sensing of changes in pressure. Chen et al.[20] developed an ionogel that functioned as both a pressure and temperature sensor. The network was primarily comprised of acrylamide and acrylic acid copolymerized in 1-ethyl-3-methylimidazolium ethyl sulfate. The presence of the IL afforded high sensitivity towards changes in pressure and temperature, which manifested as a drastic change in resistance (temperature coefficient of resistance (TCR) = 3.79 $°C^{-1}$). Jurinovs et al.[68] formulated a biobased IL gel by mixing 1-ethyl-3-methylimidazolium acetate with single walled carbon nanotubes

(SWCNTs) in acrylated rapeseed oil. The combination of IL and SWCNT provided excellent conductivity, and the material was able to be SLA 3D printed into functional actuators for soft robotics.

1.3 Controlling Properties of IL Resins

When formulating IL resins for SLA printing, two important parameters to consider are the resin viscosity and rate of photopolymerization. SLA printing involves a tray with a transparent base containing a photopolymerizable resin. When placed in the printer, the tray sits above a lens which houses a UV laser. The laser photopatterns cross-sectional areas of a 3D structure in a layer-wise fashion according to the parameters input into the CAD file. The 3D printed structure is assembled on an aluminum build plate that is suspended on a mechanical arm over the resin tray. The build plate is incrementally raised as each layer of the structure is deposited. The resin viscosity must remain below 10 Pa•s for the resin to flow during printing. This is important because as the build plate lifts out of the resin and is repositioned to print the next layer of the structure, the resin must be able to recoat the bottom of the print tray to avoid defects in the printed object. The rate of photocuring is important as well because the resin must cure quickly enough to adhere to the build plate, but not too quickly to prevent overcuring during the printing process which may result in a loss of resolution in printed features. These parameters can be controlled by modifying the amount of photoinitiator and photoabsorber incorporated into the resin.[22] The photoinitiator serves to initiate free radical polymerization of the resin, while the photoabsorber limits light scattering and improves the resolution of the printed structure.

Resin properties can also be controlled by altering the chemical structure of the ILs themselves. Subtle alterations to the chemical structure can result in significant changes in material properties. For example, in the photopolymerizable ionic liquids 1-vinyl-3-butyl imidazolium

bis(trifluoro methanesulfonyl)imide ([BVIM]TFSI) and 1-vinyl-3-ethyl imidazolium bis(trifluoromethanesulfonyl)imide ([EVIM]TFSI), the length of the alkyl substituent influences the viscosity of the IL as well as the viscoelastic properties of the resulting ion gel. The viscosity of [BVIM]TFSI resins are higher than those containing [EVIM]TFSI. Polymerized structures comprised of [BVIM]TFSI have lower Young's modulus and increased strain at break relative to structures comprised of [EVIM]TFSI. In both cases, polymerized networks solely comprising these ILs are brittle due to the formation of linear chains. Crosslinkers such as oligo and polyethylene glycol (PEG) have been demonstrated to provide increased elasticity to poly(IL) networks.[17,22,70] The amount of copolymer included in the resin affects the resin viscosity and viscoelastic properties of the polymerized network as well. In general, formulations with higher PEG content possess lower Young's modulus and increased strain at break. Higher PEG content yields a higher viscosity resin as well. The variety of parameters which can be altered to influence material properties provides a high degree of control when formulating resins for SLA printing.

1.4 CONCLUSION

The following chapters describe the formulation of IL resins for SLA printing of conductive, elastomeric ion gels. Chapter 2 introduces the application of these gels as strain sensors and investigates the effects of altering the w/w% of the resin components. Chapter 3 builds on these materials by combining multiple IL resins into one structure. Strain induced shape transformations are observed in these multi-material gels due to the difference in mechanical and shape recovery properties of the different materials. Finally, chapter 4 discusses the development of an IL covalent adaptable network (CAN) by introducing dynamic covalent bonds into the crosslinks of these polymer networks. The reversable nature of these crosslinks facilitates post-polymerization modification of the networks, allowing fabrication of modular ion gel strain sensors.

1.5 REFERENCES

[1] Swainson, W.K. Method, Medium and Apparatus for Producing Three-Dimensional Figure Product. U.S. Patent 4,041,476, 9 August **1977**.

[2] Herbert, A.J. Solid object generation. J. Appl. Photogr. Eng. **1982**

[3] Hull, C.W. Apparatus for Production of Three-Dimensional Objects by Stereolithography. U.S. Patent Appl. 638,905, **1984**

[4] Capel, A. J.; Rimington, R. P.; Lewis, M. P.; Christie, S. D. R. 3D Printing for Chemical, Pharmaceutical and Biological Applications. *Nat. Rev. Chem.* **2018**, *2* (12), 422–436.

[5] Ryan, K. R.; Down, M. P.; Banks, C. E. Future of Additive Manufacturing: Overview of 4D and 3D Printed Smart and Advanced Materials and Their Applications. *Chem. Eng. J.* **2021**, *403*, 126162.

[6] Truby, R. L.; Lewis, J. A. Printing Soft Matter in Three Dimensions. *Nature* **2016**, *540* (7633), 371–378.

[7] Sampson, K. L.; Deore, B.; Go, A.; Nayak, A.; Orth, A.; Gallerneault, M.; Malenfant, P. R. L.; Paquet, C. Multimaterial Vat Polymerization Additive Manufacturing. *ACS Appl. Polym. Mater.* **2021**, *3* (9), 4304–4324.

[8] Amziane, S.; Pierre, A.; Rangeard, D.; Sonebi, M.; Perrot, A. *3D Printing of Concrete: State of the Art and Challenges of the Digital Construction Revolution*; **2019**.

[9] Gibson, I.; Rosen, D.; Stucker, B. *Additive Manufacturing Technologies: 3D Printing, Rapid Prototyping, and Direct Digital Manufacturing, Second Edition*; **2015**.

[10] Fu, P.; Li, H.; Gong, J.; Fan, Z.; Smith, A. T.; Shen, K.; Khalfalla, T. O.; Huang, H.; Qian, X.; McCutcheon, J. R.; et al. 4D Printing of Polymers: Techniques, Materials, and Prospects. *Prog. Polym. Sci.* **2022**, *126*, 101506.

[11] Ahmed, A.; Arya, S.; Gupta, V.; Furukawa, H.; Khosla, A. 4D Printing: Fundamentals, Materials, Applications and Challenges. *Polymer* **2021**, *228*, 123926.

[12] Pacillo, G. A.; Ranocchiai, G.; Loccarini, F.; Fagone, M. Additive Manufacturing in Construction: A Review on Technologies, Processes, Materials, and Their Applications of 3D and 4D Printing. *Mater. Des. Process. Commun.* **2021**, *3* (5).

[13] Hartings, M. R.; Ahmed, Z. Chemistry from 3D Printed Objects. *Nat. Rev. Chem.* **2019**, *3*, 305–314.

[14] Wallin, T. J.; Pikul, J.; Shepherd, R. F. 3D Printing of Soft Robotic Systems. *Nat. Rev. Mater.* **2018**, *3* (6), 84–100.

[15] Liu, G.; Zhao, Y.; Wu, G.; Lu, J. Origami and 4D Printing of Elastomer-Derived Ceramic Structures. *Sci. Adv.* **2018**, *4* (8), 641–658.

[16] Wong, J.; Gong, A. T.; Defnet, P. A.; Meabe, L.; Beauchamp, B.; Sweet, R. M.; Sardon, H.; Cobb, C. L.; Nelson, A. 3D Printing Ionogel Auxetic Frameworks for Stretchable Sensors. *Adv. Mater. Technol.* **2019**, *4* (9), 1–6.

[17] Wong, J.; Basu, A.; Wende, M.; Boechler, N.; Nelson, A. Mechano-Activated Objects with Multidirectional Shape Morphing Programmed via 3D Printing. *ACS Appl. Polym. Mater.* **2020**, *2* (7), 2504–2508.

[18] Basu, A.; Wong, J.; Cao, B.; Boechler, N.; Boydston, A. J.; Nelson, A. Mechanoactivation of Color and Autonomous Shape Change in 3D-Printed Ionic Polymer Networks. *ACS Appl. Mater. Interfaces* **2021**, *13*, 19263–19270.

[19] Millik, S. C.; Dostie, A. M.; Karis, D. G.; Smith, P. T.; McKenna, M.; Chan, N.; Curtis, C. D.; Nance, E.; Theberge, A. B.; Nelson, A. 3D Printed Coaxial Nozzles for the Extrusion of Hydrogel Tubes toward Modeling Vascular Endothelium. *Biofabrication* **2019**, *11* (4).

[20] Chen, Z. J.; Sun, Y. Q.; Xiao, X.; Wang, H. Q.; Zhang, M. H.; Wang, F. Z.; Lai, J. C.; Zhang, D. S.; Pan, L. J.; Li, C. H. An Ultra-Tough and Ultra-Sensitive Ionogel Pressure/Temperature Sensor Enabled by Hierarchical Design of Both Materials and Devices. *J. Mater. Chem. A* **2023**, *11* (15), 8359–8367.

[21] Zanon, M.; Montalvillo-Jiménez, L.; Cue-López, R.; Martínez-Campos, E.; Sangermano, M.; Chiappone, A.; Bosch, P. Vat 3D Printing of Full-Alginate Hydrogels via Thiol-Ene Reactions towards Tissue Engineering Applications. *Polym. Chem.* **2023**.

[22] Narupai, B.; Wong, J.; Sanchez-Rexach, E.; Smith-Jones, J.; Le, V. C. T.; Sadaba, N.; Sardon, H.; Nelson, A. 3D Printing of Ionic Liquid Polymer Networks for Stretchable Conductive Sensors. *Adv. Mater. Technol.* **2023**, *2300226*, 1–9.

[23] Yang, W.; Cai, S.; Chen, Y.; Liang, W.; Lai, Y.; Yu, H.; Wang, Y.; Liu, L. Modular and Customized Fabrication of 3D Functional Microgels for Bottom-Up Tissue Engineering and Drug Screening. *Adv. Mater. Technol.* **2020**, *5* (5).

[24] Yang, L.; Sun, L.; Huang, H.; Zhu, W.; Wang, Y.; Wu, Z.; Neisiany, R. E.; Gu, S.; You, Z. Mechanically Robust and Room Temperature Self-Healing Ionogel Based on Ionic Liquid Inhibited Reversible Reaction of Disulfide Bonds. *Adv. Sci.* **2023**, *10* (20).

[25] Lantean, S.; Barrera, G.; Fabrizio Pirri, C.; Tiberto, P.; Sangermano, M.; Roppolo, I.; Rizza, G. 3D Printing of Magnetoresponsive Polymeric Materials with Tunable

Mechanical and Magnetic Properties by Digital Light Processing. *Adv. Mater. Technol.* **2019**, *4*, 1900505.

[26] Subbiah, R.; Hipfinger, C.; Tahayeri, A.; Athirasala, A.; Horsophonphong, S.; Thrivikraman, G.; Miranda França, C.; Araujo Cunha, D.; Mansoorifar, A.; Zahariev, A.; et al. 3D Printing of Microgel-Loaded Modular Microcages as Instructive Scaffolds for Tissue Engineering. *Adv. Mater.* **2020**, *32*, 1–7.

[27] Tibbits, S. 4D Printing: Multi-Material Shape Change. *Archit. Des.* **2014**, *84* (1), 116–121.

[28] Zhang, C.; He, B.; Wang, Z.; Zhou, Y.; Ming, A.; Thanh Dinh, N. Application and Analysis of an Ionic Liquid Gel in a Soft Robot. *Adv. Mater. Sci. Eng.* **2019**,

[29] Zhang, C.; He, B.; Ding, A.; Xu, S.; Wang, Z.; Zhou, Y. Motion Simulation of Ionic Liquid Gel Soft Actuators Based on CPG Control. *Comput. Intell. Neurosci.* **2019**.

[30] Ankit; Tiwari, N.; Ho, F.; Krisnadi, F.; Kulkarni, M. R.; Nguyen, L. L.; Koh, S. J. A.; Mathews, N. High-k, Ultrastretchable Self-Enclosed Ionic Liquid-Elastomer Composites for Soft Robotics and Flexible Electronics. *ACS Appl. Mater. Interfaces* **2020**, *12* (33), 37561–37570.

[31] Truby, R. L.; Wehner, M.; Grosskopf, A. K.; Vogt, D. M.; Uzel, S. G. M.; Wood, R. J.; Lewis, J. A. Soft Somatosensitive Actuators via Embedded 3D Printing. *Adv. Mater.* **2018**, *30* (15).

[32] He, B.; Zhou, Y.; Wang, Z.; Wang, Q.; Shen, R.; Wu, S. A Multi-Layered Touch-Pressure Sensing Ionogel Material Suitable for Sensing Integrated Actuations of Soft Robots. *Sensors Actuators, A Phys.* **2018**, *272*, 341–348.

[33] Feng, C.; Hemantha Rajapaksha, C. P.; Jákli, A. Ionic Elastomers for Electric Actuators and Sensors. *Engineering* **2021**, *7* (5), 581–602. https://doi.org/10.1016/j.eng.2021.02.014.

[34] Liu, Z.; Wang, Y.; Ren, Y.; Jin, G.; Zhang, C.; Chen, W.; Yan, F. Poly(Ionic Liquid) Hydrogel-Based Anti-Freezing Ionic Skin for a Soft Robotic Gripper. *Mater. Horizons* **2020**, *7* (3), 919–927.

[35] Gao, W.; Ota, H.; Kiriya, D.; Takei, K.; Javey, A. Flexible Electronics toward Wearable Sensing. *Acc. Chem. Res.* **2019**, *52* (3),

[36] Hao, S.; Li, T.; Yang, X.; Song, H. Ultrastretchable, Adhesive, Fast Self-Healable, and Three-Dimensional Printable Photoluminescent Ionic Skin Based on Hybrid Network Ionogels. *ACS Appl. Mater. Interfaces* **2022**, *14* (1), 2029–2037.

[37] Gao, N.; He, Y.; Tao, X.; Xu, X. Q.; Wu, X.; Wang, Y. Crystal-Confined Freestanding Ionic Liquids for Reconfigurable and Repairable Electronics. *Nat. Commun.* **2019**, *10* (1).

[38] Tie, J.; Mao, Z.; Zhang, L.; Zhong, Y.; Sui, X.; Xu, H. Highly Transparent, Self-Healing and Adhesive Wearable Ionogel as Strain and Temperature Sensor. *Polym. Chem.* **2022**, *13*, 4064–4075.

[39] Borayek, R.; Foroughi, F.; Xin, X.; Mohamed, A. M.; Abdelrahman, M. M.; Zedan, M.; Zhang, D.; Ding, J. Near-Zero Hysteresis Ionic Conductive Elastomers with Long-Term Stability for Sensing Applications. *ACS Appl. Mater. Interfaces* **2022**, *14* (9), 11727–11738.

[40] Choi, D. Y.; Kim, M. H.; Oh, Y. S.; Jung, S. H.; Jung, J. H.; Sung, H. J.; Lee, H. W.; Lee, H. M. Highly Stretchable, Hysteresis-Free Ionic Liquid-Based Strain Sensor for

Precise Human Motion Monitoring. *ACS Appl. Mater. Interfaces* **2017**, *9* (2), 1770–1780.

[41] Tian, K.; Bae, J.; Bakarich, S. E.; Yang, C.; Gately, R. D.; Spinks, G. M.; in het Panhuis, M.; Suo, Z.; Vlassak, J. J. 3D Printing of Transparent and Conductive Heterogeneous Hydrogel–Elastomer Systems. *Adv. Mater.* **2017**, *29* (10).

[42] UpNano. https://www.upnano.at/the-castle-on-a-pencil-tip/

[43] Ge, Q.; Sakhaei, A. H.; Lee, H.; Dunn, C. K.; Fang, N. X.; Dunn, M. L. Multimaterial 4D Printing with Tailorable Shape Memory Polymers. *Sci. Rep.* **2016**, *6*, 31110.

[44] Peng, W.; Yin, J.; Zhang, X.; Shi, Y.; Che, G.; Zhao, Q.; Liu, J. 4D Printed Shape Memory Anastomosis Ring with Controllable Shape Transformation and Degradation. *Adv. Funct. Mater.* **2023**, *33* (20), 2214505.

[45] Mauriello, J.; Maury, R.; Guillaneuf, Y.; Gigmes, D. 3D/4D Printing of Polyurethanes by Vat Photopolymerization. *Adv. Mater. Technol.* **2023**.

[46] Wan, X.; Luo, L.; Liu, Y.; Leng, J. Direct Ink Writing Based 4D Printing of Materials and Their Applications. *Adv. Sci.* **2020**, *7* (16).

[47] Ding, Z.; Yuan, C.; Peng, X.; Wang, T.; Qi, H. J.; Dunn, M. L. Direct 4D Printing via Active Composite Materials. *Sci. Adv.* **2017**, *3* (4).

[48] De Marco, C.; Pané, S.; Nelson, B. J. 4D Printing and Robotics. *Sci. Robot.* **2018**, *3* (18), 449.

[49] Liu, K.; Zhang, Y.; Cao, H.; Liu, H.; Geng, Y.; Yuan, W.; Zhou, J.; Wu, Z. L.; Shan, G.; Bao, Y.; et al. Programmable Reversible Shape Transformation of Hydrogels Based on Transient Structural Anisotropy. *Adv. Mater.* **2020**, *32* (28).

[50] Peng, B.; Yang, Y.; Gu, K.; Amis, E. J.; Cavicchi, K. A. Digital Light Processing 3D Printing of Triple Shape Memory Polymer for Sequential Shape Shifting. *ACS Mater. Lett.* **2019**, *1* (4), 410–417.

[51] Yi, C.; Qu, S.; Wang, Y.; Qi, H.; Zhang, Y.; Cheng, G. J. Optical Force Brush Enabled Free-Space Painting of 4D Functional Structures. *Sci. Adv.* **2023**, *9* (38), 1–13.

[52] Accardo, J. V; Kalow, J. A. Reversibly Tuning Hydrogel Stiffness through Photocontrolled Dynamic Covalent Crosslinks. Chem. Sci. **2018**, 9 (27), 5987–5993.

[53] Tang, Y.; Zhang, Y.; Chen, X.; Xie, X.; Zhou, N.; Dai, Z.; Xiong, Y. Up/Down Tuning of Poly(Ionic Liquid)s in Aqueous Two-Phase Systems. *Angew. Chemie - Int. Ed.* **2023**, *62* (4).

[54] Huang, J.; Yu, Z.; Wu, P. 3D Printing of Ionogels with Complementary Functionalities Enabled by Self-Regulating Ink. *Adv. Sci.* **2023**.

[55] Zhou, S.-W.; Yu, C.; Chen, M.; Shi, C.-Y.; Gu, R.; Qu, D.-H. Self-Healing and Shape-Shifting Polymers Controlled by Dynamic Bonds. *Smart Mol.* **2023**.

[56] Shmool, T. A.; Martin, L. K.; Jirkas, A.; Matthews, R. P.; Constantinou, A. P.; Vadukul, D. M.; Georgiou, T. K.; Aprile, F. A.; Hallett, J. P. Unveiling the Rational Development of Stimuli-Responsive Silk Fibroin-Based Ionogel Formulations. *Chem. Mater.* **2023**.

[57] Qin, J.; Sun, M.; Hu, W.; Cheng, J.; Fan, Z.; Du, J. Stimuli-Responsive Hydrogels for Cancer Immunotherapy. *Polym. Chem.* **2023**, *14* (7), 793–802.

[58] Lendlein, A.; Gould, O. E. C. Reprogrammable Recovery and Actuation Behaviour of Shape-Memory Polymers. *Nat. Rev. Mater.* **2019**, *4* (2), 116–133.

[59] Wu, H.; Wang, O.; Tian, Y.; Wang, M.; Su, B.; Yan, C.; Zhou, K.; Shi, Y. Selective Laser Sintering-Based 4D Printing of Magnetism-Responsive Grippers. *ACS Appl. Mater. Interfaces* **2021**, *13* (11), 12679–12688.

[60] Ouyang, H.; Li, X.; Lu, X.; Xia, H. Selective Laser Sintering 4D Printing of Dynamic Cross-Linked Polyurethane Containing Diels-Alder Bonds. *ACS Appl. Polym. Mater.* **2022**, *4* (5), 4035–4046.

[61] Gomez, E. F.; Wanasinghe, S. V; Flynn, A. E.; Dodo, O. J.; Sparks, J. L.; Baldwin, L. A.; Tabor, C. E.; Durstock, M. F.; Konkolewicz, D.; Thrasher, C. J. 3D-Printed Self-Healing Elastomers for Modular Soft Robotics. *ACS Appl. Mater. Interfaces* **2021**, *13*, 28870–28877.

[62] Shintake, J.; Cacucciolo, V.; Floreano, D.; Shea, H. Soft Robotic Grippers. *Adv. Mater.* **2018**, *30* (29), 1707035.

[63] Zhang, Z.; Heron, J. T.; Pena-Francesch, A. Adaptive Magnetoactive Soft Composites for Modular and Reconfigurable Actuators. *Adv. Funct. Mater.* **2023**.

[64] Migliorati, V.; Del Giudice, A.; Casu, A.; Falqui, A.; Podestà, A.; Milani, P.; Borghi, F. Crystalline Structuring of Confined Ionic Liquids at Room Temperature. *J. Phys. Chem. C* **2022**, *126* (31), 13477–13484.

[65] Fan, X.; Liu, S.; Jia, Z.; Koh, J. J.; Yeo, J. C. C.; Wang, C. G.; Surat'man, N. E.; Loh, X. J.; Le Bideau, J.; He, C.; et al. Ionogels: Recent Advances in Design, Material Properties and Emerging Biomedical Applications. *Chem. Soc. Rev.* **2023**, *52* (7), 2497–2527.

[66] Néouze, M. A.; Le Bideau, J.; Gaveau, P.; Bellayer, S.; Vioux, A. Ionogels, New Materials Arising from the Confinement of Ionic Liquids within Silica-Derived Networks. *Chem. Mater.* **2006**, *18* (17), 3931–3936.

[67] Bansal, A. K.; Hou, S.; Kulyk, O.; Bowman, E. M.; Samuel, I. D. W. Wearable Organic Optoelectronic Sensors for Medicine. *Adv. Mater.* **2015**, *27* (46), 7638–7644.

[68] Jurinovs, M.; Barkane, A.; Platnieks, O.; Grase, L.; Gaidukovs, S. Three Dimensionally Printed Biobased Electrodes: Ionic Liquid and Single-Walled Carbon Nanotube Hybrids in a Vegetable Oil Matrix for Soft Robotics. *ACS Appl. Polym. Mater.* **2023**, *5* (9), 7120–7131.

[69] Chossat, J. B.; Shin, H. S.; Park, Y. L.; Duchaine, V. Soft Tactile Skin Using an Embedded Ionic Liquid and Tomographic Imaging. *J. Mech. Robot.* **2015**, *7* (2).

[70] Zhang, J.; Chen, Z.; Zhang, Y.; Dong, S.; Chen, Y.; Zhang, S. Poly(Ionic Liquid)s Containing Alkoxy Chains and Bis(Trifluoromethanesulfonyl)Imide Anions as Highly Adhesive Materials. *Adv. Mater.* **2021**, *33* (30), 1–10.

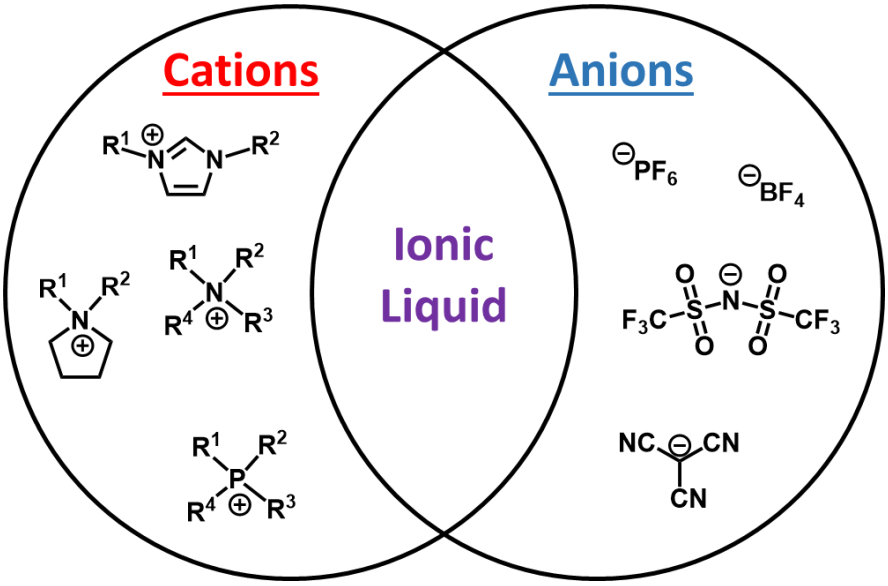

Figure 1.1 Example of cations and anions utilized to create ionic liquids.

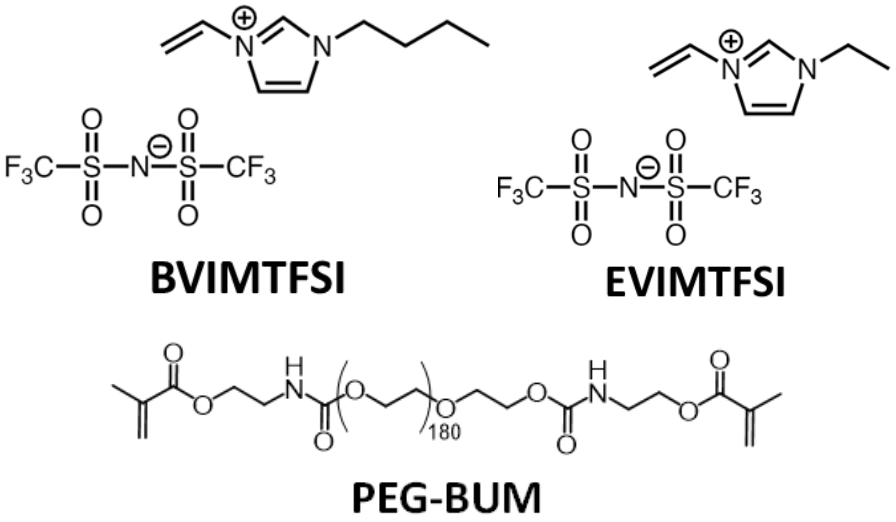

Figure 1.2 Chemical structures of photopolymerizable ionic liquids 1-vinyl-3-butyl imidazolium bis(trifluoromethanesulfonyl)imide ([BVIM]TFSI) and 1-vinyl-3-ethyl imidazolium bis(trifluoromethanesulfonyl)imide ([EVIM]TFSI), as well as crosslinker polyethylene glycol bis(urethane) methacrylate (PEG-BUM).

Chapter 2. 3D PRINTING OF IONIC LIQUID POLYMER NETWORKS FOR STRETCHABLE CONDUCTIVE SENSORS

Adapted with permission from Narupai, B.; Wong, J.; Sanchez-Rexach, E.; Smith-Jones, J.; Le, V. C. T.; Sadaba, N.; Sardon, H.; Nelson, A. 3D Printing of Ionic Liquid Polymer Networks for Stretchable Conductive Sensors. Adv. Mater. Technol. **2023**, 2300226.

2.1 ABSTRACT

Stretchable conductive materials have attracted great attention due to their potential applications as strain sensors, wearable electronics, soft robotics, and medical devices. The fabrication of these materials with customized object geometries is desirable, but the methods to achieve them are still highly limited. Additive manufacturing via vat photopolymerization can generate sophisticated object geometries, but there is still a significant need to print with materials that afford improved conductivity, mechanical properties, elastic recovery, and durability. Here we report stretchable strain sensors with a range of 3D printed designs using vat photopolymerization. Ionic liquid resins were optimized for their printability using Sudan I as a photoabsorber and used to fabricate 3D objects that were subjected to compression, stretching, and bending loads that were detected as real-time changes in current. Additionally, the self-adhesive nature of these materials enabled mechanically damaged structures to be mended together to regain their function as strain sensors. These ionic liquid resins are compatible with commercial 3D printers, which enhances their applicability for on-demand production of customized devices.

2.2 INTRODUCTION

Stretchable conductive materials are of significant attention for their use in applications that include wearable electronics,[1-3] sensors,[4] human-machine interface,[5-7] biomedical devices,[8-9] and soft robotics.[10-11] Substantial progress has been achieved in the field to create stretchable and wearable conductive devices, which can comprise conductive metals, carbon nanotubes, or graphene encapsulated in an insulating soft matrix such as silicone.[12-16] Conductive metals and fillers are intrinsically not stretchable; thus, the sensors either lack the ability to withstand large mechanical strain, or must utilize patterned metal wires that can undergo large deformations.[17-18]

Ionic liquids have emerged as a promising candidate for stretchable and wearable electronics due to high thermal and chemical stability, wide electrochemical windows, high ionic conductivity, and negligible vapor pressure.[19-26] Sun and co-workers reported an ionic conductor that comprised of poly(acrylic acid) and 1-butyl-3-methylimidazolium trifluoromethanesulfonate to afford an ion gel that exhibited high stretchability, transparency, and self-adhesion.[27] This approach used traditional casting techniques to fabricate structures, which limits the complexity of the architectures that can be formed.[28-30] The future implementation of wearable electronics and sensors may require object geometries that are specific to an individual or a specific application. In such cases, 2D patterning may be insufficient to meet the demands for more complex 3D designs.

Additive manufacturing (AM), also known as 3D printing, is a versatile platform to fabricate customized objects with locally tuned chemical compositions and intricate architectures.[31-35] AM offers the ability to print object geometries and designs such as lattice structures, hollow objects, auxetic structures and graded materials, which are not accessible through traditional manufacturing methods.[36-37] In addition, AM can fabricate personalized objects

that are customized to an individual to improve wearable comfort. While several different AM techniques are available, vat photopolymerization is especially well-suited to fabricate complex high-resolution objects with excellent accuracy and reproducibility.[38-39] However, the development of materials that are specifically designed for vat photopolymerization to afford functional stimuli-responsive objects is still limited.

A broad array of ionic liquids has been utilized to create 3D strain sensors.[40-42] Zhang and co-workers developed 3D printed strain sensors using a poly(ionic liquid) and a hyperbranched polymer as a macro-crosslinker.[43] The ionogel exhibited high stretchability (>1000% strain), high ionic conductivity (5.8 mS/cm), and excellent thermomechanical stability (-75 – 200 °C). Song and coworkers also reported 3D printed photoluminescent ionic skin based on hybrid network ionogels composed of poly(zwitterionic ionic liquid)-*co*-poly(acrylic acid) and hyperbranched polymer.[44] These ionogels were ultra-stretchable, strongly adhesive, and self-healable strain and touch sensors. Song et al. further showed the 3D printing of conductive, stretchable poly(ionic liquids) with high toughness, ultra-strong adhesive properties, and rapid self-healing.[45] Zhuo and coworkers reported 3D printed ionogels composed of a carboxylic ionic liquid and copolymerized acrylic acid/alkyl acrylate.[46] This elastomer, which also functions as a strain sensor, exhibited 100% autonomous self-healing efficiency. While these recent reports demonstrate the successful 3D printing of stretchable strain sensors using ionic liquids, the challenge of achieving complex geometries that include over-hanging features, large voids, and good resolution has not been addressed.

Here we demonstrate a low viscosity, photopolymerizable ionic liquid resin for vat photopolymerization to 3D print conductive, stretchable sensors. The ionic liquid polymer network was prepared by photopolymerization of 1-butyl-3-vinylimidazolium bis(trifluoromethane)

sulfonamide ([BVIM]TFSI), poly(ethylene glycol)-bisurethane methacrylate (PEG-BUM) as a photocrosslinker, phenylbis(2,4,6-trimethylbenzoyl) phosphine oxide (BAPO) as a photoinitiator, and Sudan-I as a photoabsorber (Figure 2.1a). Different concentrations of photoinitiator, photoabsorber, and crosslinker were studied to investigate the printability, resolution, and mechanical properties of printed structures. To the best of our knowledge, there have been no reports on using photoabsorber to tune the mechanical properties and resolution of 3D printed poly(ionic liquids) strain sensors. A variety of 3D printed complex geometries were photopatterned using a commercially available Form 2 printer and the structures were then further cured with 405 nm light to polymerize unreacted monomers (Figure 2.1b-c). The resulting ionic gels exhibited good conductivity, high stretchability, excellent elastic recovery, strong adhesion to a range of materials, and self-adhesion. Wearable stretchable sensors were 3D printed and used as strain sensors to detect human motions. The sensors exhibit an electrical response to strain and remain conductive after structural damage. Importantly, they also show self-adhesive behavior enabling the repair of mechanically damaged structures to regain ionic conductivity and mechanical strength.

2.3 Results & Discussion

2.3.1 *Resin Formulation for Vat Photopolymerization*

During vat photopolymerization, the poly(ionic liquid) networks were formed via photo-initiated radical polymerization of the vinyl imidazolium monomers with the methacrylates of the PEG-BUM cross-linker. We first investigated a series of photoinitiators including BAPO, lithium phenyl trimethylbenzoylphosphinate (LAP), ivocerin and ruthenium tris(bipyridyl) chloride with sodium persulfate ((Ru(bpy)$_3$Cl) with SPS) on resin printability. The resin formulations tested comprised 0.6 wt% photoinitiator (except for 0.05 wt% Ru(bpy)$_3$Cl with 0.18 wt% SPS), 11 wt%

PEG-BUM and [BVIM]TFSI. BAPO provided good solubility and afforded the best resolution of 3D printed architecture while $Ru(bpy)_3Cl$) with SPS system was not printable due to poor solubility (Figure A4).

Two important parameters for stereolithography apparatus (SLA) printing are resin viscosity and rate of photocuring, which can be evaluated via rheology. A resin with high viscosity (>10 Pa·s) is slow to reflow and self-level, resulting in unsuccessful prints. Additionally, a slow rate of photocuring could require long irradiation times for each layer, making it unsuitable for SLA printing.[47-52] All of the formulations tested afforded a sufficiently low viscosity (less than 1 Pa·s), which is appropriate for any type of vat photopolymerization (Figure 2.2a).[53-55] Since the irradiation time and the wavelength of light (405 nm) of Form 2 printers are not adjustable, the resin formulations required further optimization for printing. Photorheology was used to investigate the cure rate of resin formulations. Upon irradiation with 405 nm light, the storage modulus of the resin increased and plateaued at ~80 MPa within 5 s. The BAPO concentrations tested ranged from 0.04 to 4 wt%. Interestingly, the ideal range for BAPO was between 0.4-0.8 wt%; outside of this range, the cure rate was lower. These observations are consistent with too few or too many initiating sites during printing, respectively (Figure 2.2b).

2.3.2 *Effect of Resin Components on Material Properties*

We further investigated the influence of BAPO concentrations on the mechanical properties of printed cylindrical specimens via uniaxial compression tests. The compressive modulus increased with BAPO concentration between 0.04 to 0.4 wt% (Figure 2.2c) and decreased with the BAPO concentrations between 0.6 and 0.8 wt% (Figure A5). In addition, we evaluated the printability and the resolution limit of printed structures using BAPO concentrations of 0.04, 0.08, 0.2, 0.4, 0.6, 0.8, 2 and 4 wt%. The resin formulation of 0.6 wt% BAPO offered the best resolution where

the printed structure exhibited sharp edge and resolved hollow architecture (Figure A6-7). The resins of 2 wt% and 4 wt% BAPO afforded incomplete structures due to excess photoinitiator. We hypothesize that excess BAPO absorbed and blocked the light needed to penetrate and cure the rest of the structure. In contrast, using too little BAPO (0.04-0.2 wt%) resulted in unresolved features. This might be because fewer BAPO molecules absorb less light, so any excess light can penetrate and cure through previous layers of the printed structure.

Sudan-I has been used as a photoabsorber to control the optical path length of incident light.[56] In 3D printing, Sudan-I can reduce the penetration depth of the light and prevent photocuring in unwanted areas, such as in previous layers of a printed construct.[57] Therefore, Sudan-I was added in our resin formulations to improve the resolution of printed structures. We investigated the influence of Sudan-I on printability, resolution, viscosity, cure rate and mechanical properties. Resin formulations were comprised of 11 wt% PEG-BUM, 0.6 wt% BAPO, [BVIM]TFSI and different concentrations of Sudan-I including 0.01, 0.02, 0.03 and 0.04 wt%. Addition of Sudan-I at various concentrations did not increase the viscosity of the resins, which remained below 1 Pa·s (Figure 2.2d). In addition, photorheology with 405 nm irradiation showed that increasing the amount of Sudan-I reduced the rate of photocuring (Figure 2.2e). Interestingly, the addition of Sudan-I notably decreased the compressive moduli: 2.81, 1.37, 0.66 and 0.35 MPa with 0.01, 0.02, 0.03 and 0.04 wt% Sudan-I, respectively. Additionally, compressive stress at 50% strain also decreased with an increased amount of Sudan-I (Figure 2.2f, Figure A8). Stereomicroscopy was performed to evaluate the resolution of printed structures shown in Figure 2.2g. Addition of Sudan-I significantly improved the resolution of the 3D printed constructs. Using 0.04 wt% of Sudan-I afforded the best resolution with resolved complex geometry and clear hollow space (Figure 2.2g). Since Sudan-I affected both the printing resolution and mechanical properties

simultaneously, the amount of Sudan-I used in the resin formulation needed to be optimized for both properties. In this study, we selected 0.02 wt% Sudan-I as the concentration used in all subsequent experiments because higher amounts of Sudan-I afforded brittle constructs which were difficult to remove from the printer.

2.3.3 *Mechanical Properties of Ion Gel Sensors*

An important feature of flexible and wearable electronics is their stretchability and elastic recovery. We hypothesized that linear polymeric crosslinkers could afford high stretchability because a stored length of polymer chain could be released during mechanical deformation.[58-61] PEG-BUM (M_n = 8000 Da) was synthesized and used as photocrosslinker. The relationship between the amount of photocrosslinker and mechanical properties was examined using resin formulation comprising of 0.6 wt% BAPO, 0.02 wt% Sudan-I, [BVIM]TFSI and different amount of PEG-BUM (7, 11 and 15 wt%). The compressive stress-strain curve is shown in Figure 2.3a. As expected, an increase in the amount of PEG-BUM decreased the rigidity of materials. The compressive elastic modulus of 7, 11 and 15 wt% PEG-BUM were 3.23, 2.06 and 1.56 MPa, respectively (Figure A9). We further investigated the stretchability of these materials via tensile tests. 3D printed tensile dogbones with 7 wt% PEG-BUM can be elongated up to 920% strain, demonstrating excellent stretchability while 11 and 15 wt% PEG-BUM exhibited 770% and 580% strain, respectively (Figure 2.3c). The decreasing strain at break with increasing PEG-BUM content is consistent with the higher degree of crosslinking in the cured polymer network.

To examine the elastic recovery, cyclic compression tests and cyclic tensile stress-strain fatigue tests were performed. Figure 2.3b shows the fully elastic recovery of a 3D printed cylinder using 15 wt% PEG-BUM after 10 cycles of 50% strain. Additionally, Figure 2.3e and 2.3f showed the stress-strain curves of dogbones during the loading-unloading process with 50% tensile strain.

The result demonstrated good stretchability and recoverability. To highlight both the range of printable geometries and elastomeric properties of the materials, we 3D printed a puppy, lattice structure and Eiffel Tower with a formulation of 15 wt% PEG-BUM, 0.6 wt% BAPO, 0.02 wt% Sudan-I and [BVIM]TFSI. We applied mechanical loads on these 3D printed structures by stretching the puppy legs, compressing the lattice structure, and bending the Eiffel Tower (Figure 2.3g-i). All of them rapidly recovered back to the original state, confirming excellent elastic recovery behavior which is ideal for flexible electronic devices. In addition, the thermogravimetric analysis (TGA) showed negligible water absorption by these materials and a decomposition temperature above 320 °C, which confirms excellent thermal stability of the materials (Figure 2.3d).

2.3.4 *Conductivity of Ion Gel Sensors*

One of the most attractive features of ionic liquids is they offer high ionic conductivity. The electrochemical properties of these ionic liquid polymer networks were measured by electrochemical impedance spectroscopy. The as-printed ionic liquid gels showed high ionic conductivity up to 0.72 mS/cm for 7 wt% PEG-BUM, while increasing %PEG-BUM decreased ionic conductivity to 0.66 and 0.58 mS/cm for 11 and 15 wt% PEG-BUM. The decrease in conductivity is due to the reduction of ionic liquid content. Additionally, printed structures were subjected to a post-print curing step with 405 nm for 1 h to induce further cross-linking of uncured monomers and polymerizable ionic liquid within the materials. The ionic liquid gels with 7, 11 and 15 wt% PEG-BUM showed ionic conductivity of 0.014, 0.021, 0.037 mS/cm, respectively. The ionic conductivity of materials with post-curing were an order of magnitude lower than the as-printed materials, suggesting that the crosslinked network restricted the ionic mobility. This result is evidenced by a 34% mass loss for printed structures with post-print curing and 73% mass

loss for structures without post-print curing. The difference in mass loss demonstrates the influence of free ionic liquid in printed structures on ionic conductivity (Table A1). It should be noted that the mechanical properties of printed structures with post-curing were 10 times stronger than as-printed structures (Figure A10). Therefore, the materials were post-cured with 405 nm for 1 h after print in all subsequent experiments.

Based on the ionic conductivity of the materials, we tested their capability as strain sensors by applying a constant potential to 3D printed structures and measuring the changes in current in response to mechanical deformation of the printed objects. The current changes in response to the mechanical motions can be explained by the expression

$$V/I = \rho(L/A) \tag{2.1}$$

which represents the relationship between voltage (V), current (I), resistivity (ρ), material length (L), and cross-sectional area (A).[62-63] We first tested a 3D printed lattice by manually compressing it by hand and observed a large current fluctuation (Figure 2.4a). As the lattice structure was compressed, the cross-sectional area increased, causing a rise in current. Likewise, when the mechanical load was removed, the current rapidly dropped. In the second example, we tested an hourglass shaped auxetic structure (Figure 2.4b) with different tensile loads. We manually stretched the auxetic structure over multiple cycles to different magnitudes of strain. The auxetic structures were highly sensitive to slight changes in elongation. (Figure 2.4b).

A powerful feature of 3D printing is the ability to print personalized objects. To highlight this capability, a wearable strain sensor was 3D printed and used to detect various human physiological activities. The lattice cylinder can detect the bending motion of a finger in real time, demonstrating excellent performance for detecting human joint motions and differentiating between 0°, 45° and 90° bending angles (Figure 2.4c). Then, the cylinder was intentionally cut

multiple times to investigate the operation of the sensor in the event of damage. Remarkably, this lattice cylinder remained operational even after extensive structural damage (3 separate cuts) was introduced (Figure 2.4d).

2.3.5 *Adhesive Properties of Ion Gel Sensors*

An additional attractive feature of this material is its adhesive behavior, which is highly desirable for wearable devices.[64-67] We tested the adhesive performance of a 3D printed squirrel by adhering it to various substrate surfaces. The 3D printed structure strongly adhered to cardboard (2x heavier than the printed squirrel), a razor blade (2x), glass slide (10x) and glass vial (20x) as shown in Figure 2.5a. The strong adhesion between the printed ionic liquid polymer network and substrates may be explained by the various interactions between those surfaces including hydrogen bonds, electrostatic interactions, ion-dipole interactions and van der Waals interactions.[44-45] The ionic liquid polymer network also exhibited self-adhesion. For example, a 3D printed Eiffel Tower was cut and then re-attached. Surprisingly, the reattached Eiffel Tower was highly stretchable (Figure 2.5b). Moreover, when a dogbone specimen was cut and re-attached, the self-adhered structure withstood a weight up to 100 g. We hypothesized that this strong adhesion was the result of hydrogen bonding interactions together with electrostatic interaction between alkoxy moieties of PEG-BUM backbone and imidazolium cation coupled with bis(trifluoromethanesulfonimide) anion from ionic liquid. These interactions have been reported to be responsible for the adhesive behavior of other similar ionic liquid systems.[68-69] Tensile experiments were conducted to quantitatively evaluate the self-adhesion strength. The stress-strain curves showed an elongation at break around 170%, 200%, and 350% when the two halves of a dogbone were reattached under ambient conditions, in the dark, and under 405 nm exposure, respectively (Figure A11). We also

observed that the healing time and the number of reattachments influenced the self-adhesion strength (Figure A12-13).

The self-adhesive feature of these materials also enables recovery of conductivity, which can increase the reliability and service lifetime of wearable devices. Thus, we investigated the ionic conductivity of printed structures after self-adhesive reattachment. For example, the tower shown in Figure 2.5c exhibited a current of 27 nA in its resting state, but the current was lost when the structure was cut into two parts. Upon re-adhesion, the current was instantaneously recovered (45 nA, Figure 2.5c). The self-adhesive strength was further examined for the reattached dogbone. As expected, the current recovered instantly when two halves of the dogbone were reattached. Importantly, the dogbone could still be stretched and remained operational as a strain sensor, although full recovery of the material strength was not observed (Figure 2.5d). These results indicate that strain sensors based on ionic liquid polymer networks afford robust devices that can undergo self-adhesive repair to regain function.

2.4 Materials & Methods

2.4.1 *General Reagent Information*

All purchased reagents were used as received without further purification unless otherwise specified. 1-vinylimidazole (>98.0%), 1-bromobutane (>99.0%), 2-isocyanoethyl methacrylate (>98.0%, stabilized with BHT), dibutyltin dilaurate (>95.0%) were purchased from TCI America. Lithium bis(trifluoromethane) sulfonamide salt (99.95%), methanol, and ethyl acetate were purchased from Millipore Sigma. Polyethylene glycol (PEG)-8000, diethyl ether (anhydrous, stabilized with BHT), acetonitrile, and dichloromethane were purchased from Fisher Scientific. Dry dichloromethane was obtained from a Pure Process Technology purification system.

2.4.2 *General Analytical Information*

^{1}H NMR spectra were collected on a Bruker Avance 500 MHz spectrometer. The spectrometer was equipped with a Bruker triple resonance TXI probe and interfaced with a computer running Red Hat Enterprise Linux 6.3 and Topspin 2.1 software. ^{13}C NMR and ^{19}F NMR spectra were recorded on a Bruker Avance DRX499 spectrometer, equipped with a Bruker triple resonance BBO probe, and interfaced with a computer running Red Hat Enterprise Linux 6.2 and Topspin 1.3 software. Microscopy images were taken with Axiozoom: Zeiss Axio Zoom.V16 microscope, PAA A053. All rheological measurements were performed on a TA Instruments Discovery HR-2 hybrid rheometer equipped with Peltier temperature control accessory. Mechanical tests were performed on a Test Resources Universal Testing Machine. Thermogravimetric analysis was conducted on TA Instruments Q5000 TGA. Samples were sealed in an aluminum pan and heated from 10 to 600 °C under N_2 atmosphere.

2.4.3 *Synthesis of PEG-bisurethane methacrylate (PEG-BUM)*

A Teflon stir bar and 60 g of PEG-8000 (0.0075 mol) were dried under vacuum for 12 h in a single-neck 1 L round-bottom flask. The flask was then backfilled with dry nitrogen. Maintaining positive N_2 flow, 550 mL of anhydrous DCM was added to the round-bottom flask and stirred at 30 °C until PEG was fully dissolved. 0.89 mL (0.0015 mL) dibutyltin dilaurate was added to the solution. A 50 mL addition funnel was attached to the round-bottom flask. In a separate 100 mL round-bottom flask, 50 mL of anhydrous DCM and 5.3 mL (0.0375 mol) of 2-isocyanatoethyl methacrylate was added and swirled to mix. The isocyanate/DCM mixture was transferred to the addition funnel, which was adjusted to slowly (about 1 drop per second) add the isocyanate solution to the reaction mixture. Following complete addition of isocyanate, the addition funnel was removed and left to stir at 30 °C for 2 d under nitrogen. The reaction mixture was then

concentrated on a rotary evaporator at 30 °C until viscous and precipitated twice in diethyl ether. The product was then collected via vacuum filtration and dried at room temperature under high vacuum using a Schlenk manifold (Yield: 20.67 g, >95%). ^{1}H NMR (500 MHz, CDCl3) δ 6.16 (s, 1H), 5.64 (s, 1H), 5.19 (s, 1H), 4.28 (s, 4H), 1.99 (s, 3H), protons from PEG appear at 3.69 ppm. IR (ATR-FTIR, ν_{max}, cm^{-1}): 2881, 2742, 2697, 1979, 1718, 1533, 1467, 1359, 1341, 1279, 1289, 1146, 1095, 1059, 959, 945, 840.

2.4.4 *Synthesis of 1-vinyl-3-butyl imidazolium bromide ([BVIM]Br)*

Under neat conditions, 200 mL (2.2 mol) 1-vinyl imidazole and 285 mL (2.65 mol) 1-bromobutane were stirred magnetically at 45 °C for 24 h. The viscous solution was allowed to cool before washing 3-4 times with excessive diethyl ether until the liquid solidifies. The white solid product was collected by vacuum filtration and dried at room temperature under high vacuum using a Schlenk manifold (Yield: 456.23 g, 90.1%). ^{1}H NMR (500 MHz, DMSO-d_6): δ 9.61 (s, 1H), 8.24 (t, 1H), 7.97 (t, 1H), 7.33 (m, 1H), 6.00, 5.43 (d of d, 2H), 4.22 (t, 2H), 1.81 (q, 2H), 1.30 (m, 2H), 0.91 (t, 3H). ^{13}C NMR (300 MHz, $CDCl_3$): δ 135.22, 128.74, 123.17, 119.17, 108.57, 48.81, 30.98, 18.68, 13.19. IR (ATR-FTIR, ν_{max}, cm^{-1}): 3110, 3093, 3039, 3024, 2968, 2928, 2871, 1652, 1566, 1539, 1457, 1367, 1159, 982, 926, 880, 804, 739, 659, 603.

2.4.5 *Synthesis of 1-vinyl-3-butyl imidazolium bis(trifluoromethane)sulfonamide ([BVIM]TFSI)*

96.34 g (0.42 mol) of [BVIM]Br and 122.6 g (0.427 mol) of lithium bis(trifluoromethane) sulfonamide salt were dissolved in 160 mL of DI water and stirred at room temperature for 48 h. The biphasic mixture was then poured into a separatory funnel and the ionic liquid layer was extracted from the water layer and passed through a column of neutral alumina. The product

appears as a clear liquid (Yield: 152.12 g, 84%). ^{1}H NMR (500 MHz, DMSO-d_6): δ 9.46 (s, 1H), 8.18 (t, 1H), 7.91 (t, 1H), 7.28 (m, 1H), 5.96, 5.42 (d of d, 2H), 4.19 (t, 2H), 1.80 (q, 2H), 1.27 (m, 2H), 0.91 (t, 3H). ^{13}C NMR (300 MHz, $CDCl_3$): δ 135.28, 128.85, 123.21, 119.16, 108.58, 48.97, 31.03, 18.77, 13.15. ^{19}F NMR (500 MHz, DMSO-d_6): δ -78.6. IR (ATR-FTIR, ν_{max}, cm^{-1}): 3150, 3110, 2968, 2945, 2880, 1656, 1572, 1552, 1464, 1347, 1328, 1177, 1132, 1052, 952, 916, 845, 788, 739, 652, 612, 569.

2.4.6 *Resin Preparation*

To prepare 13 g of the final formulation resin, 15 wt% (2 g) PEG-BUM, 0.6 wt% (0.075 g) BAPO, and 0.02 wt% (0.0025 g) of Sudan-I were added to an amber vial. 11 g of [BVIM]TFSI was then added, and the mixture was vortexed for 10-15 mins until it was fully dissolved.

2.4.7 *3D Printing Process*

The resin was poured into a customized resin tray and the print was initiated. The completed structure was removed from the build plate carefully using a putty knife and residual resin was removed by gently rolling the structure in kimwipes until minimal resin remains. If the shape of the structure permits, the printed structures may be centrifuged at 1000 RPM for one minute to help remove residual resin. The structure was then post-cured using 405 nm light for 30 mins on one side, flipped, then cured for an additional 30 mins on the other side.

2.4.8 *Rheology*

All experiments were conducted on the TA DHR-2 rheometer. All viscosity vs. Shear rate experiments were conducted using an Advanced Peltier Plate, a stainless steel 8 mm geometry, measuring the viscosity at 25 °C over a shear range of 0.01 to 100 s^{-1}. All photorheology

experiments were performed using a 405 nm LED UV-curing accessory. The samples were first equilibrated for 60 s, followed by 9 min of irradiation with 405 nm light.

2.4.9 *Compression Test*

The compressive stress–strain curves of ionogels were obtained by applying uniaxial compression force with a universal test machine (TestResources, MN, USA) equipped with a 1 kN load cell in ambient condition. Ionogel disks with dimensions of 10 mm (diameter) and 5 mm (height) were subjected to compression at the rate of 1.3 mm/min until the specimen broke to calculate the compression stress at 50 % strain and the compressive elastic modulus from the slope of the elastic region. For cyclic compression tests, the samples were compressed at 0.5 mm/min until 50 % strain, followed by complete unloading between cycles.

2.4.10 *Tensile Test*

The tensile test was carried out on the universal test machine (TestResources) that was equipped with a 43 N load cell in ambient condition. 3D printed dogbones (ISO 527-2/5B/10) were stretched at 10 mm/min. For the compositions showing elastomeric-like behavior, the elastic modulus was calculated as the secant modulus at 2% of deformation, whereas the Young's moduli based on two specified strain values, i.e. 0.025 % and 0.05 %, were calculated for compositions showing a thermoplastic-like behavior. All the elastic modulus data, tensile strength, as well as elongation at break or ultimate strain in this study were tested in triplicate and data are expressed as mean ± standard deviation. Fatigue testing was conducted on the Instron 5585H load frame with a 50 N load cell. All tests were conducted at room temperature using a crosshead rate of 50 mm/min.

2.4.11 *Electrochemical Impedance Spectroscopy*

The ionic conductivity was studied by electrochemical AC impedance spectroscopy (EIS) with a Princeton Applied Research Ametek Parstat 4000A potentiostat with a Rhd Instruments Passive Cell Holder. Three different samples were measured for each sample set. The samples (0.5 cm radius, 0.2 cm thickness) were inserted into Teflon washers (inner area of 0.196 cm^2 and thickness of 0.2 cm). In each measurement, the washer was then placed between two stainless steel electrodes, sealed in a Metrohm TSC SW closed measuring cell, and connected to the cell holder. The frequency range was set from 5 MHz to 10 Hz and the applied amplitude was 10 mV. The measurements were performed at room temperature. The results were displayed as Nyquist plots in ZView, and the ionic conductivity (σ) was calculated by taking the ratio between the thickness of sample (length of electrode gap, L) and the product of the resistance minima (Z_0) and sample area (A).

$$\sigma = \frac{L}{Z_0 \cdot A} = \frac{0.2\ cm}{Z_0(\Omega) \cdot 0.196\ cm^2} \tag{2.2}$$

2.4.12 *Sensor Electromechanical Test*

The electromechanical characterization was performed using a source-meter (Keithley 2450, Tektronix, USA). The printed structures were connected to the leads with copper wire and conductive paint. During the test, a constant potential of 500 mV was applied while the current was measured as the printed structures undergoes deformation by hand. The current changes in response to the mechanical motions can be explained by

$$R = \rho(L/A) \tag{2.3}$$

which relates resistance (R) to resistivity (ρ), length (L) and cross-sectional area (A). The resistance is substituted by Ohm's law ($V = IR$), so the derived equation is

$$V/I = \rho(L/A) \tag{2.4}$$

demonstrating the relationship between current (I) and material geometry (L, A).

2.5 CONCLUSION

In conclusion, we developed a photopolymerizable resin based on imidazolium ionic liquids that can be 3D printed into polymer networks via vat photopolymerization. We demonstrated that the resolution of the printed structures can be controlled using a photoabsorber that enables the printing of more complex geometries that include over-hanging features. The printed networks were not only conductive, but also viscoelastic in their mechanical character. As a result, highly responsive strain sensors were 3D printed with a range of complex geometries. Additionally, the self-adhesive property of these materials allowed the mechanically damaged sensor to stick together and regain its function. These 3D printed ionic liquid polymer networks present opportunities to generate smart materials for future applications including strain sensors, wearable electronics, soft robotics, and electronic skin.

2.6 ACKNOWLEDGEMENTS

This work was supported by the U.S. Army Research Office (W911NF-17-1-0595) and the National Science Foundation (1752972).

2.7 REFERENCES

[1] Z. Huang, Y. Hao, Y. Li, H. Hu, C. Wang, A. Nomoto, T. Pan, Y. Gu, Y. Chen, T. Zhang, W. Li, Y, Lei, N. Kim, C. Wang, L. Zhang, J. W. Ward, A. Maralani, X. Li, M. F. Durstock, A. Pisano, Y. Lin, S. Xu, *Nat. Electron.* **2018**, *1*, 473.

[2] H. Wu, Y. Huang, F. Xu, Y. Duan, Z. Yin, *Adv. Mater.* **2016**, *28*, 9881.

[3] T. Q. Trung, N. Lee, *Adv. Mater.* **2016**, *28*, 4338.

[4] Y. Ye, Y. Zhang, Y. Chen, X. Han, F. Jiang, *Adv. Funct. Mater.* **2020**, *30*, 2003430.

[5] J. Wen, J. Tang, H. Ning, N. Hu, Y. Zhu, Y. Gong, C. Xu, Q. Zhao, X. Jiang, X. Hu, L. Lei, D. Wu, T. Huang, *Adv. Funct. Mater.* **2021**, *31*, 2011176.

[6] G. Gu, H. Xu, S. Peng, L. Li, S. Chen, T. Lu, X. Guo, *Soft. Robot.* **2019**, *6*, 387.

[7] S. Li, H. Pan, Y. Wang, J. Sun, *J. Mater. Chem. A* **2020**, *7*, 3667.

[8] S. Guo, K. Qiu, F. Meng, S. H. Park, M. C. McAlpine, *Adv. Mater.* **2017**, *29*, 1701218.

[9] T. Someya, M. Amagai, *Nat. Biotechnol.* **2019**, *37*, 382–388.

[10] F. Hartmann, M. Drack, M. Kaltenbrunner, *Sci. Rob.* **2018**, *3*, aat19091.

[11] H. Kim, K. Sim, A. Thukral, C. Yu. *Sci. Adv.* **2017**, *3*, 1701114.

[12] S. R. Shin, R. Farzad, A. Tamayol, V. Manoharan, P. Mostafalu, Y. S. Zhang, M. Akbari, S. M. Jung, D. Kim, M. Comotto, N. Annabi, F. E. Al-Hazmi, M. R. Dokmeci, A. Khademhosseini, *Adv. Mater.* **2016**, *28*, 3280.

[13] D. K. Patel, A. H. Sakhaei, M. Layani, B. Zhang, Q. Ge, S. Magdassi, *Adv. Mater.* **2017**, 1606000.

[14] C. Keplinger, J. Sun, C. C. Foo, P. Rothemund, G. M. Whitesides, Z. Suo, *Science* **2013**, *341*, 984.

[15] T. J. Jinton, A. Hudson, K. Pusch, A. Lee, A. W. Feinberg, *ACS Biomater. Sci. Eng.* **2016**, *2*, 1781.

[16] J. A. Fan, W. H. Yeo, Y. Su, Y. Hattori, W. Lee, S. Y. Jung, Y. Zhang, Z. Liu, H. Cheng, L. Falgout, M. Bajema, T. Coleman, D. Gregoire, R. J. Larsen, Y. Huang, J. A. Rogers, *Nat. Commun.* **2014**, *5*, 3266.

[17] D. Kim, J. A. Rogers, *Adv. Mater.* **2008**, *20*, 4887.

[18] R. L. Truby, M. Wehner, A. K. Grosskopf, D. M. Bogt, S. G.M. Uzel, R. J. Wood, J. A. Lewis, *Adv. Mater.* **2018**, *30*, 1706383.

[19] T. P. Lodge, *Science* **2008**, *321*, 50.

[20] Md. A. B. H. Susan, T. Kaneko, A. Noda, M. Watanabe, *J. Am. Chem. Soc.* **2005**, *127*, 4976.

[21] J. L. Bideau, L. Viau, A. Vioux, *Chem. Soc. Rev.* **2011**, *40*, 907.

[22] E. Kamio, T. Yasui, Y. Iida, J. P. Gong, H. Matsuyama, *Adv. Mater.* **2017**, *29*, 1704118.

[23] M. Isik, T. Lonjaret, H. Sardon, R. Marcilla, T. Herve, G. G. Malliaras, E. Ismailova, D. Mecerreyes, *J. Mater. Chem. C* **2015**, *34*, 8942.

[24] W. J. Hyun, C. M. Thomas, M. C. Hersam, *Adv. Energy Mater.* **2020**, *10*, 2002135.

[25] M. Brachet. D. Gaboriau, P. Gentile, S. Fantini, G. Bidan, S. Sadki, T. Brousse, J. L. Bideau, *J. Mater. Chem. A* **2016**, *30*, 11835.

[26] H. H. Rana, J. H. Park, E. Ducrot, H. Park, M. Kota, T. H. Han, J. Y. Lee, J. Kim, J. Kim, P. Howlett, M. Forsyth, D. MacFarlane, H. S. Park, *Energy Storage Mater.* **2019**, *19*, 197.

[27] Y. Yuan, J. Zhou, G. Lu, J. Sun, L. Tang, *ACS Appl. Polym. Mater.* **2021**, *3*, 1610.

[28] X. Xu, H. S. Hui, K. N. Hui, H. Wang, J. Liu, *Mater. Horiz.* **2020**, *7*, 1246.

[29] L. Wang, X. Zhang, T. Wang, Y. Yin, J. Shi, C. Wang, Y. Guo, *Adv. Energy Mater.* **2018**, *8*, 1801528.

[30] Z. Li, H. Xie, X. Zhang, X. Guo, *J. Mater. Chem. A* **2020**, *8*, 3892.

[31] B. Narupai, A. Nelson, *ACS Macro Lett.* **2020**, *9*, 627.

[32] A. R. Studart, *Chem. Soc. Rev.* **2016**, *45*, 359.

[33] B. Narupai, P. T. Smith, A. Nelson, *Adv. Funct. Mater.* **2021**, *31*, 2011012.

[34] S. M. Ligon, R. Liska, J. Stampfl, M. Gurr, R. Mülhaupt, *Chem. Rev.* **2017**, *117*, 10212.

[35] L. Zhou, J. Fu, Y. He, *Adv. Funct. Mater.* **2020**, *30*, 200187.

[36] A. J. Boydston, B. Cao, A. Nelson, R. J. Ono, A. Saha, J. J. Schwartz, C. J. Thrasher, *J. Mater. Chem. A* **2018**, *6*, 20621.

[37] W. Gao, Y. Zhang, D. Ramanujan, K. Ramani, Y. Chen, C. B. Williams, C. C. L. Wang, Y. C. Shin, S. Zhang, P. D. Zavattieri, *Comput. Aided Des.* **2015**, *69*, 65.

[38] P. T. Smith, B. Narupai, J. H. Tsui, S. C. Millik, R. T. Shafranek, D. H. Kim, A. Nelson, *Biomacromolecules* **2020**, *21*, 484.

[39] E. M. Wilts, A. M. Pekkanen, B. T. White, V. Meenakshisundaram, D. C. Aduba, C. B. Williams, T. E. Long, *Polym. Chem.* **2019**, *10*, 1442.

[40] J. Wong, A. T. Gong, P. A. Defnet, L. Meabe, B. Beauchamp, R. M. Sweet, H. Sardon, C. L. Cobb, A. Nelson, *Adv. Mater. Technol.* **2019**, *4*, 1900452

[41] A. R. Schultz, P. M. Lambert, N. A. Chartrain, D. M. Ruohoniemi, Z. Zhang, C. Jangu, M. Zhang, C. B. Williams, T. E. Long, *ACS Macro Lett.* **2014**, *3*, 1205.

[42] B. Tang, D. K. Schneiderman, F. Z. Bidoky, C. D. Frisbie, T. P. Lodge, *ACS Macro Lett.* **2017**, *6*, 1083.

[43] Z. Wang, J. Zhang, J. Liu, S. Hao, H. Song, J. Zhang, *ACS Appl. Mater. Interfaces* **2021**, *13*, 5614.

[44] S. Hao, T. Li, X. Yang, H. Song, *ACS Appl. Mater. Interfaces* **2022**, *14*, 2029.

[45] T. Li, F. Liu, X. Yang, S. Hao, Y. Cheng, S. Li, H. Zhu, H. Song, *ACS Applied Materials & Interfaces* **2022**, *14*, 29261.

[46] H. Chen, P. Ge, Z. Yan, M. Chen, X. Dai, H. Zhuo, S Chen, L.-B. Huang, T. Zhang, *J. Chem. Eng.* **2022**, *430*, 133111.

[47] P. T. Smith, B. Narupai, J. H. Tsui, S. C. Milik, R. T. Shafranek, D. Kim, A. Nelson, *Biomacromolecules* **2020**, *21*, 484.

[48] R. J. Mondschein, A. Kanitkar, C. B. Williams, S. S. Verbridge, T. E. Long, *Biomaterials* **2017**, *140*, 170.

[49] S. Schüller-Ravoo, S. M. Teixeira, J. Feijen, D. W. Grijpma, A. A. Poot, *Macromol. Biosci.* **2013**, *13*, 1711.

[50] C. Hinczewski, S. Corbel, T. Chartier, *J. Eur. Ceram. Soc.* **1998**, *18*, 583.

[51] J. T. Sutton, K. Rajan, D. P. Harper, S. C. Chmely, *ACS Appl. Mater. Interfaces* **2018**, *10*, 36456.

[52] Y. Luo, G. L. Fer, D. Dean, M. L. Becker, *Biomacromolecules* **2019**, *20*, 1699.

[53] R. Ni, B. Qian, C. Liu, X. Liu, J. Qiu, *RSC Adv.* **2018**, *8*, 29583.

[54] Y. Bao, N. Paunović, J. Leroux, *Adv. Funct. Mater.* **2022**, *32*, 2109864.

[55] V. Schimpf, A. Asmacher, A. Fuchs, K. Stoll, B. Bruchmann, R. Mülhaupt, *Macromol. Mater. Eng.* **2020**, *305*, 2000210.

[56] Z. D. Pritchard, M. P. de Beer, R. J. Whelan, T. F. Scott, M. A. Burns, *Adv. Mater. Technol.* **2019**, *4*, 1900700.

[57] D. Ahn, L. M. Stevens, K. Zhou, Z. A. Page, *ACS Cent. Sci.* **2020**, *6*, 1555.

[58] Q. Ge, A. H. Sahkaei, H. Lee. C. K. Dunn, N. X. Fang, M. L. Dunn, *Sci. Rep.* **2016**, *6*, 31110.

[59] D. Ye, C. Chang, L. Zhang, *Biomacromolecules* **2019**, *20*, 1989.

[60] B. Zhang, H. Li, J. Cheng, H. Ye, A. H. Sakhaei, C. Yuan, P. Rao, Y. Zhang, Z. Chen, R. Wang, X. He, J. Liu, R. Xiao, S. Qu, Q. Ge, *Adv. Mater.* **2021**, *33*, 2101298.

[61] M. A. Haq, Y. Su, D. Wang, *Mater. Sci. Eng. C* **2017**, *70*, 842.

[62] R. L. Truby, W. Wehner, A. K. Grosskopf, D. M. Vogt, S. G.M. Uzel, R. J. Wood, J. A. Lewis, *Adv. Mater.* **2018**, *30*, 1706383.

[63] J. Wong, A. T. Gong, P. A. Defnet, L. Meabe, B. Beauchamp, R. M. Sweet, H. Sardon, C. L. Cobb, A. Nelson, *Adv. Mater. Technol.* **2019**, *4*, 1900452.

[64] J. Xu, G. Gao, L. Duan, G. Sun, *Adv. Mater. Interfaces* **2020**, *7*, 1901541.

[65] Z. Sun, Z. Li, K. Qu, Z. Zhang, Y. Niu, W. Xu, C. Ren, *J. Mol. Liq.* **2021**, *325*, 115254.

[66] C. Shi, Q. Zhang, H. Tian, D. Qu, *SmartMat.* **2020**, *1*, e1012.

[67] Z. Xu, L. Chen, L. Lu, R. Du, W. Ma, Y. Cai, X. An, H. Wu, Q. Luo, Q. Xu, Q. Zhang, X. Jia, *Adv. Funct. Mater.* **2021**, *31*, 2006432.

[68] J. Zhu, X. Lu, W. Zhang, X. Liu, *Macromol. Rapid Commun.* **2020**, *41*, 2000098.

[69] W. Peng, G. Zhang, Q. Zhao, T. Xie, *Adv. Mater.* **2021**, *33*, 2102473.

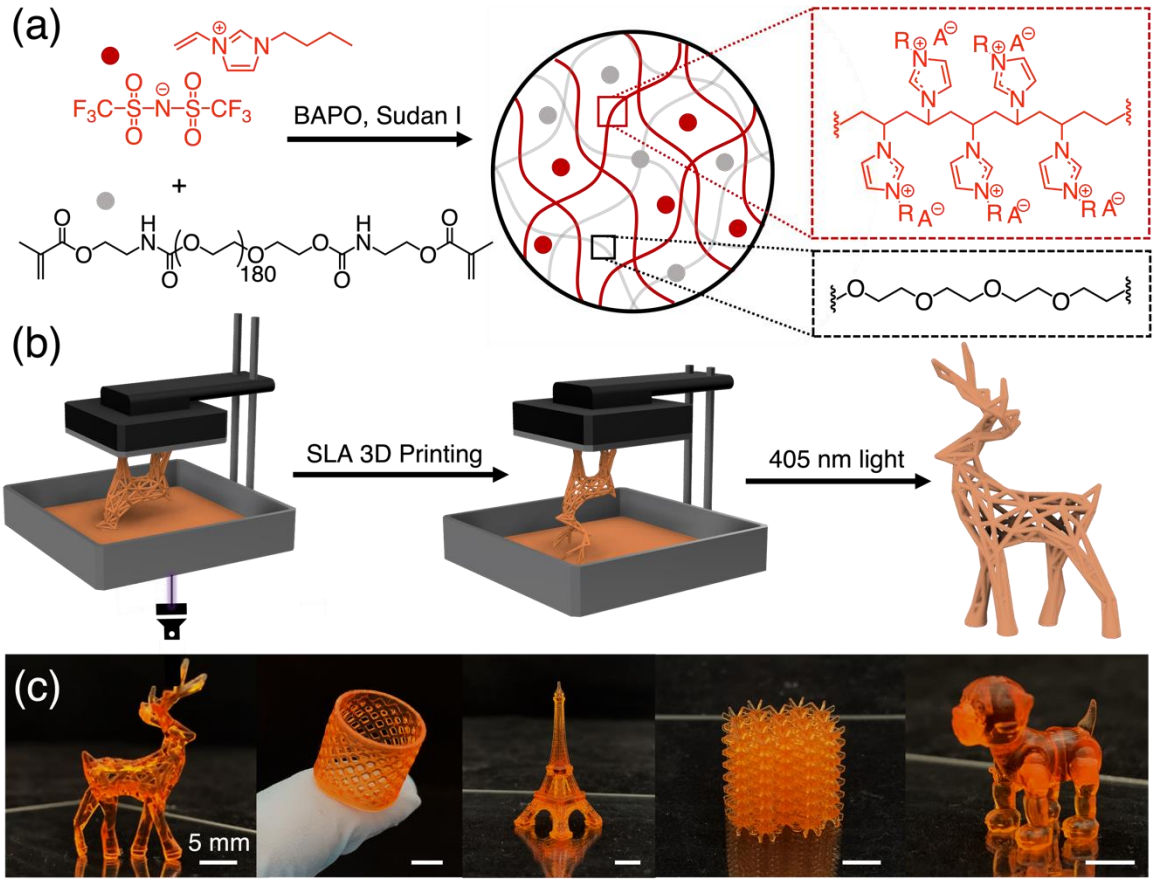

Figure 2.1 (a) Chemical scheme showing a resin comprised of photocrosslinker (PEG-BUM), polymerizable ionic liquid ([BVIM]TFSI), photoinitiator (BAPO) and photoabsorber (Sudan-I) and corresponding ionic liquid polymer network after photopolymerization. (b) Scheme of 3D printing process via Stereolithography followed by a post-print 405 nm curing step. (c) 3D printed structures with different geometries.

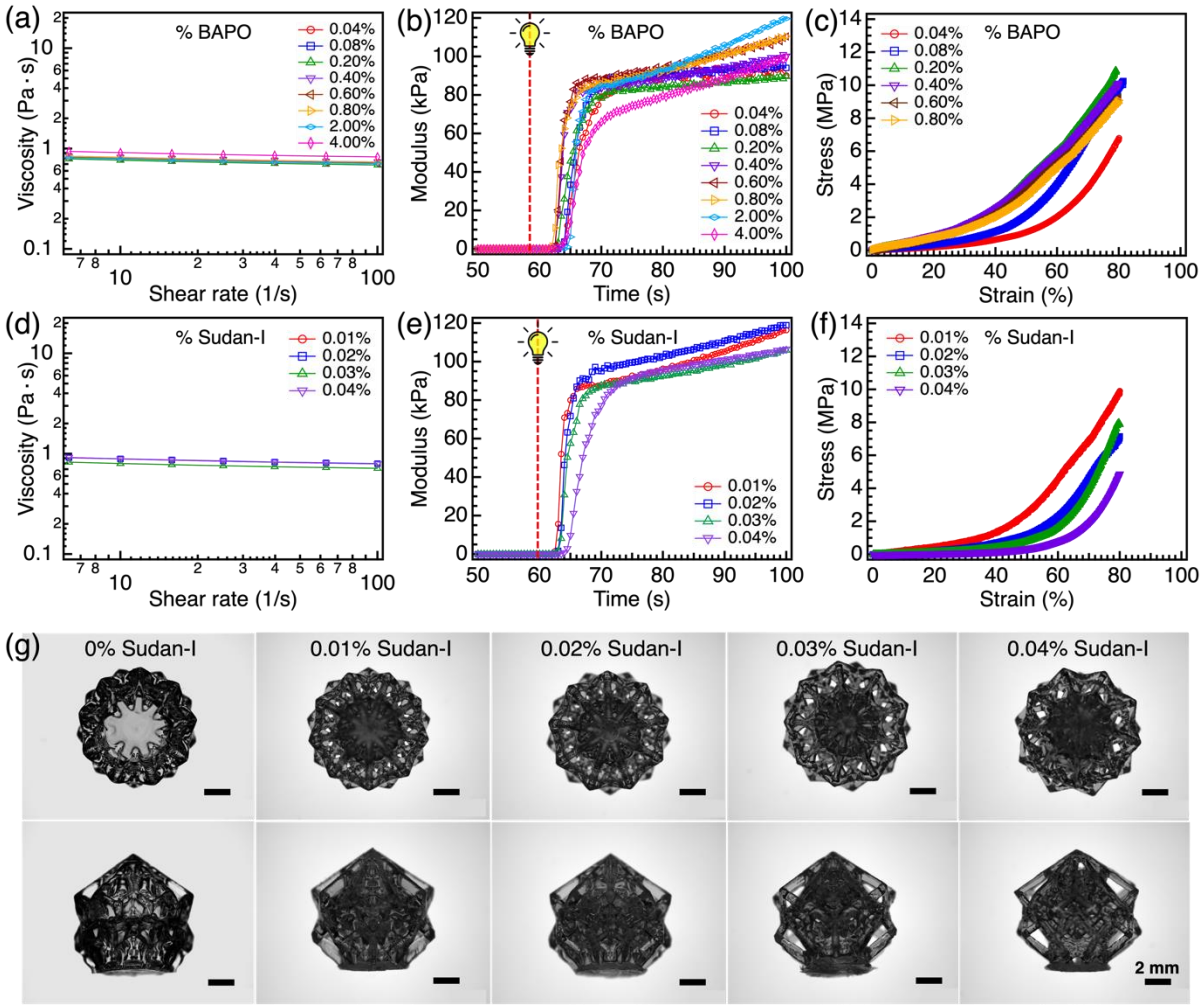

Figure 2.2 (a) Viscosity versus shear rate data for 0.04 - 4 wt% BAPO formulations. (b) Photorheology of resin with various amount of BAPO. (c) Compressive stress versus strain curves of printed cylinders using various amounts of BAPO. (d) Viscosity versus shear rate data for 0.01-0.04 wt% Sudan I formulations. (e) Photorheology of resins with various amount of Sudan-I. (f) Compressive stress versus strain curves of printed cylinders using various amounts of Sudan-I. (g) Stereomicroscopy of 3D printed structures with different concentrations of Sudan-I.

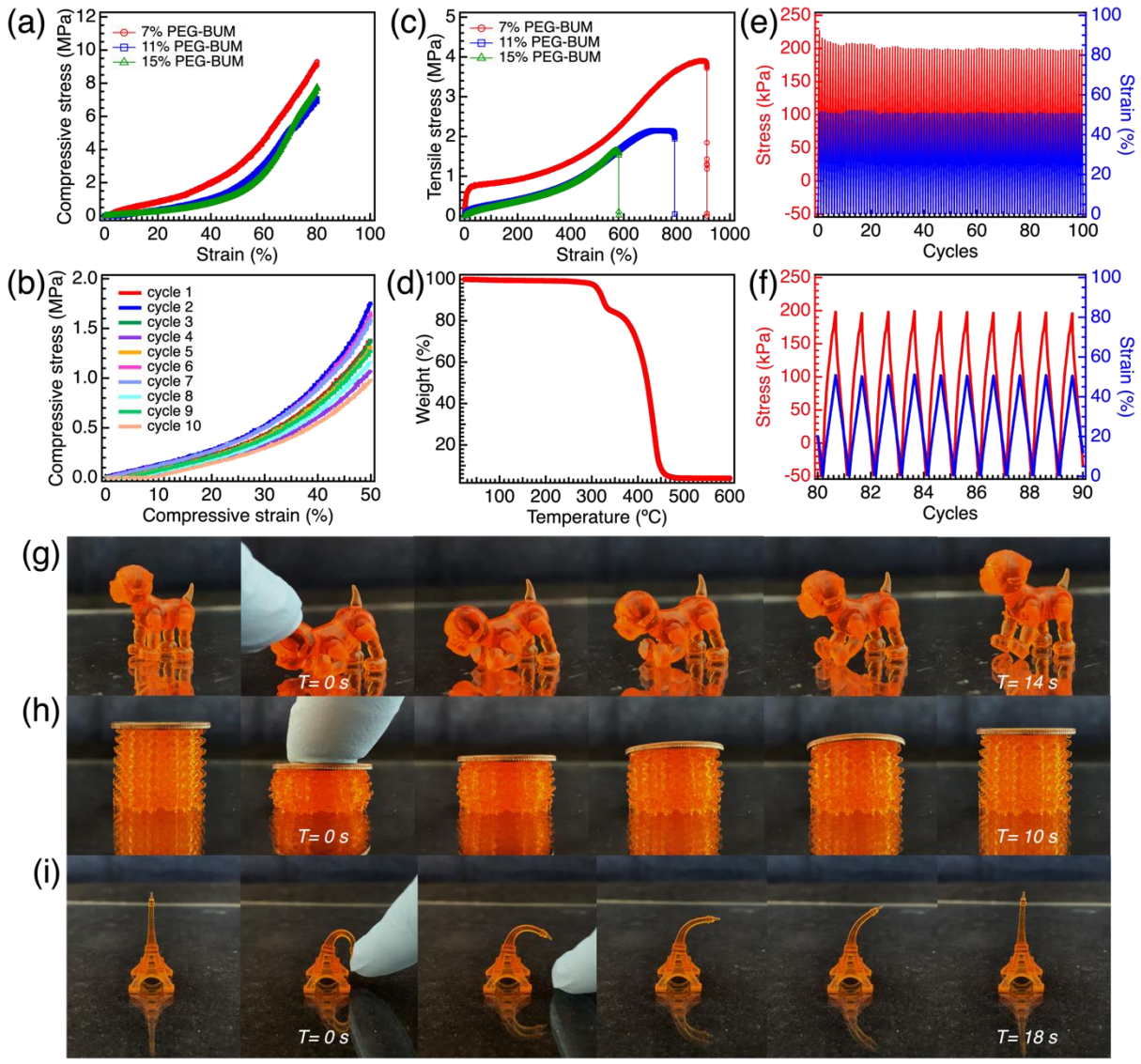

Figure 2.3 (a) Compressive stress versus strain curves of printed cylinders with various amounts of PEG-BUM. (b) Cyclic compression test of printed cylinder with 15 wt% PEG-BUM. (c) Tensile stress versus strain curves of printed dogbones with various amounts of PEG-BUM. (d) Thermogravimetric analysis (TGA) of ionic liquid polymer network with 15 wt% PEG-BUM. (e-f) Cyclic tensile stress-strain fatigue tests of a printed dogbone with 15 wt% PEG-BUM. (g) Stretching 3D printed puppy. (h) Compressing lattice structure. (i) Bending Eiffel tower.

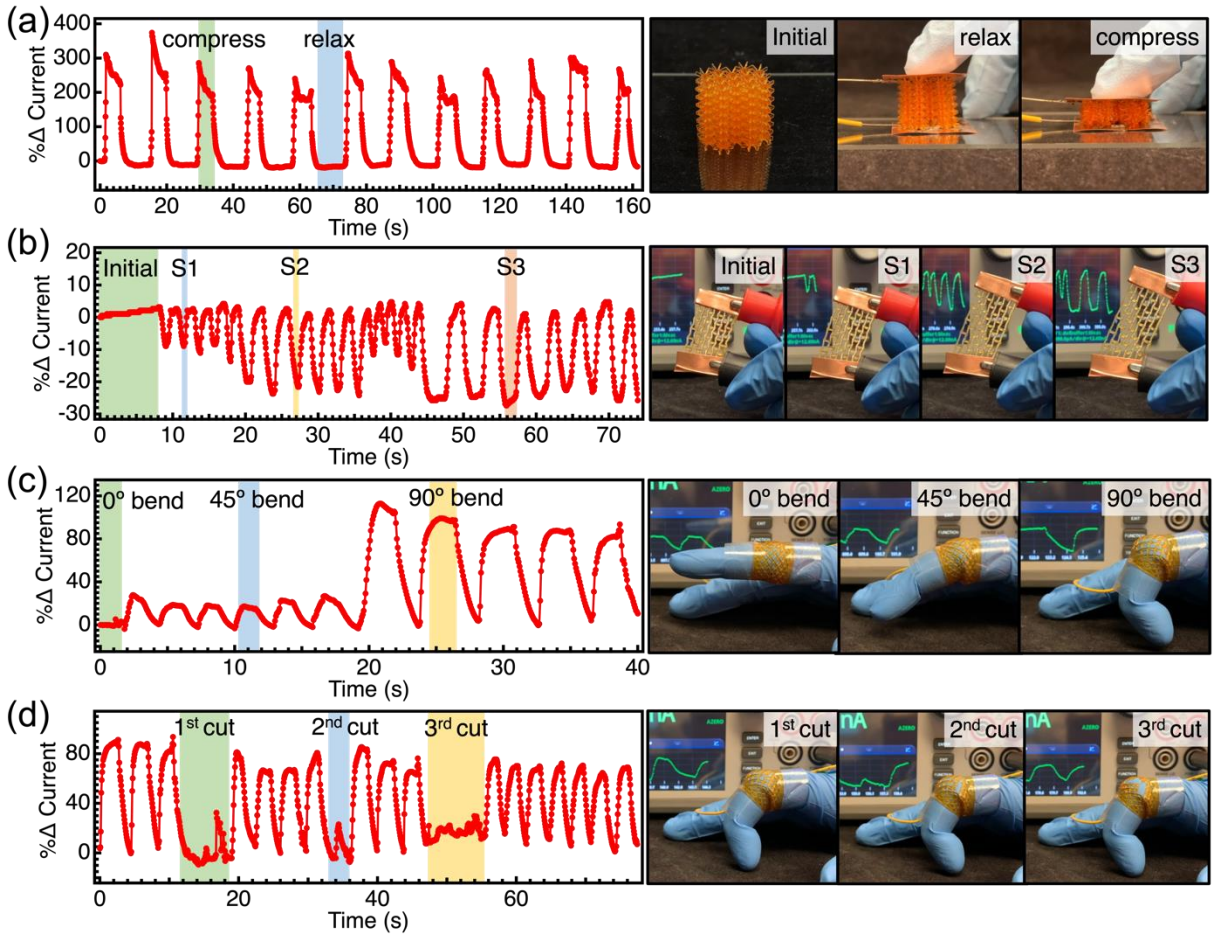

Figure 2.4 Electrochemical performance of 3D printed flexible strain sensors showing the current changes in response to mechanical motions. (a) Compressing the lattice structure. (b) Stretching the hourglass auxetic structure to different distances. (c) Bending the wearable lattice cylinder at different angles. (d) Current response after multiple intentional cuts on the lattice cylinder.

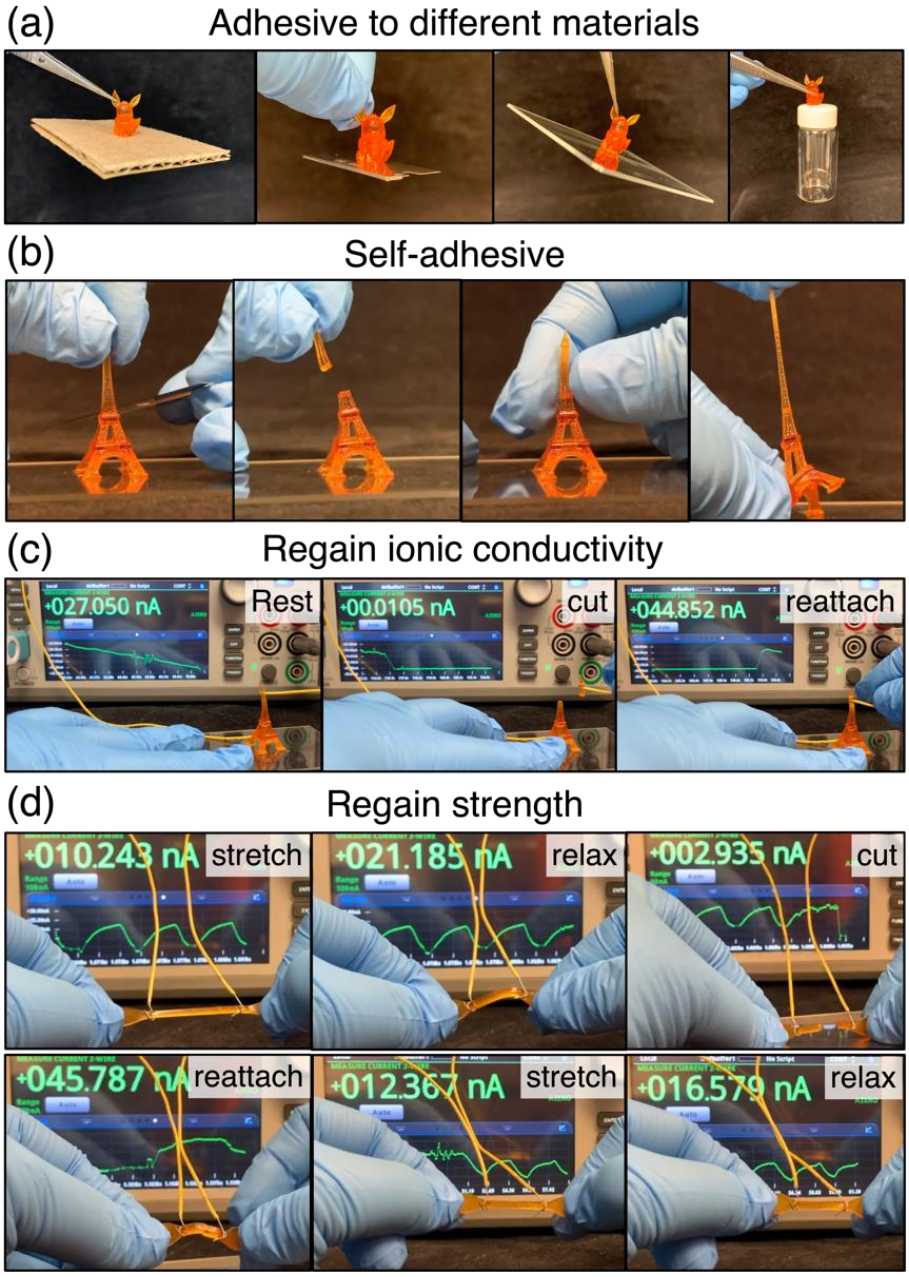

Figure 2.5 Adhesive performance of ionic liquid polymer network. (a) 3D printed squirrel adhered to an array of materials including cardboard, a razor blade, glass slide, and glass vial. (b) Self-adhesive behavior of Eiffel Tower after the cut and reattachment. (c) The current running through the Eiffel Tower decreased to 0 nA after being cut and recovered to 45 nA after reattaching. (d) Dogbone regained ionic conductivity and strength after the cut and reattachment.

Chapter 3. MECHANOMORPHIC RESPONSES IN 3D PRINTED IONIC LIQUID POLYMER NETWORKS

3.1 ABSTRACT

3D printing has gained popularity due to the ability to fabricate structures from a wide range of materials and to easily create complex structures. This has given rise to the field of 4D printing, in which 3D printed objects can change properties over time in response to applied stimuli such as heat, pH, and strain. A challenge currently faced by mechanomorphic structures is that they are often limited to 2D constructs with pre-strained layers. The form factor of these devices often lack complexity, limiting the types of shape transformation which can be achieved. Here, we present a stimuli-responsive ionic liquid gel comprised of the photopolymerizable ionic liquids 1-vinyl-3-butyl imidazolium bis(trifluoromethanesulfonyl) imide ([BVIM]TFSI) and 1-vinyl-3-ethyl imidazolium bis(trifluoromethanesulfonyl)imide ([EVIM]TFSI), crosslinked by polyethylene glycol bis(urethane) methacrylate (PEG-BUM). Combining both ionic liquids into one multi-material structure facilitates shape transformation in response to applied strain, without the need for pre-strained layers. The degree to which the shape is deformed can be controlled by the polymer content, the amount of strain applied, as well as by the geometric design of the printed object. Potential applications for these mechanomorphic structures include actuators in soft robotics.

3.2 INTRODUCTION

Since the introduction of 3D printing in the late 1970s and early 1980s, the technique has provided a platform for fabricating structures from a variety of materials including metals, concrete, and softer materials such as hydrogels and ion gels.[1-15] In addition to the wide range of applicable materials, 3D printing facilitates the fabrication of complex geometries that are inaccessible using

traditional manufacturing methods.[6,16-20] As 3D printing technology has advanced, it has given rise to the field of 4D printing, in which 3D printed objects respond to external stimuli and change their properties over time.[18,21-37] The application of external stimuli such as temperature, light, magnetic field, pH, and strain can lead to shape transformations, which can be applied in fields such as architecture, healthcare, and soft robotics.[4,6,8,25,38-47] In particular, mechano-activation of shape transformations is desirable as the amount of strain applied can be easily controlled regardless of external conditions. Mechanical stimulus can also be applied orthogonally to other stimuli, minimizing interference.[9] One of the main challenges currently faced by mechanomorphic structures is that they are often limited to 2D constructs with pre-strained layers.[15,48-51] The form factor of these devices often lack complexity, limiting the types of shape transformation which can be achieved. Current research is focused on fabricating 3D objects capable of having their properties altered over time without the need for a pre-strained layer.[9,10,13,26,52-54] Skylar Tibbits and Stratasys Ltd.[52] collaborated to demonstrate the concept with multi-material linear objects which could fold into more complex shapes such as the letters "MIT" or a Hilbert cube. Since then, numerous examples of stimuli responsive 3D printed objects have been published, such as a shape memory polymer developed by Ge et al.[53] Benzyl methacrylate was combined with various methacrylated oligo- and polyethylene glycol polymers to produce 3D printable resins which were utilized to fabricate a set of grippers which were actuated upon application of heat. Lantean et al.[13] incorporated magnetite (Fe_3O_4) particles into urethane-acrylate resins, with butyl acrylate serving as the reactive diluent. These materials were 3D printed using digital light processing (DLP) to create magnetoresponsive structures which could move or change shape in response to an external magnetic field. Stimuli responsive ion gels were developed by Wong et al.[9] which were composed of various vinyl imidazolium ionic liquids (ILs) crosslinked with bis(methacrylated) F-127

polymers. Upon the application of strain, the multi-material objects changed shape, twisting or bending into predetermined shapes based on the form factor of the printed object. Additional advancements by Basu et al.[10] incorporated methacrylated spiropyran moieties into IL polymer networks. Application of strain caused ring opening of the spiropyran into the merocyanine form, which displays a purple color. The mechanophore served as an indicator of strain applied to the object. Recently, Peng et al.[26] developed shape-shifting polymers comprised of polylactic acid and poly(lactic-co-glycolic acid). The materials were designed as anastomosis rings, capable of being deformed and recovering their initial shape upon submersion in hot water.

Polymerizable ILs present a promising platform for fabricating mechanomorphic structures. ILs possess low to negligible vapor pressures, allowing them to maintain their properties over extended periods of time. They are also intrinsically conductive due to their ionic nature. The high tunability of their chemical structure allows for a range of viscoelastic properties to be realized and allows for the incorporation of photo-responsive moieties into their chemical structure,[55,56] which allows fabrication via photopolymerization-based 3D printing. By combining two ILs with different mechanical properties into one structure, the mismatch in properties can result in shape transformations such as bending and curling when strain is applied to the structure. The resulting shape transformation can be influenced by the design of the structure, allowing for predictable, anisotropic shape transformations.

Here we present multi-material IL gels, where the two photopolymerizable IL 1-vinyl-3-butyl imidazolium bis(trifluoromethanesulfonyl)imide ([BVIM]TFSI) and 1-vinyl-3-ethyl imidazolium bis(trifluoromethanesulfonyl)imide ([EVIM]TFSI) are combined in a single structure. The difference in mechanical properties afforded conductive ionogels capable of undergoing predictable shape transformations without the need for pre-straining layers.

Polyethylene glycol bis(urethane) methacrylate (PEG-BUM) was included as a crosslinker to provide increased flexibility to the gels. The degree to which the objects changed shape was controlled by the polymer content, the amount of strain applied, as well as by the geometric design of the printed object. COMSOL simulations were employed to accurately model the deformation and stress placed on the network during compression testing.

3.3 Results & Discussion

3.3.1 *Preparing Resins for Multi-Material 3D Printing*

ILs are versatile materials. They are intrinsically conductive, possess low vapor pressures, and are stable at elevated temperatures.[38,55] The ability to tune the chemical structure of ILs allows for control over material properties such as hydrophobicity, viscosity, and solubility. The photopolymerizable ILs [BVIM]TFSI and [EVIM]TFSI were chosen for this study because the vinyl substituents were compatible with stereolithography apparatus (SLA) 3D printing. In addition, the difference in alkyl chain length influenced resin viscosity and the viscoelastic properties of the resulting gels. The longer butyl chain of [BVIM]TFSI resulted in a material with lower Young's modulus and increased strain at break relative to the shorter ethyl chain of [EVIM]TFSI.[9] Polymer networks comprised solely of polymerizable ILs are brittle, therefore PEG-BUM was incorporated as a crosslinker as it has been shown to improve flexibility.[7,9,57] (Figure 3.1).

In addition to IL and PEG-BUM, resins for SLA printing were prepared containing phenyl bis(2,4,6-trimethylbenzoyl) phosphine oxide (BAPO, 0.75 wt%) as a photoinitiator and Sudan I (0.025 wt%) as a photoabsorber. The photoinitiator initiates free radical polymerization of the vinyl and methacrylate substituents, while the photoabsorber serves to improve resolution during the printing process. The amount of photoinitiator and photo absorber were kept constant in all

resin formulations, while the amount of co-polymer present was varied from 10, 15, to 20 wt% to modulate the viscoelastic properties of the polymer network. The resin formulations were labelled according to which IL served as the reactive diluent, along with the wt% of polymer present (10B, 15B, 20B, 10E, 15E, and 20E). For example, a resin containing 10 wt% PEG-BUM dissolved in [BVIM][TFSI] was labeled 10B, while 20E corresponds to 20 wt% PEG-BUM in [EVIM][TFSI]. In general, formulations with higher PEG-BUM content resulted in lower Young's modulus and increased strain at break. To create multi-material gels, a desired resin was poured into the reservoir of a Formlabs Form 2 SLA printer. Half of the intended structure was printed, then the print was paused, and the structure was wiped free of unpolymerized resin while still attached to the build plate. This allows a clean interface between the partially printed structure and the next resin to be incorporated into the structure. Once the partial print was cleaned, a new resin was placed in the reservoir and the print was allowed to continue to completion.

Two important resin properties to consider for SLA printing are the viscosity and rate of photocuring. It is important that the viscosity of the resin remains below 10 Pa•s to allow the resin to flow properly during printing. The resin must also cure rapidly during printing to adhere to the build plate, while at the same time not polymerizing too quickly which may result in poor print resolution. The rate of photocuring and print resolution can be controlled with the quantity of photoinitiator and photoabsorber used in formulating the resin.[7] The viscosity of all formulations utilized in this study remained below 1 Pa•s, well withing the range required for printing (Figure B4).

3.3.2 *Mechanical and Shape Recovery Properties of Single-Material Ion Gels*

In order to induce shape transformation in the multi-material structures, there needs to be a mismatch in shape recovery properties of the incorporated materials. To probe the shape recovery

properties of gels comprised of only one IL, ISO 527-2 5B tensile specimens were printed and stretched until 150% strain. The length of the elongated specimens was monitored until the structures regained their original shape (Figure 3.2a, b). Gels comprised of 20B recovered the fastest, achieving nearly full shape recovery within 3 minutes. 10E gels took the longest amount of time to relax, requiring nearly 4 days to reach their initial state. The mechanical properties of the gels are displayed in Figure 3.2c, highlighting the difference in stiffness and strain at break between the various resins.

3.3.3 *Examining Strain-Induced Shape Transformation in Multi-Material Gels*

The range of shape recovery and mechanical properties observed is desirable because a larger difference in recovery time between two resins incorporated into a single structure resulted in a more drastic shape transformation. This is because the material which recovers more quickly pulls on the slower recovering material, causing the structure to bend towards the more elastic material. This effect can be observed most clearly in multi-material tensile specimens, which bend upon the application of strain. The amount of strain applied had a strong influence on the degree of bending (Figure 3.3a). When subjected to 25% strain, samples consisting of 10E/20B experienced 72° bending (Figure B5). When the strain increased to 75%, the degree of bending increased significantly to 227°. 10B/20B samples displayed a similar trend in the degree of bending, with 93° at 25% strain and 221° at 75% strain. On the other hand, samples of 15E/15B, which possessed more similar recovery properties, achieved 50° bending at 25% strain and 115° bending at 75% strain. The composite structures took different amounts of time to recover their initial shape; 10B/20B gels fully recovered within 30 minutes, 15E/15B gels recovered in 52 minutes, while 10E/20B gels took 9 hours to fully recover (Figure B8-11).

3.3.4 *Anisotropic Strain-Induced Shape Transformation in Multi-Material Gels*

To display the versatility and high resolution of the IL resins, a range of intricate structures were printed (Figure 3.4a). Each structure was composed of multiple materials, yet no discontinuity was visible at the point where the resins were changed. In an effort to explore shape transformations in more complex objects, a multi-material octet-truss lattice was printed (Figure 3.1b). Upon the application of strain, the lattice bent into an arch, similarly to what was observed with the tensile specimens. The degree of bending could be controlled by how much strain was applied, and the structure was able to relax to its original shape over time. Anisotropic shape transformation was observed in a second multi-material structure, named "wheel-to-box." This object consisted of three parallel rectangular panels connected by four hinges (Figure 3.4b). Upon the application of strain perpendicular to the longest side of the rectangles (x-axis), the shape folded along the hinges into a triangular box. Increasing the amount of strain applied resulted in the panels completely folding over one another, with the rectangles stacked on top of one another (Figure B7). When strain was applied parallel to the longest side of the rectangles (y-axis), the wheel-to-box rolled up into a cylinder. This demonstration highlights the ability to control shape transformations not only with the composition of the resins, but also with the form factor of the printed object.

3.3.5 *COMSOL Simulations of Deformation and Stress Distribution*

COMSOL simulations were applied to model the deformation and stress distribution of a lattice cylinder during compression testing (Figure 3.5a, b). In order to model the viscoelastic properties, the software required the material density (1200 kg/m^3), Young's modulus (720 kPa and 77.2 MPa for 20B and 10E, respectively), Poisson's ratio (0.45), and relaxation time (40.4828 s and 253.4399 s for 20B and 10E respectively). A 2D model containing two linear elastic materials was created with solid-mechanics and a time-dependent study. After running the study, a video of the stress

distribution throughout the cylinder was created and compared with an experimental video of the cylinder being compressed, with 20B on the left and 10E on the right. Snapshots of this process are displayed in Figure 3.5c, d. The simulation was not only able to accurately model the deformation of the cylinder, but also demonstrated that the majority of the stress was placed on the stiffer material.

3.4 MATERIALS & METHODS

3.4.1 *General Reagent Information*

All purchased reagents were used as received without further purification unless otherwise specified. 1-vinylimidazole (>98.0%), 1-bromobutane (>99.0%), 1-bromoethane (>98.0), 2-isocyanoethyl methacrylate (>98.0%, stabilized with BHT), dibutyltin dilaurate (>95.0%), triethylamine (>99.0%), were purchased from TCI America. Lithium bis(trifluoromethanesulfonyl)imide salt (99.95%), methanol (>99.9%), aluminum oxide (activated, neutral, Brockmann I) and ethyl acetate (>99.7%) were purchased from Sigma Aldrich. PEG-8000, diethyl ether (anhydrous, stabilized with BHT, >99.0%), and dichloromethane (>99.9%) were purchased from Fisher Scientific. Dry dichloromethane was obtained from a Pure Process Technology purification system.

3.4.2 *General Analytical Information*

Nuclear magnetic resonance spectra were recorded on a Bruker 300 or 500 MHz instrument. Rheology measurements were performed on a TA Discovery HR-2 Hybrid Rheometer. Mechanical stress/strain measurements were performed on a Test Resources Universal Testing Machine. 3D printed structures were printed using a Formlabs Form 2 SLA printer. Mass Spec measurements were performed on a Bruker Esquire LC - Ion Trap Mass Spectrometer.

3.4.3 *Synthesis of PEG-bis(urethane) methacrylate (PEG-BUM)*

A Teflon stir bar and 60 g of PEG-8000 (0.0075 mol) were dried under vacuum for 12 hours in a single-neck 1 L round-bottom flask. The flask was then backfilled with dry nitrogen. Maintaining positive N_2 flow, 550 mL of anhydrous DCM was added to the round-bottom flask and stirred at 30 °C until PEG is fully dissolved. Add 0.89 mL (0.0015 mL) dibutyltin dilaurate to the PEG solution. Attach a 50 mL addition funnel to the 1 L round-bottom flask. In a separate 100 mL round-bottom flask, add 50 mL of anhydrous DCM along with 5.3 mL (0.0375 mol) of 2-isocyanatoethyl methacrylate and swirl to mix. Pour the isocyanate/DCM mixture into the 50 mL addition funnel. Adjust the flow rate of the addition funnel so that the isocyanate is added *slowly* (about 1 drop per second) to the reaction mixture. This can take up to 2 hours. Following the complete addition of isocyanate, remove the addition funnel and reattach the vacuum adapter to the round-bottom flask. Stir reaction mixture at 30 °C for 2 days under nitrogen. The reaction mixture is then concentrated on a rotary evaporator at 30 °C until viscous. The product is precipitated twice in diethyl ether. The product was collected by vacuum filtration and dried at room temperature under high vacuum using a Schlenk manifold (Yield: 19.48 g, 93.7%). ^{1}H NMR (500 MHz, $CDCl_3$): δ 6.04 (s, 2H), 5.52 (t, 2H), 5.18 (t, 1H) 1.87 (s, 6H), protons from PEG appear at 4.14 ppm and 3.57 ppm. ^{13}C NMR (300 MHz, $CDCl_3$): δ 70.59. IR (ATR-FTIR, ν_{max}, cm^{-1}): 2880, 1720, 1468, 1340, 1280, 1092, 960, 840.

3.4.4 *Synthesis of 1-vinyl-3-butyl imidazolium bromide ([BVIM]Br)*

200 mL (2.2 mol) of 1-vinyl imidazole and 285 mL (2.65 mol) of 1-bromobutane were stirred magnetically at 45 °C for 24 hours. The viscous solution was allowed to cool before washing 3-4 times with excessive diethyl ether until the liquid solidifies. The product was collected by vacuum filtration and dried at room temperature under high vacuum using a Schlenk manifold. The product

appears as a white solid (Yield: 456.23 g, 90.1%). ^{1}H NMR (500 MHz, DMSO-D6): δ 9.61 (s, 1H), 8.24 (t, 1H), 7.97 (t, 1H), 7.33 (m, 1H), 6.00, 5.43 (d of d, 2H), 4.22 (t, 2H), 1.81 (q, 2H), 1.30 (m, 2H), 0.91 (t, 3H). ^{13}C NMR (300 MHz, $CDCl_3$): δ 135.22, 128.74, 123.17, 119.17, 108.57, 48.81, 30.98, 18.68, 13.19. IR (ATR-FTIR, ν_{max}, cm^{-1}): 3092, 3040, 2956, 1652, 1568, 1540, 1456, 1160, 984, 928, 880, 804, 740, 724, 660, 636, 604.

3.4.5 *Synthesis of 1-vinyl-3-butyl imidazolium bis(trifluoromethane sulfonyl)imide ([BVIM]TFSI)*

96.34 g (0.42 mol) of [BVIM]Br and 122.6 g (0.427 mol) of Lithium bis(trifluoromethanesulfonyl) imide salt were dissolved in 160 mL of DI water and stirred at room temperature for 48 hours. The mixture was then poured into a separatory funnel and the ionic liquid layer was allowed to separate. The ionic liquid was separated from the water layer, then passed through a column of neutral alumina. The product appears as a clear liquid. (Yield: 152.12 g, 84%). ^{1}H NMR (500 MHz, DMSO-D6): δ 9.46 (s, 1H), 8.18 (t, 1H), 7.91 (t, 1H), 7.28 (m, 1H), 5.96, 5.42 (d of d, 2H), 4.19 (t, 2H), 1.80 (q, 2H), 1.27 (m, 2H), 0.91 (t, 3H). ^{13}C NMR (300 MHz, $CDCl_3$): δ 135.28, 128.85, 123.21, 119.16, 108.58, 48.97, 31.03, 18.77, 13.15. IR (ATR-FTIR, ν_{max}, cm^{-1}): 3156, 2972, 1660, 1552, 1348, 1180, 1132, 1052, 956, 920, 740, 612, 568, 508.

3.4.6 *Ion Gel Resin Preparation*

Example of a typical procedure to prepare 20 g of 20B resin for 3D printing:

20 wt% (4 g) of PEG-BUM is added to an amber vial. 0.75 wt% (0.15 g) of BAPO was added, followed by 0.025 wt% (0.005 g) of Sudan 1. 15.85 mL of [BVIM]TFSI (~80 wt%) is then added and the mixture is vortexed for 10-15 mins before being stored at 4 °C overnight. Solution is

vortexed again if the PEG is not fully dissolved. The amount of each component used to make the ion gels are summarized in Table B1.

3.4.7 *3D Printing Single-Material Ion Gels Using a Stereolithographic Apparatus (SLA) 3D Printer*

The desired resin was poured into the resin tray and the print was initiated on a Formlabs Form 2 SLA printer in open mode. The z-axis step size was 0.100 mm. CAD files used for building blocks were downloaded from Thingiverse.com. Upon print completion, the structure was removed from the build plate carefully using a metal scraper and residual resin was removed by gently rolling the structure in kimwipes until minimal resin remained. If the shape of the structure permits, the printed structures may be centrifuged at 1000 RPM for one minute to help remove residual resin. The structure was then cured using 405 nm light for 30 mins on one side, flipped, then cured for an additional 30 mins on the other side.

3.4.8 *3D Printing Multi-Material Ion Gel Objects Using a SLA 3D Printer*

To create multi-material gels, a desired resin was poured into the reservoir of a Formlabs Form 2 SLA printer. Half of the intended structure was printed, then the print was paused, and the structure was wiped free of unpolymerized resin while still attached to the build plate. This allows a clean interface between the partially printed structure and the next resin to be incorporated into the structure. The first resin was then removed from the print tray, and it was cleaned thoroughly with methanol. Once the partial print and the print tray were cleaned, a new resin was placed in the reservoir and the print was allowed to continue to completion.

3.4.9 *Rheology*

Rheometrical characterization was performed on a TA Instruments DHR-2 equipped with an Advanced Peltier Plate system. Experiments were performed using either an 8 mm flat stainless steel upper plate or a 40 mm hard anodized aluminum conical upper plate with a cone angle of 1°. Resin samples were loaded via glass pipette onto the bottom plate. The sample is then trimmed after the upper plate was lowered to the trim gap at 600 μm. The final geometry gap was then set to 500 μm, and pre-shear was applied at 5 °C for 10 s before additional sample conditioning at 25 °C for 8 min. Viscosity vs Shear Rate experiments were performed to measure the viscosity of the ion gel resins. The viscosity of resins must remain below 10 Pa•s for resin to flow properly during SLA printing. All resins reported in this manuscript had viscosities below this threshold. Resins were found to increase in viscosity with increasing amount of PEG co-polymer present. Photorheology experiments were also conducted to ensure resins cured rapidly enough for SLA printing.

3.4.10 *Tensile Tests*

TestResources Universal Test System 1.1 kN electromechanical actuator single column load frame with a 43 N high accuracy S10 type load cell was used to evaluate the mechanical properties of 3D printed ion gels. For dimensions of all tensile specimens, ISO 527-2 5B specimen specifications were used. The samples were attached to vice grips with diamond grit jaw and subjected to increasing strain at a constant rate of 5 mm/min until mechanical failure.

3.5 CONCLUSION

This study presented multi-material IL gel structures fabricated using SLA 3D printing. The structures possessed a range of mechanical and shape recovery properties, which could be

controlled by altering the substituents on the IL as well as by changing the wt% of co-polymer added to the resins. We demonstrated that by combining materials with different mechanical and shape recovery properties into a single structure, complex shape transformations could be achieved without the need for pre-straining any layers. In addition, COMSOL simulations were employed to model deformation and stress distribution on a lattice cylinder during compression testing.

3.6 ACKNOWLEDGEMENTS

This work was supported by the U.S. Army Research Office (W911NF-17-1-0595) and the National Science Foundation (1752972).

3.7 REFERENCES

[1] Swainson, W.K. Method, Medium and Apparatus for Producing Three-Dimensional Figure Product. U.S. Patent 4,041,476, 9 August **1977**.

[2] Herbert, A.J. Solid object generation. J. Appl. Photogr. Eng. **1982**.

[3] Hull, C.W. Apparatus for Production of Three-Dimensional Objects by Stereolithography. U.S. Patent Appl. 638,905, **1984**.

[4] Amziane, S.; Pierre, A.; Rangeard, D.; Sonebi, M.; Perrot, A. *3D Printing of Concrete: State of the Art and Challenges of the Digital Construction Revolution*; **2019**.

[5] Hartings, M. R.; Ahmed, Z. Chemistry from 3D Printed Objects. *Nat. Rev. Chem.* **2019**, *3*, 305–314.

[6] Pacillo, G. A.; Ranocchiai, G.; Loccarini, F.; Fagone, M. Additive Manufacturing in Construction: A Review on Technologies, Processes, Materials, and Their Applications of 3D and 4D Printing. *Mater. Des. Process. Commun.* **2021**, *3* (5).

[7] Narupai, B.; Wong, J.; Sanchez-Rexach, E.; Smith-Jones, J.; Le, V. C. T.; Sadaba, N.; Sardon, H.; Nelson, A. 3D Printing of Ionic Liquid Polymer Networks for Stretchable Conductive Sensors. *Adv. Mater. Technol.* **2023**, *2300226*, 1–9.

[8] Wong, J.; Gong, A. T.; Defnet, P. A.; Meabe, L.; Beauchamp, B.; Sweet, R. M.; Sardon, H.; Cobb, C. L.; Nelson, A. 3D Printing Ionogel Auxetic Frameworks for Stretchable Sensors. *Adv. Mater. Technol.* **2019**, *4* (9), 1–6.

[9] Wong, J.; Basu, A.; Wende, M.; Boechler, N.; Nelson, A. Mechano-Activated Objects with Multidirectional Shape Morphing Programmed via 3D Printing. *ACS Appl. Polym. Mater.* **2020**, *2* (7), 2504–2508.

[10] Basu, A.; Wong, J.; Cao, B.; Boechler, N.; Boydston, A. J.; Nelson, A. Mechanoactivation of Color and Autonomous Shape Change in 3D-Printed Ionic Polymer Networks. *ACS Appl. Mater. Interfaces* **2021**, *13*, 19263–19270.

[11] Yang, W.; Cai, S.; Chen, Y.; Liang, W.; Lai, Y.; Yu, H.; Wang, Y.; Liu, L. Modular and Customized Fabrication of 3D Functional Microgels for Bottom-Up Tissue Engineering and Drug Screening. *Adv. Mater. Technol.* **2020**, *5* (5).

[12] Yang, L.; Sun, L.; Huang, H.; Zhu, W.; Wang, Y.; Wu, Z.; Neisiany, R. E.; Gu, S.; You, Z. Mechanically Robust and Room Temperature Self-Healing Ionogel Based on Ionic Liquid Inhibited Reversible Reaction of Disulfide Bonds. *Adv. Sci.* **2023**, *10* (20).

[13] Lantean, S.; Barrera, G.; Fabrizio Pirri, C.; Tiberto, P.; Sangermano, M.; Roppolo, I.; Rizza, G. 3D Printing of Magnetoresponsive Polymeric Materials with Tunable Mechanical and Magnetic Properties by Digital Light Processing. *Adv. Mater. Technol.* **2019**, *4*, 1900505.

[14] Subbiah, R.; Hipfinger, C.; Tahayeri, A.; Athirasala, A.; Horsophonphong, S.; Thrivikraman, G.; Miranda França, C.; Araujo Cunha, D.; Mansoorifar, A.; Zahariev, A.; et al. 3D Printing of Microgel-Loaded Modular Microcages as Instructive Scaffolds for Tissue Engineering. *Adv. Mater.* **2020**, *32*, 1–7.

[15] Liu, G.; Zhao, Y.; Wu, G.; Lu, J. Origami and 4D Printing of Elastomer-Derived Ceramic Structures. *Sci. Adv.* **2018**, *4* (8), 641–658.

[16] Wallin, T. J.; Pikul, J.; Shepherd, R. F. 3D Printing of Soft Robotic Systems. *Nat. Rev. Mater.* **2018**, *3* (6), 84–100.

[17] Millik, S. C.; Dostie, A. M.; Karis, D. G.; Smith, P. T.; McKenna, M.; Chan, N.; Curtis, C. D.; Nance, E.; Theberge, A. B.; Nelson, A. 3D Printed Coaxial Nozzles for the Extrusion of Hydrogel Tubes toward Modeling Vascular Endothelium. *Biofabrication* **2019**, *11* (4).

[18] Ahmed, A.; Arya, S.; Gupta, V.; Furukawa, H.; Khosla, A. 4D Printing: Fundamentals, Materials, Applications and Challenges. *Polymer* **2021**, *228*, 123926.

[19] Ryan, K. R.; Down, M. P.; Banks, C. E. Future of Additive Manufacturing: Overview of 4D and 3D Printed Smart and Advanced Materials and Their Applications. *Chem. Eng. J.* **2021**, *403*, 126162.

[20] Jia, Y.; Xie, H.; Qian, J.; Zhang, Y.; Zheng, H.; Wei, F.; Li, Y.; Zhao, Z. Recent Progress on the 3D Printing of Dynamically Cross-Linked Polymers. *Adv. Funct. Mater.* **2023**.

[21] Mauriello, J.; Maury, R.; Guillaneuf, Y.; Gigmes, D. 3D/4D Printing of Polyurethanes by Vat Photopolymerization. *Adv. Mater. Technol.* **2023**.

[22] Wan, X.; Luo, L.; Liu, Y.; Leng, J. Direct Ink Writing Based 4D Printing of Materials and Their Applications. *Adv. Sci.* **2020**, *7* (16).

[23] Huang, J.; Yu, Z.; Wu, P. 3D Printing of Ionogels with Complementary Functionalities Enabled by Self-Regulating Ink. *Adv. Sci.* **2023**.

[24] Ding, Z.; Yuan, C.; Peng, X.; Wang, T.; Qi, H. J.; Dunn, M. L. Direct 4D Printing via Active Composite Materials. *Sci. Adv.* **2017**, *3* (4).

[25] De Marco, C.; Pané, S.; Nelson, B. J. 4D Printing and Robotics. *Sci. Robot.* **2018**, *3* (18), 449.

[26] Peng, W.; Yin, J.; Zhang, X.; Shi, Y.; Che, G.; Zhao, Q.; Liu, J. 4D Printed Shape Memory Anastomosis Ring with Controllable Shape Transformation and Degradation. *Adv. Funct. Mater.* **2023**, *33* (20), 2214505.

[27] Zhou, S.-W.; Yu, C.; Chen, M.; Shi, C.-Y.; Gu, R.; Qu, D.-H. Self-Healing and Shape-Shifting Polymers Controlled by Dynamic Bonds. *Smart Mol.* **2023**.

[28] Peng, B.; Yang, Y.; Gu, K.; Amis, E. J.; Cavicchi, K. A. Digital Light Processing 3D Printing of Triple Shape Memory Polymer for Sequential Shape Shifting. *ACS Mater. Lett.* **2019**, *1* (4), 410–417.

[29] Yi, C.; Qu, S.; Wang, Y.; Qi, H.; Zhang, Y.; Cheng, G. J. Optical Force Brush Enabled Free-Space Painting of 4D Functional Structures. *Sci. Adv.* **2023**, *9* (38), 1–13.

[30] Accardo, J. V; Kalow, J. A. Reversibly Tuning Hydrogel Stiffness through Photocontrolled Dynamic Covalent Crosslinks. Chem. Sci. **2018**, 9 (27), 5987–5993.

[31] Tang, Y.; Zhang, Y.; Chen, X.; Xie, X.; Zhou, N.; Dai, Z.; Xiong, Y. Up/Down Tuning of Poly(Ionic Liquid)s in Aqueous Two-Phase Systems. *Angew. Chemie - Int. Ed.* **2023**, *62* (4).

[32] Shmool, T. A.; Martin, L. K.; Jirkas, A.; Matthews, R. P.; Constantinou, A. P.; Vadukul, D. M.; Georgiou, T. K.; Aprile, F. A.; Hallett, J. P. Unveiling the Rational Development of Stimuli-Responsive Silk Fibroin-Based Ionogel Formulations. *Chem. Mater.* **2023**.

[33] Qin, J.; Sun, M.; Hu, W.; Cheng, J.; Fan, Z.; Du, J. Stimuli-Responsive Hydrogels for Cancer Immunotherapy. *Polym. Chem.* **2023**, *14* (7), 793–802.

[34] Lendlein, A.; Gould, O. E. C. Reprogrammable Recovery and Actuation Behaviour of Shape-Memory Polymers. *Nat. Rev. Mater.* **2019**, *4* (2), 116–133.

[35] Wu, H.; Wang, O.; Tian, Y.; Wang, M.; Su, B.; Yan, C.; Zhou, K.; Shi, Y. Selective Laser Sintering-Based 4D Printing of Magnetism-Responsive Grippers. *ACS Appl. Mater. Interfaces* **2021**, *13* (11), 12679–12688.

[36] Ouyang, H.; Li, X.; Lu, X.; Xia, H. Selective Laser Sintering 4D Printing of Dynamic Cross-Linked Polyurethane Containing Diels-Alder Bonds. *ACS Appl. Polym. Mater.* **2022**, *4* (5), 4035–4046.

[37] Liu, K.; Zhang, Y.; Cao, H.; Liu, H.; Geng, Y.; Yuan, W.; Zhou, J.; Wu, Z. L.; Shan, G.; Bao, Y.; et al. Programmable Reversible Shape Transformation of Hydrogels Based on Transient Structural Anisotropy. *Adv. Mater.* **2020**, *32* (28).

[38] Tie, J.; Mao, Z.; Zhang, L.; Zhong, Y.; Sui, X.; Xu, H. Highly Transparent, Self-Healing and Adhesive Wearable Ionogel as Strain and Temperature Sensor. *Polym. Chem.* **2022**, *13*, 4064–4075.

[39] Fan, X.; Liu, S.; Jia, Z.; Koh, J. J.; Yeo, J. C. C.; Wang, C. G.; Surat'man, N. E.; Loh, X. J.; Le Bideau, J.; He, C.; et al. Ionogels: Recent Advances in Design, Material Properties and Emerging Biomedical Applications. *Chem. Soc. Rev.* **2023**, *52* (7), 2497–2527.

[40] Zanon, M.; Montalvillo-Jiménez, L.; Cue-López, R.; Martínez-Campos, E.; Sangermano, M.; Chiappone, A.; Bosch, P. Vat 3D Printing of Full-Alginate Hydrogels via Thiol-Ene Reactions towards Tissue Engineering Applications. *Polym. Chem.* **2023**.

[41] Borayek, R.; Foroughi, F.; Xin, X.; Mohamed, A. M.; Abdelrahman, M. M.; Zedan, M.; Zhang, D.; Ding, J. Near-Zero Hysteresis Ionic Conductive Elastomers with Long-Term Stability for Sensing Applications. *ACS Appl. Mater. Interfaces* **2022**, *14* (9), 11727–11738.

[42] Choi, D. Y.; Kim, M. H.; Oh, Y. S.; Jung, S. H.; Jung, J. H.; Sung, H. J.; Lee, H. W.; Lee, H. M. Highly Stretchable, Hysteresis-Free Ionic Liquid-Based Strain Sensor for Precise Human Motion Monitoring. *ACS Appl. Mater. Interfaces* **2017**, *9* (2), 1770–1780.

[43] Bansal, A. K.; Hou, S.; Kulyk, O.; Bowman, E. M.; Samuel, I. D. W. Wearable Organic Optoelectronic Sensors for Medicine. *Adv. Mater.* **2015**, *27* (46), 7638–7644.

[44] Jurinovs, M.; Barkane, A.; Platnieks, O.; Grase, L.; Gaidukovs, S. Three Dimensionally Printed Biobased Electrodes: Ionic Liquid and Single-Walled Carbon Nanotube Hybrids in a Vegetable Oil Matrix for Soft Robotics. *ACS Appl. Polym. Mater.* **2023**, *5* (9), 7120–7131.

[45] Chossat, J. B.; Shin, H. S.; Park, Y. L.; Duchaine, V. Soft Tactile Skin Using an Embedded Ionic Liquid and Tomographic Imaging. *J. Mech. Robot.* **2015**, *7* (2).

[46] Shintake, J.; Cacucciolo, V.; Floreano, D.; Shea, H. Soft Robotic Grippers. *Adv. Mater.* **2018**, *30* (29), 1707035.

[47] Gomez, E. F.; Wanasinghe, S. V; Flynn, A. E.; Dodo, O. J.; Sparks, J. L.; Baldwin, L. A.; Tabor, C. E.; Durstock, M. F.; Konkolewicz, D.; Thrasher, C. J. 3D-Printed Self-

Healing Elastomers for Modular Soft Robotics. *ACS Appl. Mater. Interfaces* **2021**, *13*, 28870–28877.

[48] Song, S. W.; Lee, S.; Choe, J. K.; Kim, N. H.; Kang, J.; Lee, A. C.; Choi, Y.; Choi, A.; Jeong, Y.; Lee, W.; et al. Direct 2D-to-3D Transformation of Pen Drawings. *Sci. Adv.* **2021**, *7* (13).

[49] Cafferty, B. J.; Campbell, V. E.; Rothemund, P.; Preston, D. J.; Ainla, A.; Fulleringer, N.; Diaz, A. C.; Fuentes, A. E.; Sameoto, D.; Lewis, J. A.; et al. Fabricating 3D Structures by Combining 2D Printing and Relaxation of Strain. *Adv. Mater. Technol.* **2019**, *4* (1), 1–9.

[50] Matsuhisa, N.; Niu, S.; K O, S. J.; Kang, J.; Ochiai, Y.; Katsumata, T.; Wu, H.-C.; Ashizawa, M.; Nathan Wang, G.-J.; Zhong, D.; et al. High-Frequency and Intrinsically Stretchable Polymer Diodes. *Nature* **2021**, *600*, 246–252.

[51] Liu, Y.; Boyles, J. K.; Genzer, J.; Dickey, M. D. Self-Folding of Polymer Sheets Using Local Light Absorption. *Soft Matter* **2012**, *8* (6), 1764–1769.

[52] Tibbits, S. 4D Printing: Multi-Material Shape Change. *Archit. Des.* **2014**, *84* (1), 116–121.

[53] Ge, Q.; Sakhaei, A. H.; Lee, H.; Dunn, C. K.; Fang, N. X.; Dunn, M. L. Multimaterial 4D Printing with Tailorable Shape Memory Polymers. *Sci. Rep.* **2016**, *6*, 31110.

[54] Sampson, K. L.; Deore, B.; Go, A.; Nayak, A.; Orth, A.; Gallerneault, M.; Malenfant, P. R. L.; Paquet, C. Multimaterial Vat Polymerization Additive Manufacturing. *ACS Appl. Polym. Mater.* **2021**, *3* (9), 4304–4324.

[55] Wang, M.; Hu, J.; Dickey, M. D. Tough Ionogels: Synthesis, Toughening Mechanisms, and Mechanical Properties-A Perspective. *JACS Au*. **2022**, *2* (12), 2645–2657

[56] Néouze, M. A.; Le Bideau, J.; Gaveau, P.; Bellayer, S.; Vioux, A. Ionogels, New Materials Arising from the Confinement of Ionic Liquids within Silica-Derived Networks. *Chem. Mater.* **2006**, *18* (17), 3931–3936.

[57] Zhang, J.; Chen, Z.; Zhang, Y.; Dong, S.; Chen, Y.; Zhang, S. Poly(Ionic Liquid)s Containing Alkoxy Chains and Bis(Trifluoromethanesulfonyl)Imide Anions as Highly Adhesive Materials. *Adv. Mater.* **2021**, *33* (30), 1–10.

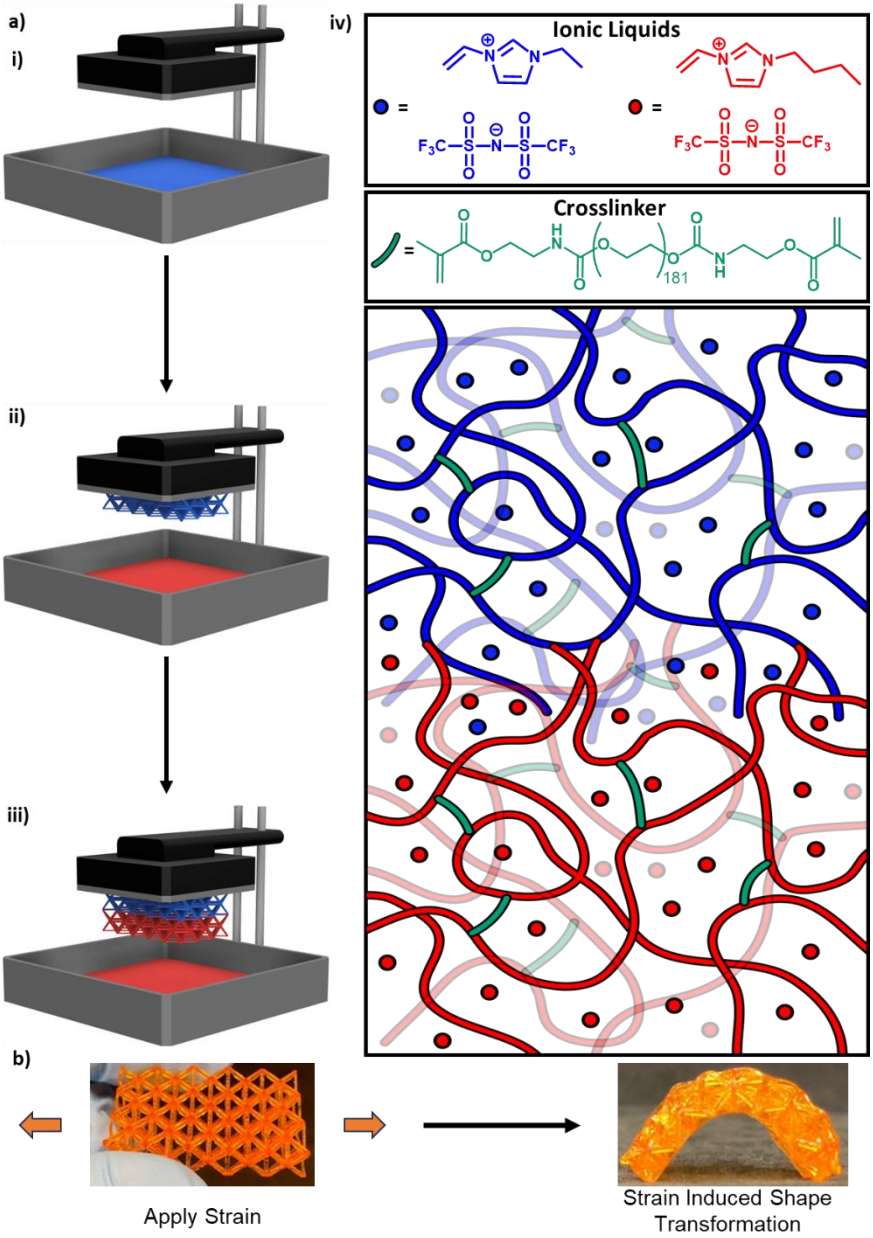

Figure 3.1 a) Overview of SLA multi-material printing process. i) Initial resin is loaded into the print tray. ii) Print is paused halfway, the printed object is cleaned, and the resin is removed from the tray. New resin is then introduced to the print tray. iii) Print is allowed to proceed to completion. iv) Chemical structure of reactive diluents [BVIM]TFSI and [EVIM]TFSI are shown, along with crosslinker PEG-BUM. Not included: BAPO and Sudan 1. The cartoon is a representation of the polymerized multi-material ionic liquid polymer networks. b) Example of stain induced shape transformation in a multi-material tensile specimen.

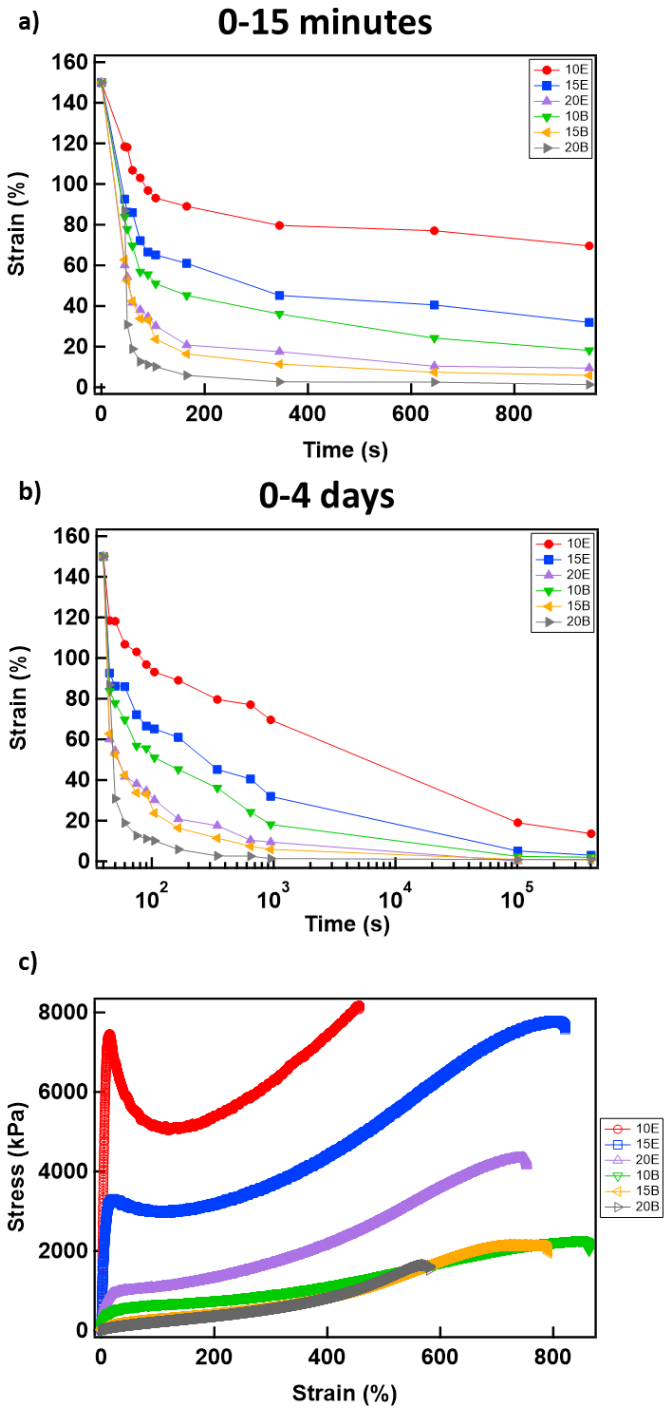

Figure 3.2 a) Graph of shape recovery properties of IL gels as a function of time. The first 15 minutes are displayed. b) Full shape recovery experiment over four days. c) Stress−strain curves of individual resins.

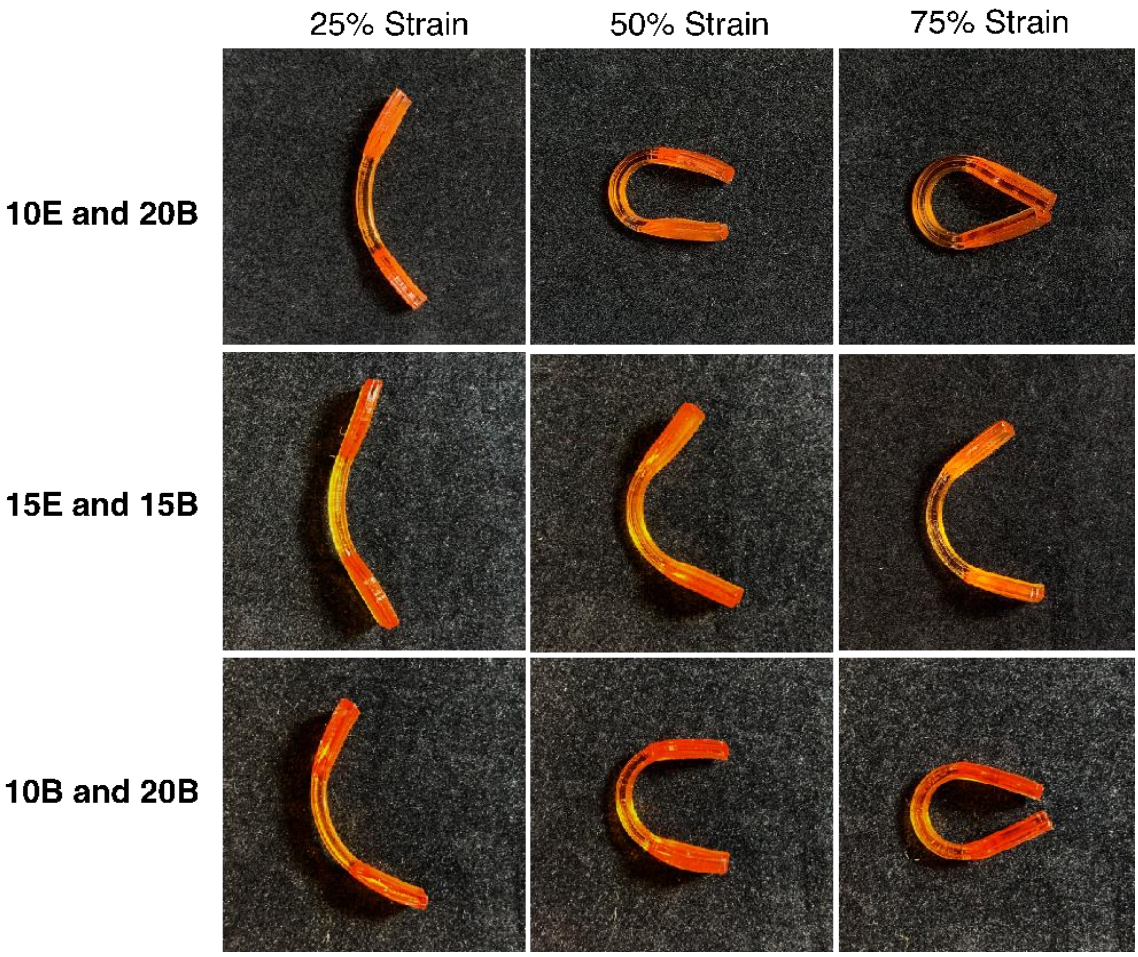

Figure 3.3 a) Multi-material tensile specimens experienced different degrees of bending depending on the amount of strain applied. b) Shape recovery rate of multi-material tensile specimens.

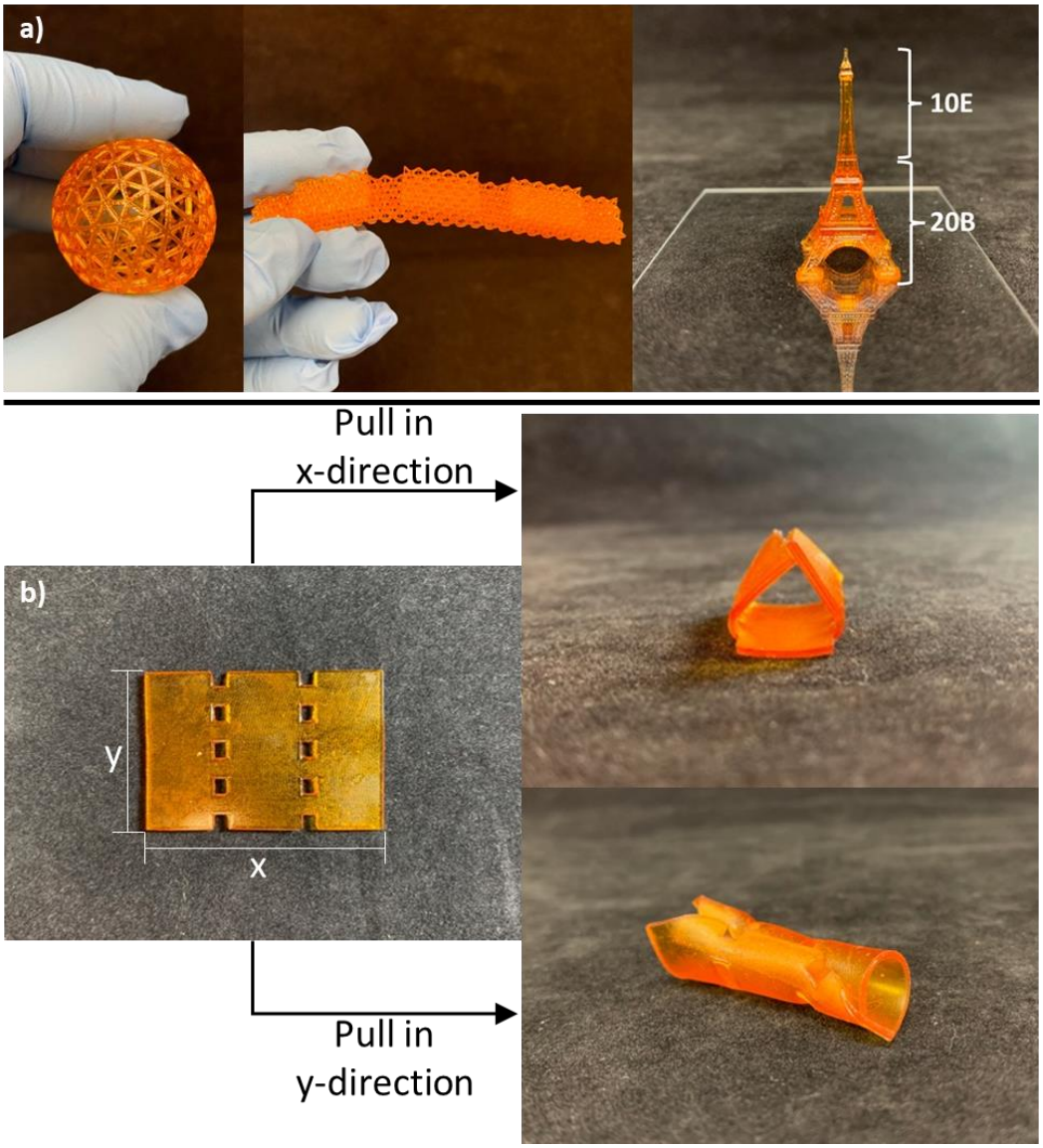

Figure 3.4 a) Multi-material geodesic lattice sphere, horizontal lattice with panels, and Eiffel tower. b) Shape transformation of octet-truss lattice. c) Anisotropic shape transformation in wheel-to-box construct.

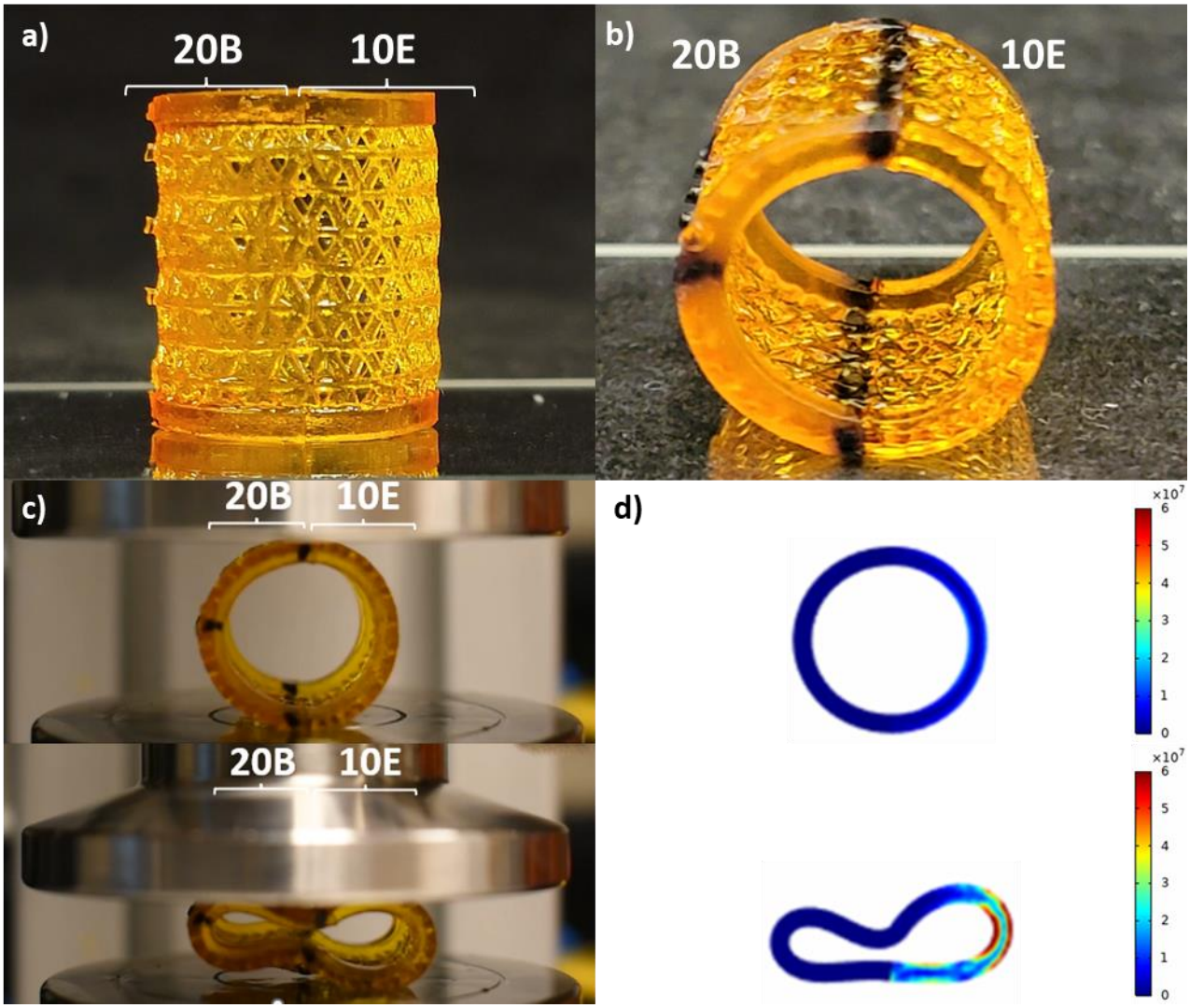

Figure 3.5 COMSOL modeling of deformation and stress distribution in lattice cylinder during compression testing. The units for von Mises stress scale bar are in N/m^2.

Chapter 4. 3D PRINTED MODULAR STRAIN SENSORS BASED ON IMIDAZOLIUM IONIC LIQUIDS

4.1 ABSTRACT

Flexible and lightweight sensors can assess their environment for a broad range of applications that include wearables for health monitoring and soft robotics. While 2D and 3D printing enables control over sensor design in multiple dimensions, customizability of a sensor toward different individual use cases is still limited because each sensor requires a new design and manufacturing step. Thus, there is a need for methodologies that produce modular sensor components that can be assembled into a larger system that fits the needs of an individual user. Herein, we demonstrate 3D printed, elastomeric, ionogels comprising covalent adaptable networks (CANs) for modular sensor assemblies. Reversible Diels-Alder connections incorporated into the network can occur at the interface between two 3D printed objects in physical contact with each other. As a result, modular components can be combined and assembled on-demand into customized sensors. This concept was demonstrated by 3D printing ionogel building blocks comprising reversible Diels-Alder connections. Thermal curing of these modular blocks triggered the dynamic remodeling of the polymer networks that caused them to become fused together. Three different configurations (linear, cyclic, and cubic arrays) were demonstrated to afford piezoelectric sensors from the same set of 3D printed building blocks. This study highlights the benefits of modular approaches that enable customization of 3D printed parts without the need for modifying the original design.

4.2 INTRODUCTION

Flexible electronic devices have gained significant interest as sensors for soft robotics,[1-6] artificial skins,[7-12] and biomedical monitors.[13-16] At a minimum, the operational device must be conductive,

elastomeric, and maintain functionality after storage under ambient conditions. Traditional sensor materials such as carbon nanotubes,[17-19] liquid metals,[8,20,21] or organic field effect transistors (OFET)[22-25] show great promise, however, when placed inside a soft matrix such as silicone, these conductive elements often limit the amount of deformation the material can withstand. The trade-offs between electronic performance, device shape, and mechanical flexibility also place limitations on the implementation and versatility of these sensors. Furthermore, the form factor required by the end-user can be specific to a particular scenario (or use case), but each one may require a new manufacturing process. The ability for an end-user to build a sensor from a set of simple building blocks presents an opportunity for greater versatility, design flexibility, and rapid implementation of these sensors.

Ionic liquids (ILs) are organic salts that are liquid at ambient temperatures, and these functional solvents are attractive as components of flexible strain sensors.[1-3,5-7,9-15,26-29] ILs can swell polymer networks to form ionic liquid gels (ionogels),[11,30,31] which can have many similarities to water-swollen hydrogels.[7,8,10,16] The advantages of IL gels include their intrinsic ionic conductivity and their negligible vapor pressure that limits solvent evaporation. The chemical structures of ILs are highly tunable, and they can be made to be stable at elevated temperatures, which affords ionic sensors with a wide operational temperature range.[32-33] While the composition of the ionic liquid can have a significant effect upon the conductive performance of the material,[11] the polymer network can be optimized to enhance the mechanical properties. For example, Wang et al.[33] demonstrated that ionogels comprised of acrylamide and acrylic acid in 1-ethyl-3-methylimidazolium ethyl sulfate afforded tough ionogels (Young's modulus of 46.5 MPa). Zhao et al.[34] demonstrated a fluorescent double network ionogel strain sensor which possessed self-healing properties due to dynamic imine bonds and hydrogen bonds. More recently, Chen et al.[35]

demonstrated an ultra-tough ionic liquid gel with a Young's modulus of 325 MPa and strain at break of 1120%, in addition to modest self-healing due to dynamic transition metal crosslinks. In all the examples discussed, the sensors were generated through traditional casting methods, which limits the range of potential form factors that can be easily fabricated.

3D printing has been gaining significant interest due to the ability to produce a complex part or product on demand.[36-41] In particular, vat photopolymerization 3D printing allows for facile fabrication of devices with complex geometries which would otherwise be inaccessible. Wang et al.[42] demonstrated an ionogel comprised of 1-vinyl-3-butylimidazolium tetrafluoroborate and acrylate-terminated hyperbranched polymer swelled with 1-butyl-3-methylimidazolium tetrafluoroborate. The resin produced strain sensors with high stretchability, sensitivity, and a wide operating temperature range. Hao et al.[9] developed an ultra-stretchable ionic skin (strain at break >10,000%) capable of sensing over a temperature range of −40 to 150 °C. The material comprised of poly (zwitterionic ionic liquid)-co-poly (acrylic acid) in 1-ethyl-3-methyl- imidazolium ethyl sulfate could be SLA 3D printed into sensors used for monitoring human hand motion. Jurinovs et al.[17] formulated an SLA 3D printable biobased IL gel by mixing 1-ethyl-3-methylimidazolium acetate with single walled carbon nanotubes (SWCNTs) in acrylated rapeseed oil. The combination of IL and SWCNT provided excellent conductivity and allowed the material to function as electrodes in soft robotics and flexible sensors. Recently, Narupai et al.[36] demonstrated an elastomeric, SLA printable ionogel containing 1-butyl-3-vinylimidazolium bis(trifluoromethanesulfonyl)imide and polyethylene glycol (PEG). The gels displayed good conductivity, high elastic recovery, and strong adhesive properties. While 3D printing is advantageous because new design iterations can be made easily using computer-aided design (CAD) software, a modular system based on building blocks that can be arbitrarily assembled post-

3D printing would allow for the facile combination of individual components without the need to alter the original design.[43,44] Morin et al.[45] demonstrated the concept using “Click-e-bricks", which are elastomeric bricks fabricated through molding that can be connected by peg/recess click connections. The modular structures were pneumatically actuated, and by varying the shape of the bricks they were able to achieve different geometries and shape transformations. The designs are applicable to a range of materials (e.g., PDMS, Ecoflex) and provide access to structures which would be difficult to create in one molding step. Gomez et al.[46] developed a thiol-acrylate resin which could be photopolymerized into self-healing elastomeric gels. SLA printing allowed the researchers to produce individual parts which could be combined using heat to produce modular elastomeric actuators. Extending this modular approach to sensors would not only enable personalized devices to be fabricated, but also would be advantageous under conditions where it may not be possible to know what form factor is required for the sensor.

Herein, we demonstrate 3D printed, elastomeric ionogels comprising covalent adaptable networks (CANs) for modular piezoelectric sensor assemblies. CANs are covalently crosslinked polymer networks (i.e., thermosets) which contain reversible covalent bonds that enable the network to rearrange in response to an external stimulus such as mechanical force, light, or heat.[47-52] We developed a resin for vat photopolymerization which afforded polymer networks comprising reversible Diels-Alder connections. The resins were formulated in ionic liquid solvents, and thus, the resulting networks were ionogels. The 3D printed components were elastomeric with failure strains ranging from 600% to 1200%, low hysteresis over multiple deformation cycles, and high sensitivity (gauge factor = 3.59). The thermal reversibility of the dynamic bonds enabled 3D printed components in physical contact to fuse together via remodeling of the polymer networks.

Thus, the 3D printed parts could be assembled into any arbitrary design and perform as piezoelectric sensors.

4.3 Results & Discussion

4.3.1 *Preparing Resins for SLA Printing of Ionic liquid CANs*

Butyl-vinyl imidazolium bis(trifluoromethanesulfonyl)imide ([BVIM][TFSI]) is an ionic liquid that can be co-polymerized with dimethacrylate cross-linkers to form polymer networks (Figure 4.1).[12,27,36] The vinyl substituent on the imidazolium is reactive to photo-initiated free radical polymerization, while the length of the alkyl substituent influences the resin viscosity of the uncured resin and the mechanical properties of the resulting network. We chose butyl as the alkyl chain based on the viscosity of the resin, as well as the viscoelasticity of the resulting polymer network (in general, as the length of the alkyl chain increases, Young's modulus decreases and the elongation at break increases).[27] Networks solely comprising of the polymerizable ILs are brittle,[27,36] but the presence of oligo- and poly-ethylene glycol (PEG) is known to reduce brittleness.[18,36] To introduce reversible Diels-Alder linkages into the polymer network, PEG cross-linker **DA-PEG 1** was synthesized (Scheme S1). The telechelic polymer has reversible Diels-Alder adducts at each end, and the polymer is terminated by methacrylate functionalities to facilitate its incorporation into the polymer network. **DA-PEG-1** was synthesized from PEG (M_n = 8000 g/ mol), which was transformed into a bis-maleimide terminated polymer. Separately, furfuryl methacrylate was synthesized by reacting furfuryl alcohol with methacrylic anhydride. The Diels-Alder reaction between furfuryl methacrylate and the bis-maleimide terminated polymer was performed neat at 70 °C overnight to yield **DA-PEG-1**.

Resins for vat photopolymerization were formulated comprising cross-linker **DA-PEG-1**, [BVIM][TFSI], photoinitiator, and photoabsorber. The amount of **DA-PEG-1** included in the

resins varied from 10, 15, to 20 w/w % to modulate the viscoelastic properties of the polymer network. The resin formulations were labelled according to the w/w % of polymer present (10-BVIM, 15-BVIM, and 20-BVIM). For example, a resin containing 10 w/w % **DA-PEG-1** dissolved in [BVIM][TFSI] was labeled 10-BVIM, while 20-BVIM corresponds to 20 w/w % **DA-PEG-1** in [BVIM][TFSI]. To further improve the structural integrity of the gels at elevated temperatures, we formulated a resin with a 1:1 ratio of the non-dynamic crosslinker PEG bis(urethane) methacrylate (PEG-BUM)[36,53] in addition to the dynamic crosslinker **DA-PEG-1** in [BVIM][TFSI] (we refer to this resin as 7.5-7.5-BVIM). Phenyl bis(2,4,6-trimethylbenzoyl) phosphine oxide (BAPO) was included (0.75 w/w %) as a photoinitiator in all of the formulations. Sudan I was included (0.025 w/w %) as a photoabsorber to improve the resolution during the printing process. Two important parameters to consider for SLA printing are the resin viscosity and rate of photocuring. It is important that the viscosity of the resin remains below 10 Pa·s to allow the resin to flow properly during printing. The resin must also cure rapidly during printing to adhere to the build plate, while at the same time not polymerizing too quickly which may result in poorly resolved features. This can be controlled with the quantity of photoabsorber used in formulating the resin. The viscosity of the ionic liquid resins presented here were approximately 1 Pa·s, well within the range required for printing.[36] The rheological properties of the resins are provided in the supporting information (Figure C12).

Ionogels were 3D printed on a Formlabs Form 2 printer. Stereolithographic apparatus (SLA) 3D printing is a form of vat photopolymerization wherein a tray with a transparent base is filled with a photo-curable resin, and a 405 nm laser photopatterns cross-sectional areas of a 3D structure in a layer-wise fashion. Tensile specimens were printed to characterize mechanical properties, and modular building blocks were also printed to demonstrate the modularity of the

system. All of the samples were subjected to a 1 h post cure in which both sides of the structure were irradiated with 405 nm light for 30 min each. Gel fraction experiments revealed that printed and cured specimens have a gel content of approximately 64.8% (Table S2-S5). The unpolymerized ionic liquid remaining in the networks is important because it contributes to the ionic conductivity and viscoelasticity of the materials, which enables the printed objects to function as strain sensors.

4.3.2 *Mechanical Properties of the Dynamic Ion Gels*

Figure 4.2 shows the mechanical characterization data for the printed ionogels. Uniaxial tensile experiments were performed using ISO 527-2 5B specimens on a TestResources universal testing machine. The mass fraction of cross-linker **DA-PEG-1** in the resin has substantial effects on the viscoelastic properties of the ionogels. The data in Figure 4.2a shows that with increasing mass fraction of **DA-PEG-1**, the Young's modulus decreases and the ionogels show lower nominal tensile strain prior to failure. The Young's moduli for 10-BVIM, 15-BVIM, and 20-BVIM were 739.3 ± 217.9 kPa, 119.1 ± 18.7 kPa, and 67.3 ± 16.2 kPa, respectively, and the corresponding strains at break were 1184.9 ± 121.5%, 860.6 ± 21.1%, and 693.5 ± 33.2% (Table S6). The decrease in elongation at break is consistent with a higher degree of chemical cross-linking in the polymer network. The decrease in Young's modulus is likely due to the plasticizing effect of PEG, which has been shown to improve the chain mobility of polymerized ionic liquid networks.[36,54,55] For 7.5-7.5-BVIM gels, the Young's modulus was 235.7 ± 25.3 kPa and the strain at break was 898.0 ± 30.2% (Figure 4.2a). The increased Young's modulus relative to 15-BVIM is due to the presence of permanent crosslinks, while the similar strain at break is because both networks possess the same w/w % of crosslinker.

We next investigated the ability of these networks to remodel at the interface between two different substrates. Tensile specimens were printed, cut in half, and mended either mechanically (pushed together) or thermally. Interestingly, the Young's modulus is comparable between the mechanically reattached and thermally treated samples. As expected, both of these values are lower relative to the original sample before cutting due to the loss of the permanent cross-links within the network. Tensile specimens of 7.5-7.5-BVIM which had been cut and mended thermally exhibited a larger strain at break (1086.3 ± 180.7%) compared to samples which were cut and mechanically reattached (773.6 ± 34.4%) (Figure 4.2b). This difference can be attributed to a greater number of Diels-Alder cross-links re-forming across the damaged interface. In comparison, we observed a similar trend for mechanically mended 15-BVIM samples, which exhibited a strain at break of 240.0 ± 27.7% versus the thermally mended 15-BVIM samples which improved to 654.9 ± 22.5%.

A crucial element of any material intended for sensing is its ability to conduct electricity. Electrical impedance spectroscopy (EIS) measurements carried out on an Autolab 302N potentiostat galvanostat (Figure 4.2c) demonstrated the material is conductive both as a resin and as a printed gel. Conductivity in the cured material is decreased due to immobilization of the IL.

4.3.3 *Stress Relaxation Measurements*

Stress relaxation experiments were performed to determine the relaxation time across a range of temperatures from 75 °C to 105 °C (Figure 4.3a). A 5% strain was applied to the network, and the relaxation times were determined by using the normalized modulus of the sample at 1/e of its initial value. This data was plotted versus 1000/T to determine an activation energy for the Diels-Alder adducts of 84 ± 5 kJ/mol (Figure 4.3b). This value is similar to those reported in the literature that had a range of 98 - 115 kJ/ mol.[56] The position of the functional groups on furan and maleimide

derivatives, as well as the solvent, are known to strongly influence the activation energy of the reverse Diels-Alder reaction and can lead to the range of values observed.

4.3.4 *Demonstration of Modular Ion Gel Sensors*

To explore the suitability of the resin formulations for producing modular piezoelectric sensors, blocks in the shape of a cube, bent arm, and cross, were printed and arranged into a linear, cyclic, or cubic configurations (Figure 4.4a, b). Blocks composed of 10-BVIM, 15-BVIM, or 20-BVIM were placed in contact with one another and heated at 60 °C overnight to initiate the reversible Diels-Alder reaction at the interface between the blocks. The modular pieces were successfully combined into one continuous structure, however, there was a significant loss in the resolution of the printed shape. In contrast, the 7.5-7.5-BVIM ionogels successfully maintained their shape fidelity as a consequence of the non-reversible cross-links present in the network. Heating these samples at 85 °C for 4.5 h was sufficient to fuse the polymer networks at the interface between two modular building blocks without diminishing the resolution of the printed features (Figure 4.4b, c).

4.3.5 *Cyclic Uniaxial Tensile Measurements*

We investigated the hysteresis in these materials over multiple deformation cycles.[13-16] Cyclic uniaxial tensile experiments show the hysteresis of 7.5-7.5-BVIM gels under different strain rates ranging from 5 to 100 mm/min at 50% strain (Figure 4.5a). The results showed that sensors stretched at slower strain rates experienced lower amounts of hysteresis and lower stress values because the network had more time to relax between cycles. When the material was stretched at higher strain rates, more force was required, and a larger hysteresis was observed. In all cases, the greatest amount of hysteresis was observed between the first and second cycles and decreased

significantly after the second cycle. Similarly, when the sensors were stretched at a constant strain rate of 50 mm/min at strains ranging from 5-100%, lower amounts of strain resulted in smaller hysteresis and lower stress (Figure 4.5b, Figure C16). As the % strain increased, the stress experienced by the network increased along with a slight increase in hysteresis.

4.3.6 *Conductivity and Gauge Factor Measurements*

In order to examine the performance of the modular sensors, conductivity measurements were performed with a Keithley 2400 source measure unit (SMU). Blocks of 7.5-7.5-BVIM were first fused into a loop-shaped structure. Electrodes were attached to opposite ends of the loop and connected to the SMU (Figure C15). Stretching the loop provokes a decrease in the measured current. The decrease in current is a result of an increase in length and a decrease in the cross-sectional area of the structure as described by the equation:

$$V/I = \rho(L/A) \tag{4.5}$$

which relates resistance (R), resistivity (ρ), length (L) and cross-sectional area (A) of the sample. Since the applied voltage and resistivity are constant, the current drops in response to the deformation. Once the applied strain is removed, the current increases (Figure 4.5c). To evaluate the performance of a piezoelectric device under compression, printed blocks were arranged into a box and thermally cured into a continuous network structure. The box was connected to the SMU using electrodes and copper plates (Figure C15). As expected, compression led to an increase in current due to the decrease in the shortest path between the electrodes. The strain-dependent sensitivity of the sensors is evaluated as the gauge factor (GF), which is the ratio of change in electrical resistance to applied mechanical strain The GF was 2.08 under 5-50% strain (Figure C27), which increased to 3.59 under 50-200% strain (Figure 4.5d). Larger strains cause a larger

deformation to the network, which interrupts conductive pathways by increasing the separation between anions and cations, leading to higher resistance.[34]

4.3.7 *Adhesive Strength*

All of the ionogels also exhibited an adhesive character, which was characterized using lap-shear adhesion tests. The adhesive strength of the ionogels were evaluated for glass, aluminum, cardboard, and Teflon substrates (Figure 4.5e). The gels adhered best to glass (5.45 MPa) and maintained their adhesive strength after being detached and reapplied (5.37 MPa). The strong adhesive properties of these materials are attributed to the broad range of noncovalent interactions (hydrogen bonding, electrostatic, ion-dipole, and van der Waals interactions) between the ion gels and the substrate.[9,18,57,58] The adhesion to different substrate types could be advantageous for these sensors to remain in place once they are installed.

4.4 MATERIALS & METHODS

4.4.1 *General Reagent Information*

All purchased reagents were used as received without further purification unless otherwise specified. 1-vinylimidazole (>98.0%), 1-bromobutane (>99.0%), 1-bromoethane (>98.0), 2-isocyanoethyl methacrylate (>98.0%, stabilized with BHT), dibutyltin dilaurate (>95.0%), triethylamine (>99.0%), furan (stabilized with BHT, >99.0+%), maleic anhydride (>99.0%), Propargyl amine (>97.0%), 1,1,1,3,3,3-hexamethyldisilazane (>96.0%), CuBr (>98.0%), *N*,*N*,*N*',*N*'',*N*''-Pentamethyldiethylenetriamine (PMDETA, >99.0%), and 4-methoxyphenol (MEHQ, >99.0%) were purchased from TCI America. Lithium bis(trifluoromethanesulfonyl)imide salt (99.95%), 4-dimethylaminopyridine (>99.0%), p-toluenesulfonyl chloride (>98.0%), *N*,*N*-dimethylformamide (anhydrous, 99.8%), toluene

(anhydrous, 99.8%), sodium azide (>99.5%), furfuryl alcohol (98%), methacrylic anhydride (contains 2,000 ppm topanol A as inhibitor, ≥94%), methanol (>99.9%), (+)-sodium L-ascorbate (>99.0%), aluminum oxide (activated, neutral, Brockmann I) and ethyl acetate (>99.7%) were purchased from Sigma Aldrich. PEG-8000, diethyl ether (anhydrous, stabilized with BHT, >99.0%), acetonitrile, tetrahydrofuran (>99.8%), and dichloromethane (>99.9%) were purchased from Fisher Scientific. Dry tetrahydrofuran and dichloromethane were obtained from a Pure Process Technology purification system.

4.4.2 *General Analytical Information*

^{1}H NMR spectra were recorded on a Bruker 300 or 500 MHz instrument. Rheology measurements were performed on a TA Discovery HR-2 Hybrid Rheometer. Mechanical stress/strain measurements were performed on a Test Resources Universal Testing Machine. 3D printed structures were printed using a Formlabs Form 2 SLA printer. Mass Spec measurements were performed on a Bruker Esquire LC - Ion Trap Mass Spectrometer. DSC measurements were performed on a TA Discovery DSC 2500 instrument. Dynamical Mechanical Thermal Analysis (DMTA) was recorded on a TA Instruments DMA 850. Electrical impedance spectroscopy (EIS) measurements carried out on an Autolab 302N potentiostat galvanostat. Conductivity measurements were performed with a Keithley 2400 source measure unit (SMU). Cyclic tensile experiments were conducted on an Instron 5585H load frame with a 50 N load cell. Thermogravimetric analysis was conducted on a TA Q5000 thermogravimetric analyzer.

4.4.3 *Synthesis of exo-3,6-epoxy-1,2,3,6-tetrahydrophtalic anhydride (maleic anhydride Diels-Alder adduct)*

A Teflon stir bar, 10 g of maleic anhydride (0.102 mol), 9.86 mL of furan (0.136 mol), and 30 mL of ethyl acetate were added to a 250 mL round-bottom flask. The reaction mixture was left to stir at room temperature for 24 h under N_2. The product was collected via vacuum filtration and dried at room temperature under high vacuum using a Schlenk manifold (Yield: 11.79 g, 69.60%). ^{1}H NMR (300 MHz, DMSO-d_6): δ 6.60 (d, 2H), 5.36 (dd, 2H), 3.33 (d, 2H).

4.4.4 *Synthesis of alkyne functionalized maleimide Diels-Alder adduct (alkyne maleimide)*

A Teflon stir bar and 11.80 g of exo-3,6-epoxy-1,2,3,6-tetrahydrophtalic anhydride (0.071 mol) was dissolved in 150 mL of methanol and 150 mL of THF in a single-neck 500 mL round-bottom flask under N_2 and subsequently cooled to 0 °C. 4.55 mL of propargylamine (0.071 mol), 25 mL of methanol, and 25 mL of THF were added to a separate 100 mL single-neck round-bottom flask. A 100 mL addition funnel was attached to the 500 mL round-bottom flask and the contents of the 100 mL round-bottom flask were poured into the addition funnel. The contents of the addition funnel were added dropwise to the 500 mL round-bottom flask and left to stir for an additional 30 minutes at 0 °C upon completion. 17.76 mL of hexamethyldisilizane (0.085 mol) was added to the round-bottom flask and the reaction mixture was left to stir at 65 °C for 3 days under N_2. The reaction mixture is then cooled to room temperature and the remaining liquid is removed with a rotary evaporator from the orange product. The product is redissolved in minimal DCM and washed twice with a saturated sodium bicarbonate solution, twice with 2 M hydrochloric acid. The product is then dried using magnesium sulfate and vacuum filtered to remove solid impurities. Product was put on rotary evaporator at 30 °C to obtain off-white residue. The product is then recrystallized in acetone, collected via vacuum filtration, and dried at room temperature under high

vacuum using a Schlenk manifold (Yield 5.19 g, 36.0%). ^{1}H NMR (300 MHz, $CDCl_3$): δ 6.52 (d, 2H), 5.30 (dd, 2H), 4.23 (s, 2H), 2.90 (s, 2H), 2.19 (s, 1H).

4.4.5 *Synthesis of furfuryl methacrylate*

A Teflon stir bar, 1.41 g of 4-dimethylaminopyridine (0.0116 mol), 43.38 mL of triethylamine (0.347 mol), 20 mL of furfuryl alcohol (0.231 mol), and 20 mL of ethyl acetate were added to a 500 mL single-neck round-bottom flask and left to stir for 5 minutes under N_2. 36.19 mL of methacrylic anhydride (0.243 mol) and 30 mL of ethyl acetate were added to a separate 100 mL single-neck round-bottom flask. A 100 mL addition funnel was attached to the 500 mL round-bottom flask and the contents of the 100 mL round-bottom flask were poured into the addition funnel. The contents of the addition funnel were added dropwise to the 500 mL round-bottom flask. Upon completion, the reaction mixture was left to stir at 55 °C for 24 hours under N_2. Any precipitated salts were removed via vacuum filtration and the remaining reaction mixture was diluted with ethyl acetate. The reaction mixture was washed twice with deionized water, twice with 1 M hydrochloric acid, twice with a saturated sodium bicarbonate solution and twice with a saturated brine solution. The product is then dried using magnesium sulfate and vacuum filtered to remove solid impurities. The product was then run through a neutral alumina column with a 10:1 mixture of hexanes: ethyl acetate as the eluent. The first analyte was collected and put on the rotary evaporator at 35 °C to obtain the product. Minimal MEHQ is added to the product to prevent crosslinking. ^{1}H NMR (300 MHz $CDCl_3$): δ 7.43 (d, 1H), 6.42 (dd, 1H), 6.36 (d, 1H), 6.13 (s, 1H), 5.57 (s, 1H), 5.14 (s, 2H), 1.95 (s, 3H).

4.4.6 *Synthesis of PEG-tosylate*

A Teflon stir bar and 10 g of PEG-8000 (0.00125 mol) was dissolved in 100 mL of anhydrous DCM in a single-neck 250 mL round-bottom flask under N_2 and cooled to 0 °C. Maintaining positive N_2 flow, 2.38 g of tosyl chloride (0.0125 mol) and 0.100 g of 4-dimethylaminopyridine (0.00075 mol) were added portion-wise to the round-bottom flask, followed by 1.74 mL of triethylamine (0.0125 mol) added dropwise with stirring at 0 °C. The reaction mixture was stirred for an additional hour at 0 °C and then left to stir at room temperature for 24 hours under nitrogen. The reaction mixture is then washed twice with deionized water, twice with saturated sodium bicarbonate solution and twice with a saturated brine solution. The product is then dried using magnesium sulfate and vacuum filtered to remove solid impurities and then precipitated twice in diethyl ether. The product was collected via vacuum filtration and dried at room temperature under high vacuum using a Schlenk manifold (Yield: 6.74 g, 64.6%). ^{1}H NMR (500 MHz $CDCl_3$): δ 7.82 (d, 4H), 7.36 (d, 4H), 4.19 (t, 4H), 2.48 (s, 6H), protons from PEG appear at 3.67 ppm.

4.4.7 *Synthesis of PEG-azide*

A Teflon stir bar and 5.98 g of PEG-tosylate (0.00072 mol) was dissolved in 100 mL of DMF in a single-neck 250 mL round-bottom flask under N_2. Maintaining positive N_2 flow, 0.470 g of sodium azide (0.0072 mol) was added to the round-bottom flask. The reaction mixture is then left to stir at 80 °C for 2 days under N_2. DMF is then removed using a rotary evaporator. The product is then redissolved in minimal DCM and washed twice with deionized water and then twice with a saturated brine solution. The product is then dried using magnesium sulfate and vacuum filtered to remove solid impurities. The product is then precipitated twice in diethyl ether, collected via vacuum filtration, and dried at room temperature under high vacuum using a Schlenk manifold

(Yield: 4.41 g, 76.1%). ^{1}H NMR (500 MHz $CDCl_3$): δ 3.36 (t, 4H), protons from PEG appear at 3.62 ppm.

4.4.8 *Synthesis of protected PEG-maleimide*

A Teflon stir bar and 0.17 g of copper (I) bromide (0.00123 mol) were added to a 250 mL single-neck round-bottom flask and pump purged with N_2. 36 mL of methanol, 4 mL of water, 0.257 mL of N,N,N',N'',N''-pentamethyldiethylenetriamine (0.00123 mol), and 0.6 of sodium ascorbate (0.00303 mol) were added to the round-bottom flask and allowed to stir under N_2 for 24 hours. 10 g of PEG-azide (0.00123 mol) and 2.5 g of alkyne maleimide (0.0123 mol) were added to the round-bottom flask and allowed to stir under N_2 for 24 hours. The reaction mixture was then filtered through neutral alumina and put on the rotary evaporator initially at 35 °C to remove DCM, then 50 °C to remove methanol and water. The product is then precipitated twice in diethyl ether, collected via vacuum filtration, and dried at room temperature under high vacuum using a Schlenk manifold (Yield: 7.8 g, 74.7%). ^{1}H NMR (500 MHz $CDCl_3$): δ 7.65 (s, 2H), 6.51 (d, 4H), 5.28 (dd, 4H), 4.78 (s, 4H), 4.48 (t, 4H), 2.88 (d, 4H), protons from PEG appear at 3.63 ppm.

4.4.9 *Deprotection of PEG-maleimide*

A Teflon stir bar, 1.7 g of PEG-maleimide (0.000200 mol), and 50 mL of toluene were added to a 100 mL single-neck round-bottom flask. The flask was left to stir and refluxed for 24 hours at 140 °C under N_2. The product mixture was placed on the rotary evaporator at 55 °C to remove toluene and then redissolved in DCM. The product is then precipitated twice in diethyl ether, collected via vacuum filtration, and dried at room temperature under high vacuum using a Schlenk manifold (Yield: 1.49 g, 88.9%). ^{1}H NMR (500 MHz $CDCl_3$): δ 7.71 (s, 2H), 6.73 (s, 4H), 4.82 (s, 4H), 4.50 (t, 4H), protons from PEG appear at 3.64 ppm.

4.4.10 *Synthesis of **DA-PEG-1** (methacrylated PEG-maleimide)*

A Teflon stir bar and 4.78 g of deprotected PEG-maleimide (0.000578 mol) were added to a 100 mL single-neck round-bottom flask under N_2 and heated to 70 °C. Once the polymer was fully melted, 1.77 mL of furfuryl methacrylate (0.0115 mol) was added to the round-bottom flask. The reaction was left to stir at 70 °C for 24 hours under N_2. The product was dissolved in minimal DCM then precipitated twice in diethyl ether, collected via vacuum filtration, and dried at room temperature under high vacuum using a Schlenk manifold (Yield: 4.40 g, 88.5%). ^{1}H NMR (500 MHz, $CDCl_3$): δ 7.64 (s, 2H), 6.54 (d, 2H), 6.43 (dd, 2H), 6.12 (dd, 2H), 5.55 (s, 2H), 5.25 (s, 2H), 4.89 (s, 4H), 4.58 (d, 4H), 4.46 (t, 4H), 3.38 (s, 2H), 3.00 (d, 1H), 2.92 (d, 1H), 1.91 (s, 6H).

4.4.11 *Synthesis of PEG-bis(urethane) methacrylate (PEG-BUM)*

A Teflon stir bar and 60 g of PEG-8000 (0.0075 mol) were dried under vacuum for 12 hours in a single-neck 1 L round-bottom flask. The flask was then backfilled with dry nitrogen. Maintaining positive N_2 flow, 550 mL of anhydrous DCM was added to the round-bottom flask and stirred at 30 °C until PEG is fully dissolved. Add 0.89 mL (0.0015 mL) dibutyltin dilaurate to the PEG solution. Attach a 50 mL addition funnel to the 1 L round-bottom flask. In a separate 100 mL round-bottom flask, add 50 mL of anhydrous DCM along with 5.3 mL (0.0375 mol) of 2-isocyanatoethyl methacrylate and swirl to mix. Pour the isocyanate/DCM mixture into the 50 mL addition funnel. Adjust the flow rate of the addition funnel so that the isocyanate is added *slowly* (about 1 drop per second) to the reaction mixture. This can take up to 2 hours. Following the complete addition of isocyanate, remove the addition funnel and reattach the vacuum adapter to the round-bottom flask. Stir reaction mixture at 30 °C for 2 days under nitrogen. The reaction mixture is then concentrated on a rotary evaporator at 30 °C until viscous. The product is

precipitated twice in diethyl ether. The product was collected by vacuum filtration and dried at room temperature under high vacuum using a Schlenk manifold (Yield: 19.48 g, 93.7%). ^{1}H NMR (500 MHz, $CDCl_3$): δ 6.04 (s, 2H), 5.52 (t, 2H), 5.18 (t, 1H) 1.87 (s, 6H), protons from PEG appear at 4.14 ppm and 3.57 ppm. ^{13}C NMR (300 MHz, $CDCl_3$): δ 70.59. IR (ATR-FTIR, ν_{max}, cm^{-1}): 2880, 1720, 1468, 1340, 1280, 1092, 960, 840.

4.4.12 *Synthesis of 1-vinyl-3-butyl imidazolium bromide ([BVIM]Br)*

200 mL (2.2 mol) of 1-vinyl imidazole and 285 mL (2.65 mol) of 1-bromobutane were stirred magnetically at 45 °C for 24 hours. The viscous solution was allowed to cool before washing 3-4 times with excessive diethyl ether until the liquid solidifies. The product was collected by vacuum filtration and dried at room temperature under high vacuum using a Schlenk manifold. The product appears as a white solid (Yield: 456.23 g, 90.1%). ^{1}H NMR (500 MHz, DMSO-D6): δ 9.61 (s, 1H), 8.24 (t, 1H), 7.97 (t, 1H), 7.33 (m, 1H), 6.00, 5.43 (d of d, 2H), 4.22 (t, 2H), 1.81 (q, 2H), 1.30 (m, 2H), 0.91 (t, 3H). ^{13}C NMR (300 MHz, $CDCl_3$): δ 135.22, 128.74, 123.17, 119.17, 108.57, 48.81, 30.98, 18.68, 13.19. IR (ATR-FTIR, ν_{max}, cm^{-1}): 3092, 3040, 2956, 1652, 1568, 1540, 1456, 1160, 984, 928, 880, 804, 740, 724, 660, 636, 604.

4.4.13 *Synthesis of 1-vinyl-3-butyl imidazolium bis(trifluoromethane) sulfonamide ([BVIM]TFSI)*

96.34 g (0.42 mol) of [BVIM]Br and 122.6 g (0.427 mol) of Lithium bis(trifluoromethanesulfonyl) imide salt were dissolved in 160 mL of DI water and stirred at room temperature for 48 hours. The mixture was then poured into a separatory funnel and the ionic liquid layer was allowed to separate. The ionic liquid was separated from the water layer, then passed through a column of neutral alumina. The product appears as a clear liquid. (Yield: 152.12 g, 84%). ^{1}H NMR (500 MHz,

DMSO-D6): δ 9.46 (s, 1H), 8.18 (t, 1H), 7.91 (t, 1H), 7.28 (m, 1H), 5.96, 5.42 (d of d, 2H), 4.19 (t, 2H), 1.80 (q, 2H), 1.27 (m, 2H), 0.91 (t, 3H). ^{13}C NMR (300 MHz, $CDCl_3$): δ 135.28, 128.85, 123.21, 119.16, 108.58, 48.97, 31.03, 18.77, 13.15. IR (ATR-FTIR, ν_{max}, cm^{-1}): 3156, 2972, 1660, 1552, 1348, 1180, 1132, 1052, 956, 920, 740, 612, 568, 508.

4.4.14 *Ion Gel Resin Preparation*

Ion Gel Resin Preparation:

Example of a typical procedure to prepare 20 g of 7.5-7.5-BVIM resin for 3D printing:

7.5 wt% (1.5 g) of PEG-BUM and 7.5 wt% (1.5 g) of **DA-PEG-1** is added to an amber vial. 0.75 wt% (0.15 g) of BAPO was added, followed by 0.025 wt% (0.005 g) of Sudan 1. 16.85 mL of [BVIM]TFSI (~85 wt%) is then added and the mixture is vortexed for 10-15 mins before being stored at 4 °C overnight. Solution is vortexed again if the PEG is not fully dissolved. The amount of each component used to make the fusible ion gels are summarized in Table C1.

4.4.15 *General process for 3D Printing Ion Gel Objects Using a Stereolithographic Apparatus (SLA) 3D Printer*

The desired resin was poured into the resin tray and the print was initiated on a Formlabs Form 2 SLA printer in open mode. The z-axis step size was 0.100 mm. CAD files used for building blocks were downloaded from Thingiverse.com (credit to mathgrrl and Rob65). Upon print completion, the structure was removed from the build plate carefully using a metal scraper and residual resin was removed by gently rolling the structure in kimwipes until minimal resin remained. If the shape of the structure permits, the printed structures may be centrifuged at 1000 RPM for one minute to help remove residual resin. The structure was then cured using 405 nm light for 30 mins on one side, flipped, then cured for an additional 30 mins on the other side.

4.4.16 *Creating Modular 3D Printed Ion Gel Sensors*

3D printed blocks were stuck together in the desired configuration and placed in a parafilm covered glass petri dish. Samples were then heated in a vacuum oven. 10-BVIM, 15-BVIM, and 20-BVIM samples were heated overnight at 60 °C under ambient pressure. 7.5-7.5-BVIM samples were heated at 85 °C for 4 hours under ambient pressure. Fused structures were then removed from the oven and allowed to reach room temperature.

4.4.17 *Rheology*

Rheometrical characterization was performed on a TA Instruments DHR-2 equipped with an Advanced Peltier Plate system. Experiments were performed using an 8 mm flat stainless steel upper plate. Resin samples were loaded via glass pipette onto the bottom plate. The sample is then trimmed after the upper plate was lowered to the trim gap at 600 μm. The final geometry gap was then set to 500 μm, and pre-shear was applied at 5 °C for 10 s before additional sample conditioning at 25 °C for 8 min. Viscosity vs Shear Rate experiments were performed to measure the viscosity of the ion gel resins. The viscosity of resins must remain below 10 Pa*s for resin to flow properly during SLA printing. All resins reported in this manuscript had viscosities below this threshold. Resins were found to increase in viscosity with increasing amount of PEG co-polymer present.

4.4.18 *Tensile Tests*

A TestResources Universal Test System 1.1 kN electromechanical actuator single column load frame with a 43 N high accuracy S10 type load cell was used to evaluate the mechanical properties of 3D printed ion gels. For dimensions of all tensile specimens, ISO 527-2 5B specimen specifications were used. The samples were attached to vice grips with diamond grit jaw and subjected to increasing strain at a constant rate of 5 mm/min until mechanical failure. Samples designated “mechanically mended” were cut with a razor at the center of the gauge region and

stuck together mechanically by pushing the two ends of the pieces together. The samples were self-adhered prior to loading. Samples designated “thermally mended” were cut with a razor at the center of the gauge region and heated together at 85 °C for 4 h prior to loading.

4.4.19 *Dynamic Mechanical Thermal Analysis*

Dynamical Mechanical Thermal Analysis (DMTA) was recorded on a TA Instruments DMA 850 equipped with a liquid nitrogen purge cooler. Specimens with dimensions of 20 mm x 3 mm x 0.6 mm were tested using a tensile dual screw film clamp. The experiment was carried out over a temperature range of –50 °C to 120 °C at a ramp rate of 2 °C/ min, with an amplitude of 10 μm and a frequency of 1 Hz. A glass transition temperature (T_g) of 15 °C was determined from the peak in tan (δ).

4.4.20 *Electrical Impedance Spectroscopy*

Ionic conductivities were determined by electrochemical impedance spectroscopy (EIS) in an Autolab 302N potentiostat galvanostat at various temperatures (20-100 °C) using a temperature control Microcell HC station. Samples were placed between stainless steel electrodes (surface area = 0.5 cm2). The plots were obtained using 10 mV amplitude in the 100 kHz to 1 Hz range.

4.4.21 *Stress Relaxation Measurements*

Relaxation modulus and activation energy was determined by stress relaxation experiments performed in an ARES rheometer (Rheometrics) using a film tension fixture and 5 % of strain at temperatures ranging from 75 °C to 105 °C. The samples used for these measurements had a width between 2.5 to 3 mm and thickness between 0.75 to 1.05 mm. Temperature dependent relaxation times are described by the Arrhenious equation:

$$\tau(T) = e^{Ea/RT} \tag{4.6}$$

The activation energy of the dynamic bond was determined from the slope of the natural logarithm of τ plotted against 1000/T.

4.4.22 *Thermogravimetric Analysis*

Thermogravimetric analysis was conducted on a TA Q5000 thermogravimetric analyzer. Samples were examined over a temperature range of 30-500 °C at a rate of 10 °C/ min under N_2 atmosphere. The first derivative (blue) shows the decomposition temperatures of the sample, while the weight loss thermogram (red) demonstrates the amount of mass lost from the sample. Material decomposition began at 300 °C (10% mass lost), followed by complete decomposition at 417 °C, exhibiting good thermal stability. The initial mass loss is likely due to unpolymerized ionic liquid remaining in the gels.

4.4.23 *Source Measuring Unit Conductivity Experiments*

Conductivity measurements were performed with a Keithley 2400 source measure unit (SMU). Electrodes were attached to the sensors by wrapping wires around the object or placing copper plating in contact with the sample and wiring. Results from the compression of the cubic sensor are displayed in Figure C15.

4.4.24 *Cyclic Uniaxial Tensile Tests*

Cyclic tensile experiments were conducted on an Instron 5585H load frame with a 50 N load cell. Constant strain of 50% was applied at strain rates ranging from 5 to 100 mm/ min. Additionally, a constant strain rate of 50 mm/ min was applied over strains ranging from 5% to 200%.

4.4.25 *Gauge Factor Determination*

The gauge factor of a material is the ratio of change in electrical resistance to applied mechanical strain:

$$GF = \frac{\Delta R/R_0}{\varepsilon} \tag{4.7}$$

Gauge factor measurements for the ion gel sensors were conducted on a 5585H load frame with a 50 N load cell while connected to a Keithley 2400 SMU. Samples were subjected to tensile strain ranging from 5-200% at a strain rate of 50 mm/ min. The change in resistance was plotted against % strain to determine the gauge factor.

4.4.26 *Adhesion Tests*

To determine the adhesive strength of the ion gels to a variety of substrates, square patches (2.5 cm x 2.5 cm) were sandwiched between two offset pieces of the relevant material. Substrates used were glass, aluminum, cardboard, and Teflon. The setup was attached to the grips of a TestResources Universal Test System with 1 kN load cell and pulled until the sample was detached.

4.5 CONCLUSION

A photopolymerizable ionic liquid resin was developed for 3D printing ionogel CANs that can be fused together to create piezoelectric sensors. During the 3D printing process, the resin was transformed into dynamic ionogel networks, wherein Diels-Alder adducts were utilized to create reversible cross-links. The printed structures demonstrate high print quality, as well as desirable mechanical properties such as good elasticity (1184% strain at break) and strength (739 kPa), which can be tuned by altering the number of dynamic crosslinks in the material. These dynamic covalent bonds imbued a mechanism for self-repair in the material and were also active at the substrate surface, such that two different 3D printed networks could be fused into a single continuous network. Within these ionogels, the unpolymerized ionic liquid is mobile within the network. Thus, the printed and fused ionogels were conductive and performed as piezoelectric sensors. As a representative demonstration, three different modular building blocks were 3D printed. Using these building blocks, an end-user can assemble a piezoelectric sensor with any

arbitrary design, as necessary. This strategy, wherein 3D printed parts can be assembled into a larger functional system, showcases a decentralized manufacturing approach for future on-demand production of active devices.

4.6 ACKNOWLEDGEMENTS

This research is financially supported by the Center for the Chemistry of Molecularly Optimized Networks (MONET), a National Science Foundation (NSF) Center for Chemical Innovation (CHE-2116298). We also gratefully acknowledge support from the U.S. Army Research Office (W911NF-17-1-0595) for this work.

4.7 REFERENCES

[1] Zhang, C.; He, B.; Wang, Z.; Zhou, Y.; Ming, A.; Thanh Dinh, N. Application and Analysis of an Ionic Liquid Gel in a Soft Robot. *Adv. Mater. Sci. Eng.* **2019**, 2857282

[2] Zhang, C.; He, B.; Ding, A.; Xu, S.; Wang, Z.; Zhou, Y. Motion Simulation of Ionic Liquid Gel Soft Actuators Based on CPG Control. *Comput. Intell. Neurosci.* **2019**, 8256723.

[3] Ankit; Tiwari, N.; Ho, F.; Krisnadi, F.; Kulkarni, M. R.; Nguyen, L. L.; Koh, S. J. A.; Mathews, N. High-k, Ultrastretchable Self-Enclosed Ionic Liquid-Elastomer Composites for Soft Robotics and Flexible Electronics. *ACS Appl. Mater. Interfaces* **2020**, *12* (33), 37561–37570.

[4] Truby, R. L.; Wehner, M.; Grosskopf, A. K.; Vogt, D. M.; Uzel, S. G. M.; Wood, R. J.; Lewis, J. A. Soft Somatosensitive Actuators via Embedded 3D Printing. *Adv. Mater.* **2018**, *30* (15), 1706383.

[5] He, B.; Zhou, Y.; Wang, Z.; Wang, Q.; Shen, R.; Wu, S. A Multi-Layered Touch-Pressure Sensing Ionogel Material Suitable for Sensing Integrated Actuations of Soft Robots. *Sensors Actuators, A Phys.* **2018**, *272*, 341–348.

[6] Feng, C.; Hemantha Rajapaksha, C. P.; Jákli, A. Ionic Elastomers for Electric Actuators and Sensors. *Engineering* **2021**, *7* (5), 581–602.

[7] Liu, Z.; Wang, Y.; Ren, Y.; Jin, G.; Zhang, C.; Chen, W.; Yan, F. Poly(Ionic Liquid) Hydrogel-Based Anti-Freezing Ionic Skin for a Soft Robotic Gripper. *Mater. Horizons* **2020**, *7* (3), 919–927.

[8] Gao, W.; Ota, H.; Kiriya, D.; Takei, K.; Javey, A. Flexible Electronics toward Wearable Sensing. *Acc. Chem. Res.* **2019**, *52* (3), 523–533.

[9] Hao, S.; Li, T.; Yang, X.; Song, H. Ultrastretchable, Adhesive, Fast Self-Healable, and Three-Dimensional Printable Photoluminescent Ionic Skin Based on Hybrid Network Ionogels. *ACS Appl. Mater. Interfaces* **2022**, *14* (1), 2029–2037.

[10] Gao, N.; He, Y.; Tao, X.; Xu, X. Q.; Wu, X.; Wang, Y. Crystal-Confined Freestanding Ionic Liquids for Reconfigurable and Repairable Electronics. *Nat. Commun.* **2019**, *10* (1), 547.

[11] Tie, J.; Mao, Z.; Zhang, L.; Zhong, Y.; Sui, X.; Xu, H. Highly Transparent, Self-Healing and Adhesive Wearable Ionogel as Strain and Temperature Sensor. *Polym. Chem.* **2022**, *13*, 4064–4075.

[12] Basu, A.; Wong, J.; Cao, B.; Boechler, N.; Boydston, A. J.; Nelson, A. Mechanoactivation of Color and Autonomous Shape Change in 3D-Printed Ionic Polymer Networks. *ACS Appl. Mater. Interfaces* **2021**, *13*, 19263-19270.

[13] Borayek, R.; Foroughi, F.; Xin, X.; Mohamed, A. M.; Abdelrahman, M. M.; Zedan, M.; Zhang, D.; Ding, J. Near-Zero Hysteresis Ionic Conductive Elastomers with Long-Term Stability for Sensing Applications. *ACS Appl. Mater. Interfaces* **2022**, *14* (9), 11727–11738.

[14] Choi, D. Y.; Kim, M. H.; Oh, Y. S.; Jung, S. H.; Jung, J. H.; Sung, H. J.; Lee, H. W.; Lee, H. M. Highly Stretchable, Hysteresis-Free Ionic Liquid-Based Strain Sensor for Precise Human Motion Monitoring. *ACS Appl. Mater. Interfaces* **2017**, *9* (2), 1770–1780.

[15] Wong, J.; Gong, A. T.; Defnet, P. A.; Meabe, L.; Beauchamp, B.; Sweet, R. M.; Sardon, H.; Cobb, C. L.; Nelson, A. 3D Printing Ionogel Auxetic Frameworks for Stretchable Sensors. *Adv. Mater. Technol.* **2019**, *4* (9), 1–6.

[16] Tian, K.; Bae, J.; Bakarich, S. E.; Yang, C.; Gately, R. D.; Spinks, G. M.; in het Panhuis, M.; Suo, Z.; Vlassak, J. J. 3D Printing of Transparent and Conductive Heterogeneous Hydrogel–Elastomer Systems. *Adv. Mater.* **2017**, *29* (10).

[17] Jurinovs, M.; Barkane, A.; Platnieks, O.; Grase, L.; Gaidukovs, S. Three Dimensionally Printed Biobased Electrodes: Ionic Liquid and Single-Walled Carbon Nanotube Hybrids in a Vegetable Oil Matrix for Soft Robotics. *ACS Appl. Polym. Mater.* **2023**, *5* (9), 7120–7131.

[18] Zhang, J.; Chen, Z.; Zhang, Y.; Dong, S.; Chen, Y.; Zhang, S. Poly(Ionic Liquid)s Containing Alkoxy Chains and Bis(Trifluoromethanesulfonyl)Imide Anions as Highly Adhesive Materials. *Adv. Mater.* **2021**, *33* (30), 1–10.

[19] Fan, X.; Liu, S.; Jia, Z.; Koh, J. J.; Yeo, J. C. C.; Wang, C. G.; Surat'man, N. E.; Loh, X. J.; Le Bideau, J.; He, C.; et al. Ionogels: Recent Advances in Design, Material Properties and Emerging Biomedical Applications. *Chem. Soc. Rev.* **2023**, *52* (7), 2497–2527.

[20] Shen, Q.; Jiang, M.; Wang, R.; Song, K.; Hou Vong, M.; Jung, W.; Krisnadi, F.; Kan, R.; Zheng, F.; Fu, B.; et al. Liquid Metal-Based Soft, Hermetic, and Wireless-Communicable Seals for Stretchable Systems. *Science* **2023**, *379* (6631), 488–493.

[21] Xu, J.; Wang, Z.; Wang, X.; Wu, Y.; Xing, R.; Yu, T.; Li, Y.; Ao, J.; Tao, Y.; Bai, B.; et al. Breathable Encapsulated Liquid Metal Foam-Based Soft Stress Sensor. *Adv. Mater. Technol.* **2023**, *8* (6), 2201193.

[22] Mannsfeld, S. C. B.; Tee, B. C. K.; Stoltenberg, R. M.; Chen, C. V. H. H.; Barman, S.; Muir, B. V. O.; Sokolov, A. N.; Reese, C.; Bao, Z. Highly Sensitive Flexible Pressure Sensors with Microstructured Rubber Dielectric Layers. *Nat. Mater.* **2010**, *9* (10), 859–864.

[23] Yeol Lee, M.; Rang Lee, H.; Hee Park, C.; Gi Han, S.; Hak Oh, J. Organic Transistor-Based Chemical Sensors for Wearable Bioelectronics. *Acc. Chem. Res.* **2018**, *51* (11), 2829–2838.

[24] Shen, Z.; Huang, W.; Li, L.; Li, H.; Huang, J.; Cheng, J.; Fu, Y. Research Progress of Organic Field-Effect Transistor Based Chemical Sensors. *Small* **2023**, 2302406.

[25] Liu, K.; Ouyang, B.; Guo, X.; Guo, Y.; Liu, Y. Advances in Flexible Organic Field-Effect Transistors and Their Applications for Flexible Electronics. *npj Flex. Electron.* **2022**, *6* (1).

[26] Chossat, J. B.; Shin, H. S.; Park, Y. L.; Duchaine, V. Soft Tactile Skin Using an Embedded Ionic Liquid and Tomographic Imaging. *J. Mech. Robot.* **2015**, *7* (2), 021008.

[27] Wong, J.; Basu, A.; Wende, M.; Boechler, N.; Nelson, A. Mechano-Activated Objects with Multidirectional Shape Morphing Programmed via 3D Printing. *ACS Appl. Polym. Mater.* **2020**, *2* (7), 2504–2508.

[28] Kunz, W.; Häckl, K. The Hype with Ionic Liquids as Solvents. *Chem. Phys. Lett.* **2016**, *661*, 6–12.

[29] Kim, Y. M.; Kwon, J. H.; Kim, S.; Choi, U. H.; Moon, H. C. Ion-Cluster-Mediated Ultrafast Self-Healable Ionoconductors for Reconfigurable Electronics. *Nat. Commun.* **2022**, *13* (1), 3769.

[30] Rebei, M.; Mahun, A.; Walterova, Z.; Trhlikova, O.; Donato, R. K.; Beneš, H. VOC-Free Tricomponent Reaction Platform for Epoxy Network Formation Mediated by a Recyclable Ionic Liquid. *Polym. Chem.* **2022**, *13*, 5380-5388.

[31] Livi, S.; Baudoux, J.; Gérard, J. F.; Duchet-Rumeau, J. Ionic Liquids: A Versatile Platform for the Design of a Multifunctional Epoxy Networks 2.0 Generation. *Prog. Polym. Sci.* **2022**, *132*, 101581.

[32] Cassity, C. G.; Mirjafari, A.; Mobarrez, N.; Strickland, K. J.; O'brien, R. A.; Davis, J. H. Ionic Liquids of Superior Thermal Stability. *Chem. Commun.* **2013**, *49* (69), 7590–7592.

[33] Wang, M.; Zhang, P.; Shamsi, M.; Thelen, J. L.; Qian, W.; Truong, V. K.; Ma, J.; Hu, J.; Dickey, M. D. Tough and Stretchable Ionogels by in Situ Phase Separation. *Nat. Mater.* **2022**, *21* (3), 359–365.

[34] Zhao, X.; Xu, J.; Zhang, J.; Guo, M.; Wu, Z.; Li, Y.; Xu, C.; Yin, H.; Wang, X. Fluorescent Double Network Ionogels with Fast Self-Healability and High Resilience for Reliable Human Motion Detection. *Mater. Horizons* **2022**, *10*, 646–656.

[35] Chen, Z. J.; Sun, Y. Q.; Xiao, X.; Wang, H. Q.; Zhang, M. H.; Wang, F. Z.; Lai, J. C.; Zhang, D. S.; Pan, L. J.; Li, C. H. An Ultra-Tough and Ultra-Sensitive Ionogel Pressure/Temperature Sensor Enabled by Hierarchical Design of Both Materials and Devices. *J. Mater. Chem. A* **2023**, *11* (15), 8359–8367.

[36] Narupai, B.; Wong, J.; Sanchez-Rexach, E.; Smith-Jones, J.; Le, V. C. T.; Sadaba, N.; Sardon, H.; Nelson, A. 3D Printing of Ionic Liquid Polymer Networks for Stretchable Conductive Sensors. *Adv. Mater. Technol.* **2023**, *2300226*, 1–9.

[37] Amziane, S.; Pierre, A.; Rangeard, D.; Sonebi, M.; Perrot, A. *3D Printing of Concrete: State of the Art and Challenges of the Digital Construction Revolution*; 2019.

[38] Truby, R. L.; Lewis, J. A. Printing Soft Matter in Three Dimensions. *Nature* **2016**, *540* (7633), 371–378.

[39] Hartings, M. R.; Ahmed, Z. Chemistry from 3D Printed Objects. *Nat. Rev. Chem.* **2019**, *3*, 305–314.

[40] Wallin, T. J.; Pikul, J.; Shepherd, R. F. 3D Printing of Soft Robotic Systems. *Nat. Rev. Mater.* **2018**, *3* (6), 84–100.

[41] Capel, A. J.; Rimington, R. P.; Lewis, M. P.; Christie, S. D. R. 3D Printing for Chemical, Pharmaceutical and Biological Applications. *Nat. Rev. Chem.* **2018**, *2* (12), 422–436.

[42] Wang, Z.; Zhang, J.; Liu, J.; Hao, S.; Song, H.; Zhang, J. 3D Printable, Highly Stretchable, Superior Stable Ionogels Based on Poly(Ionic Liquid) with Hyperbranched Polymers as Macro-Cross-Linkers for High-Performance Strain Sensors. *ACS Appl. Mater. Interfaces* **2021**, *13* (4), 5614–5624.

[43] Onal, C. D.; Rus, D. A Modular Approach to Soft Robots. In *Proceedings of the IEEE RAS and EMBS International Conference on Biomedical Robotics and Biomechatronics*; **2012**, 1038–1045.

[44] Zhang, C.; Zhu, P.; Lin, Y.; Jiao, Z.; Zou, J. Modular Soft Robotics: Modular Units, Connection Mechanisms, and Applications. *Adv. Intell. Syst.* **2020**, *2* (6), 1900166.

[45] Morin, S. A.; Shevchenko, Y.; Lessing, J.; Kwok, S. W.; Shepherd, R. F.; Stokes, A. A.; Whitesides, G. M. Using "Click-e-Bricks" to Make 3D Elastomeric Structures. *Adv. Mater.* **2014**, *26* (34), 5991–5999.

[46] Gomez, E. F.; Wanasinghe, S. V; Flynn, A. E.; Dodo, O. J.; Sparks, J. L.; Baldwin, L. A.; Tabor, C. E.; Durstock, M. F.; Konkolewicz, D.; Thrasher, C. J. 3D-Printed Self-Healing Elastomers for Modular Soft Robotics. *ACS Appl. Mater. Interfaces* **2021**, *13*, 28870–28877.

[47] Bowman, C.; Du Prez, F.; Kalow, J. Introduction to Chemistry for Covalent Adaptable Networks. *Polym. Chem.* **2020**, *11* (33), 5295–5296.

[48] Kloxin, C. J.; Scott, T. F.; Adzima, B. J.; Bowman, C. N. Covalent Adaptable Networks (CANs): A Unique Paradigm in Cross-Linked Polymers. *Macromolecules* **2010**, *43*, 2643.

[49] Accardo, J. V; Kalow, J. A. Reversibly Tuning Hydrogel Stiffness through Photocontrolled Dynamic Covalent Crosslinks. *Chem. Sci.* **2018**, *9* (27), 5987–5993.

[50] Gulyuz, S.; Yagci, Y.; Kiskan, B. Exploiting the Reversible Covalent Bonding of Boronic Acids for Self-Healing/Recycling of Main-Chain Polybenzoxazines. *Polym. Chem.* **2022**, *13* (24), 3631–3638.

[51] Thongsomboon, W.; Sherwood, M.; Arellano, N.; Nelson, A. Thermally Induced Nanoimprinting of Biodegradable Polycarbonates Using Dynamic Covalent Cross-Links. *ACS Macro Lett.* **2013**, *2* (1), 19–22.

[52] Jung, S.; Kim, S. Y.; Kim, J. C.; Noh, S. M.; Oh, J. K. Ambient Temperature Induced Diels-Alder Crosslinked Networks Based on Controlled Methacrylate Copolymers for Enhanced Thermoreversibility and Self-Healability. *RSC Adv.* **2017**, *7* (42), 26496–26506.

[53] Millik, S. C.; Dostie, A. M.; Karis, D. G.; Smith, P. T.; McKenna, M.; Chan, N.; Curtis, C. D.; Nance, E.; Theberge, A. B.; Nelson, A. 3D Printed Coaxial Nozzles for the Extrusion of Hydrogel Tubes toward Modeling Vascular Endothelium. *Biofabrication* **2019**, *11* (4).

[54] Kokubo, H.; Sano, R.; Murai, K.; Ishii, S.; Watanabe, M. Ionic Polymer Actuators Using Poly(Ionic Liquid) Electrolytes. *Eur. Polym. J.* **2018**, *106*, 266–272.

[55] Zhao, R.; Yang, J.; Wang, B.; Ma, Z.; Pan, L.; Li, Y. Block Copolymer Solid Electrolytes Based on Comb-Like Poly(Ethylene Glycol) Plasticized Poly(Ionic Liquid)s for Lithium-Ion Batteries. *Chin. J. Chem.* **2023**, *41* (19), 2493–2501.

[56] Koehler, K. C.; Durackova, A.; Kloxin, C. J.; Bowman, C. N. Kinetic and Thermodynamic Measurements for the Facile Property Prediction of Diels-Alder-Conjugated Material Behavior. *AIChE J* **2012**, *58* (11), 3545–3552.

[57] Xia, Q.; Li, W.; Zou, X.; Zheng, S.; Liu, Z.; Li, L.; Yan, F. Metal-Organic Frameworks (MOFs) Facilitated Highly Stretchable, and Fatigue-Resistant Ionogels for Recyclable Sensors. *Mater. Horizons* **2022**, 9, 2881-2892.

[58] Zhu, J.; Lu, X.; Zhang, W.; Liu, X. Substrate-Independent, Reversible, and Easy-Release Ionogel Adhesives with High Bonding Strength. *Macromol. Rapid Commun.* **2020**, *41* (24), 2000098.

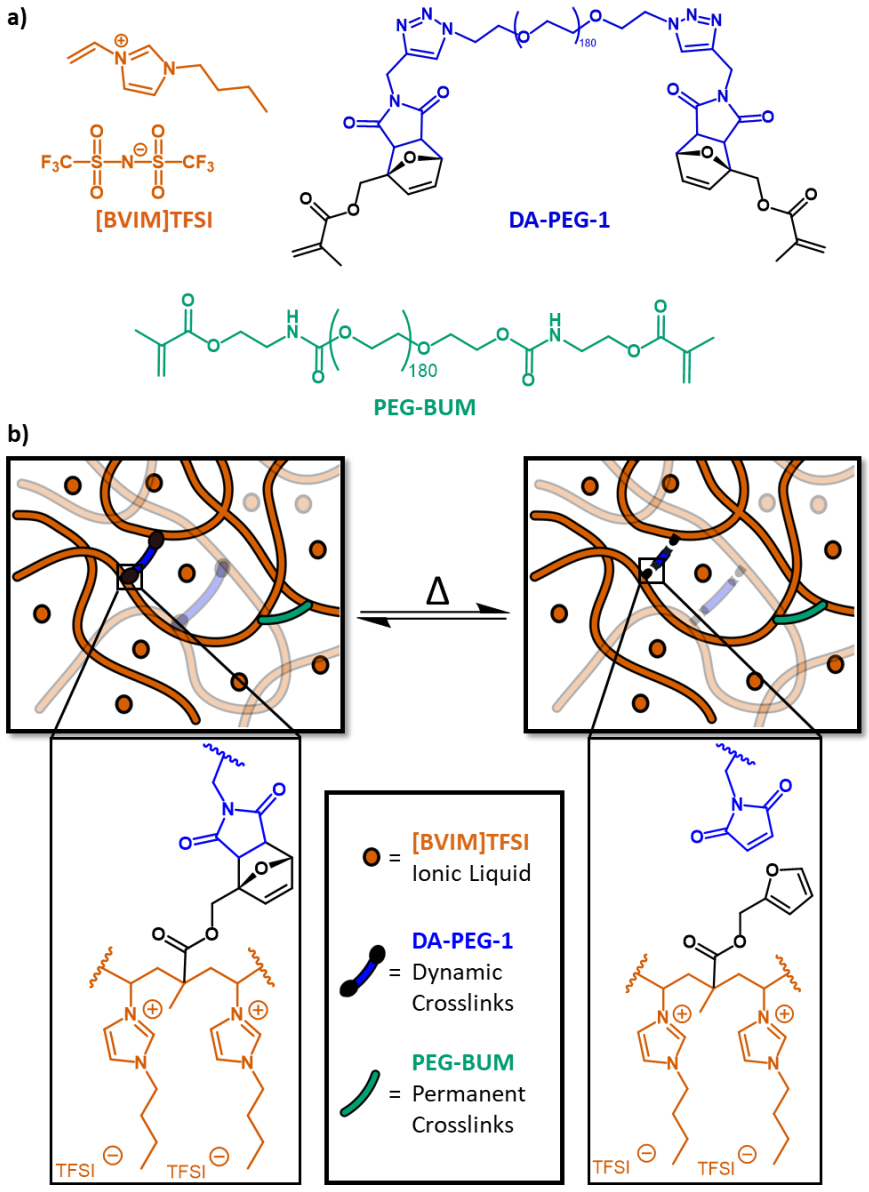

Figure 4.1 Overview of resin components and representation of dynamic polymer network. A) Components of ionic liquid gel resin. Not shown: BAPO (photoinitiator) and Sudan 1 (photoabsorber). The photoinitiator initiates radical polymerization during SLA printing and the photoabsorber improves the resolution of printed objects by limiting light penetration. B) Representation of dynamic bonds within polymerized polymer network. Reversable Diels-Alder substituents in the crosslinks of the material allow for modification of the network post polymerization. Permanent crosslinks provide improved shape retention under heating.

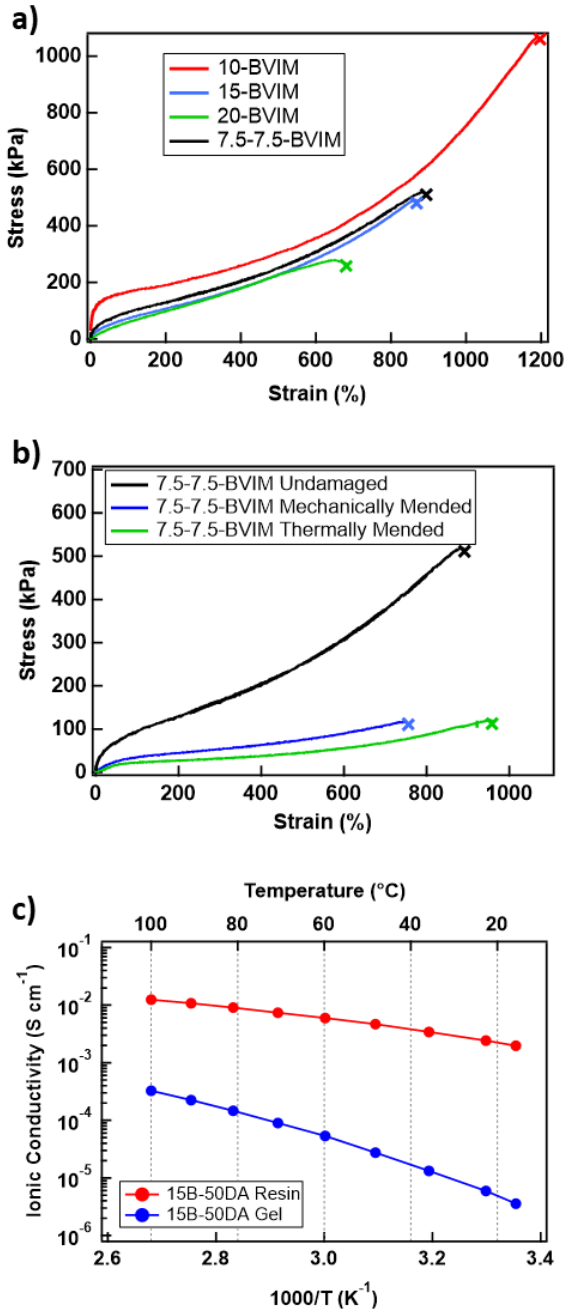

Figure 4.2 Characterization of ionic liquid gels. A) Tensile strength of gels with varying amounts of copolymer. B) Tensile experiments of formulation 7.5-7.5-BVIM after printing, after being cut and mechanically mended, and after being fused using heat. C) Electrical Impedance Spectroscopy (EIS) data of formulation 7.5-7.5-BVIM as a resin (red) and after printing (blue) over a range of temperatures (20-100 °C).

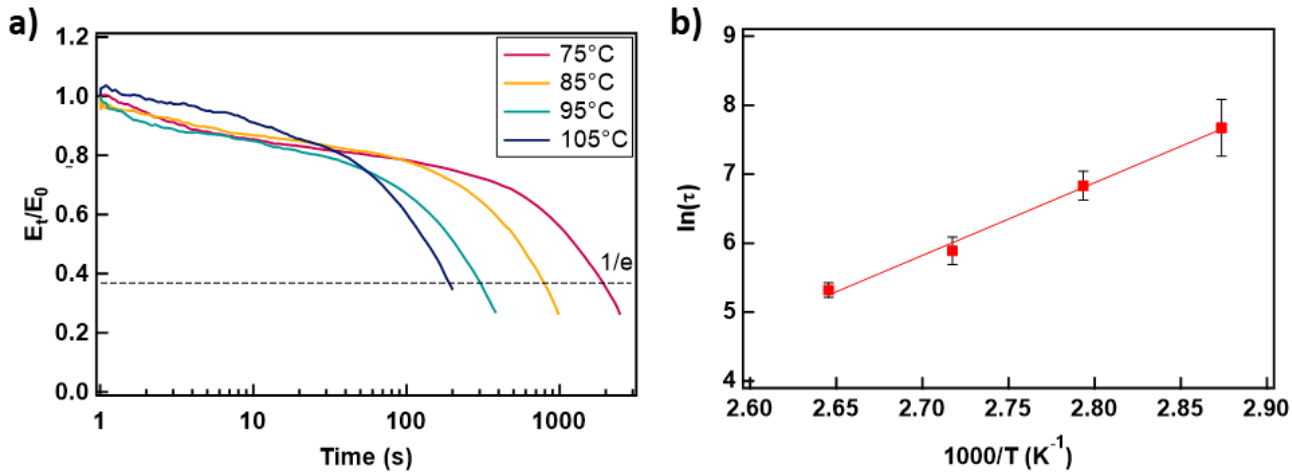

Figure 4.3 a) Stress relaxation of 7.5-7.5-BVIM gels at varying temperatures. Relaxation times (τ) are determined when the normalized modulus reaches 1/e of the initial value. b) Activation energy (E_a) of Diels-Alder bonds in the network was determined from the slope of the natural logarithm of τ plotted against 1000/T (E_a = 84 ± 5 kJ/mol).

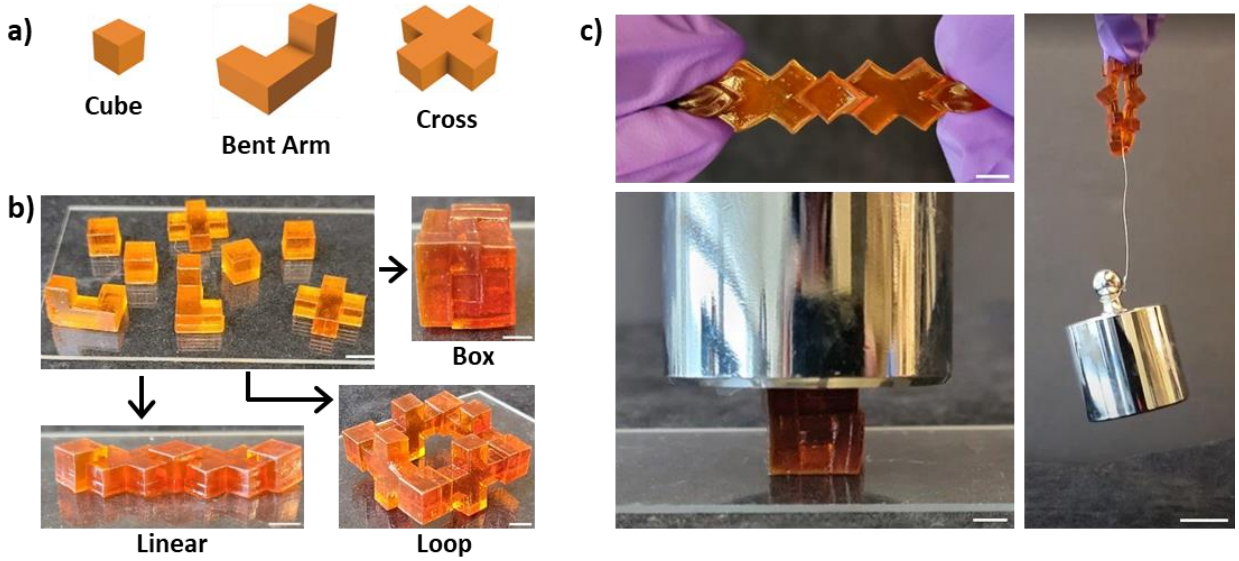

Figure 4.4 Demonstration of the modularity of dynamic ionic liquid gels. a) CAD file of building blocks used to create modular sensors. b) Individually printed blocks of 7.5-7.5-BVIM can be combined into modular strain sensors of different shapes without any loss of resolution. Scale bars represent 5 mm. c) Fused structures can support a 500 g weight without sustaining damage. Scale

bar for linear and box structures represents 5 mm. Scale bar for loop represents 20 mm.

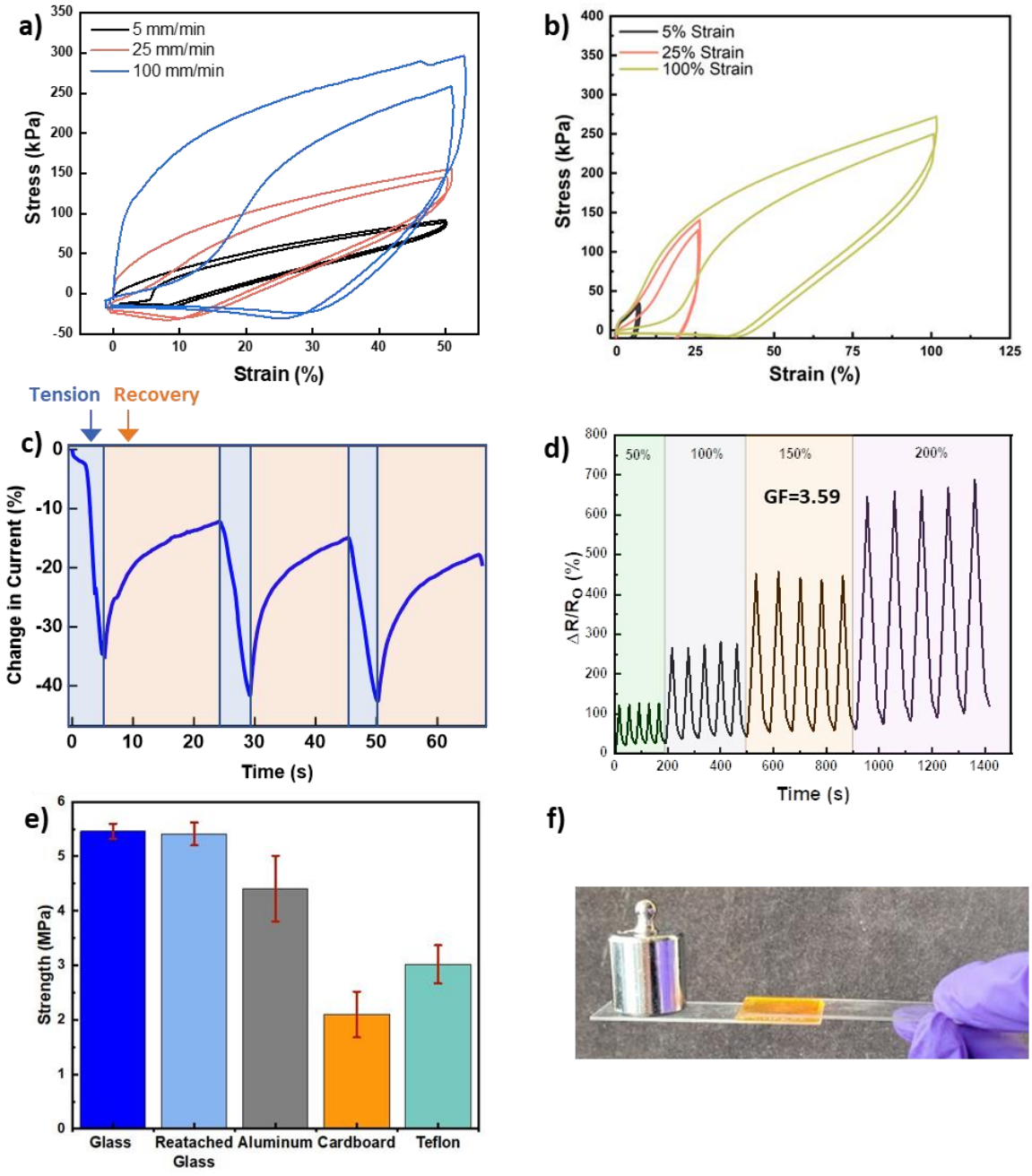

Figure 4.5 Dynamic properties of modular sensors. a) Cyclic uniaxial tensile experiments performed at strain rates of 5, 25, and 100 mm/ min at 50% strain; two cycles for each strain rate are shown and additional cycles are included in the supporting information. b) Cyclic uniaxial

tensile experiments performed at 5%, 25%, and 100% strain at a strain rate of 50 mm/ min; two cycles for each % strain are shown and additional cycles are included in the supporting information. c) Electrical response of sensors attached to a source measuring unit. Current passing through the device decreases as the device is placed under tension, as predicted by modified Ohm's Law. d) A plot showing the cyclic loading and unloading to different strains to determine the gauge factor for strains ranging from 50-200%. e) Adhesive strength of 7.5-7.5-BVIM gels in contact with a variety of substrates. f) Square adhesive ion gel patch supporting a 100 g weight on glass slides.

BIBLIOGRAPHY

[1] Swainson, W.K. Method, Medium and Apparatus for Producing Three-Dimensional Figure Product. U.S. Patent 4,041,476, 9 August **1977**.

[2] Herbert, A.J. Solid object generation. J. Appl. Photogr. Eng. **1982**

[3] Hull, C.W. Apparatus for Production of Three-Dimensional Objects by Stereolithography. U.S. Patent Appl. 638,905, **1984**

[4] Capel, A. J.; Rimington, R. P.; Lewis, M. P.; Christie, S. D. R. 3D Printing for Chemical, Pharmaceutical and Biological Applications. *Nat. Rev. Chem.* **2018**, *2* (12), 422–436.

[5] Ryan, K. R.; Down, M. P.; Banks, C. E. Future of Additive Manufacturing: Overview of 4D and 3D Printed Smart and Advanced Materials and Their Applications. *Chem. Eng. J.* **2021**, *403*, 126162.

[6] Truby, R. L.; Lewis, J. A. Printing Soft Matter in Three Dimensions. *Nature* **2016**, *540* (7633), 371–378.

[7] Sampson, K. L.; Deore, B.; Go, A.; Nayak, A.; Orth, A.; Gallerneault, M.; Malenfant, P. R. L.; Paquet, C. Multimaterial Vat Polymerization Additive Manufacturing. *ACS Appl. Polym. Mater.* **2021**, *3* (9), 4304–4324.

[8] Amziane, S.; Pierre, A.; Rangeard, D.; Sonebi, M.; Perrot, A. *3D Printing of Concrete: State of the Art and Challenges of the Digital Construction Revolution*; **2019**.

[9] Gibson, I.; Rosen, D.; Stucker, B. *Additive Manufacturing Technologies: 3D Printing, Rapid Prototyping, and Direct Digital Manufacturing, Second Edition*; **2015**.

[10] Fu, P.; Li, H.; Gong, J.; Fan, Z.; Smith, A. T.; Shen, K.; Khalfalla, T. O.; Huang, H.; Qian, X.; McCutcheon, J. R.; et al. 4D Printing of Polymers: Techniques, Materials, and Prospects. *Prog. Polym. Sci.* **2022**, *126*, 101506.

[11] Ahmed, A.; Arya, S.; Gupta, V.; Furukawa, H.; Khosla, A. 4D Printing: Fundamentals, Materials, Applications and Challenges. *Polymer* **2021**, *228*, 123926.

[12] Pacillo, G. A.; Ranocchiai, G.; Loccarini, F.; Fagone, M. Additive Manufacturing in Construction: A Review on Technologies, Processes, Materials, and Their Applications of 3D and 4D Printing. *Mater. Des. Process. Commun.* **2021**, *3* (5).

[13] Hartings, M. R.; Ahmed, Z. Chemistry from 3D Printed Objects. *Nat. Rev. Chem.* **2019**, *3*, 305–314.

[14] Wallin, T. J.; Pikul, J.; Shepherd, R. F. 3D Printing of Soft Robotic Systems. *Nat. Rev. Mater.* **2018**, *3* (6), 84–100.

[15] Liu, G.; Zhao, Y.; Wu, G.; Lu, J. Origami and 4D Printing of Elastomer-Derived Ceramic Structures. *Sci. Adv.* **2018**, *4* (8), 641–658.

[16] Wong, J.; Gong, A. T.; Defnet, P. A.; Meabe, L.; Beauchamp, B.; Sweet, R. M.; Sardon, H.; Cobb, C. L.; Nelson, A. 3D Printing Ionogel Auxetic Frameworks for Stretchable Sensors. *Adv. Mater. Technol.* **2019**, *4* (9), 1–6.

[17] Wong, J.; Basu, A.; Wende, M.; Boechler, N.; Nelson, A. Mechano-Activated Objects with Multidirectional Shape Morphing Programmed via 3D Printing. *ACS Appl. Polym. Mater.* **2020**, *2* (7), 2504–2508.

[18] Basu, A.; Wong, J.; Cao, B.; Boechler, N.; Boydston, A. J.; Nelson, A. Mechanoactivation of Color and Autonomous Shape Change in 3D-Printed Ionic Polymer Networks. *ACS Appl. Mater. Interfaces* **2021**, *13*, 19263–19270.

[19] Millik, S. C.; Dostie, A. M.; Karis, D. G.; Smith, P. T.; McKenna, M.; Chan, N.; Curtis, C. D.; Nance, E.; Theberge, A. B.; Nelson, A. 3D Printed Coaxial Nozzles for the Extrusion of Hydrogel Tubes toward Modeling Vascular Endothelium. *Biofabrication* **2019**, *11* (4).

[20] Chen, Z. J.; Sun, Y. Q.; Xiao, X.; Wang, H. Q.; Zhang, M. H.; Wang, F. Z.; Lai, J. C.; Zhang, D. S.; Pan, L. J.; Li, C. H. An Ultra-Tough and Ultra-Sensitive Ionogel Pressure/Temperature Sensor Enabled by Hierarchical Design of Both Materials and Devices. *J. Mater. Chem. A* **2023**, *11* (15), 8359–8367.

[21] Zanon, M.; Montalvillo-Jiménez, L.; Cue-López, R.; Martínez-Campos, E.; Sangermano, M.; Chiappone, A.; Bosch, P. Vat 3D Printing of Full-Alginate Hydrogels via Thiol-Ene Reactions towards Tissue Engineering Applications. *Polym. Chem.* **2023**.

[22] Narupai, B.; Wong, J.; Sanchez-Rexach, E.; Smith-Jones, J.; Le, V. C. T.; Sadaba, N.; Sardon, H.; Nelson, A. 3D Printing of Ionic Liquid Polymer Networks for Stretchable Conductive Sensors. *Adv. Mater. Technol.* **2023**, *2300226*, 1–9.

[23] Yang, W.; Cai, S.; Chen, Y.; Liang, W.; Lai, Y.; Yu, H.; Wang, Y.; Liu, L. Modular and Customized Fabrication of 3D Functional Microgels for Bottom-Up Tissue Engineering and Drug Screening. *Adv. Mater. Technol.* **2020**, *5* (5).

[24] Yang, L.; Sun, L.; Huang, H.; Zhu, W.; Wang, Y.; Wu, Z.; Neisiany, R. E.; Gu, S.; You, Z. Mechanically Robust and Room Temperature Self-Healing Ionogel Based on Ionic Liquid Inhibited Reversible Reaction of Disulfide Bonds. *Adv. Sci.* **2023**, *10* (20).

[25] Lantean, S.; Barrera, G.; Fabrizio Pirri, C.; Tiberto, P.; Sangermano, M.; Roppolo, I.; Rizza, G. 3D Printing of Magnetoresponsive Polymeric Materials with Tunable

Mechanical and Magnetic Properties by Digital Light Processing. *Adv. Mater. Technol.* **2019**, *4*, 1900505.

[26] Subbiah, R.; Hipfinger, C.; Tahayeri, A.; Athirasala, A.; Horsophonphong, S.; Thrivikraman, G.; Miranda França, C.; Araujo Cunha, D.; Mansoorifar, A.; Zahariev, A.; et al. 3D Printing of Microgel-Loaded Modular Microcages as Instructive Scaffolds for Tissue Engineering. *Adv. Mater.* **2020**, *32*, 1–7.

[27] Tibbits, S. 4D Printing: Multi-Material Shape Change. *Archit. Des.* **2014**, *84* (1), 116–121.

[28] Zhang, C.; He, B.; Wang, Z.; Zhou, Y.; Ming, A.; Thanh Dinh, N. Application and Analysis of an Ionic Liquid Gel in a Soft Robot. *Adv. Mater. Sci. Eng.* **2019**,

[29] Zhang, C.; He, B.; Ding, A.; Xu, S.; Wang, Z.; Zhou, Y. Motion Simulation of Ionic Liquid Gel Soft Actuators Based on CPG Control. *Comput. Intell. Neurosci.* **2019**.

[30] Ankit; Tiwari, N.; Ho, F.; Krisnadi, F.; Kulkarni, M. R.; Nguyen, L. L.; Koh, S. J. A.; Mathews, N. High-k, Ultrastretchable Self-Enclosed Ionic Liquid-Elastomer Composites for Soft Robotics and Flexible Electronics. *ACS Appl. Mater. Interfaces* **2020**, *12* (33), 37561–37570.

[31] Truby, R. L.; Wehner, M.; Grosskopf, A. K.; Vogt, D. M.; Uzel, S. G. M.; Wood, R. J.; Lewis, J. A. Soft Somatosensitive Actuators via Embedded 3D Printing. *Adv. Mater.* **2018**, *30* (15).

[32] He, B.; Zhou, Y.; Wang, Z.; Wang, Q.; Shen, R.; Wu, S. A Multi-Layered Touch-Pressure Sensing Ionogel Material Suitable for Sensing Integrated Actuations of Soft Robots. *Sensors Actuators, A Phys.* **2018**, *272*, 341–348.

[33] Feng, C.; Hemantha Rajapaksha, C. P.; Jákli, A. Ionic Elastomers for Electric Actuators and Sensors. *Engineering* **2021**, *7* (5), 581–602. https://doi.org/10.1016/j.eng.2021.02.014.

[34] Liu, Z.; Wang, Y.; Ren, Y.; Jin, G.; Zhang, C.; Chen, W.; Yan, F. Poly(Ionic Liquid) Hydrogel-Based Anti-Freezing Ionic Skin for a Soft Robotic Gripper. *Mater. Horizons* **2020**, *7* (3), 919–927.

[35] Gao, W.; Ota, H.; Kiriya, D.; Takei, K.; Javey, A. Flexible Electronics toward Wearable Sensing. *Acc. Chem. Res.* **2019**, *52* (3),

[36] Hao, S.; Li, T.; Yang, X.; Song, H. Ultrastretchable, Adhesive, Fast Self-Healable, and Three-Dimensional Printable Photoluminescent Ionic Skin Based on Hybrid Network Ionogels. *ACS Appl. Mater. Interfaces* **2022**, *14* (1), 2029–2037.

[37] Gao, N.; He, Y.; Tao, X.; Xu, X. Q.; Wu, X.; Wang, Y. Crystal-Confined Freestanding Ionic Liquids for Reconfigurable and Repairable Electronics. *Nat. Commun.* **2019**, *10* (1).

[38] Tie, J.; Mao, Z.; Zhang, L.; Zhong, Y.; Sui, X.; Xu, H. Highly Transparent, Self-Healing and Adhesive Wearable Ionogel as Strain and Temperature Sensor. *Polym. Chem.* **2022**, *13*, 4064–4075.

[39] Borayek, R.; Foroughi, F.; Xin, X.; Mohamed, A. M.; Abdelrahman, M. M.; Zedan, M.; Zhang, D.; Ding, J. Near-Zero Hysteresis Ionic Conductive Elastomers with Long-Term Stability for Sensing Applications. *ACS Appl. Mater. Interfaces* **2022**, *14* (9), 11727–11738.

[40] Choi, D. Y.; Kim, M. H.; Oh, Y. S.; Jung, S. H.; Jung, J. H.; Sung, H. J.; Lee, H. W.; Lee, H. M. Highly Stretchable, Hysteresis-Free Ionic Liquid-Based Strain Sensor for

Precise Human Motion Monitoring. *ACS Appl. Mater. Interfaces* **2017**, *9* (2), 1770–1780.

[41] Tian, K.; Bae, J.; Bakarich, S. E.; Yang, C.; Gately, R. D.; Spinks, G. M.; in het Panhuis, M.; Suo, Z.; Vlassak, J. J. 3D Printing of Transparent and Conductive Heterogeneous Hydrogel–Elastomer Systems. *Adv. Mater.* **2017**, *29* (10).

[42] UpNano. https://www.upnano.at/the-castle-on-a-pencil-tip/

[43] Ge, Q.; Sakhaei, A. H.; Lee, H.; Dunn, C. K.; Fang, N. X.; Dunn, M. L. Multimaterial 4D Printing with Tailorable Shape Memory Polymers. *Sci. Rep.* **2016**, *6*, 31110.

[44] Peng, W.; Yin, J.; Zhang, X.; Shi, Y.; Che, G.; Zhao, Q.; Liu, J. 4D Printed Shape Memory Anastomosis Ring with Controllable Shape Transformation and Degradation. *Adv. Funct. Mater.* **2023**, *33* (20), 2214505.

[45] Mauriello, J.; Maury, R.; Guillaneuf, Y.; Gigmes, D. 3D/4D Printing of Polyurethanes by Vat Photopolymerization. *Adv. Mater. Technol.* **2023**.

[46] Wan, X.; Luo, L.; Liu, Y.; Leng, J. Direct Ink Writing Based 4D Printing of Materials and Their Applications. *Adv. Sci.* **2020**, *7* (16).

[47] Ding, Z.; Yuan, C.; Peng, X.; Wang, T.; Qi, H. J.; Dunn, M. L. Direct 4D Printing via Active Composite Materials. *Sci. Adv.* **2017**, *3* (4).

[48] De Marco, C.; Pané, S.; Nelson, B. J. 4D Printing and Robotics. *Sci. Robot.* **2018**, *3* (18), 449.

[49] Liu, K.; Zhang, Y.; Cao, H.; Liu, H.; Geng, Y.; Yuan, W.; Zhou, J.; Wu, Z. L.; Shan, G.; Bao, Y.; et al. Programmable Reversible Shape Transformation of Hydrogels Based on Transient Structural Anisotropy. *Adv. Mater.* **2020**, *32* (28).

[50] Peng, B.; Yang, Y.; Gu, K.; Amis, E. J.; Cavicchi, K. A. Digital Light Processing 3D Printing of Triple Shape Memory Polymer for Sequential Shape Shifting. *ACS Mater. Lett.* **2019**, *1* (4), 410–417.

[51] Yi, C.; Qu, S.; Wang, Y.; Qi, H.; Zhang, Y.; Cheng, G. J. Optical Force Brush Enabled Free-Space Painting of 4D Functional Structures. *Sci. Adv.* **2023**, *9* (38), 1–13.

[52] Accardo, J. V; Kalow, J. A. Reversibly Tuning Hydrogel Stiffness through Photocontrolled Dynamic Covalent Crosslinks. Chem. Sci. **2018**, 9 (27), 5987–5993.

[53] Tang, Y.; Zhang, Y.; Chen, X.; Xie, X.; Zhou, N.; Dai, Z.; Xiong, Y. Up/Down Tuning of Poly(Ionic Liquid)s in Aqueous Two-Phase Systems. *Angew. Chemie - Int. Ed.* **2023**, *62* (4).

[54] Huang, J.; Yu, Z.; Wu, P. 3D Printing of Ionogels with Complementary Functionalities Enabled by Self-Regulating Ink. *Adv. Sci.* **2023**.

[55] Zhou, S.-W.; Yu, C.; Chen, M.; Shi, C.-Y.; Gu, R.; Qu, D.-H. Self-Healing and Shape-Shifting Polymers Controlled by Dynamic Bonds. *Smart Mol.* **2023**.

[56] Shmool, T. A.; Martin, L. K.; Jirkas, A.; Matthews, R. P.; Constantinou, A. P.; Vadukul, D. M.; Georgiou, T. K.; Aprile, F. A.; Hallett, J. P. Unveiling the Rational Development of Stimuli-Responsive Silk Fibroin-Based Ionogel Formulations. *Chem. Mater.* **2023**.

[57] Qin, J.; Sun, M.; Hu, W.; Cheng, J.; Fan, Z.; Du, J. Stimuli-Responsive Hydrogels for Cancer Immunotherapy. *Polym. Chem.* **2023**, *14* (7), 793–802.

[58] Lendlein, A.; Gould, O. E. C. Reprogrammable Recovery and Actuation Behaviour of Shape-Memory Polymers. *Nat. Rev. Mater.* **2019**, *4* (2), 116–133.

[59] Wu, H.; Wang, O.; Tian, Y.; Wang, M.; Su, B.; Yan, C.; Zhou, K.; Shi, Y. Selective Laser Sintering-Based 4D Printing of Magnetism-Responsive Grippers. *ACS Appl. Mater. Interfaces* **2021**, *13* (11), 12679–12688.

[60] Ouyang, H.; Li, X.; Lu, X.; Xia, H. Selective Laser Sintering 4D Printing of Dynamic Cross-Linked Polyurethane Containing Diels-Alder Bonds. *ACS Appl. Polym. Mater.* **2022**, *4* (5), 4035–4046.

[61] Gomez, E. F.; Wanasinghe, S. V; Flynn, A. E.; Dodo, O. J.; Sparks, J. L.; Baldwin, L. A.; Tabor, C. E.; Durstock, M. F.; Konkolewicz, D.; Thrasher, C. J. 3D-Printed Self-Healing Elastomers for Modular Soft Robotics. *ACS Appl. Mater. Interfaces* **2021**, *13*, 28870–28877.

[62] Shintake, J.; Cacucciolo, V.; Floreano, D.; Shea, H. Soft Robotic Grippers. *Adv. Mater.* **2018**, *30* (29), 1707035.

[63] Zhang, Z.; Heron, J. T.; Pena-Francesch, A. Adaptive Magnetoactive Soft Composites for Modular and Reconfigurable Actuators. *Adv. Funct. Mater.* **2023**.

[64] Migliorati, V.; Del Giudice, A.; Casu, A.; Falqui, A.; Podestà, A.; Milani, P.; Borghi, F. Crystalline Structuring of Confined Ionic Liquids at Room Temperature. *J. Phys. Chem. C* **2022**, *126* (31), 13477–13484.

[65] Fan, X.; Liu, S.; Jia, Z.; Koh, J. J.; Yeo, J. C. C.; Wang, C. G.; Surat'man, N. E.; Loh, X. J.; Le Bideau, J.; He, C.; et al. Ionogels: Recent Advances in Design, Material Properties and Emerging Biomedical Applications. *Chem. Soc. Rev.* **2023**, *52* (7), 2497–2527.

[66] Néouze, M. A.; Le Bideau, J.; Gaveau, P.; Bellayer, S.; Vioux, A. Ionogels, New Materials Arising from the Confinement of Ionic Liquids within Silica-Derived Networks. *Chem. Mater.* **2006**, *18* (17), 3931–3936.

[67] Bansal, A. K.; Hou, S.; Kulyk, O.; Bowman, E. M.; Samuel, I. D. W. Wearable Organic Optoelectronic Sensors for Medicine. *Adv. Mater.* **2015**, *27* (46), 7638–7644.

[68] Jurinovs, M.; Barkane, A.; Platnieks, O.; Grase, L.; Gaidukovs, S. Three Dimensionally Printed Biobased Electrodes: Ionic Liquid and Single-Walled Carbon Nanotube Hybrids in a Vegetable Oil Matrix for Soft Robotics. *ACS Appl. Polym. Mater.* **2023**, *5* (9), 7120–7131.

[69] Chossat, J. B.; Shin, H. S.; Park, Y. L.; Duchaine, V. Soft Tactile Skin Using an Embedded Ionic Liquid and Tomographic Imaging. *J. Mech. Robot.* **2015**, *7* (2).

[70] Zhang, J.; Chen, Z.; Zhang, Y.; Dong, S.; Chen, Y.; Zhang, S. Poly(Ionic Liquid)s Containing Alkoxy Chains and Bis(Trifluoromethanesulfonyl)Imide Anions as Highly Adhesive Materials. *Adv. Mater.* **2021**, *33* (30), 1–10.

[71] Z. Huang, Y. Hao, Y. Li, H. Hu, C. Wang, A. Nomoto, T. Pan, Y. Gu, Y. Chen, T. Zhang, W. Li, Y, Lei, N. Kim, C. Wang, L. Zhang, J. W. Ward, A. Maralani, X. Li, M. F. Durstock, A. Pisano, Y. Lin, S. Xu, *Nat. Electron.* **2018**, *1*, 473.

[72] H. Wu, Y. Huang, F. Xu, Y. Duan, Z. Yin, *Adv. Mater.* **2016**, *28*, 9881.

[73] T. Q. Trung, N. Lee, *Adv. Mater.* **2016**, *28*, 4338.

[74] Y. Ye, Y. Zhang, Y. Chen, X. Han, F. Jiang, *Adv. Funct. Mater.* **2020**, *30*, 2003430.

[75] J. Wen, J. Tang, H. Ning, N. Hu, Y. Zhu, Y. Gong, C. Xu, Q. Zhao, X. Jiang, X. Hu, L. Lei, D. Wu, T. Huang, *Adv. Funct. Mater.* **2021**, *31*, 2011176.

[76] G. Gu, H. Xu, S. Peng, L. Li, S. Chen, T. Lu, X. Guo, *Soft. Robot.* **2019**, *6*, 387.

[77] S. Li, H. Pan, Y. Wang, J. Sun, *J. Mater. Chem. A* **2020**, *7*, 3667.

[78] S. Guo, K. Qiu, F. Meng, S. H. Park, M. C. McAlpine, *Adv. Mater.* **2017**, *29*, 1701218.

[79] T. Someya, M. Amagai, *Nat. Biotechnol.* **2019**, *37*, 382–388.

[80] F. Hartmann, M. Drack, M. Kaltenbrunner, *Sci. Rob.* **2018**, *3*, aat19091.

[81] H. Kim, K. Sim, A. Thukral, C. Yu. *Sci. Adv.* **2017**, *3*, 1701114.

[82] S. R. Shin, R. Farzad, A. Tamayol, V. Manoharan, P. Mostafalu, Y. S. Zhang, M. Akbari, S. M. Jung, D. Kim, M. Comotto, N. Annabi, F. E. Al-Hazmi, M. R. Dokmeci, A. Khademhosseini, *Adv. Mater.* **2016**, *28*, 3280.

[83] D. K. Patel, A. H. Sakhaei, M. Layani, B. Zhang, Q. Ge, S. Magdassi, *Adv. Mater.* **2017**, 1606000.

[84] C. Keplinger, J. Sun, C. C. Foo, P. Rothemund, G. M. Whitesides, Z. Suo, *Science* **2013**, *341*, 984.

[85] T. J. Jinton, A. Hudson, K. Pusch, A. Lee, A. W. Feinberg, *ACS Biomater. Sci. Eng.* **2016**, *2*, 1781.

[86] J. A. Fan, W. H. Yeo, Y. Su, Y. Hattori, W. Lee, S. Y. Jung, Y. Zhang, Z. Liu, H. Cheng, L. Falgout, M. Bajema, T. Coleman, D. Gregoire, R. J. Larsen, Y. Huang, J. A. Rogers, *Nat. Commun.* **2014**, *5*, 3266.

[87] D. Kim, J. A. Rogers, *Adv. Mater.* **2008**, *20*, 4887.

[88] T. P. Lodge, *Science* **2008**, *321*, 50.

[89] Md. A. B. H. Susan, T. Kaneko, A. Noda, M. Watanabe, *J. Am. Chem. Soc.* **2005**, *127*, 4976.

[90] J. L. Bideau, L. Viau, A. Vioux, *Chem. Soc. Rev.* **2011**, *40*, 907.

[91] E. Kamio, T. Yasui, Y. Iida, J. P. Gong, H. Matsuyama, *Adv. Mater.* **2017**, *29*, 1704118.

[92] M. Isik, T. Lonjaret, H. Sardon, R. Marcilla, T. Herve, G. G. Malliaras, E. Ismailova, D. Mecerreyes, *J. Mater. Chem. C* **2015**, *34*, 8942.

[93] W. J. Hyun, C. M. Thomas, M. C. Hersam, *Adv. Energy Mater.* **2020**, *10*, 2002135.

[94] M. Brachet. D. Gaboriau, P. Gentile, S. Fantini, G. Bidan, S. Sadki, T. Brousse, J. L. Bideau, *J. Mater. Chem. A* **2016**, *30*, 11835.

[95] H. H. Rana, J. H. Park, E. Ducrot, H. Park, M. Kota, T. H. Han, J. Y. Lee, J. Kim, J. Kim, P. Howlett, M. Forsyth, D. MacFarlane, H. S. Park, *Energy Storage Mater.* **2019**, *19*, 197.

[96] Y. Yuan, J. Zhou, G. Lu, J. Sun, L. Tang, *ACS Appl. Polym. Mater.* **2021**, *3*, 1610.

[97] X. Xu, H. S. Hui, K. N. Hui, H. Wang, J. Liu, *Mater. Horiz.* **2020**, *7*, 1246.

[98] L. Wang, X. Zhang, T. Wang, Y. Yin, J. Shi, C. Wang, Y. Guo, *Adv. Energy Mater.* **2018**, *8*, 1801528.

[99] Z. Li, H. Xie, X. Zhang, X. Guo, *J. Mater. Chem. A* **2020**, *8*, 3892.

[100] B. Narupai, A. Nelson, *ACS Macro Lett.* **2020**, *9*, 627.

[101] A. R. Studart, *Chem. Soc. Rev.* **2016**, *45*, 359.

[102] B. Narupai, P. T. Smith, A. Nelson, *Adv. Funct. Mater.* **2021**, *31*, 2011012.

[103] S. M. Ligon, R. Liska, J. Stampfl, M. Gurr, R. Mülhaupt, *Chem. Rev.* **2017**, *117*, 10212.

[104] L. Zhou, J. Fu, Y. He, *Adv. Funct. Mater.* **2020**, *30*, 200187.

[105] A. J. Boydston, B. Cao, A. Nelson, R. J. Ono, A. Saha, J. J. Schwartz, C. J. Thrasher, *J. Mater. Chem. A* **2018**, *6*, 20621.

[106] W. Gao, Y. Zhang, D. Ramanujan, K. Ramani, Y. Chen, C. B. Williams, C. C. L. Wang, Y. C. Shin, S. Zhang, P. D. Zavattieri, *Comput. Aided Des.* **2015**, *69*, 65.

[107] P. T. Smith, B. Narupai, J. H. Tsui, S. C. Millik, R. T. Shafranek, D. H. Kim, A. Nelson, *Biomacromolecules* **2020**, *21*, 484.

[108] E. M. Wilts, A. M. Pekkanen, B. T. White, V. Meenakshisundaram, D. C. Aduba, C. B. Williams, T. E. Long, *Polym. Chem.* **2019**, *10*, 1442.

[109] A. R. Schultz, P. M. Lambert, N. A. Chartrain, D. M. Ruohoniemi, Z. Zhang, C. Jangu, M. Zhang, C. B. Williams, T. E. Long, *ACS Macro Lett.* **2014**, *3*, 1205.

[110] B. Tang, D. K. Schneiderman, F. Z. Bidoky, C. D. Frisbie, T. P. Lodge, *ACS Macro Lett.* **2017**, *6*, 1083.

[111] T. Li, F. Liu, X. Yang, S. Hao, Y. Cheng, S. Li, H. Zhu, H. Song, *ACS Applied Materials & Interfaces* **2022**, *14*, 29261.

[112] H. Chen, P. Ge, Z. Yan, M. Chen, X. Dai, H. Zhuo, S Chen, L.-B. Huang, T. Zhang, *J. Chem. Eng.* **2022**, *430*, 133111.

[113] R. J. Mondschein, A. Kanitkar, C. B. Williams, S. S. Verbridge, T. E. Long, *Biomaterials* **2017**, *140*, 170.

[114] S. Schüller-Ravoo, S. M. Teixeira, J. Feijen, D. W. Grijpma, A. A. Poot, *Macromol. Biosci.* **2013**, *13*, 1711.

[115] C. Hinczewski, S. Corbel, T. Chartier, *J. Eur. Ceram. Soc.* **1998**, *18*, 583.

[116] J. T. Sutton, K. Rajan, D. P. Harper, S. C. Chmely, *ACS Appl. Mater. Interfaces* **2018**, *10*, 36456.

[117] Y. Luo, G. L. Fer, D. Dean, M. L. Becker, *Biomacromolecules* **2019**, *20*, 1699.

[118] R. Ni, B. Qian, C. Liu, X. Liu, J. Qiu, *RSC Adv.* **2018**, *8*, 29583.

[119] Y. Bao, N. Paunović, J. Leroux, *Adv. Funct. Mater.* **2022**, *32*, 2109864.

[120] V. Schimpf, A. Asmacher, A. Fuchs, K. Stoll, B. Bruchmann, R. Mülhaupt, *Macromol. Mater. Eng.* **2020**, *305*, 2000210.

[121] Z. D. Pritchard, M. P. de Beer, R. J. Whelan, T. F. Scott, M. A. Burns, *Adv. Mater. Technol.* **2019**, *4*, 1900700.

[122] D. Ahn, L. M. Stevens, K. Zhou, Z. A. Page, *ACS Cent. Sci.* **2020**, *6*, 1555.

[123] Q. Ge, A. H. Sahkaei, H. Lee. C. K. Dunn, N. X. Fang, M. L. Dunn, *Sci. Rep.* **2016**, *6*, 31110.

[124] D. Ye, C. Chang, L. Zhang, *Biomacromolecules* **2019**, *20*, 1989.

[125] B. Zhang, H. Li, J. Cheng, H. Ye, A. H. Sakhaei, C. Yuan, P. Rao, Y. Zhang, Z. Chen, R. Wang, X. He, J. Liu, R. Xiao, S. Qu, Q. Ge, *Adv. Mater.* **2021**, *33*, 2101298.

[126] M. A. Haq, Y. Su, D. Wang, *Mater. Sci. Eng. C* **2017**, *70*, 842.

[127] J. Xu, G. Gao, L. Duan, G. Sun, *Adv. Mater. Interfaces* **2020**, *7*, 1901541.

[128] Z. Sun, Z. Li, K. Qu, Z. Zhang, Y. Niu, W. Xu, C. Ren, *J. Mol. Liq.* **2021**, *325*, 115254.

[129] C. Shi, Q. Zhang, H. Tian, D. Qu, *SmartMat.* **2020**, *1*, e1012.

[130] Z. Xu, L. Chen, L. Lu, R. Du, W. Ma, Y. Cai, X. An, H. Wu, Q. Luo, Q. Xu, Q. Zhang, X. Jia, *Adv. Funct. Mater.* **2021**, *31*, 2006432.

[131] J. Zhu, X. Lu, W. Zhang, X. Liu, *Macromol. Rapid Commun.* **2020**, *41*, 2000098.

[132] W. Peng, G. Zhang, Q. Zhao, T. Xie, *Adv. Mater.* **2021**, *33*, 2102473.

[133] Jia, Y.; Xie, H.; Qian, J.; Zhang, Y.; Zheng, H.; Wei, F.; Li, Y.; Zhao, Z. Recent Progress on the 3D Printing of Dynamically Cross-Linked Polymers. *Adv. Funct. Mater.* **2023**.

[134] Song, S. W.; Lee, S.; Choe, J. K.; Kim, N. H.; Kang, J.; Lee, A. C.; Choi, Y.; Choi, A.; Jeong, Y.; Lee, W.; et al. Direct 2D-to-3D Transformation of Pen Drawings. *Sci. Adv.* **2021**, *7* (13).

[135] Cafferty, B. J.; Campbell, V. E.; Rothemund, P.; Preston, D. J.; Ainla, A.; Fulleringer, N.; Diaz, A. C.; Fuentes, A. E.; Sameoto, D.; Lewis, J. A.; et al. Fabricating 3D Structures by Combining 2D Printing and Relaxation of Strain. *Adv. Mater. Technol.* **2019**, *4* (1), 1–9.

[136] Matsuhisa, N.; Niu, S.; K O, S. J.; Kang, J.; Ochiai, Y.; Katsumata, T.; Wu, H.-C.; Ashizawa, M.; Nathan Wang, G.-J.; Zhong, D.; et al. High-Frequency and Intrinsically Stretchable Polymer Diodes. *Nature* **2021**, *600*, 246–252.

[137] Liu, Y.; Boyles, J. K.; Genzer, J.; Dickey, M. D. Self-Folding of Polymer Sheets Using Local Light Absorption. *Soft Matter* **2012**, *8* (6), 1764–1769.

[138] Wang, M.; Hu, J.; Dickey, M. D. Tough Ionogels: Synthesis, Toughening Mechanisms, and Mechanical Properties-A Perspective. *JACS Au*. **2022**, *2* (12), 2645–2657

[139] Shen, Q.; Jiang, M.; Wang, R.; Song, K.; Hou Vong, M.; Jung, W.; Krisnadi, F.; Kan, R.; Zheng, F.; Fu, B.; et al. Liquid Metal-Based Soft, Hermetic, and Wireless-Communicable Seals for Stretchable Systems. *Science* **2023**, *379* (6631), 488–493.

[140] Xu, J.; Wang, Z.; Wang, X.; Wu, Y.; Xing, R.; Yu, T.; Li, Y.; Ao, J.; Tao, Y.; Bai, B.; et al. Breathable Encapsulated Liquid Metal Foam-Based Soft Stress Sensor. *Adv. Mater. Technol.* **2023**, *8* (6), 2201193.

[141] Mannsfeld, S. C. B.; Tee, B. C. K.; Stoltenberg, R. M.; Chen, C. V. H. H.; Barman, S.; Muir, B. V. O.; Sokolov, A. N.; Reese, C.; Bao, Z. Highly Sensitive Flexible Pressure

Sensors with Microstructured Rubber Dielectric Layers. *Nat. Mater.* **2010**, *9* (10), 859–864.

[142] Yeol Lee, M.; Rang Lee, H.; Hee Park, C.; Gi Han, S.; Hak Oh, J. Organic Transistor-Based Chemical Sensors for Wearable Bioelectronics. *Acc. Chem. Res.* **2018**, *51* (11), 2829–2838.

[143] Shen, Z.; Huang, W.; Li, L.; Li, H.; Huang, J.; Cheng, J.; Fu, Y. Research Progress of Organic Field-Effect Transistor Based Chemical Sensors. *Small* **2023**, 2302406.

[144] Liu, K.; Ouyang, B.; Guo, X.; Guo, Y.; Liu, Y. Advances in Flexible Organic Field-Effect Transistors and Their Applications for Flexible Electronics. *npj Flex. Electron.* **2022**, *6* (1).

[145] Kunz, W.; Häckl, K. The Hype with Ionic Liquids as Solvents. *Chem. Phys. Lett.* **2016**, *661*, 6–12.

[146] Kim, Y. M.; Kwon, J. H.; Kim, S.; Choi, U. H.; Moon, H. C. Ion-Cluster-Mediated Ultrafast Self-Healable Ionoconductors for Reconfigurable Electronics. *Nat. Commun.* **2022**, *13* (1), 3769.

[147] Rebei, M.; Mahun, A.; Walterova, Z.; Trhlikova, O.; Donato, R. K.; Beneš, H. VOC-Free Tricomponent Reaction Platform for Epoxy Network Formation Mediated by a Recyclable Ionic Liquid. *Polym. Chem.* **2022**, *13*, 5380-5388.

[148] Livi, S.; Baudoux, J.; Gérard, J. F.; Duchet-Rumeau, J. Ionic Liquids: A Versatile Platform for the Design of a Multifunctional Epoxy Networks 2.0 Generation. *Prog. Polym. Sci.* **2022**, *132,* 101581.

[149] Cassity, C. G.; Mirjafari, A.; Mobarrez, N.; Strickland, K. J.; O'brien, R. A.; Davis, J. H. Ionic Liquids of Superior Thermal Stability. *Chem. Commun.* **2013**, *49* (69), 7590–7592.

[150] Wang, M.; Zhang, P.; Shamsi, M.; Thelen, J. L.; Qian, W.; Truong, V. K.; Ma, J.; Hu, J.; Dickey, M. D. Tough and Stretchable Ionogels by in Situ Phase Separation. *Nat. Mater.* **2022**, *21* (3), 359–365.

[151] Zhao, X.; Xu, J.; Zhang, J.; Guo, M.; Wu, Z.; Li, Y.; Xu, C.; Yin, H.; Wang, X. Fluorescent Double Network Ionogels with Fast Self-Healability and High Resilience for Reliable Human Motion Detection. *Mater. Horizons* **2022**, *10*, 646–656.

[152] Wang, Z.; Zhang, J.; Liu, J.; Hao, S.; Song, H.; Zhang, J. 3D Printable, Highly Stretchable, Superior Stable Ionogels Based on Poly(Ionic Liquid) with Hyperbranched Polymers as Macro-Cross-Linkers for High-Performance Strain Sensors. *ACS Appl. Mater. Interfaces* **2021**, *13* (4), 5614–5624.

[153] Onal, C. D.; Rus, D. A Modular Approach to Soft Robots. In *Proceedings of the IEEE RAS and EMBS International Conference on Biomedical Robotics and Biomechatronics*; **2012**, 1038–1045.

[154] Zhang, C.; Zhu, P.; Lin, Y.; Jiao, Z.; Zou, J. Modular Soft Robotics: Modular Units, Connection Mechanisms, and Applications. *Adv. Intell. Syst.* **2020**, *2* (6), 1900166.

[155] Morin, S. A.; Shevchenko, Y.; Lessing, J.; Kwok, S. W.; Shepherd, R. F.; Stokes, A. A.; Whitesides, G. M. Using "Click-e-Bricks" to Make 3D Elastomeric Structures. *Adv. Mater.* **2014**, *26* (34), 5991–5999.

[156] Bowman, C.; Du Prez, F.; Kalow, J. Introduction to Chemistry for Covalent Adaptable Networks. *Polym. Chem.* **2020**, *11* (33), 5295–5296.

[157] Kloxin, C. J.; Scott, T. F.; Adzima, B. J.; Bowman, C. N. Covalent Adaptable Networks (CANs): A Unique Paradigm in Cross-Linked Polymers. *Macromolecules* **2010**, *43*, 2643.

[158] Gulyuz, S.; Yagci, Y.; Kiskan, B. Exploiting the Reversible Covalent Bonding of Boronic Acids for Self-Healing/Recycling of Main-Chain Polybenzoxazines. *Polym. Chem.* **2022**, *13* (24), 3631–3638.

[159] Thongsomboon, W.; Sherwood, M.; Arellano, N.; Nelson, A. Thermally Induced Nanoimprinting of Biodegradable Polycarbonates Using Dynamic Covalent Cross-Links. *ACS Macro Lett.* **2013**, *2* (1), 19–22.

[160] Jung, S.; Kim, S. Y.; Kim, J. C.; Noh, S. M.; Oh, J. K. Ambient Temperature Induced Diels-Alder Crosslinked Networks Based on Controlled Methacrylate Copolymers for Enhanced Thermoreversibility and Self-Healability. *RSC Adv.* **2017**, *7* (42), 26496–26506.

[161] Kokubo, H.; Sano, R.; Murai, K.; Ishii, S.; Watanabe, M. Ionic Polymer Actuators Using Poly(Ionic Liquid) Electrolytes. *Eur. Polym. J.* **2018**, *106*, 266–272.

[162] Zhao, R.; Yang, J.; Wang, B.; Ma, Z.; Pan, L.; Li, Y. Block Copolymer Solid Electrolytes Based on Comb-Like Poly(Ethylene Glycol) Plasticized Poly(Ionic Liquid)s for Lithium-Ion Batteries. *Chin. J. Chem.* **2023**, *41* (19), 2493–2501.

[163] Koehler, K. C.; Durackova, A.; Kloxin, C. J.; Bowman, C. N. Kinetic and Thermodynamic Measurements for the Facile Property Prediction of Diels-Alder-Conjugated Material Behavior. *AIChE J* **2012**, *58* (11), 3545–3552.

[164] Xia, Q.; Li, W.; Zou, X.; Zheng, S.; Liu, Z.; Li, L.; Yan, F. Metal-Organic Frameworks (MOFs) Facilitated Highly Stretchable, and Fatigue-Resistant Ionogels for Recyclable Sensors. *Mater. Horizons* **2022**, 9, 2881-2892.

[165] Zhu, J.; Lu, X.; Zhang, W.; Liu, X. Substrate-Independent, Reversible, and Easy-Release Ionogel Adhesives with High Bonding Strength. *Macromol. Rapid Commun.* **2020**, *41* (24), 2000098.

APPENDIX A

3D Printing of Ionic Liquid Polymer Network for Stretchable Conductive Sensors

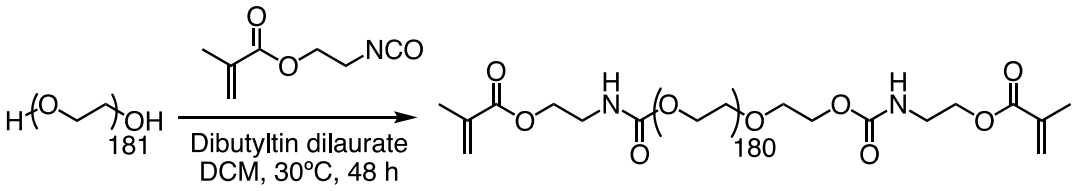

Scheme A1 Synthetic route to PEG-bisurethane methacrylate.

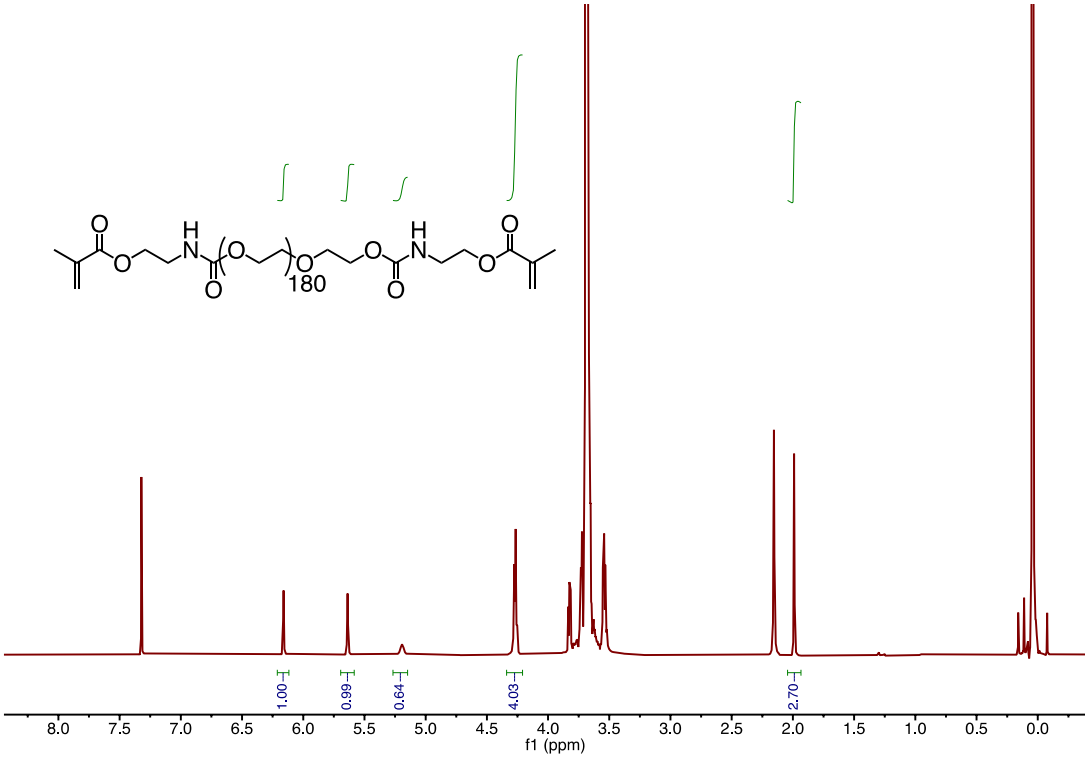

Figure A1 ^{1}H NMR spectrum of PEG-BUM in $CDCl_3$.

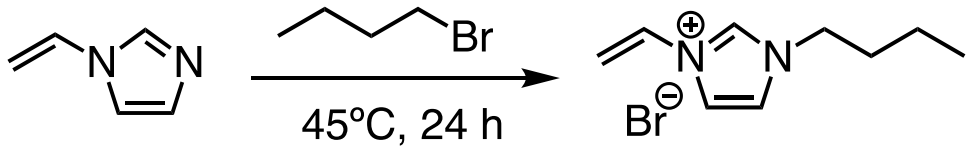

Scheme A2 Synthetic route to 1-vinyl-3-butyl imidazolium bromide.

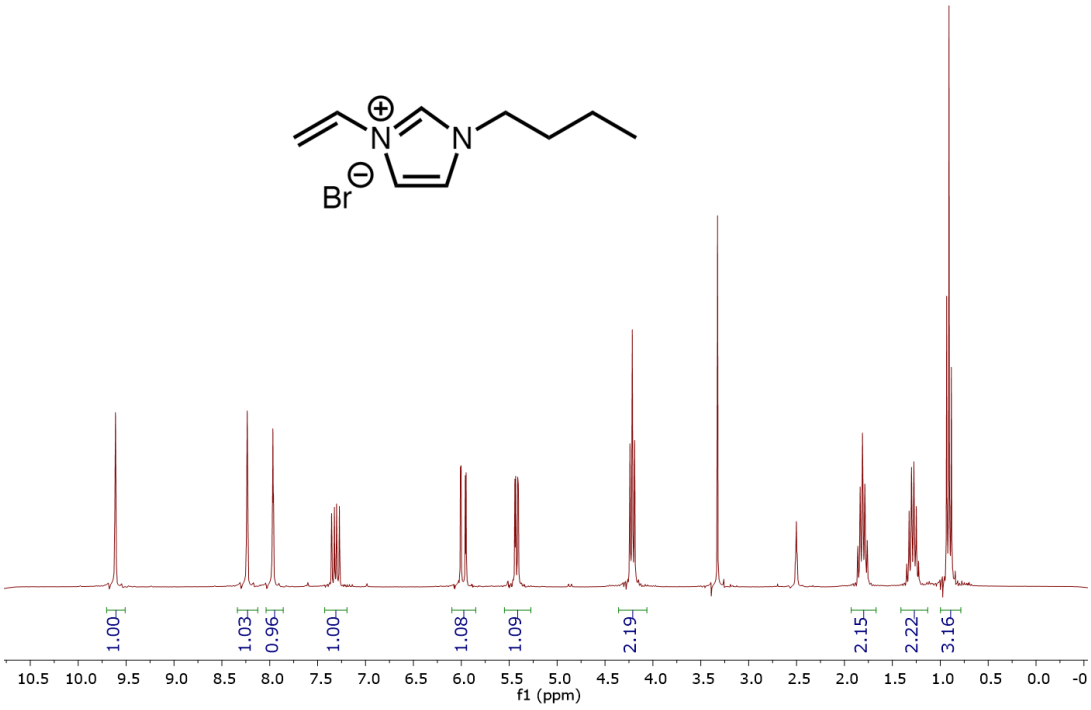

Figure A2 ^{1}H NMR of [BVIM]Br in DMSO-d_6.

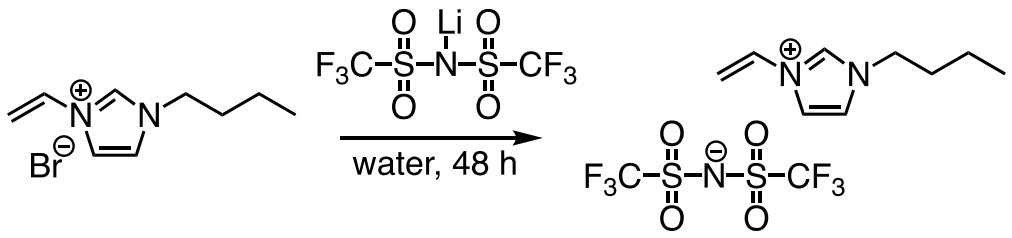

Scheme A3 Synthetic route to 1-vinyl-3-butyl imidazolium bis(trifluoromethane)sulfonamide.

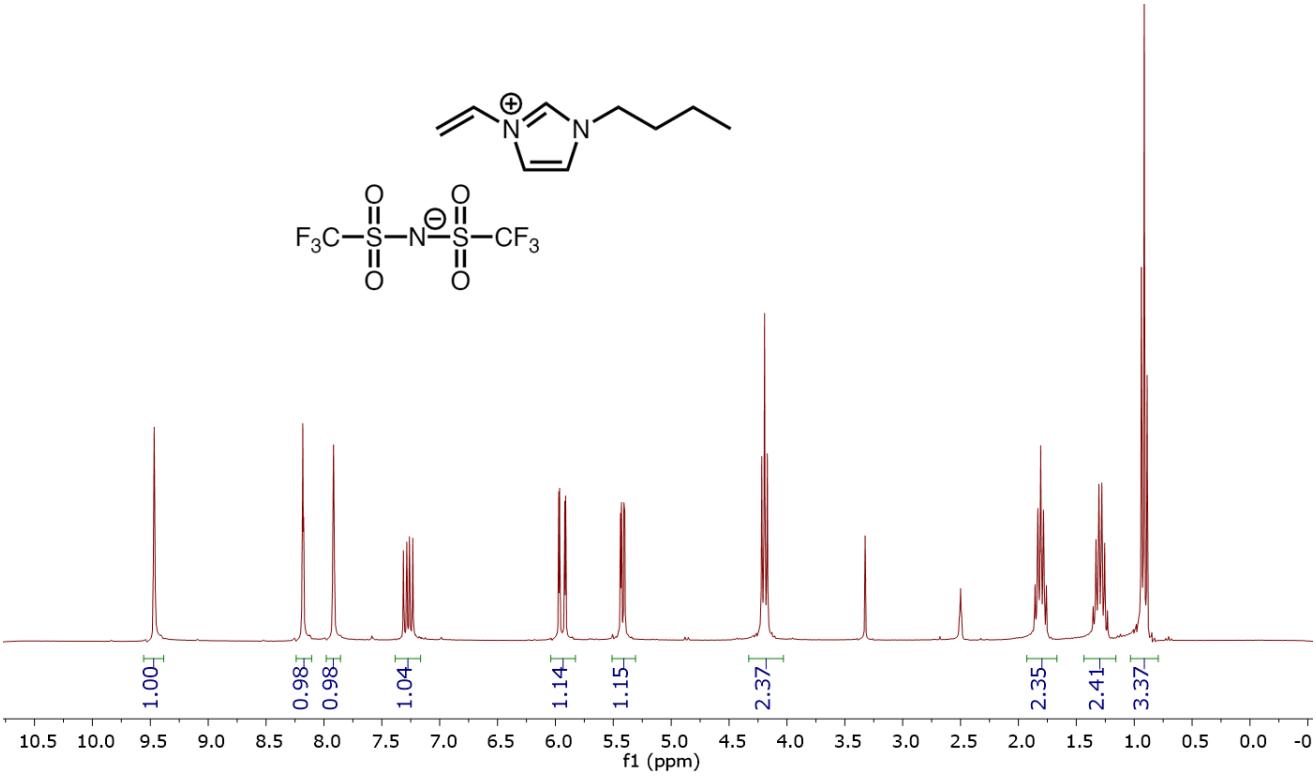

Figure A3 ^{1}H NMR of [BVIM]TFSI in DMSO-d_6.

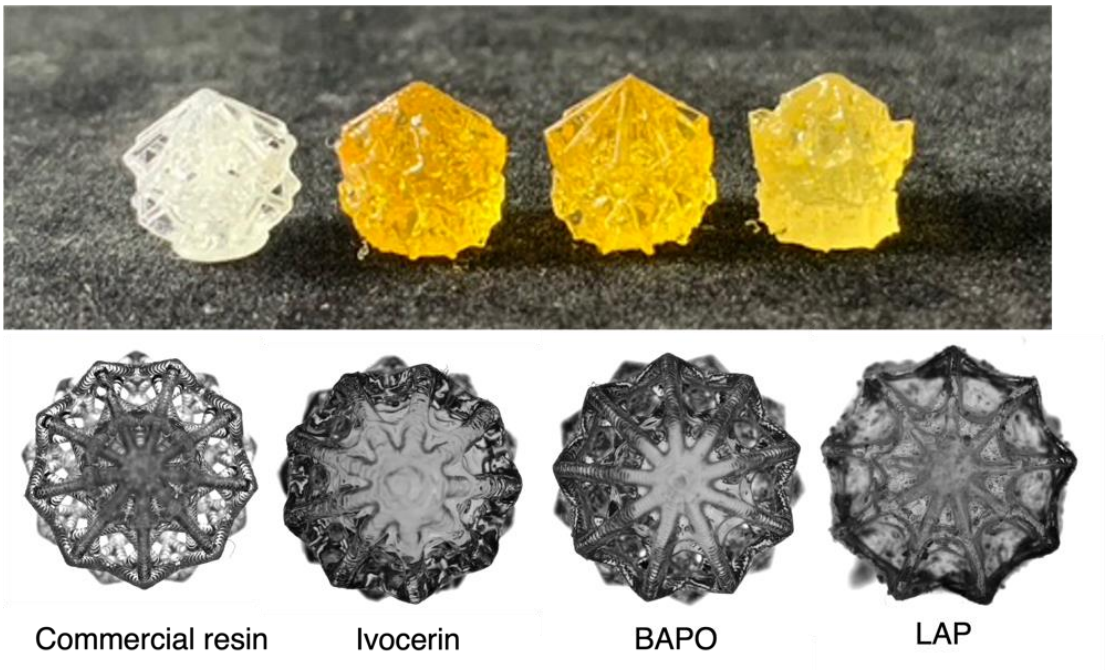

Figure A4 Printed structures using a series of photoinitiators including ivocerin, BAPO, and LAP.

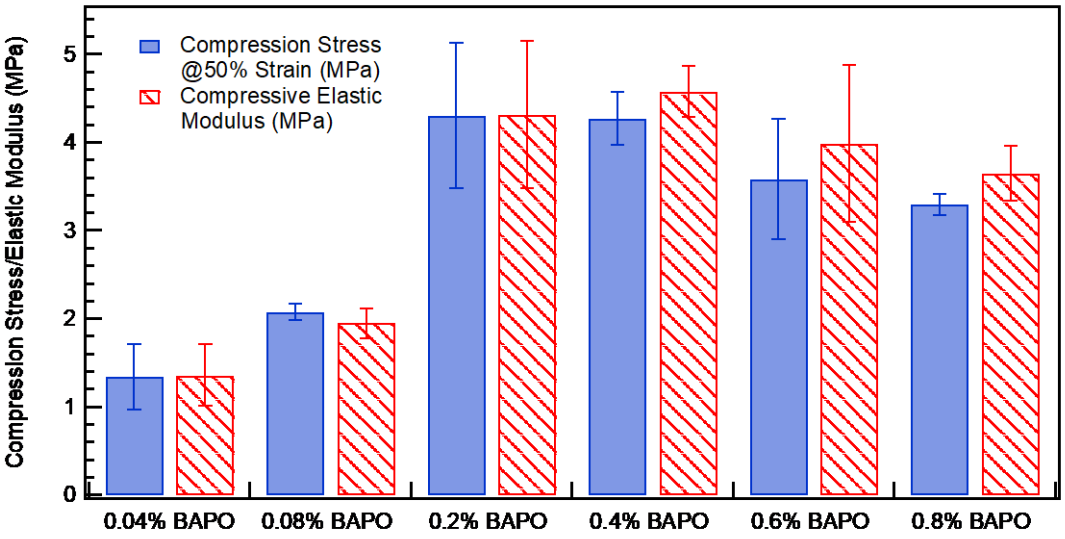

Figure A5 Compressive tests of printed cylinders using various amounts of BAPO.

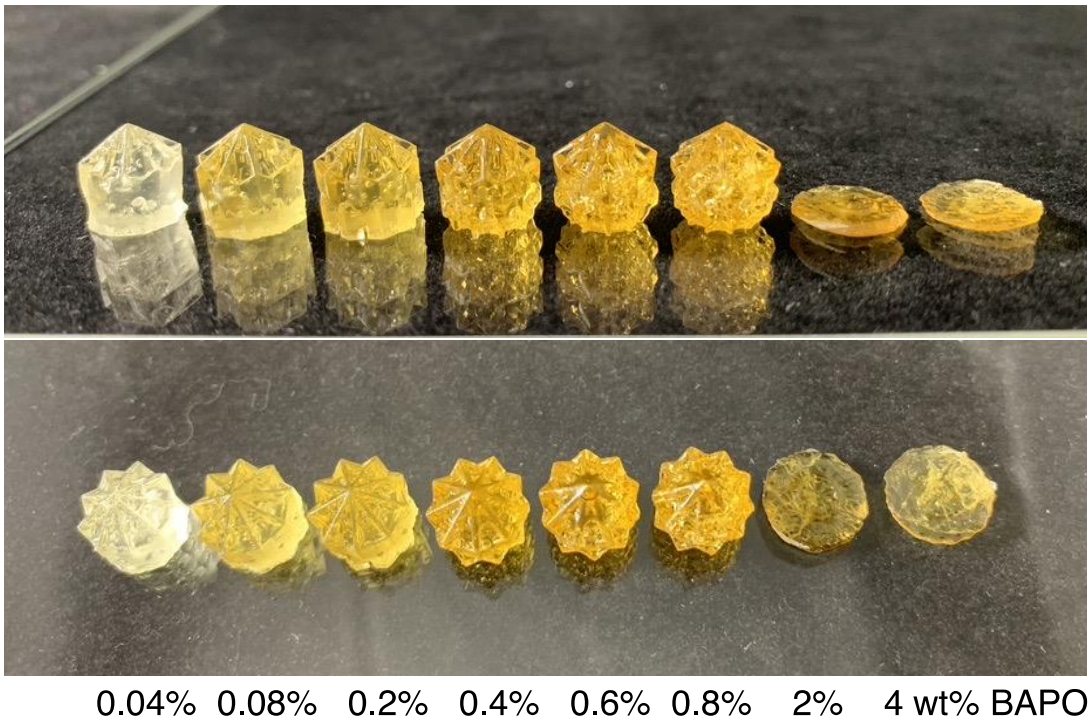

Figure A6 3D printed structures using various amounts of BAPO.

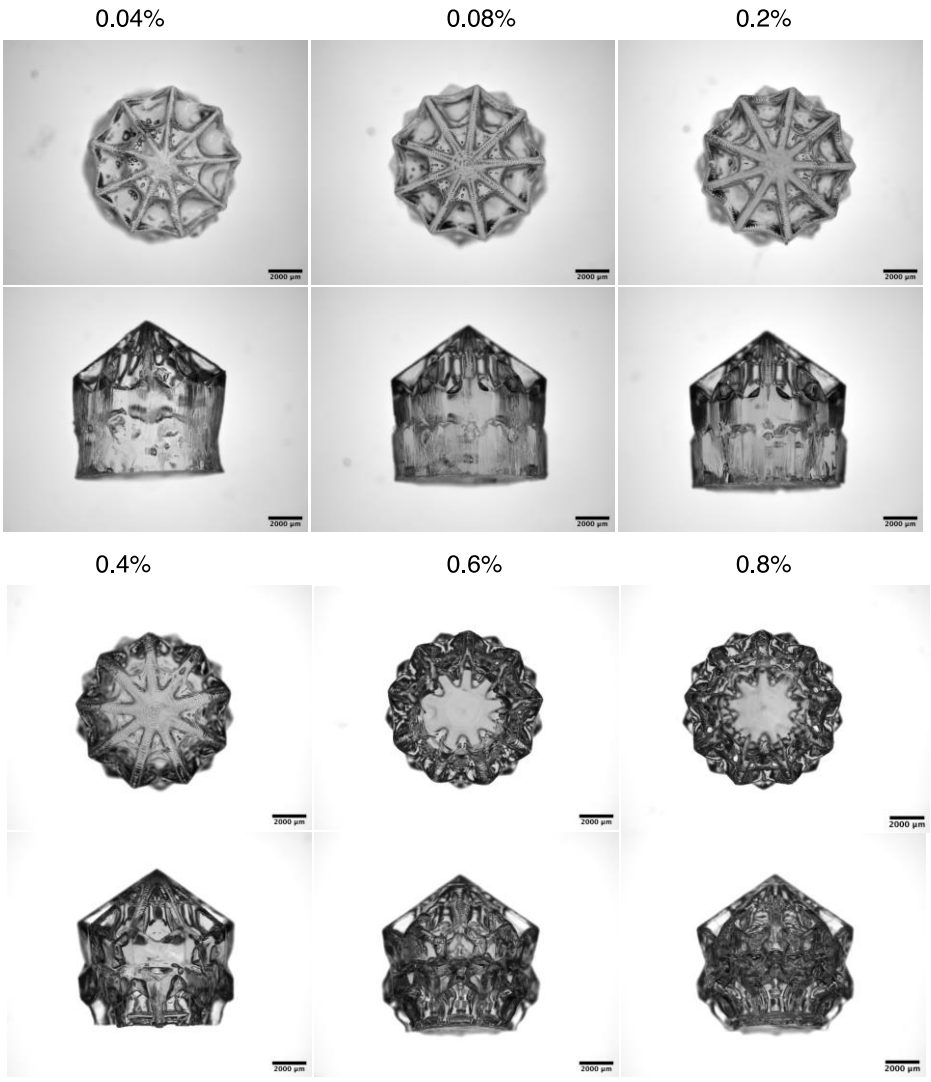

Figure A7 Stereomicroscopic images of 3D printed structures using various amounts of BAPO.

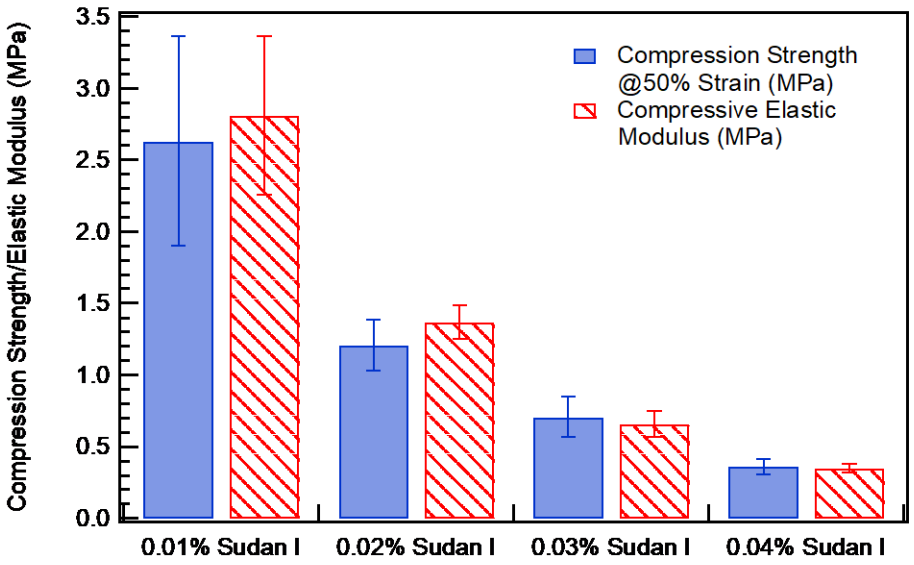

Figure A8 Compressive tests of printed cylinders using various amount of Sudan-I.

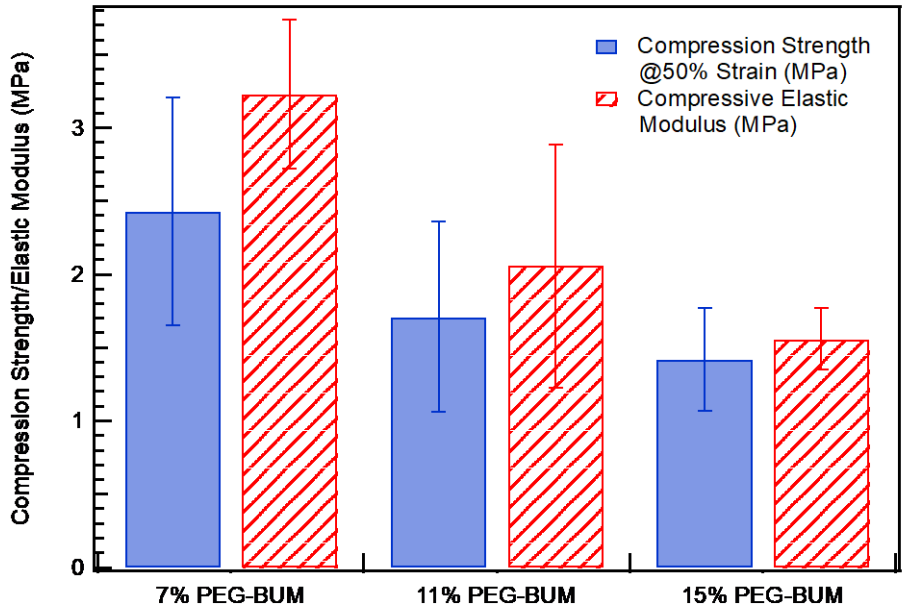

Figure A9 Compressive tests of printed cylinders using various amounts of PEG-BUM.

Determine %Mass Loss

To determine the amount of unpolymerized ionic liquid in printed structures with and without post-print curing step, cylindrical samples were printed on a Form 2 SLA printer. After printing, the samples with post-print curing step were cured for 1 h with 405 nm light under a flow of nitrogen, while the samples without post-print curing step were directly extracted as is. Each sample was submerged in 50 mL of methanol for one week, with the solvent being replaced three times over that period. After one week, the samples were placed in a vacuum oven at 50 °C overnight. To determine the amount of unpolymerized materials, the mass of the fully dried sample is subtracted from the original mass of the puck. The mass lost is due to uncured monomers and polymerizable ionic liquid being extracted out by methanol. The average results are displayed in the table below. The data reveals a portion of the ionic liquid remains unpolymerized after printing, leaving the networks swollen. The unpolymerized ionic liquid allows these gels to remain conductive.

Table A1. % Mass loss of 3D printed structure with and without post-print curing step.

Samples	With post-print curing step	Avg. initial mass (g)	Avg. final mass (g)	Avg. % mass loss	Avg. % mass loss
7wt% PEG-BUM	Yes	0.6403	0.4123	35.60	34
11 wt% PEG-BUM	Yes	0.6388	0.4378	31.37	
15 wt% PEG-BUM	Yes	0.6261	0.4024	35.81	
7 wt% PEG-BUM	No	0.6269	0.1572	74.99	73
11 wt% PEG-BUM	No	0.6353	0.1865	70.65	
15 wt% PEG-BUM	No	0.6211	0.1745	71.91	

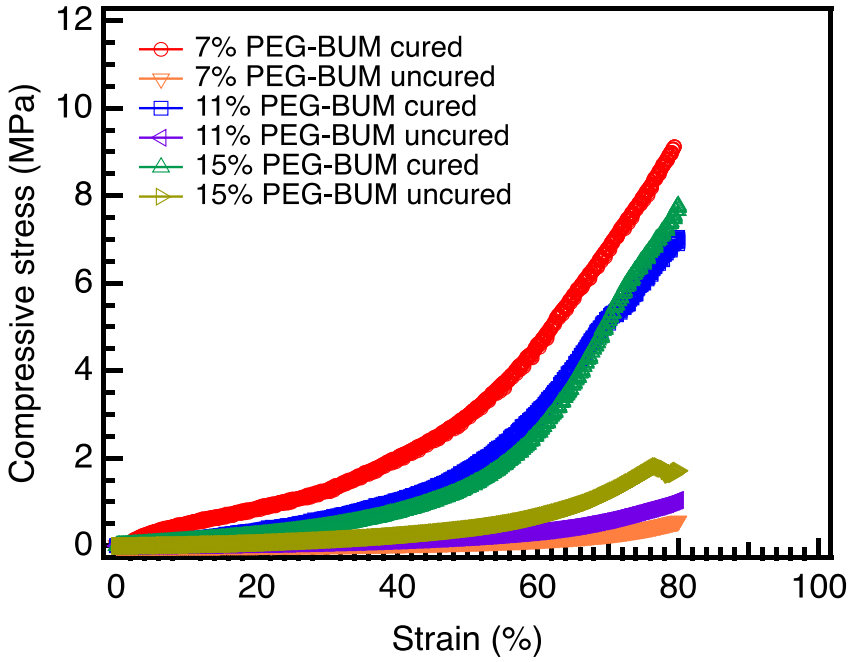

Figure A10 Tensile stress versus strain curves of printed dogbones using various amounts of PEG-BUM with and without post-print curing step.

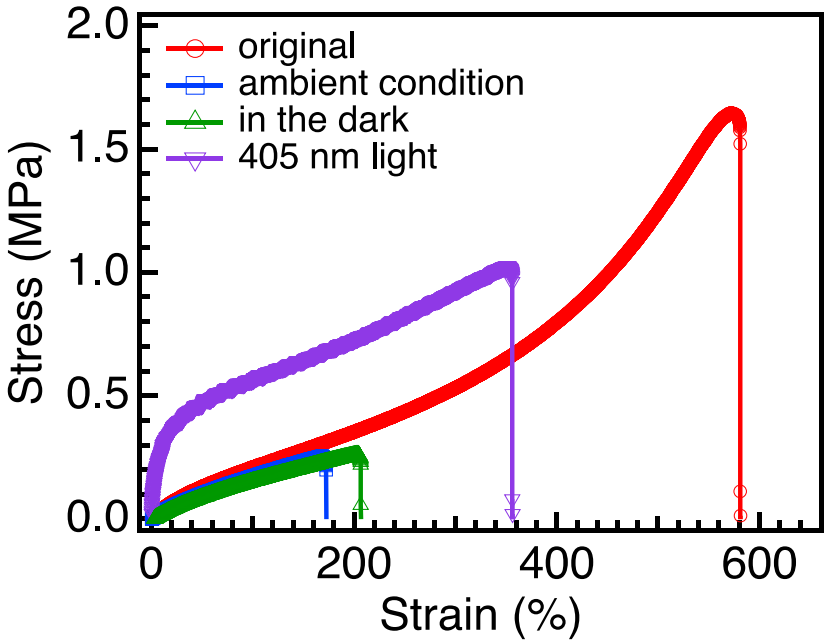

Figure A11 Self-adhesion experiments with different healing conditions.

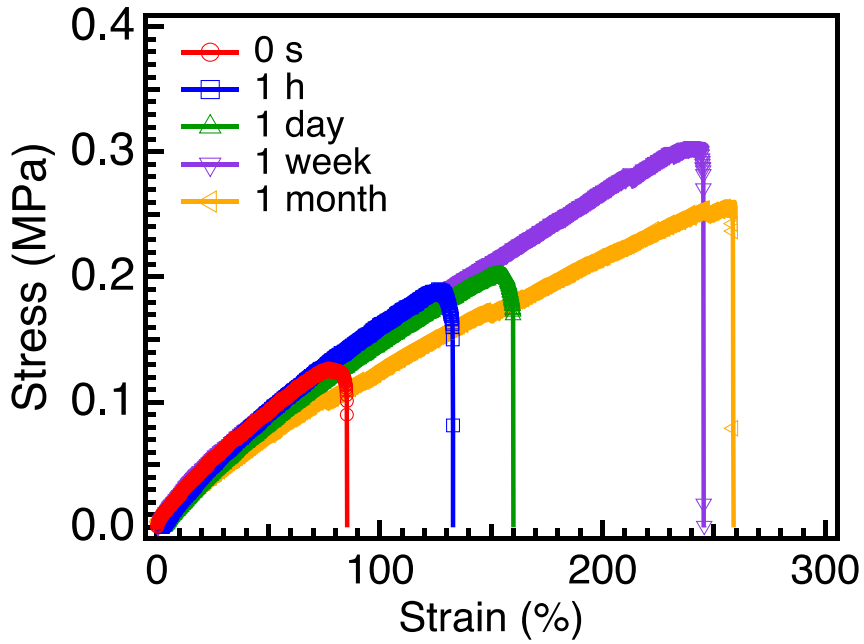

Figure A12 Self-adhesion experiments with different healing times under ambient conditions.

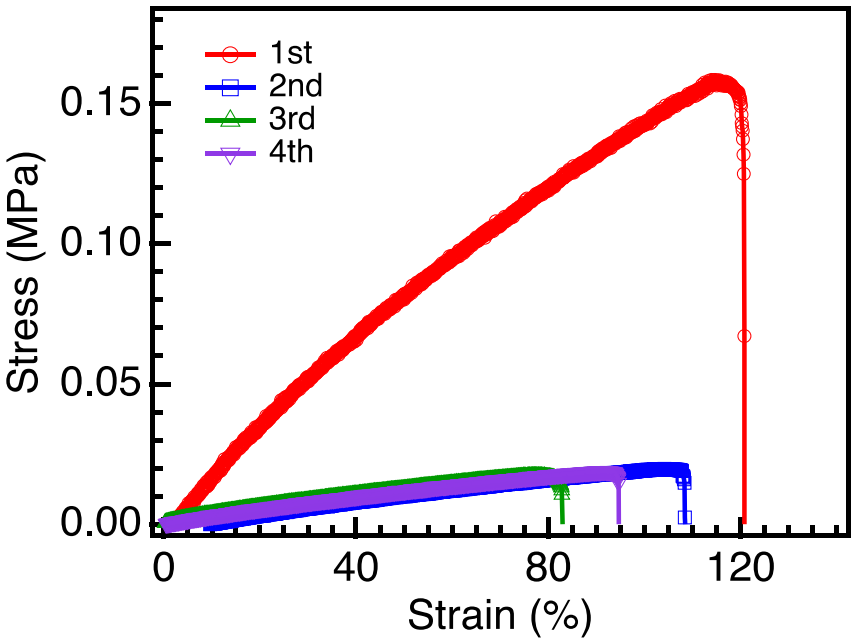

Figure A13 Self-adhesion experiments with different numbers of reattachments under ambient condition.

APPENDIX B

Mechanomorphic Responses in 3D Printed Ionic Liquid Polymer Networks

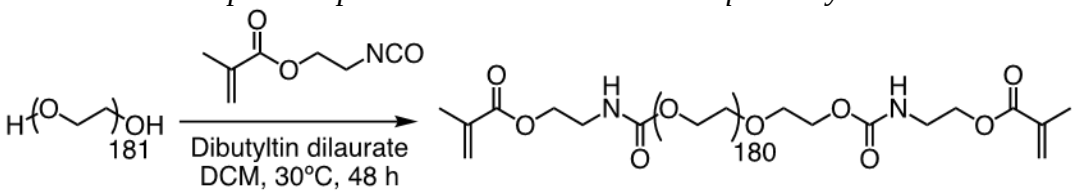

Scheme B1 Synthetic route to PEG-BUM.

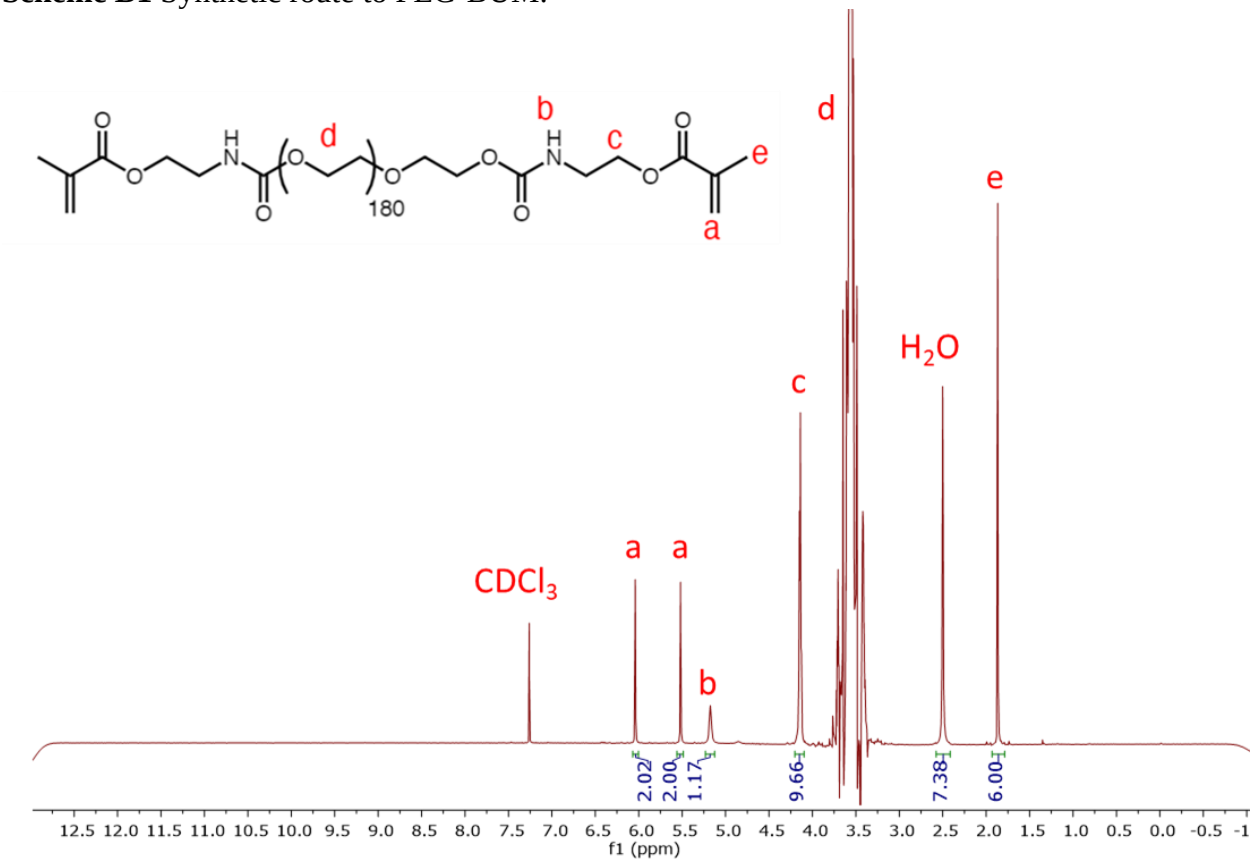

Figure B1 ^{1}H NMR spectrum of PEG-BUM in $CDCl_3$.

Scheme B2 Synthetic route to [BVIM]Br.

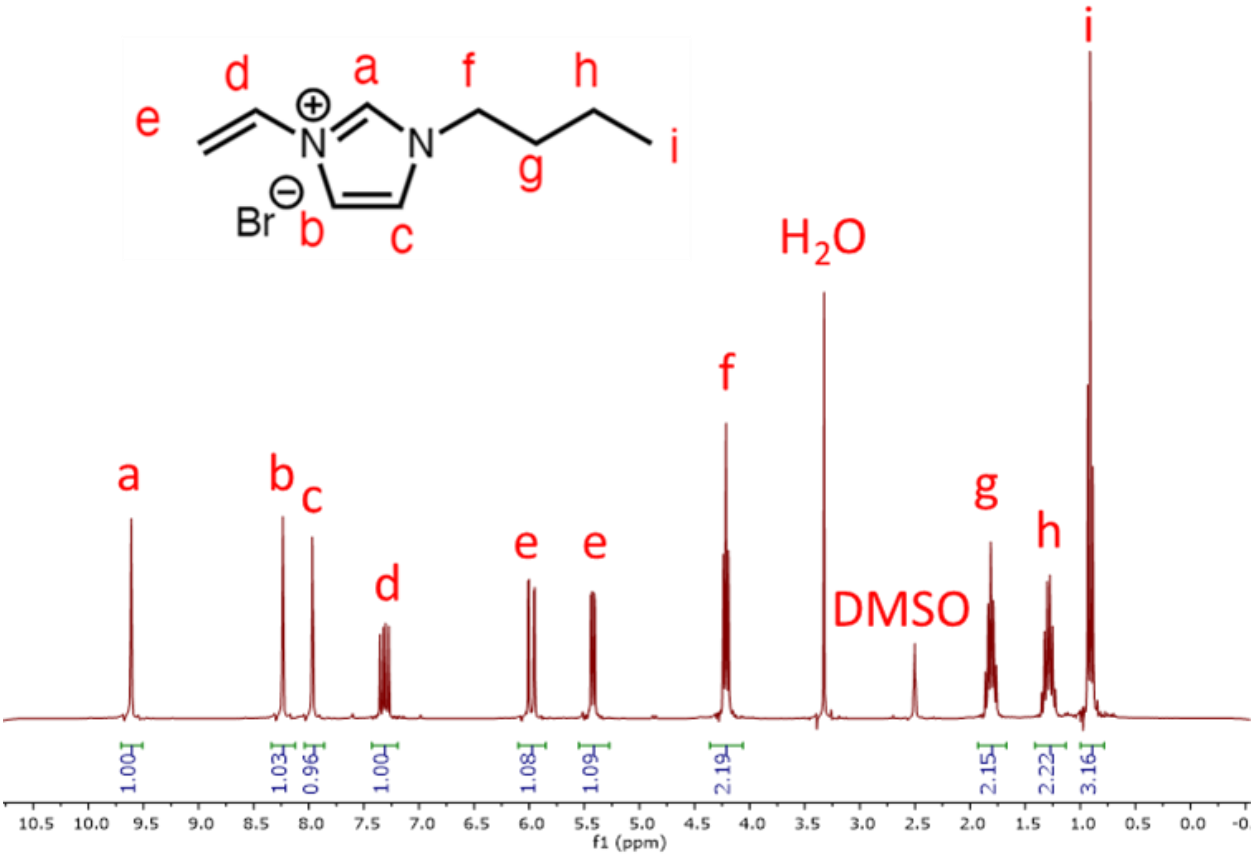

Figure B2 ^{1}H NMR spectrum of [BVIM]Br in DMSO-d_6.

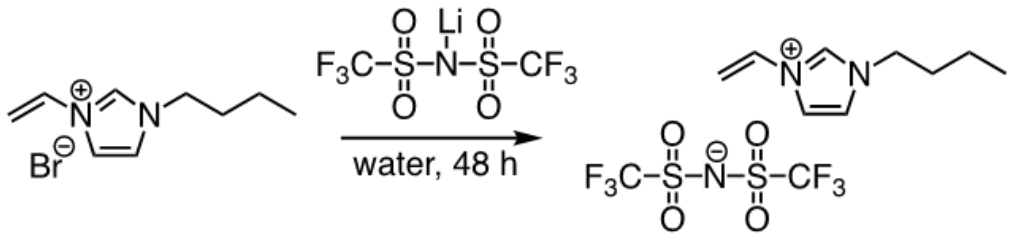

Scheme B3 Synthetic route to [BVIM]TFSI.

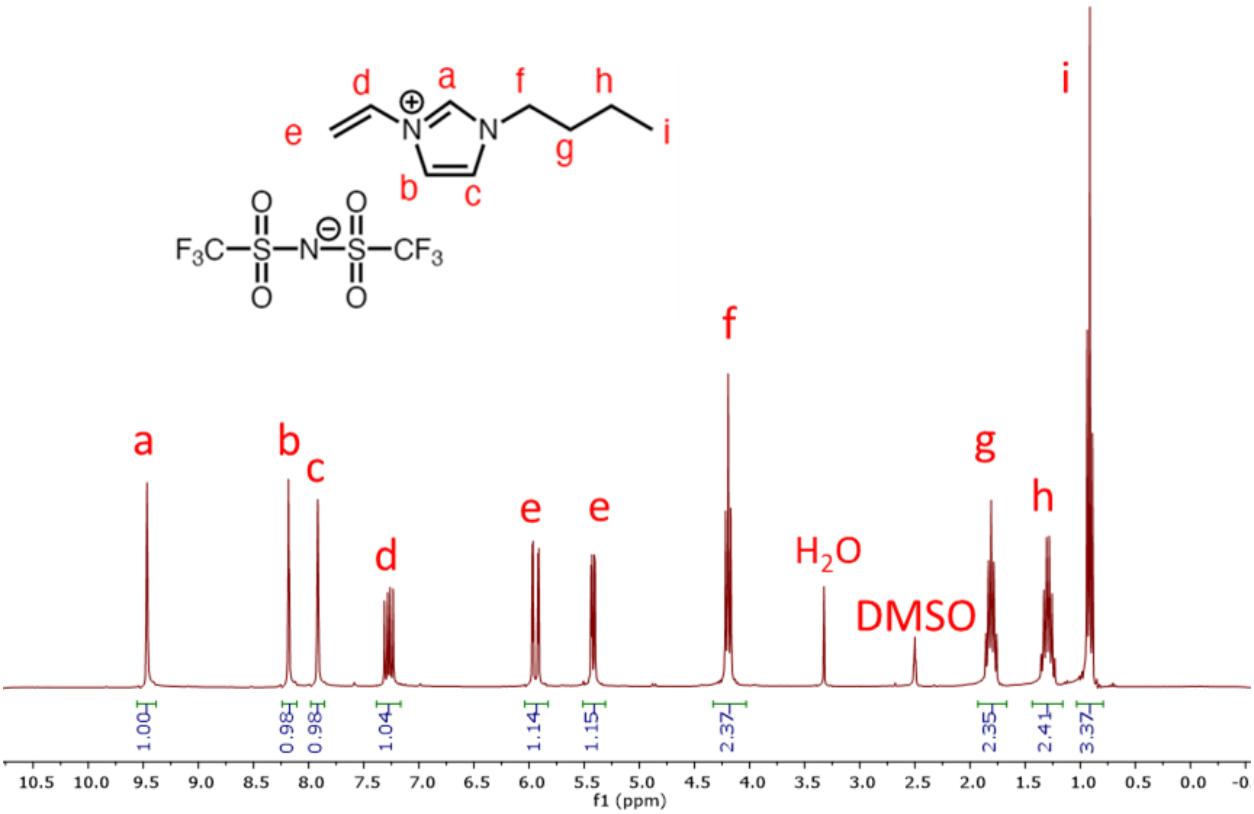

Figure B3 ^{1}H NMR spectrum of [BVIM]TFSI in DMSO-d_6.

Table B1 Formulations for Ion Gel Resins (20 g scale).

Resin Formulation	PEG-BUM [g]	BAPO [g]	Sudan 1 [g]	[BVIM]TFSI [mL]	[EVIM]TFSI [mL]
10B	2	0.15	0.005	17.85	0
15B	3	0.15	0.005	16.85	0
20B	4	0.15	0.005	15.85	0
10E	2	0.15	0.005	0	17.85
15E	3	0.15	0.005	0	16.85
20E	4	0.15	0.005	0	15.85

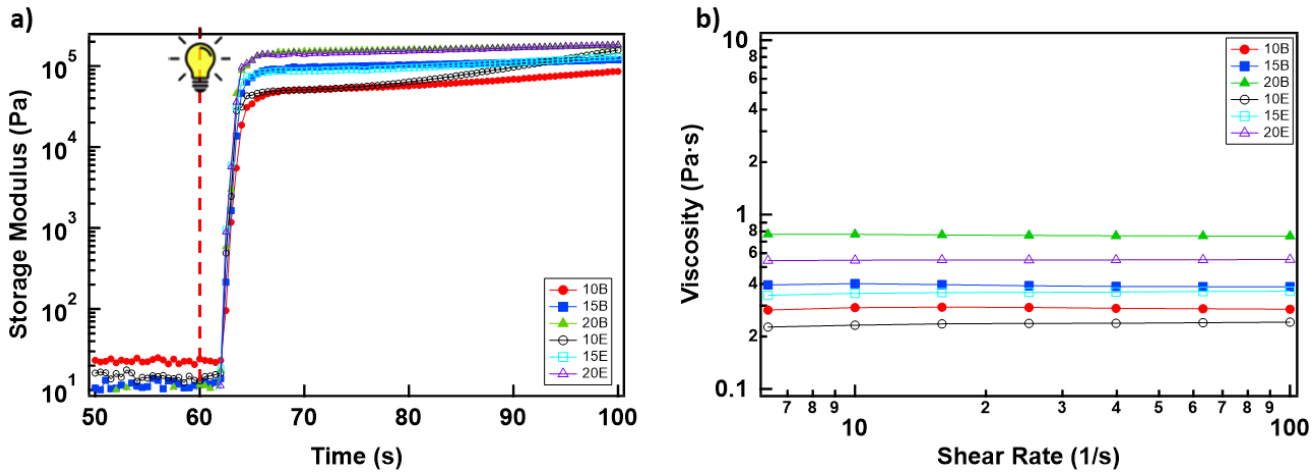

Figure B4 a) Photocuring rate of resins with varying w/w% PEG-BUM. The irradiation began after 60 seconds. b) Viscosity vs shear rate of resins with varying w/w% PEG-BUM.

Table B2 Summary of Mechanical Properties.

Materials	E10	E15	E20	B10	B15	B20
Strength (kPa)	8700 ± 1000	6870 ± 800	3940 ± 440	3760 ± 190	2370 ± 360	1630 ± 24
Strain (mm/mm)	5.5 ± 0.4	7.8 ± 0.5	7.5 ±0.06	9.2 ± 0.5	7.7 ± 1.1	5.8 ±0.25
Modulus (kPa)	77230 ± 2510	32680 ± 1930	10410 ± 580	9830 ± 540	2930 ± 180	720 ± 140

Gel Fraction:

To determine the amount of unpolymerized ionic liquid in a fully cured structure, cylindrical pucks (d = 10 mm, h = 5 mm) of each resin formulation (10B, 15B, 20B) were printed on a Form 2 SLA printer. After printing, each sample was cured for one hour with 405 nm light under a flow of nitrogen. Each puck was soaked in 50 mL of methanol for one week, with the solvent being replaced three times over that period. After one week, the samples were removed and placed in a vacuum oven at 50 °C overnight. To determine the amount of polymerized material remaining, the mass of the fully dried sample is subtracted from the original mass of the puck. The mass lost is due to unpolymerized ionic liquid being washed out by methanol. The average results are displayed in the table below. The data reveals that under all conditions, a portion of the ionic liquid remains unpolymerized after printing, leaving the networks swollen.

Table B3 Summary of Gel Fraction Data.

Materials	Ionic liquid	% Weight loss	%Gel fraction
10% PEG-BUM	[EVIM]TFSI	25	75
15% PEG-BUM		24	76
20% PEG-BUM		24	76
10% PEG-BUM	[BVIM]TFSI	49	51
15% PEG-BUM		41	59
20% PEG-BUM		36	64

Figure B5 Degree of bending in multi-material tensile specimens is strongly influenced by the amount of strain applied.

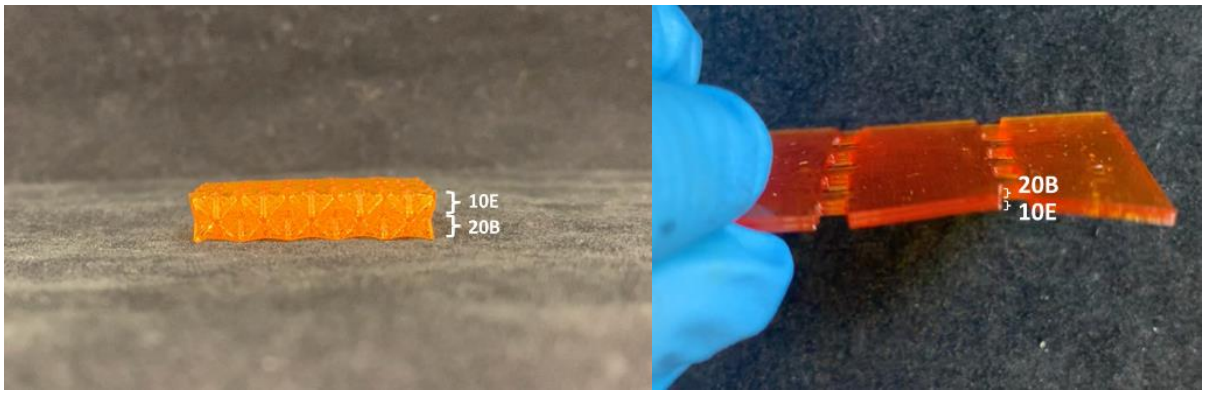

Figure B6 Images of octet-truss lattice and wheel-to-box structures. The layers containing different resin compositions are labelled.

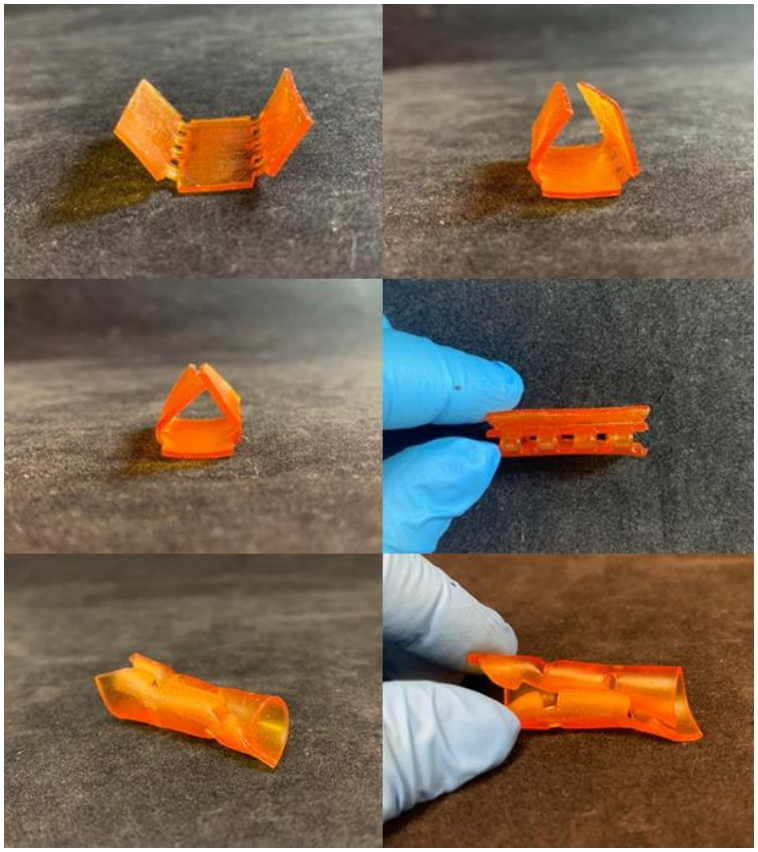

Figure B7 Images demonstrating the anisotropic shape transformation of the wheel-to-box structure. The degree of shape transformation is influenced by the amount of strain applied.

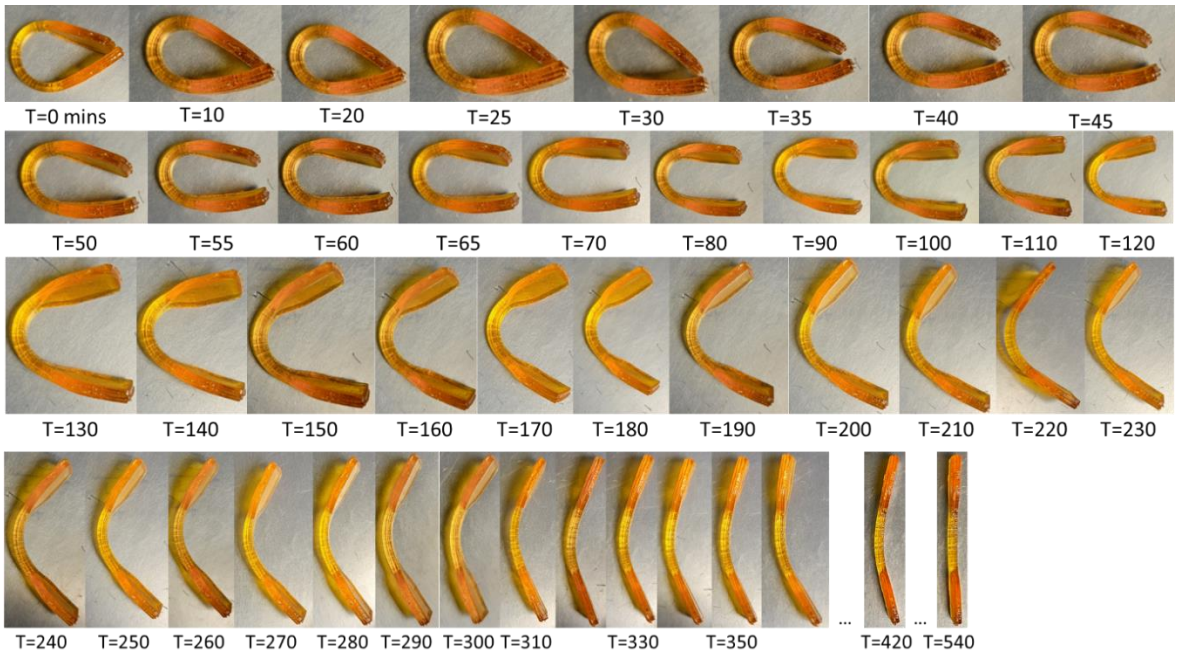

Figure B8 Images of shape recovery of 10E/20B tensile specimens.

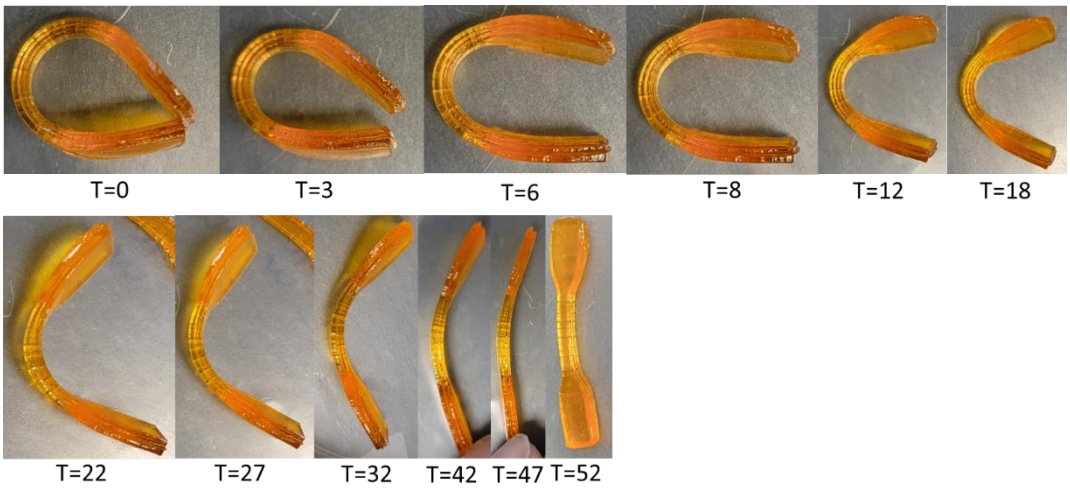

Figure B9 Images of shape recovery of 15E/15B tensile specimens.

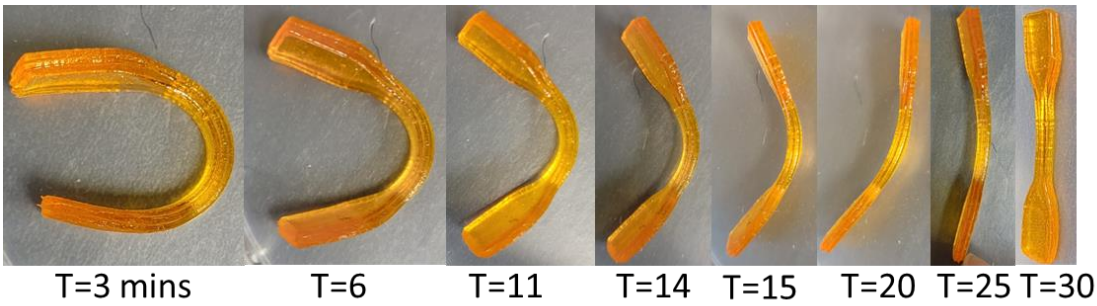

Figure B10 Images of shape recovery of 10B/20B tensile specimens.

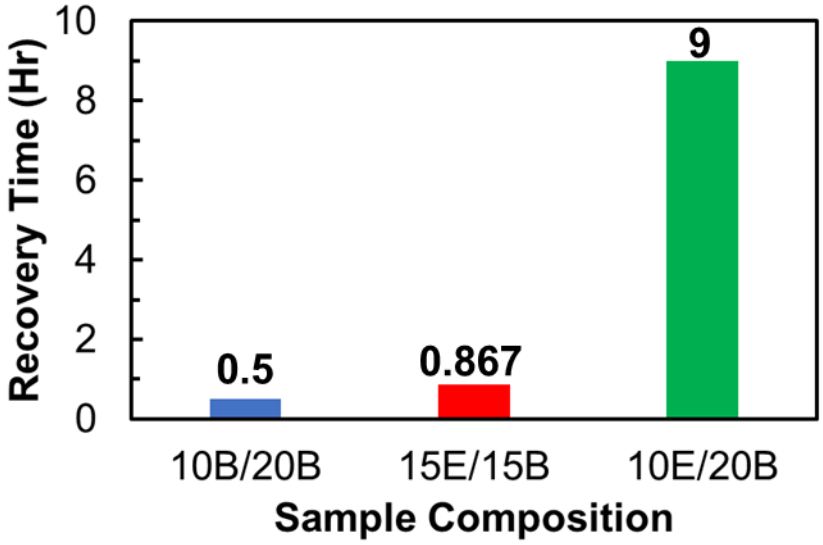

Figure B11 Graphical representation of shape recovery rate of multi-material tensile specimens.

APPENDIX C

3D Printed Modular Strain Sensors Based on Imidazolium Ionic Liquids

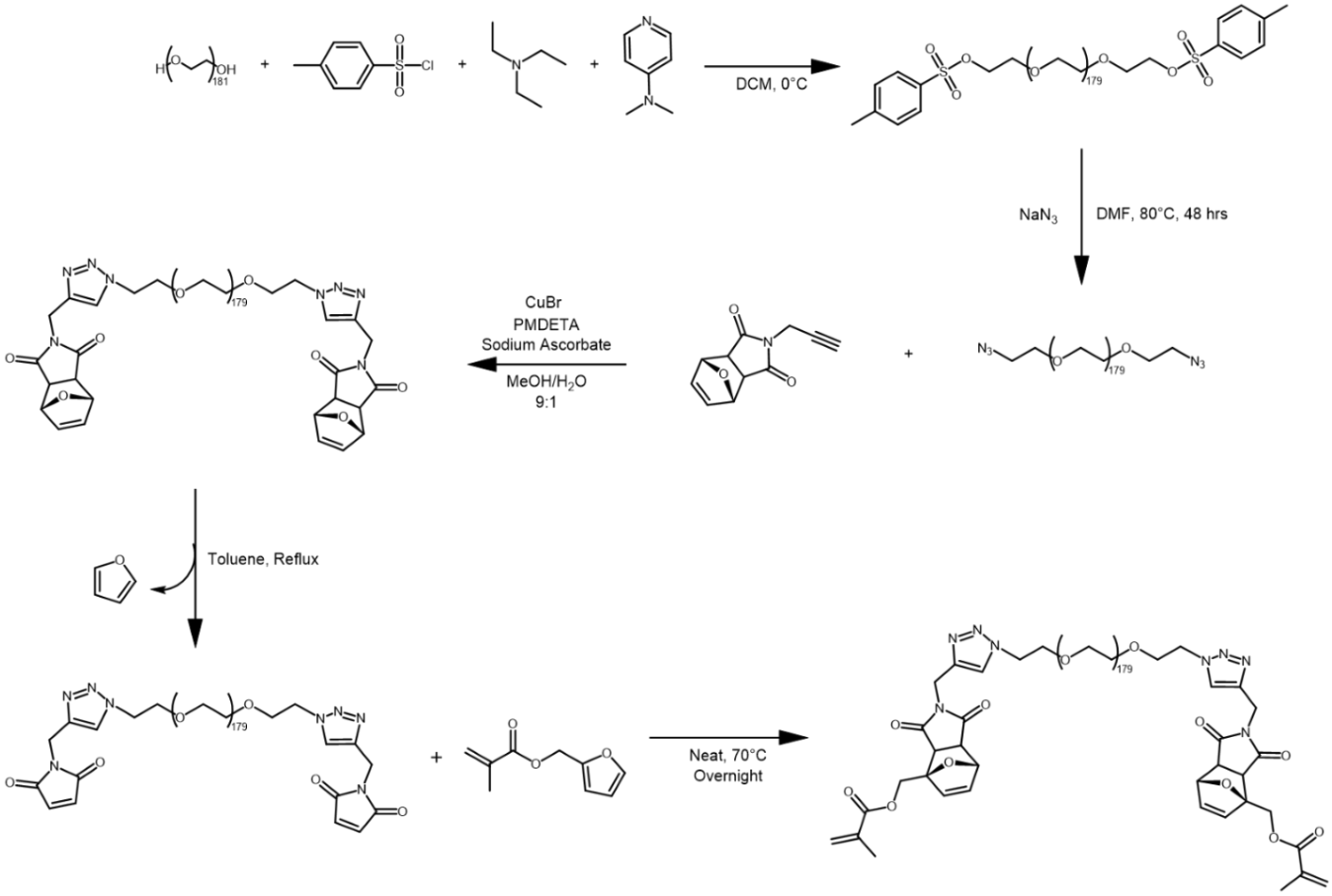

Scheme C1 Overview of synthetic route to **DA-PEG-1**.

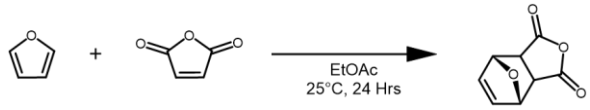

Scheme C2 Synthetic route to exo-3,6-epoxy-1,2,3,6-tetrahydrophtalic anhydride.

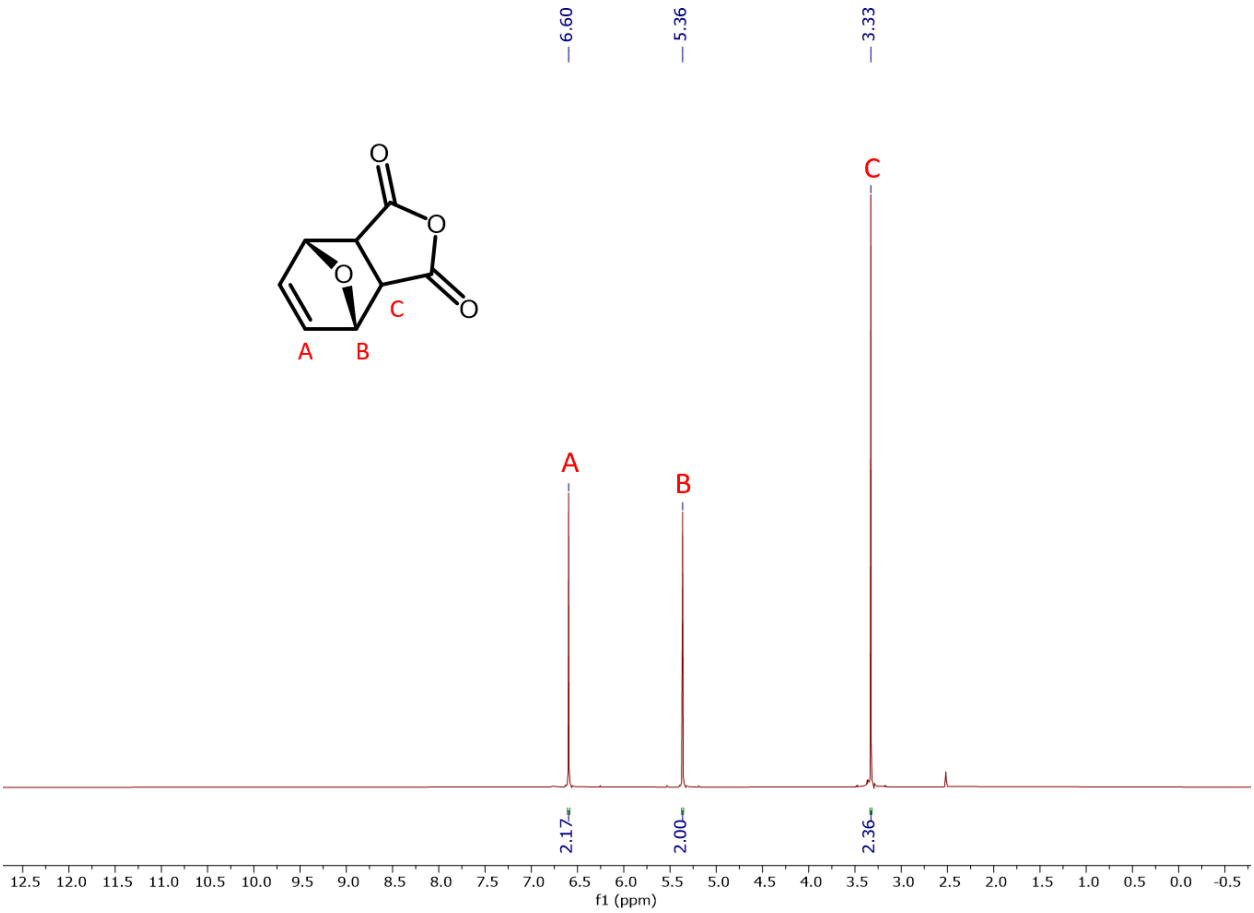

Figure C1 ^{1}H NMR spectrum of exo-3,6-epoxy-1,2,3,6-tetrahydrophtalic anhydride in DMSO-d_6.

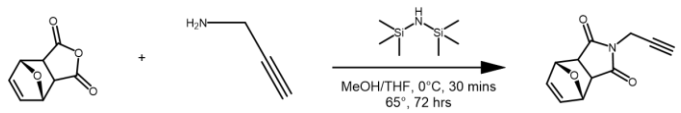

Scheme C3 Synthetic route to alkyne maleimide.

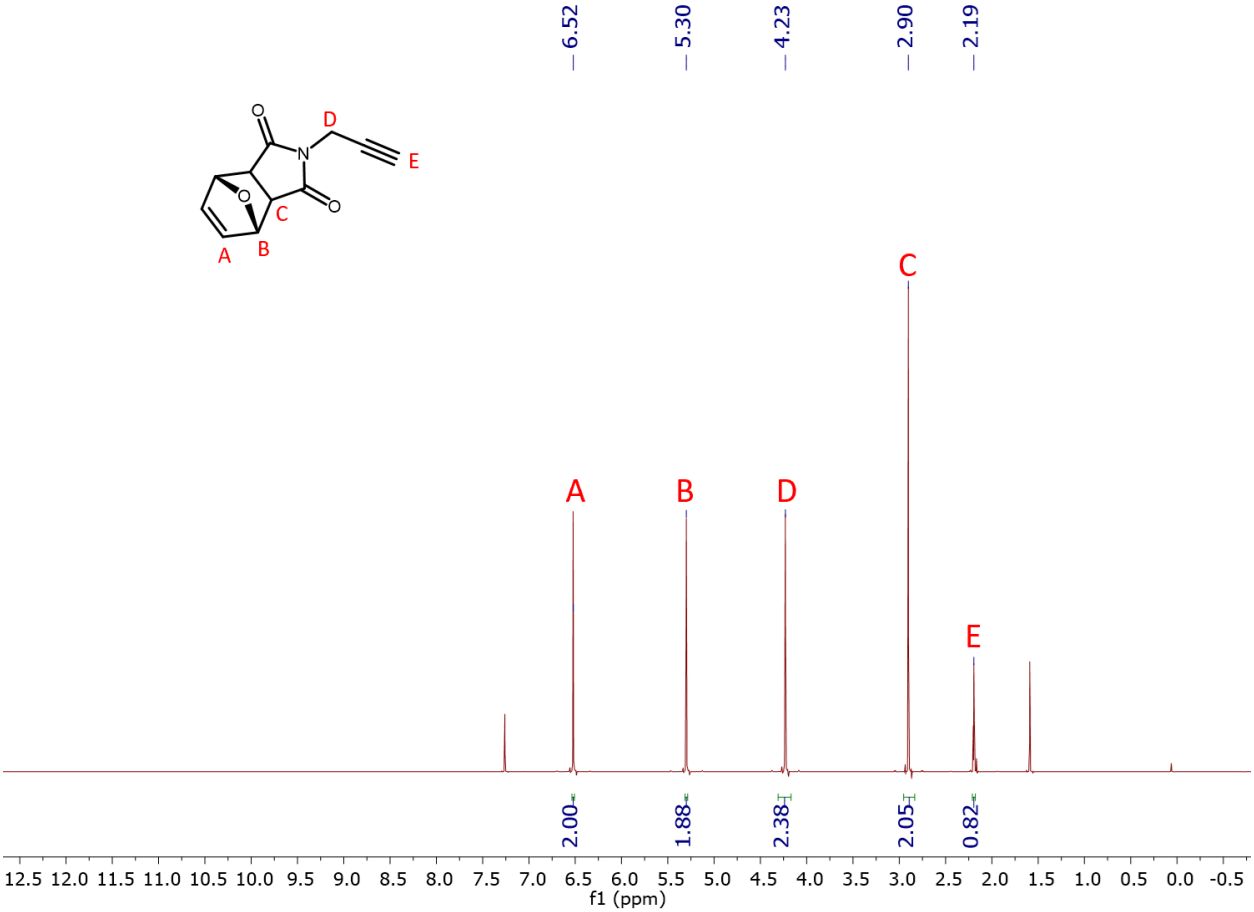

Figure C2 ^{1}H NMR spectrum of 3a,4,7,7a-Tetrahydro-2-(2-propyn-1-yl)-4,7-epoxy-1H-isoindole-1,3(2H)-dione in $CDCl_3$.

Scheme C4 Synthetic route to furfuryl methacrylate.

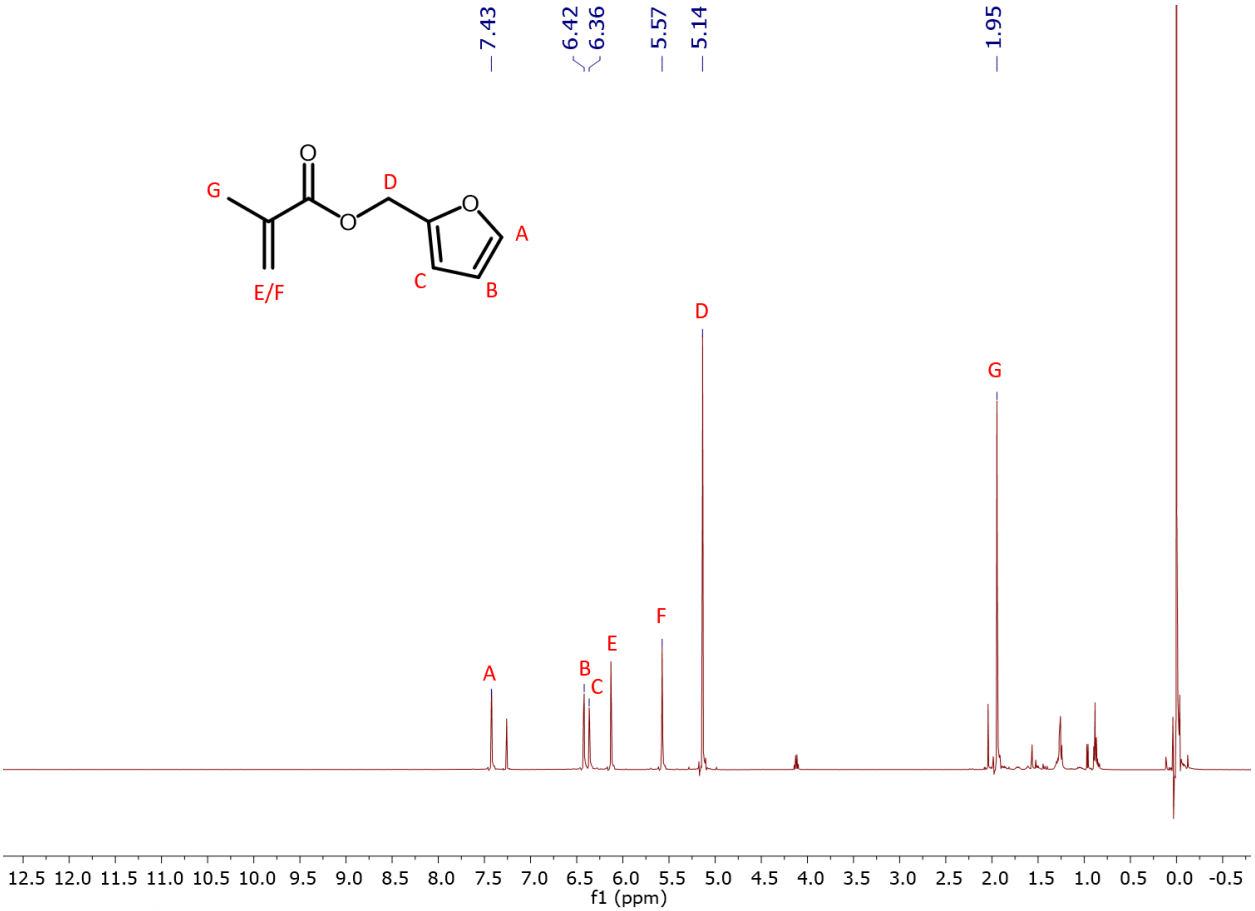

Figure C3 ^{1}H NMR spectrum of furfuryl methacrylate in $CDCl_3$.

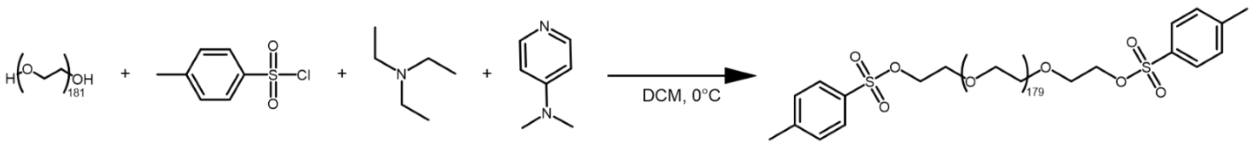

Scheme C5 Synthetic route to PEG-tosylate.

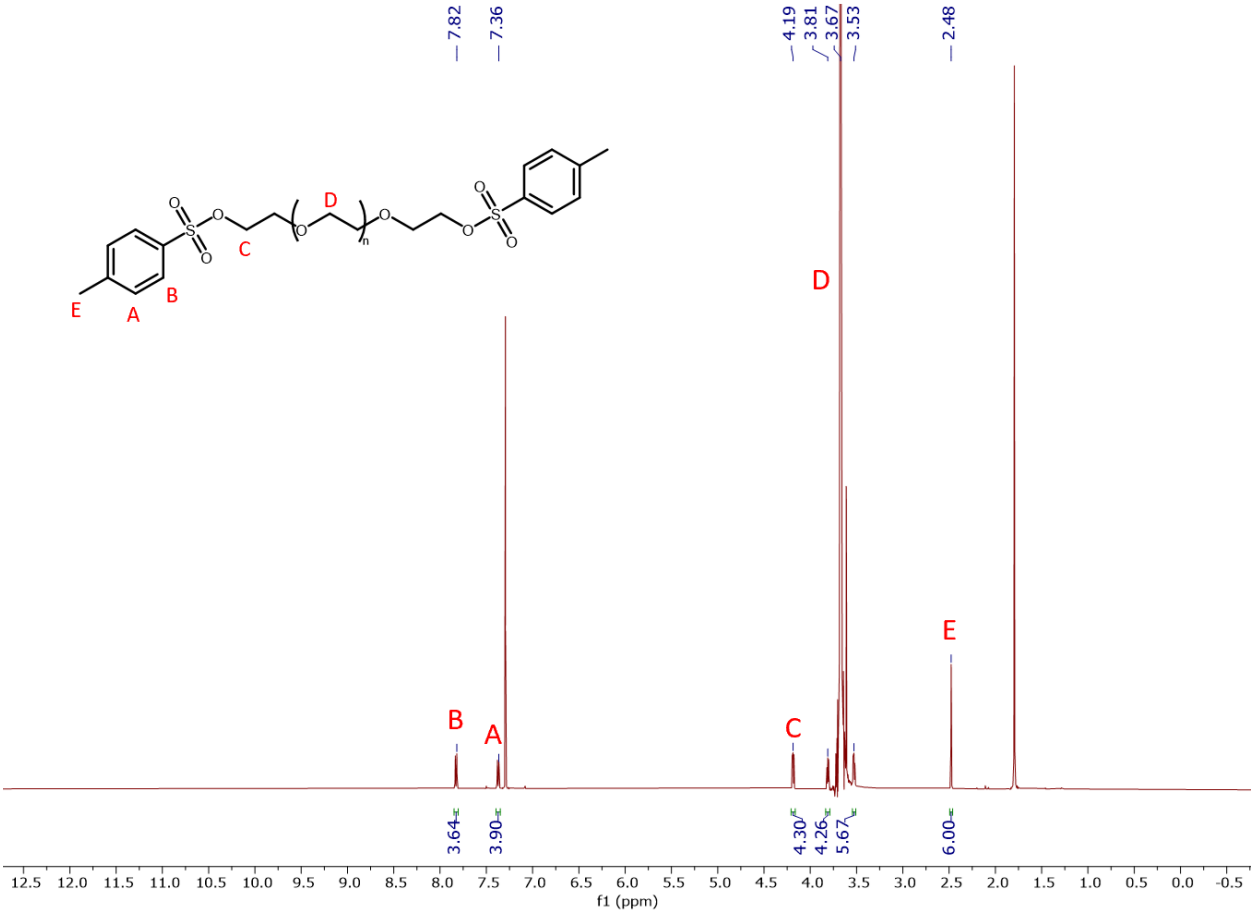

Figure C4 ^{1}H NMR spectrum of PEG-tosylate in $CDCl_3$.

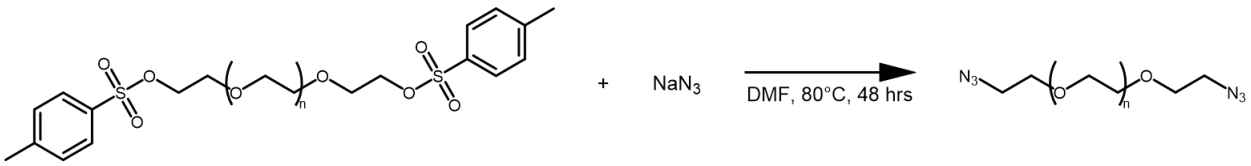

Scheme C6 Synthetic route to PEG-azide.

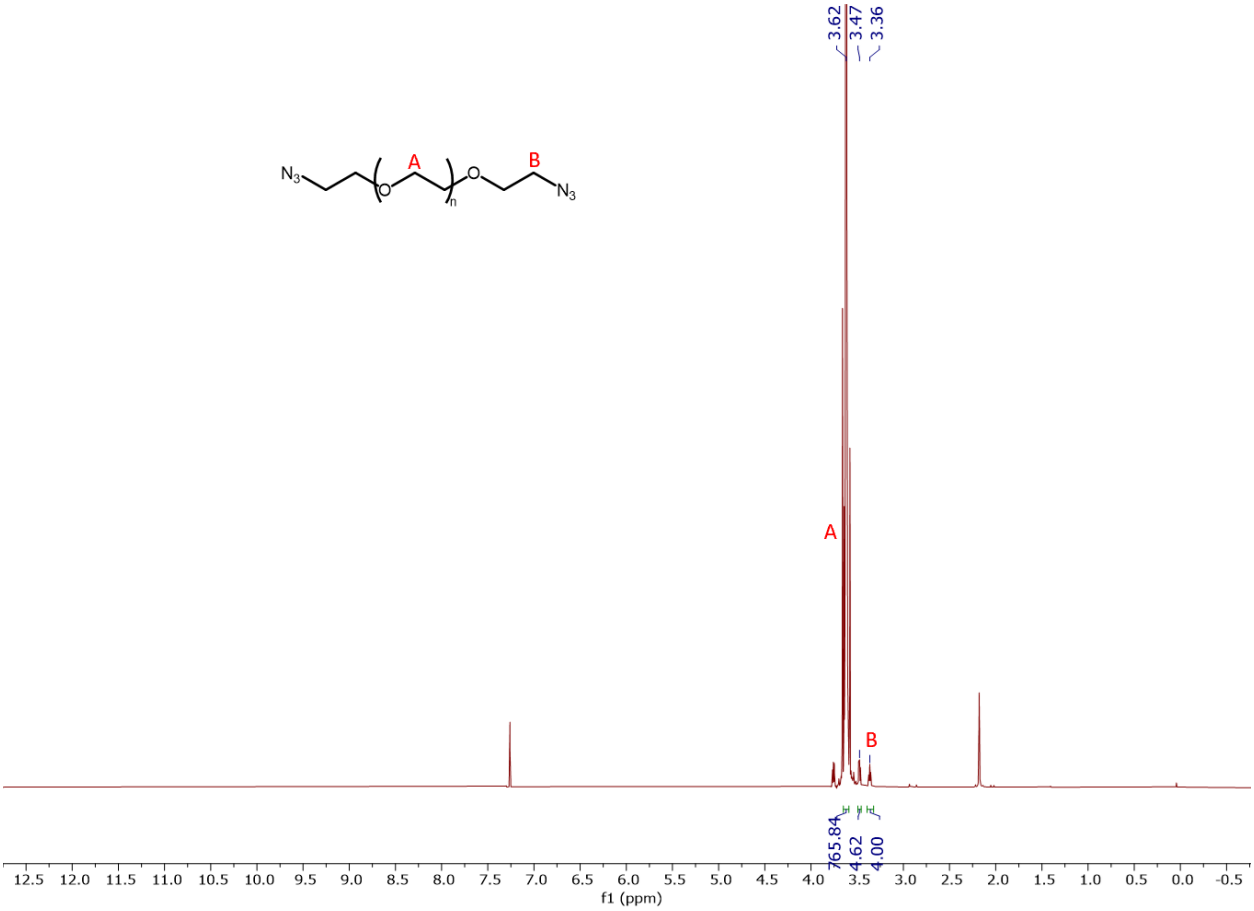

Figure C5 ^{1}H NMR spectrum of PEG-azide in $CDCl_3$.

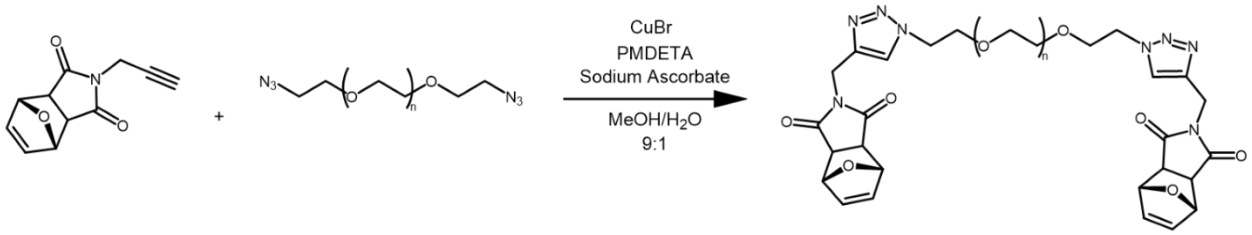

Scheme C7 Synthetic route to PEG-maleimide.

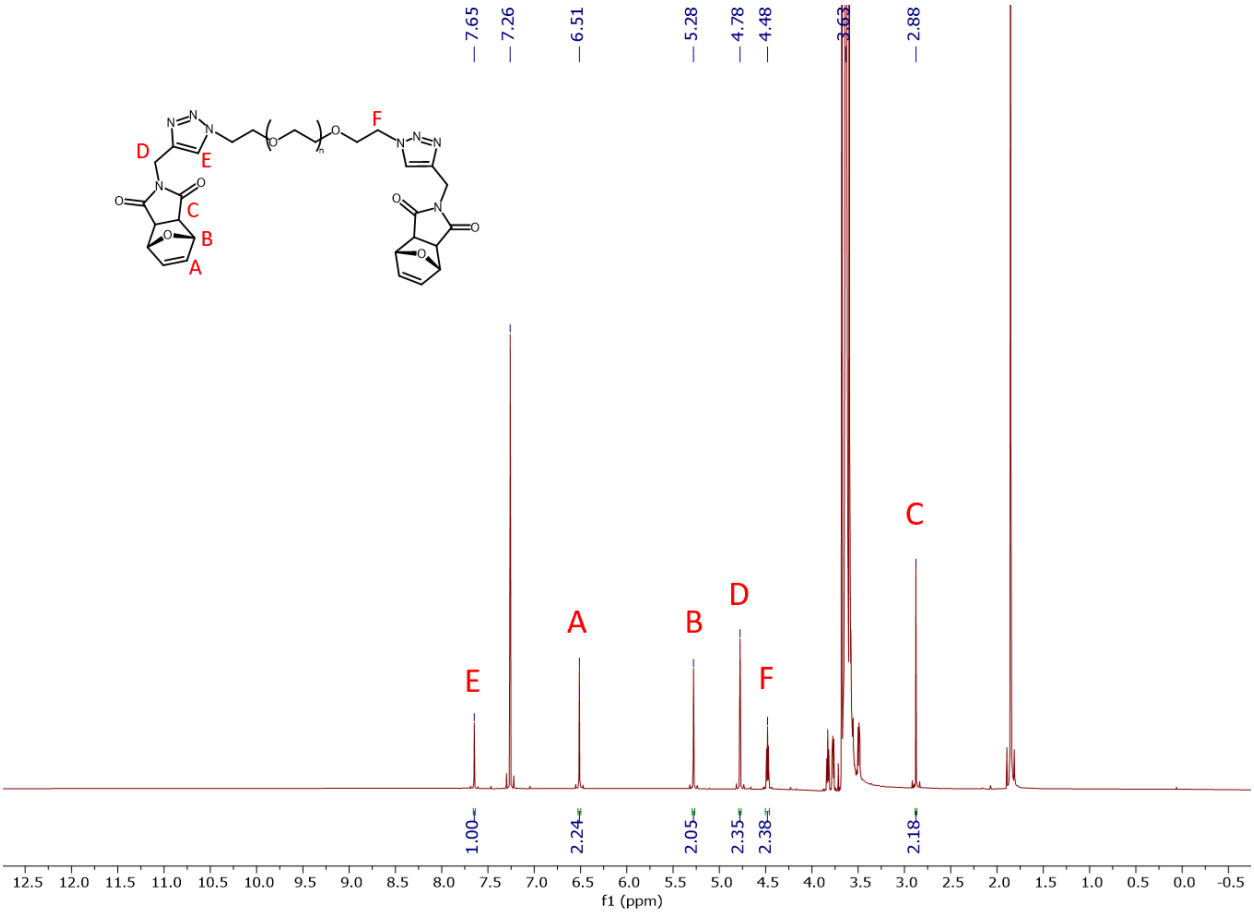

Figure C6 ^{1}H NMR spectrum of PEG-maleimide in $CDCl_3$.

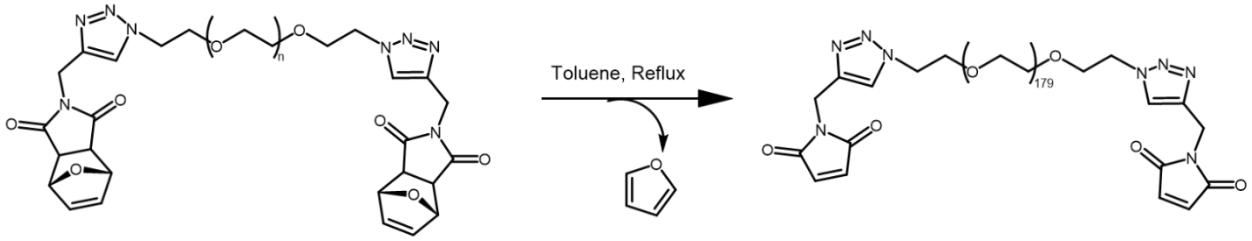

Scheme C8 Synthetic route to deprotect PEG-maleimide.

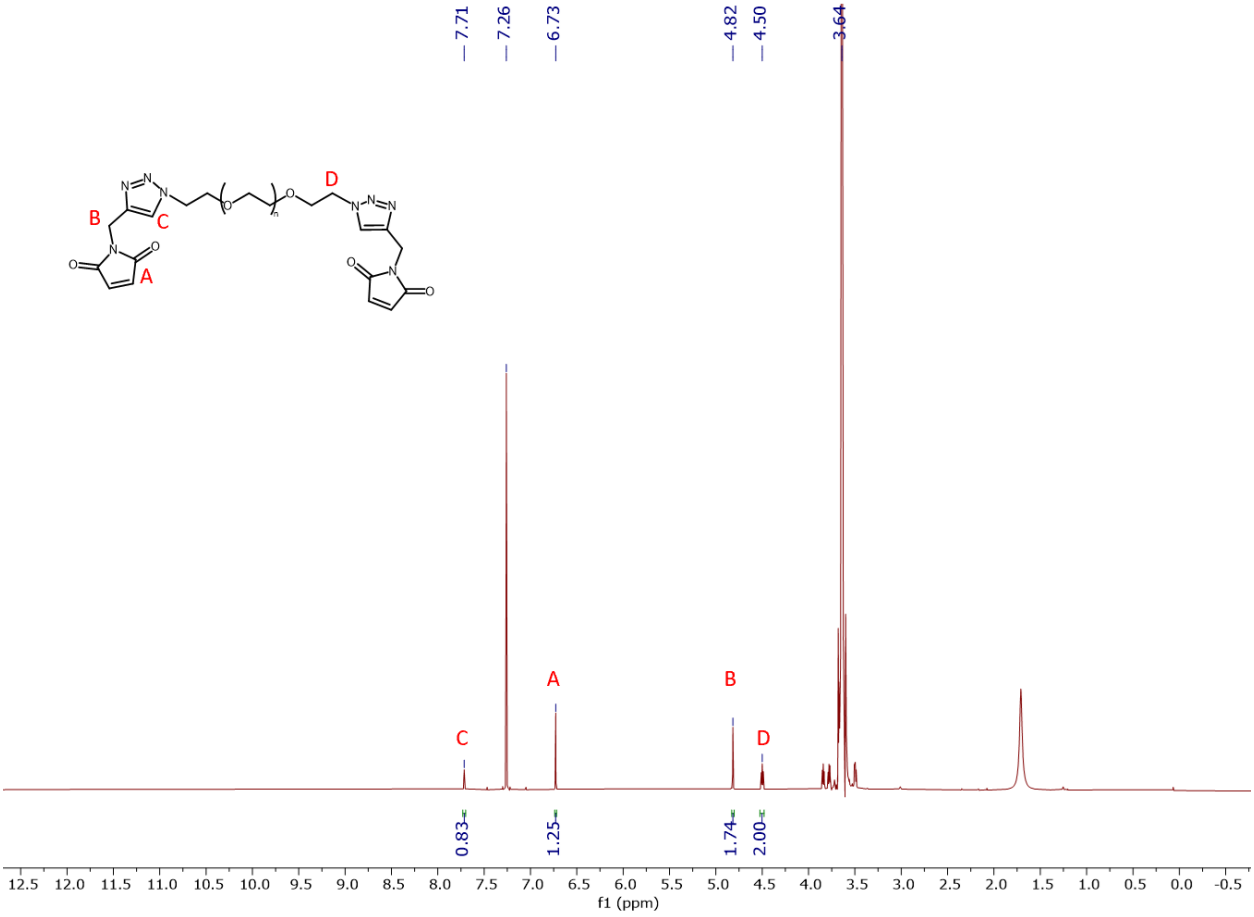

Figure C7 ^{1}H NMR spectrum of deprotected PEG-maleimide in $CDCl_3$.

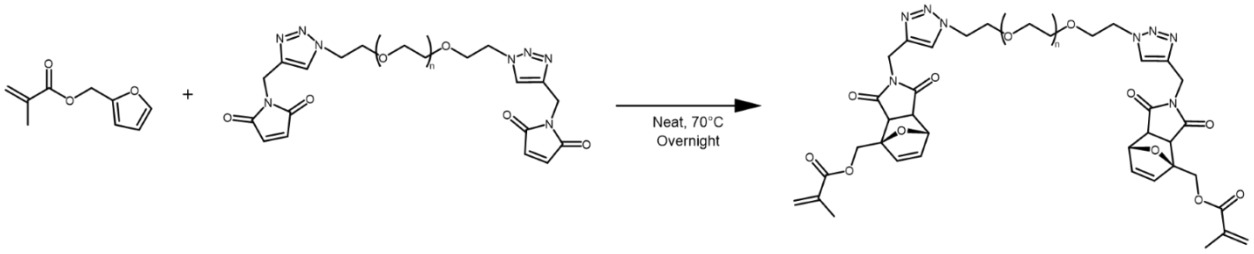

Scheme C9 Synthetic route to **DA-PEG-1**.

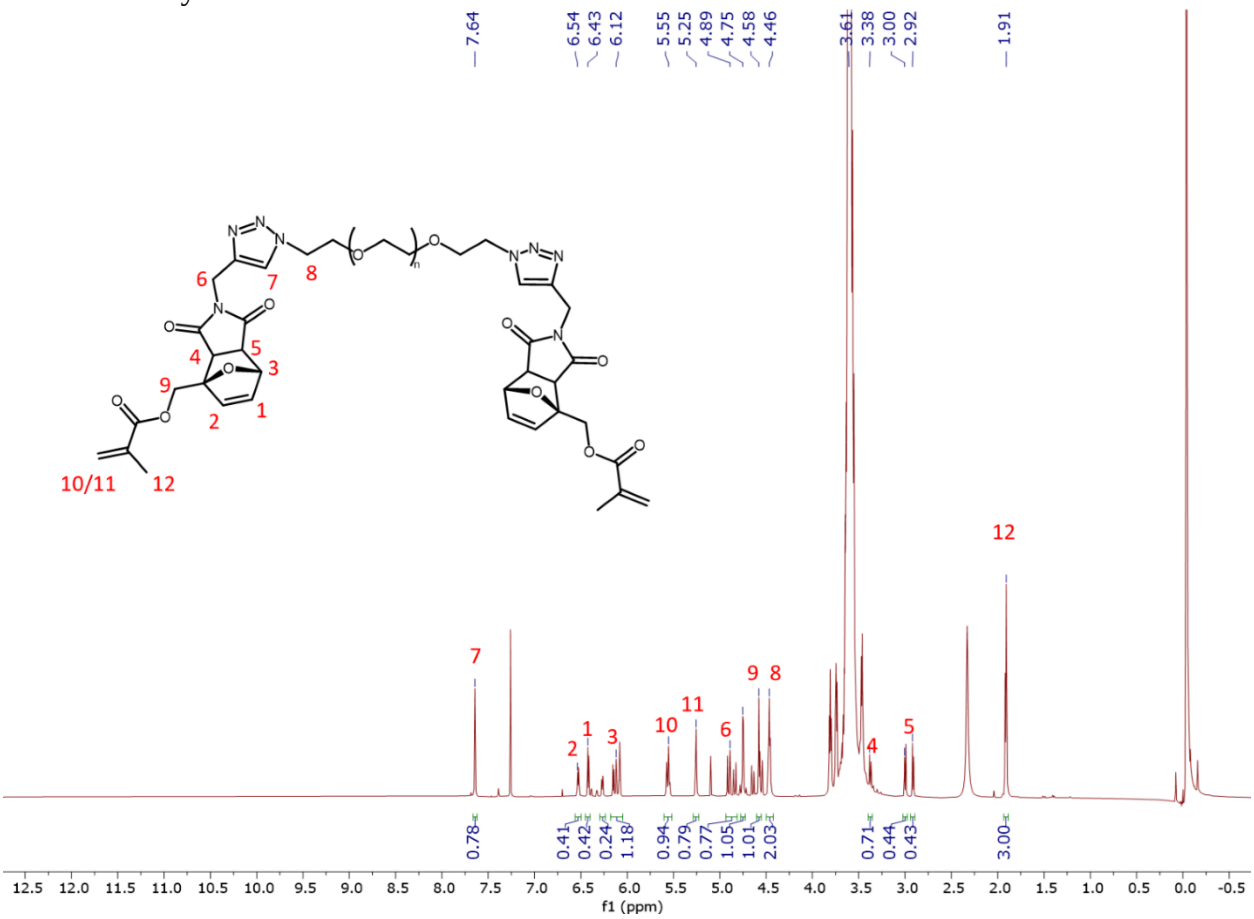

Figure C8 ^{1}H NMR spectrum of **DA-PEG-1** in $CDCl_3$.

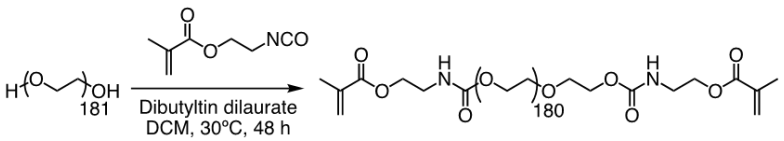

Scheme C10 Synthetic route to PEG-BUM.

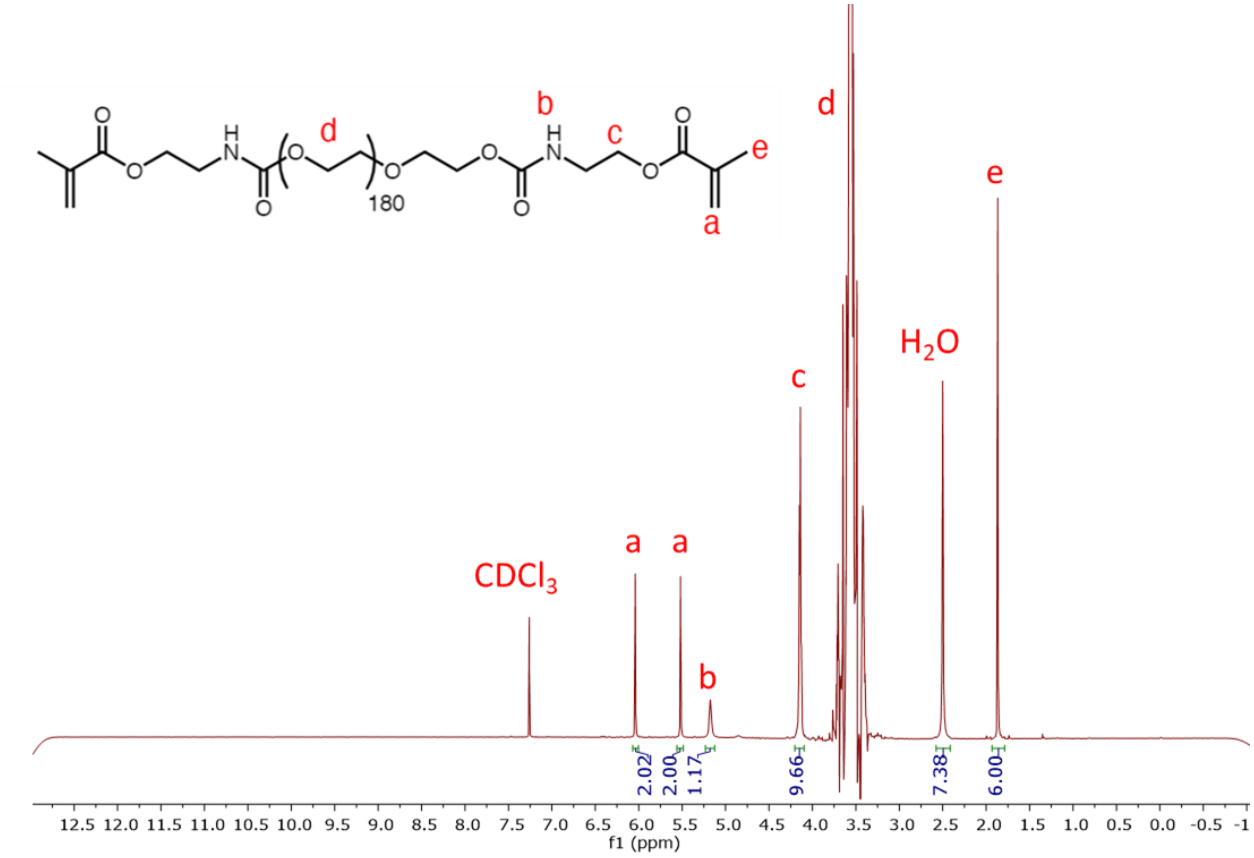

Figure C9 ^{1}H NMR spectrum of PEG-BUM in $CDCl_3$.

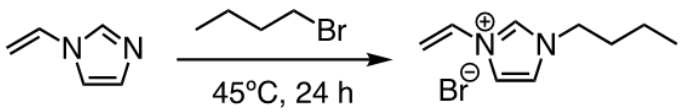

Scheme C11 Synthetic route to [BVIM]Br.

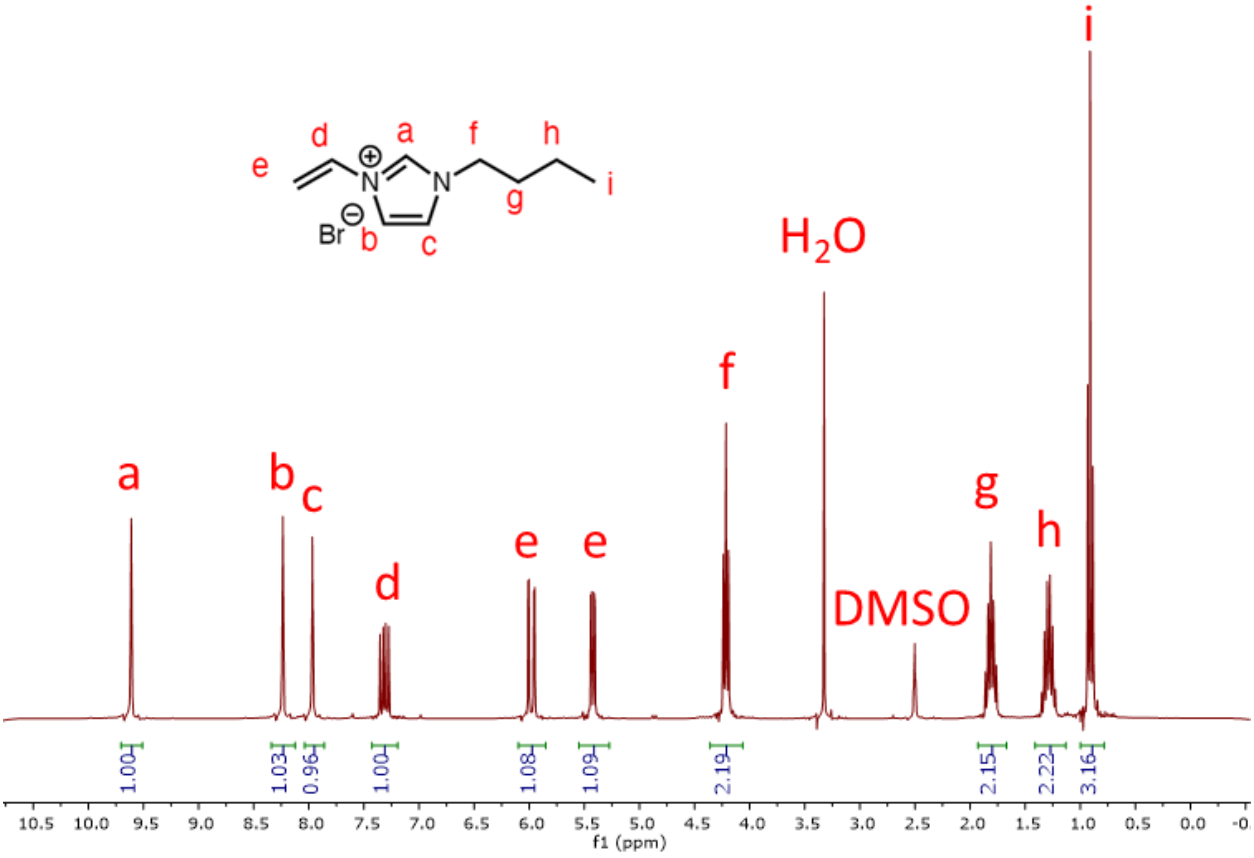

Figure C10 ^{1}H NMR spectrum of [BVIM]Br in DMSO-d_6.

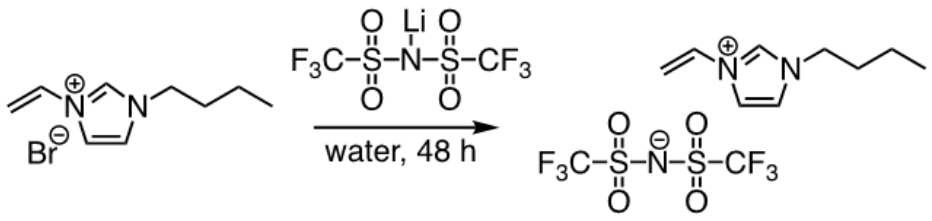

Scheme C12 Synthetic route to [BVIM]TFSI.

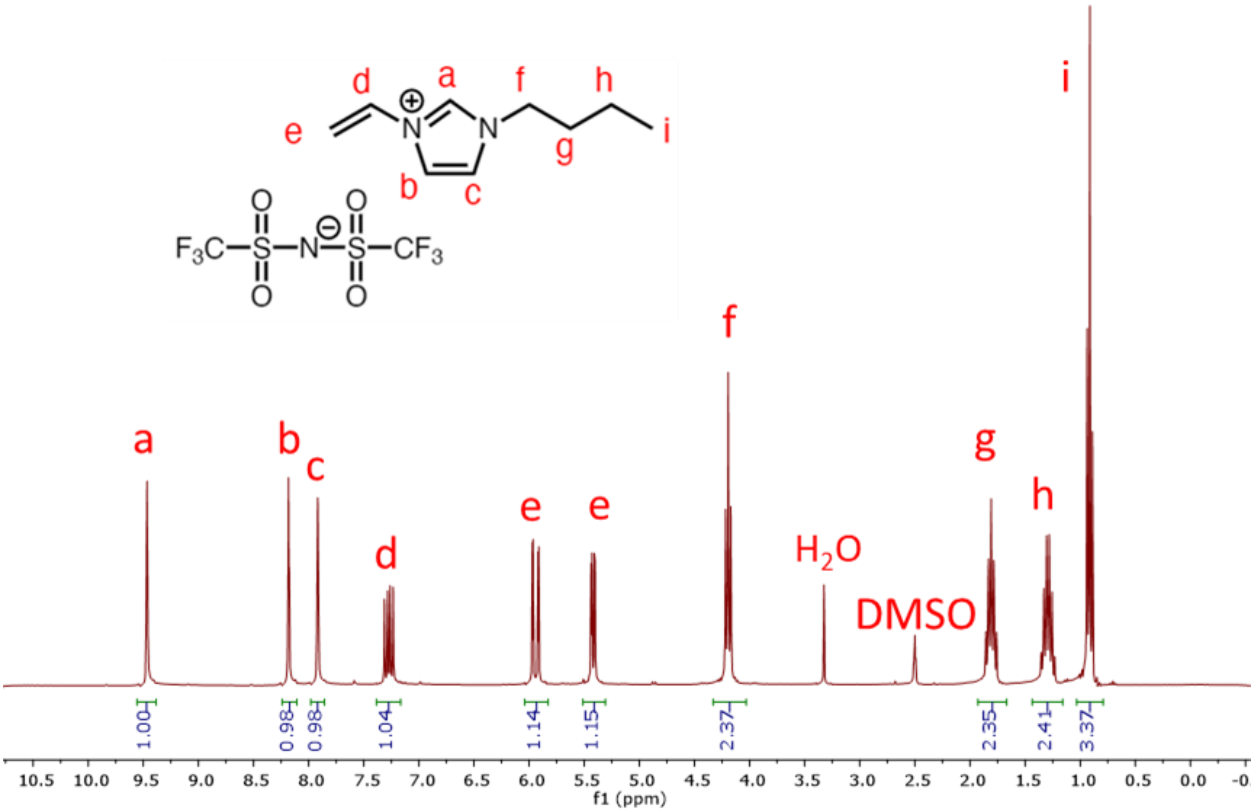

Figure C11 ^{1}H NMR spectrum of [BVIM]TFSI in DMSO-d_6.

Table C1 Formulations for Fusible Ion Gels (20 g scale).

Resin Formulation	PEG-BUM [g]	**DA-PEG-1** [g]	BAPO [g]	Sudan 1 [g]	[BVIM]TFSI [mL]
10-BVIM	0	2.0	0.15	0.005	17.85
15-BVIM	0	3.0	0.15	0.005	16.85
20-BVIM	0	4.0	0.15	0.005	15.85
7.5-7.5-BVIM	1.5	1.5	0.15	0.005	16.85

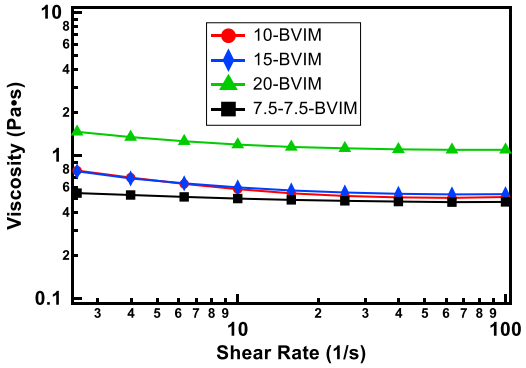

Figure C12 Viscosity vs Shear rate of ionic liquid gel resins.

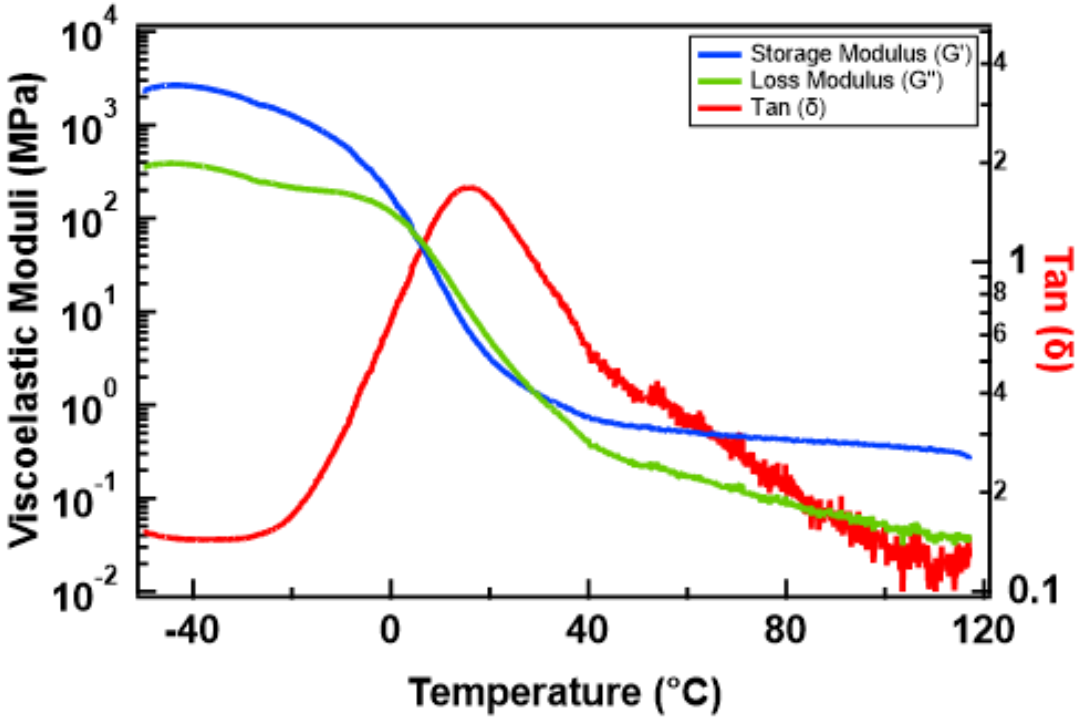

Figure C13 Dynamic Mechanical Analysis (DMA) thermogram of 7.5-7.5-BVIM sensors, demonstrating the T_g (15 °C) of the gels. Results over a temperature range of –50 °C to 120 °C are shown.

Gel Fraction:

To determine the amount of unpolymerized ionic liquid in a fully cured structure, cylindrical pucks (d = 10 mm, h = 5 mm) of each resin formulation (10-BVIM, 15-BVIM, 20-BVIM) were printed on a Form 2 SLA printer. After printing, each sample was cured for 1 h with 405 nm light under a flow of nitrogen. Each puck was soaked in 50 mL of methanol for one week, with the solvent being replaced three times over that period. After one week, the samples were removed and placed in a vacuum oven at 50 °C overnight. To determine the amount of polymerized material remaining, the mass of the fully dried sample is subtracted from the original mass of the puck. The mass lost is due to unpolymerized ionic liquid being washed out by methanol. The average results are displayed in the table below. The data reveals that under all conditions, a portion of the ionic liquid remains unpolymerized after printing, leaving the networks swollen.

Table C2 Gel fraction data of 10-BVIM.

Name	**Initial Mass (g)**	**Final Mass (g)**	**% mass lost**	**Gel Fraction**
10-BVIM (1)	0.5878	0.3742	36.33%	63.66%
10-BVIM (2)	0.5816	0.3590	37.26%	62.74%
10-BVIM (3)	0.5722	0.3462	39.49%	60.50%
Averages	0.5805 ± 0.0078	0.3598 ± 0.0140	37.69 ± 1.6239	62.30 ± 1.6252

Table C3 Gel fraction data of 15-BVIM.

Name	**Initial Mass (g)**	**Final Mass (g)**	**% mass lost**	**Gel Fraction**
15-BVIM (1)	0.5718	0.3413	40.31%	59.68%
15-BVIM (2)	0.5844	0.3659	37.39%	62.61%
15-BVIM (3)	0.5791	0.3627	37.37%	62.63%
Averages	0.5784 ± 0.0063	0.3566 ± 0.0133	38.35 ± 1.6916	61.64 ± 1.6974

Table C4 Gel fraction data of 20-BVIM.

Name	**Initial Mass (g)**	**Final Mass (g)**	**% mass lost**	**Gel Fraction**
20-BVIM (1)	0.5668	0.3583	36.78%	63.21%
20-BVIM (2)	0.5606	0.3569	36.33%	63.66%
20-BVIM (3)	0.5751	0.3642	36.67%	63.32%
Averages	0.5675 ± 0.0072	0.3598 ± 0.0038	36.59 ± 0.2345	63.39 ± 0.2345

Table C5 Gel fraction data of 7.5-7.5-BVIM.

Name	Initial Mass (g)	Final Mass (g)	% mass lost	Gel Fraction
7.5-7.5-BVIM (1)	0.5814	0.3765	35.24%	64.75%
7.5-7.5-BVIM (2)	0.5781	0.3724	35.58%	64.41%
7.5-7.5-BVIM (3)	0.5774	0.3767	34.76%	65.24%
Averages	0.5789 ± 0.0021	0.3752 ± 0.0024	35.19% ± 0.4119	64.8% ± 0.4172

Table C6 Summary of Mechanical Characterization Data.

Materials	10-BVIM	15-BVIM	7.5-7.5-BVIM	20-BVIM
Nominal Stress at Break, σ_b (kPa)	1090.51 ± 122.51	468.02 ± 43.31	485.79 ± 24.34	253.51 ± 3.18
Nominal Strain at Break, ε_{tb} (%)	1184.91 ± 121.47	860.59 ± 21.12	897.96 ± 30.20	693.52 ± 33.24
Young's Modulus, E_t (kPa)	739.30 ± 217.89	119.09 ± 18.68	235.67 ± 25.31	67.32 ± 16.17

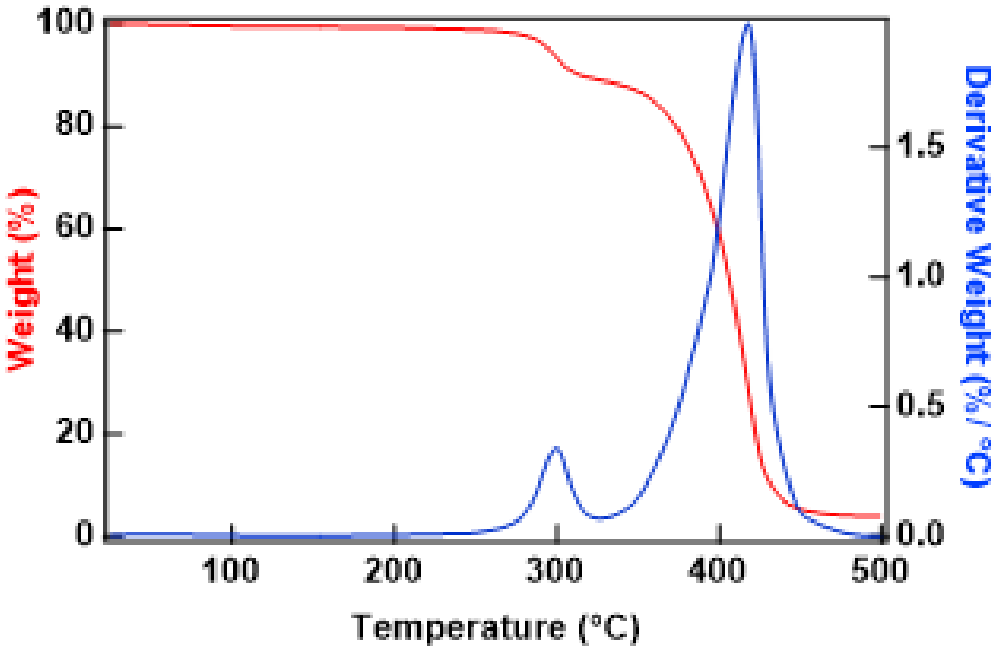

Figure C14 TGA thermogram of 7.5-7.5-BVIM. In red is the mass loss (%) of sample during heating. In blue is the derivative of mass loss (%/ °C) of samples during heating.

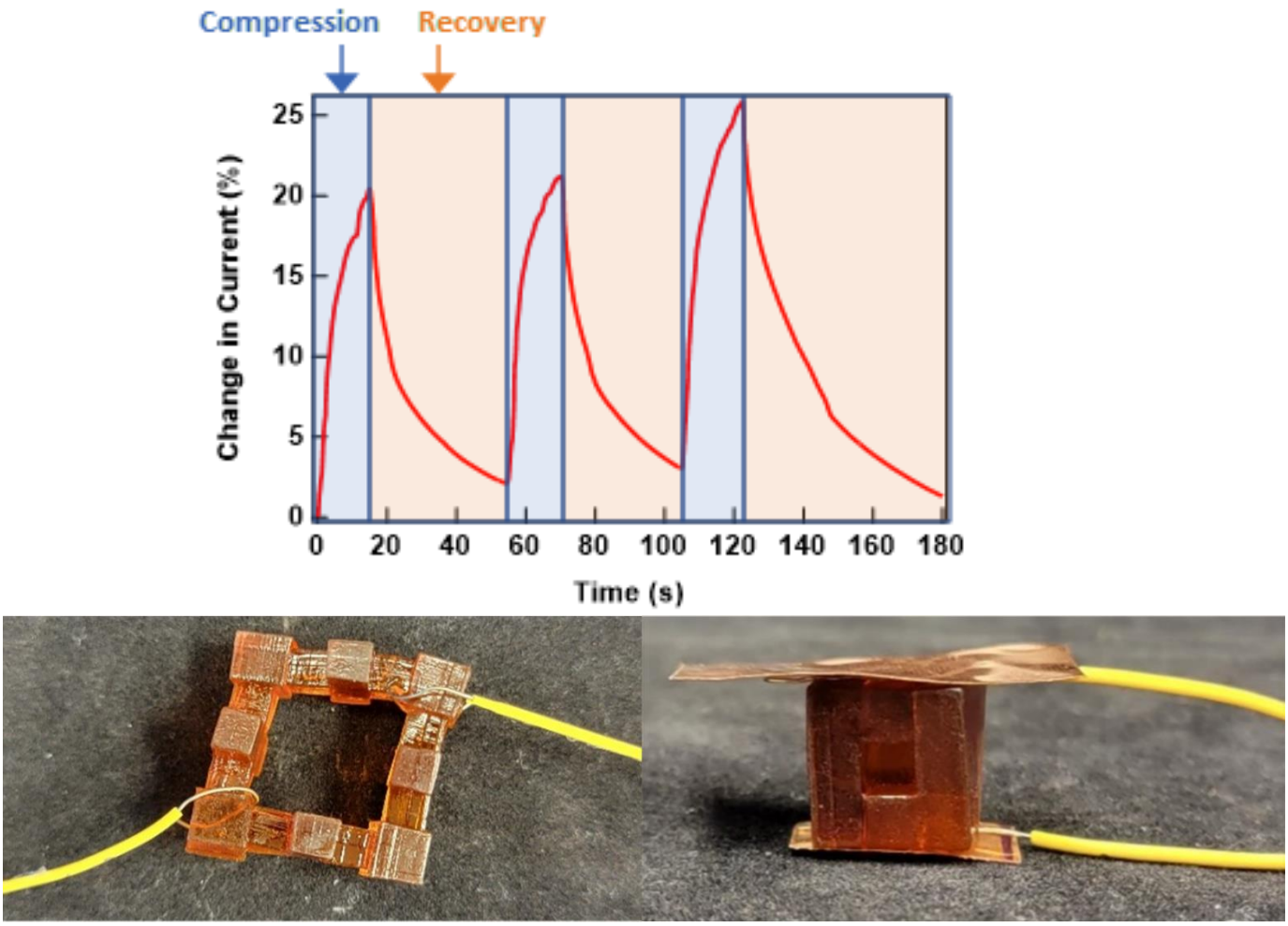

Figure C15 SMU graph demonstrating change in conductivity of cubic sensor in response to compression. Also shown is the connection of the sensors to the SMU.

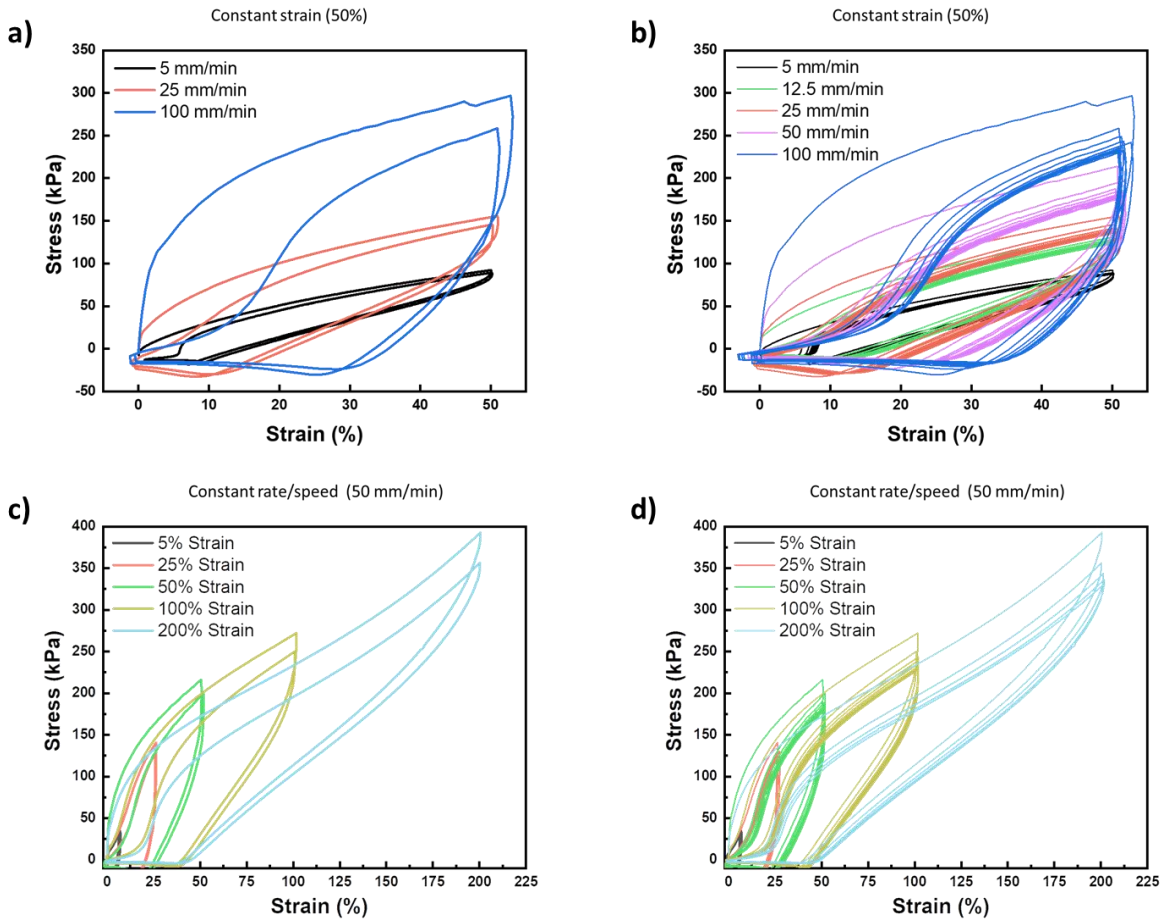

Figure C16 Cyclic tensile stress-strain fatigue test a) 2 cycles b) 10 cycles. Also shown are cyclic tensile stress-strain curves at different strain rates c) 2 cycles d) 10 cycles.

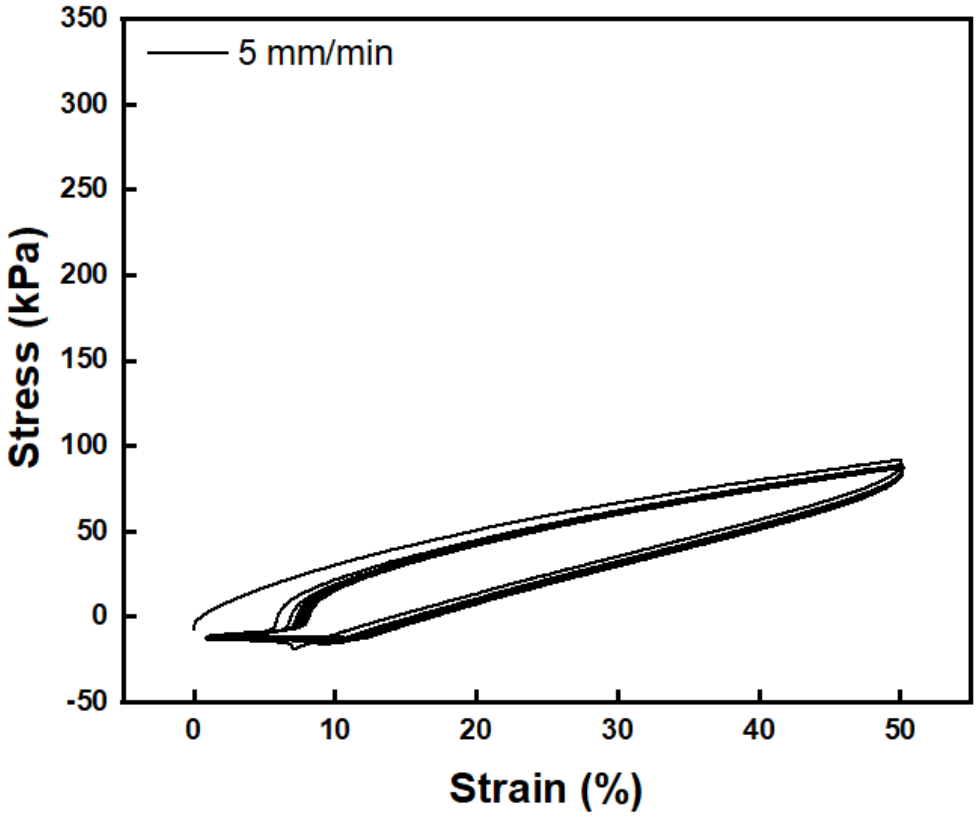

Figure C17. Cyclic tensile stress-strain fatigue test at rate of 5 mm/ min at 50% strain.

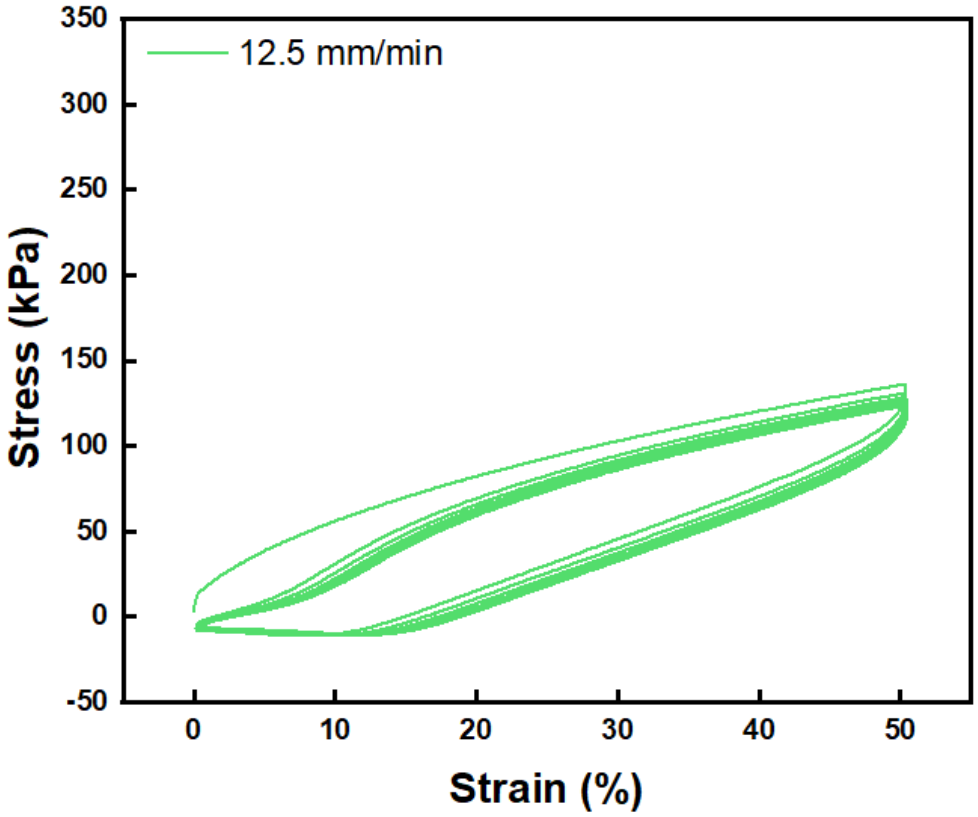

Figure C18. Cyclic tensile stress-strain fatigue test at rate of 12.5 mm/ min at 50% strain.

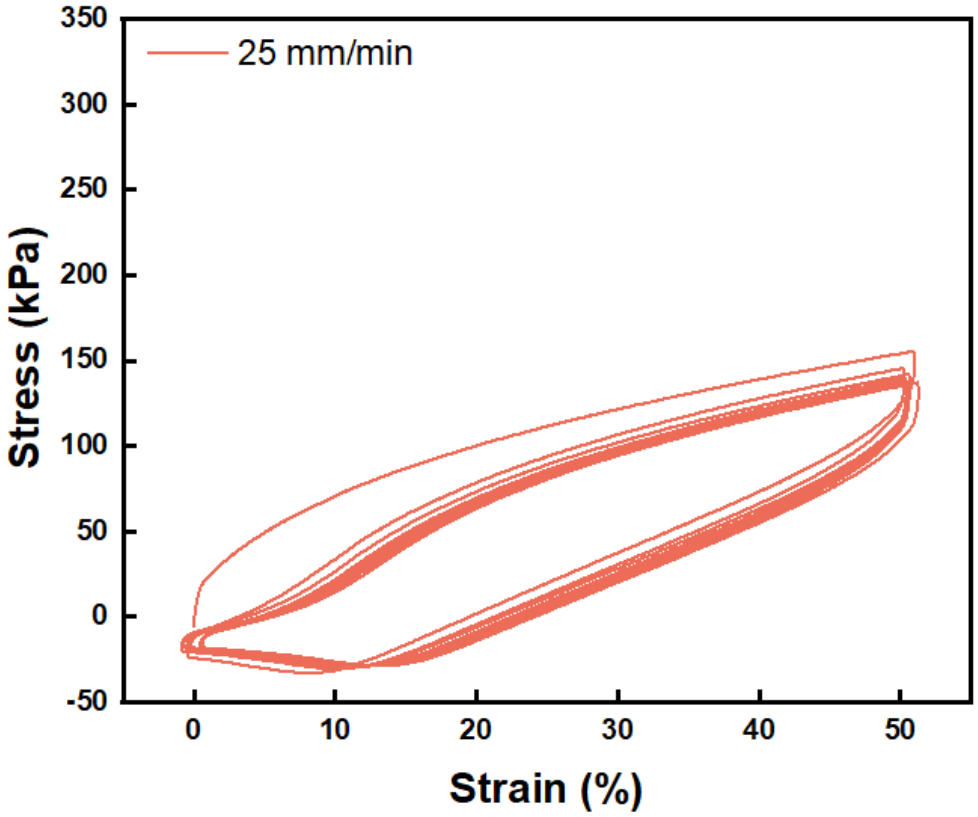

Figure C19. Cyclic tensile stress-strain fatigue test at rate of 25 mm/ min at 50% strain.

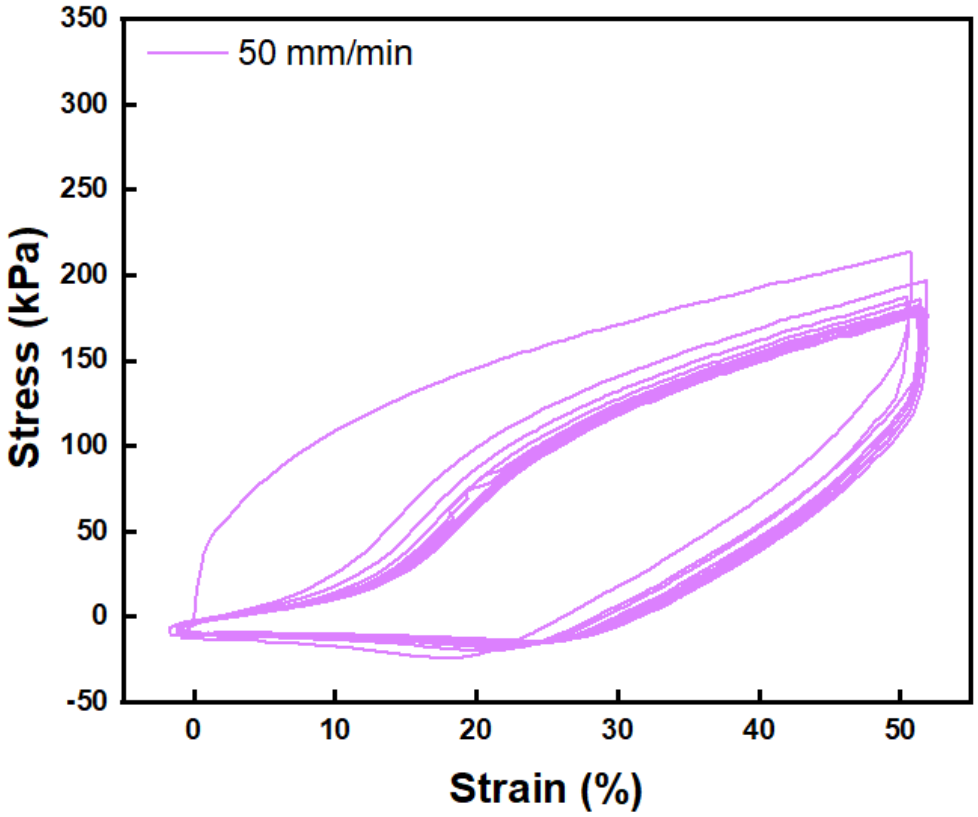

Figure C20. Cyclic tensile stress-strain fatigue test at rate of 50 mm/ min at 50% strain.

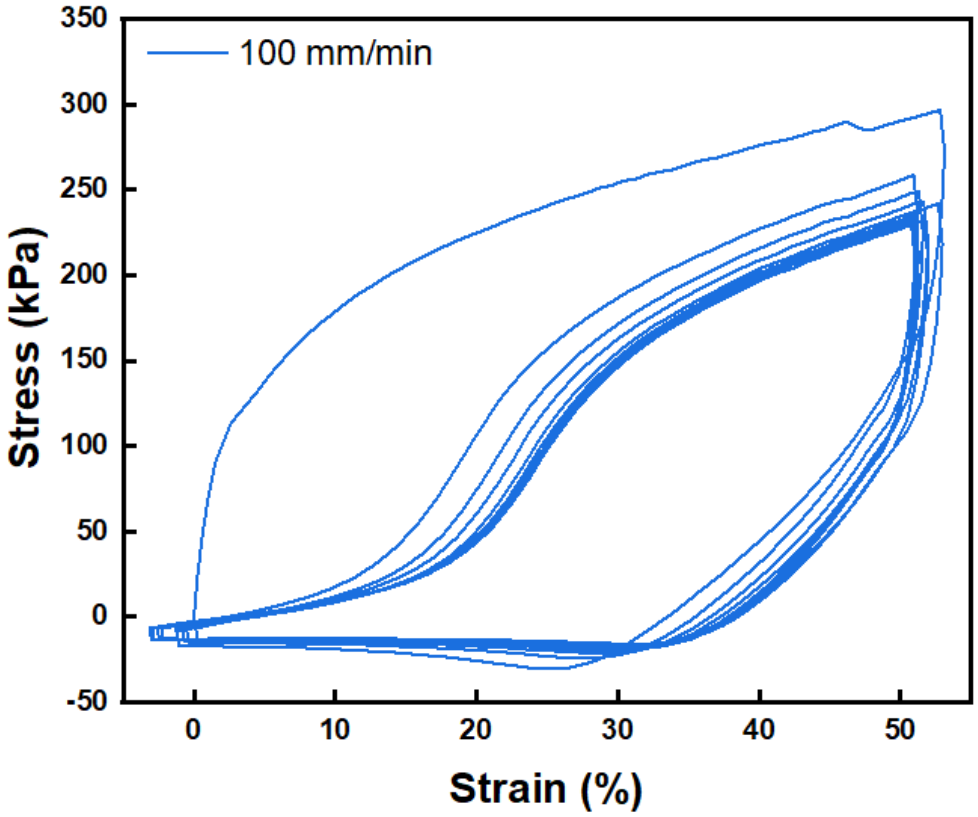

Figure C21. Cyclic tensile stress-strain fatigue test at rate of 100 mm/ min at 50% strain.

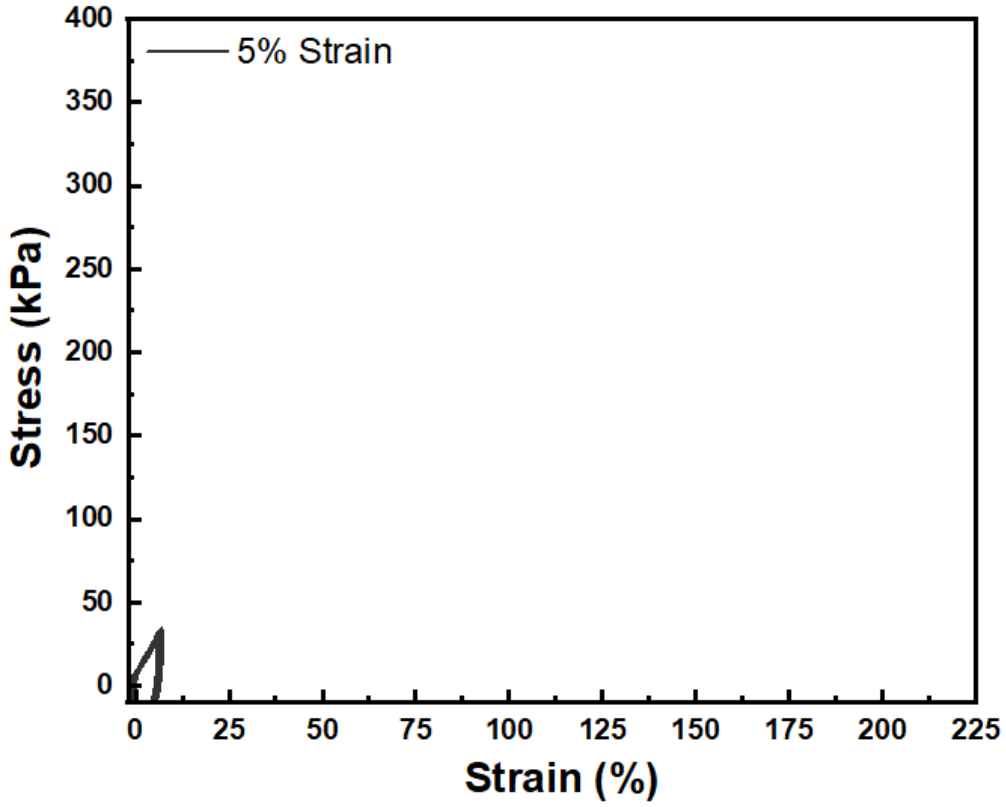

Figure C22. Cyclic tensile stress-strain fatigue test at 5% strain at a rate of 50 mm/ min.

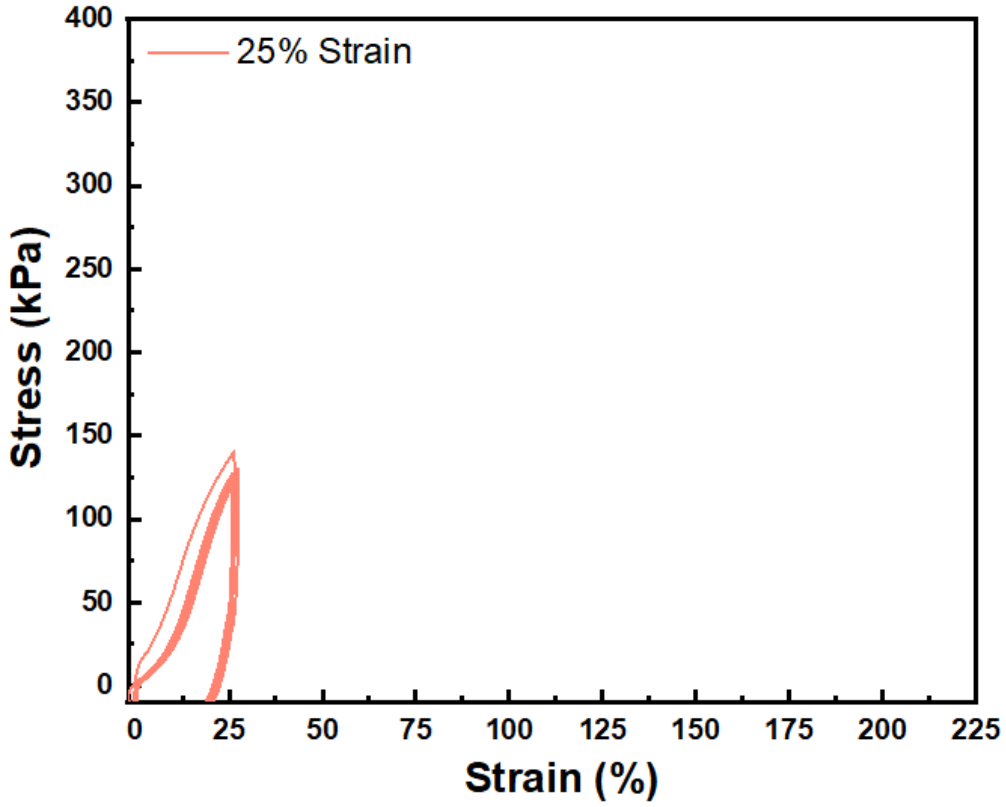

Figure C23. Cyclic tensile stress-strain fatigue test at 25% strain at a rate of 50 mm/ min.

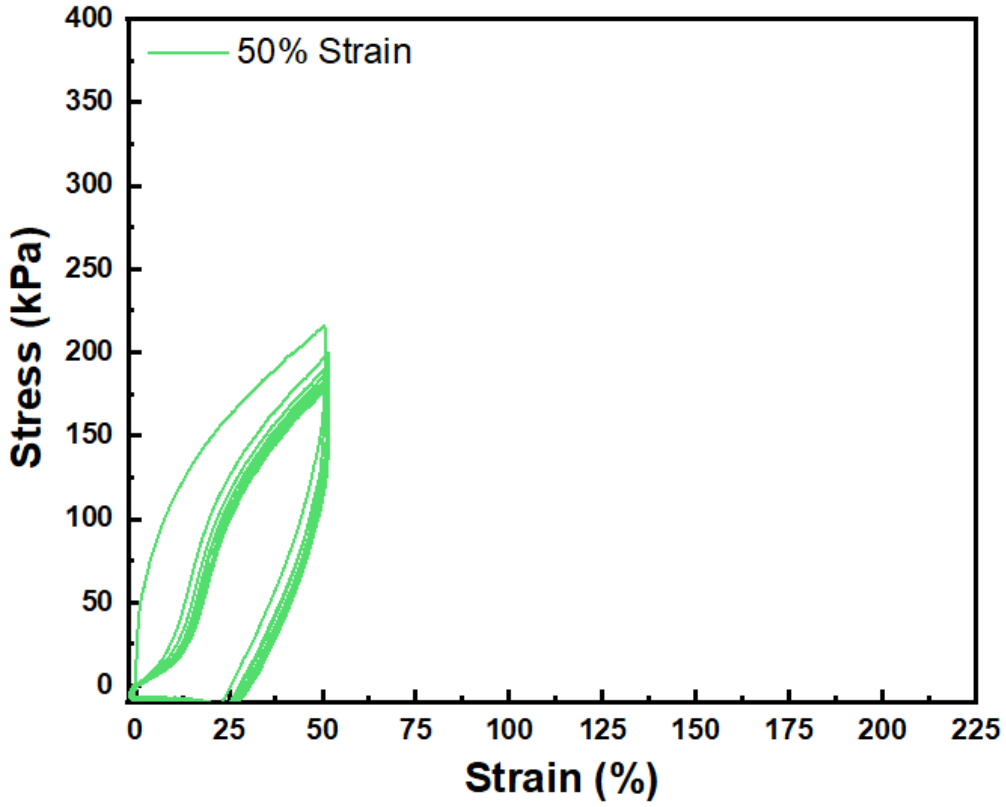

Figure C24. Cyclic tensile stress-strain fatigue test at 50% strain at a rate of 50 mm/ min.

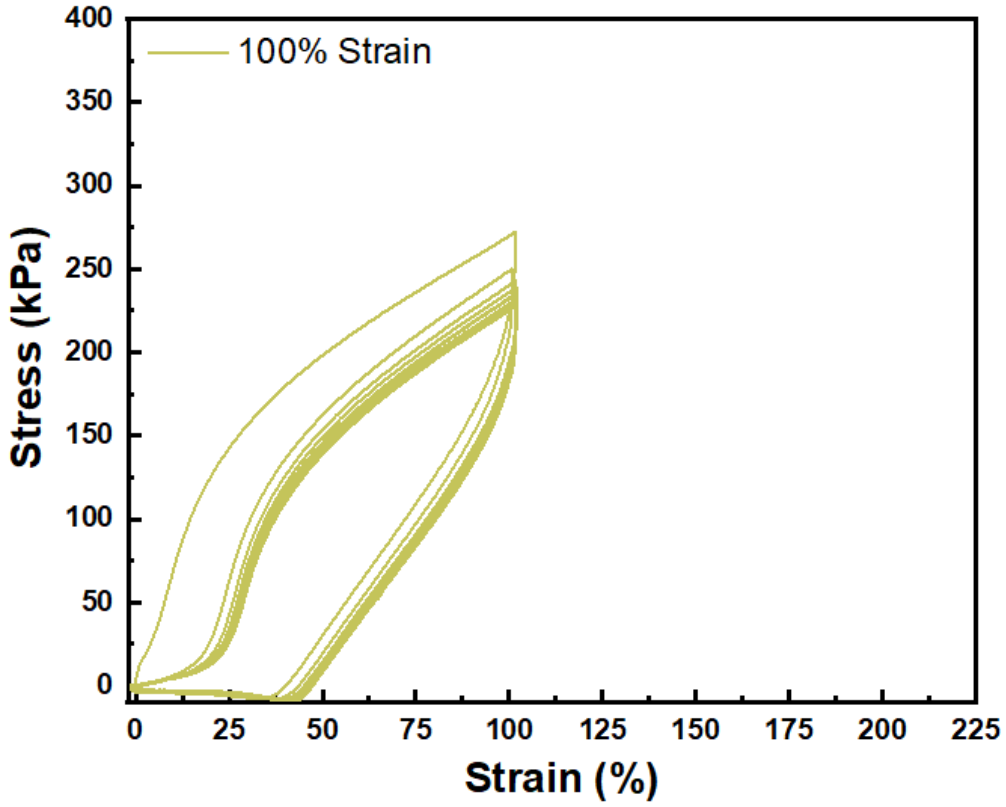

Figure C25. Cyclic tensile stress-strain fatigue test at 100% strain at a rate of 50 mm/ min.

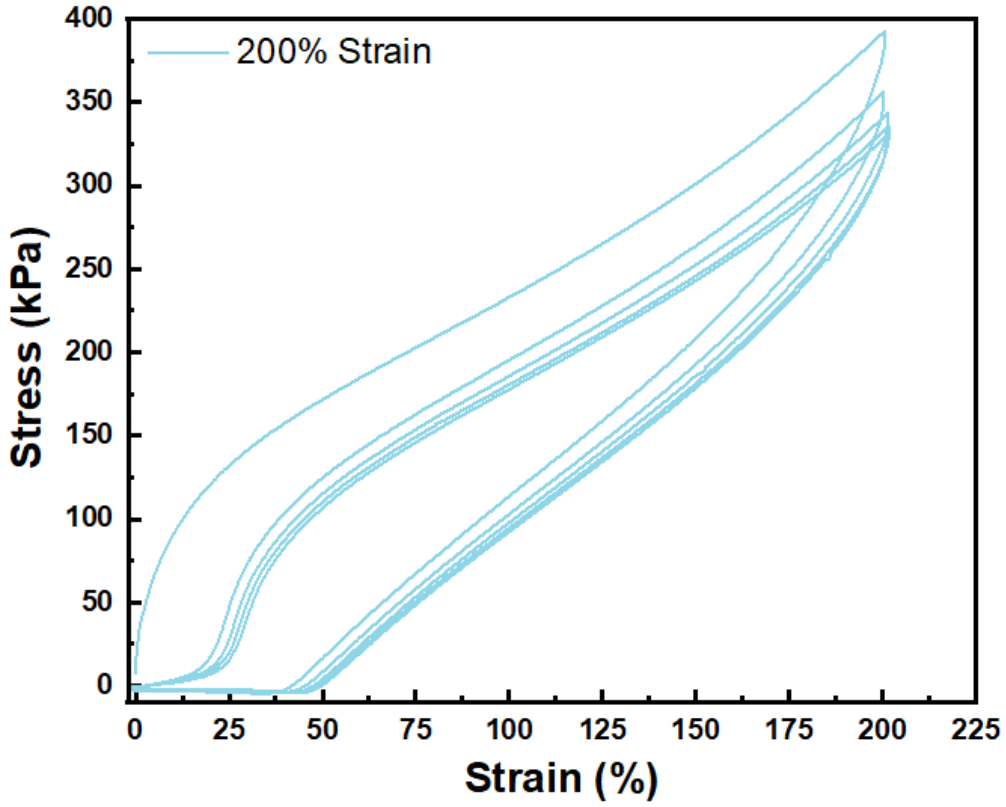

Figure C26. Cyclic tensile stress-strain fatigue test at 200% strain at a rate of 50 mm/ min.

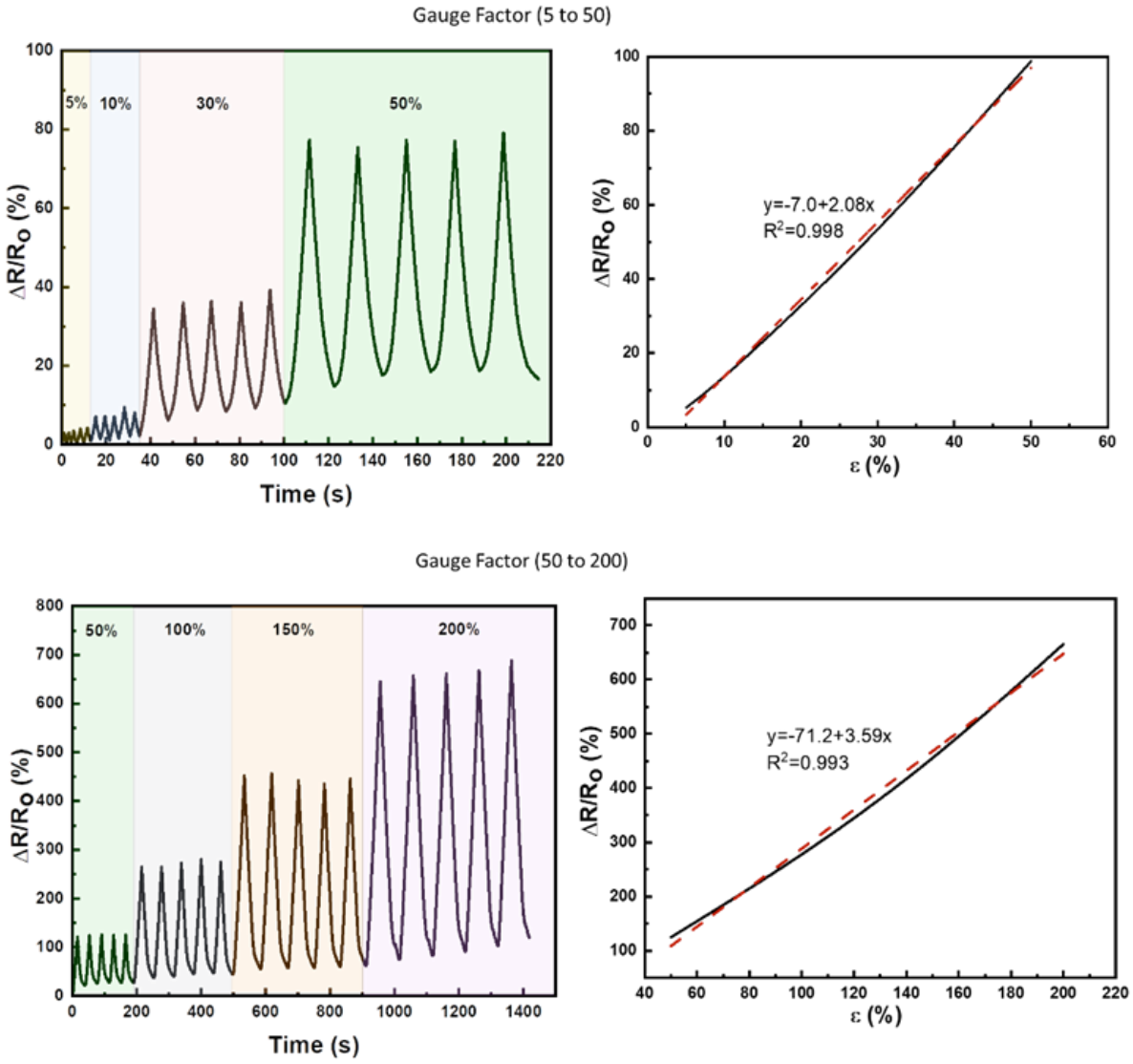

Figure C27 Top Left & Bottom Left: Change in resistance at different strain amounts, ranging from 5-50% strain and 50-200% strain. Top Right & Bottom Right: Change in resistance vs % strain. The slope of the line is the gauge factor.

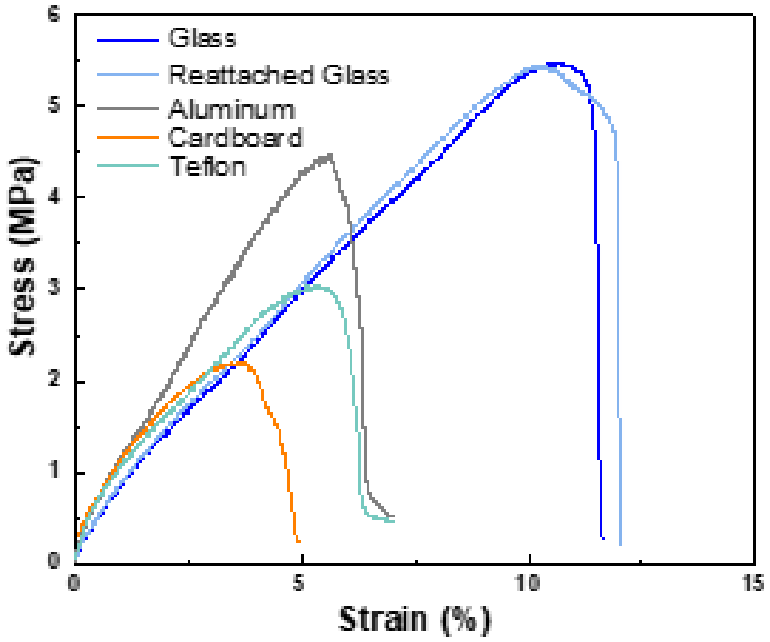

Figure C28 Stress vs strain graph demonstrating adhesion of ion gel sensors to various substrates.

Table C7 Summary of adhesion data.

Substrate	Stress at Break (MPa)	Strain at Break (%)
Glass	5.45 ± 0.14	10.9 ± 0.56
Reattached Glass	5.37 ± 0.8	10.34 ± 0.21
Aluminum	4.42 ± 0.6	5.62 ± 0.32
Cardboard	2.02 ± 0.35	3.65 ± 1.05
Teflon	3.04 ± 0.42	5.36 ± 0.98

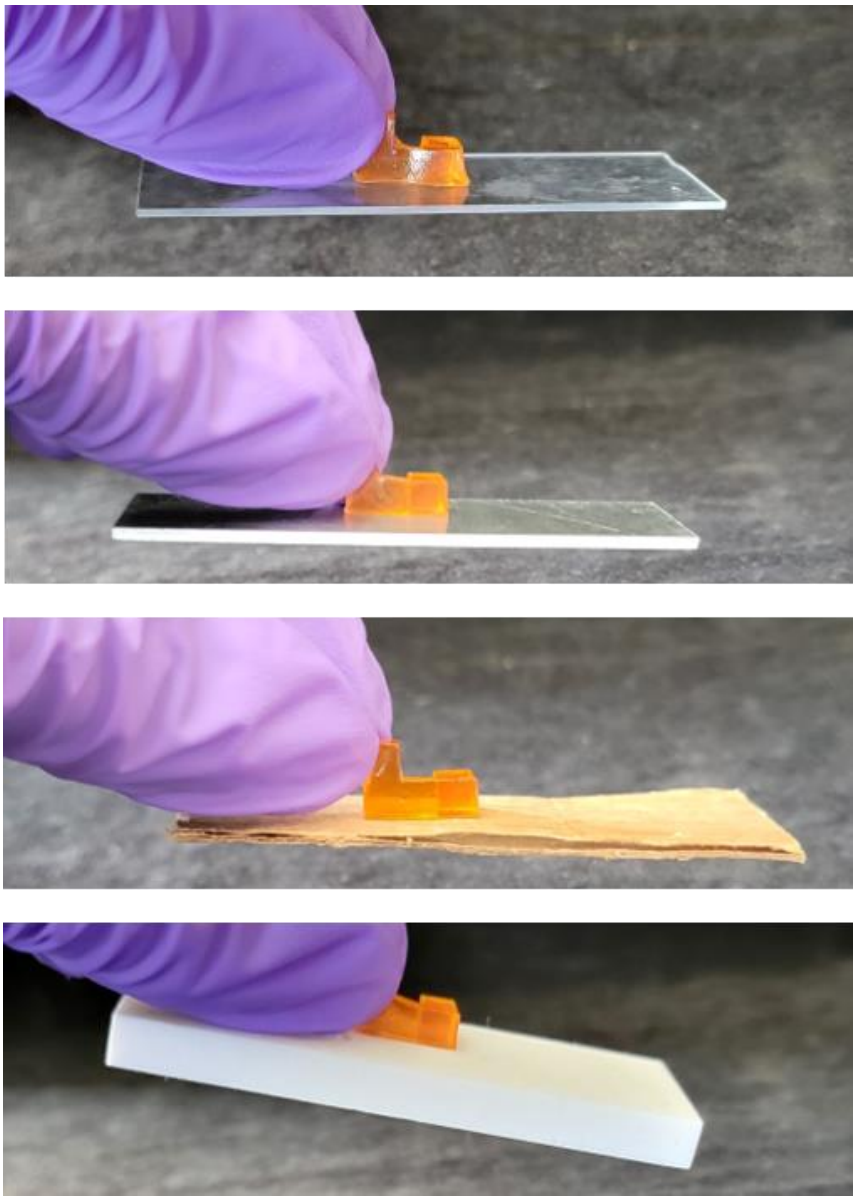

Figure C29 Images demonstrating sensor adhesion to glass, aluminum, cardboard, and Teflon.

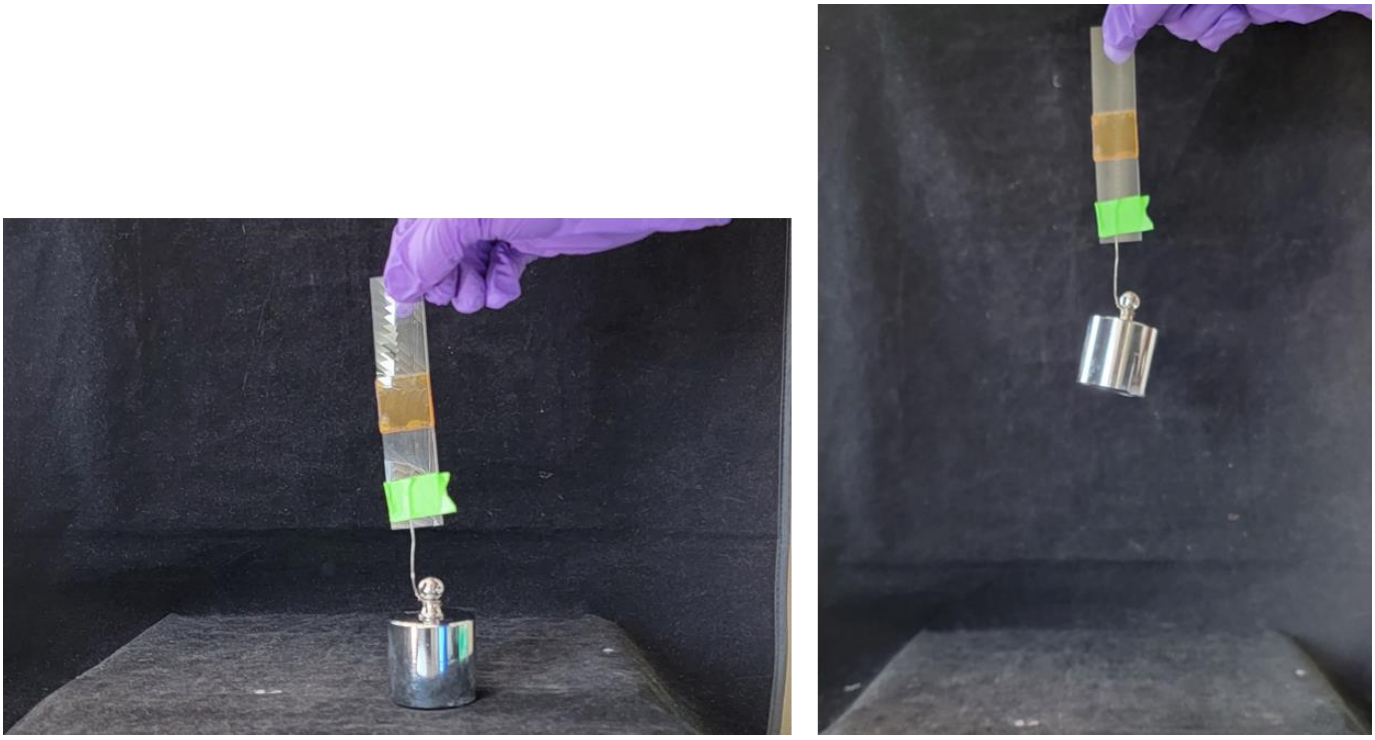

Figure C30 Image demonstrating adhesive patch (2.5 cm x 2.5 cm) supporting a 500g weight.

Figure C31. 15-BVIM gels, which contain solely dynamic crosslinks, experienced loss of fidelity during heating at 60 °C.

VITA

Julian Smith-Jones was raised in Takoma Park, MD. He lived there until he graduated from high school in 2013, after which he attended Morehouse College in Atlanta, GA as an undergraduate. He graduated with a BS in chemistry in 2017 before moving west to attend the University of Washington for his graduate studies. Julian conducted graduate research in the lab of Professor Alshakim Nelson, where he worked on the synthesis and characterization of ionic liquid gels as a platform for creating conductive elastomeric sensors.